The Parent Bodies of Fine-grained Micrometeorites: A *Petrologic & Spectroscopic Perspective*

A thesis submitted for the degree of

Doctor of Philosophy

By

Martin David Suttle

Department of Earth Science and Engineering,

Imperial College London

In association with The Natural History Museum, London

April 2018

Abstract

Micrometeorites are millimetre-scale cosmic dust grains, derived from asteroids and comets. They represent the largest flux of extraterrestrial material currently falling to Earth, with an estimated contribution of 20,000-60,000 tons per year. In this thesis, the geological history, parent body properties and atmospheric entry of fine-grained micrometeorites are investigated through micro-analysis and spectroscopic techniques.

The degree of aqueous alteration within fine-grained micrometeorites was investigated using criteria initially developed for CM chondrites (Chapt.3). This revealed that most particles are intensely altered, with petrologic subtypes <CM2.3. Textural and geochemical evidence of aqueous alteration is seen in the form of hydrated CAIs, hydrated sulfides, pseudomorphic chondrules and complex intergrown and cross-cut assemblages of phyllosilicate, which attest to extended periods in contact with liquid water. Likewise, the apparent overabundance of CM-like matrix and the relative paucity of C2 chondrule material among fine-grained micrometeorites suggest that the parent bodies of fine-grained micrometeorites are predominantly intensely aqueously altered bodies.

This study also identified the first evidence for shock deformation in fine-grained micrometeorites (Chapt.6). Weak, pervasive petrofabrics, formed by aligned phyllosilicates and inferred from dehydration crack orientations were observed in the majority of micrometeorites studied (21). This requires relatively low peak pressures (<5GPa) and is most likely achieved by successive low-intensity impact events. The presence of a single micrometeorite containing brittle deformation cataclasis fabrics also provides evidence for brittle deformation shock processing of micrometeorites.

The first near-IR spectra of micrometeorites were collected and directly compared against the NIR spectra of young C-type asteroids (Chapt.8). Although these comparisons proved inconclusive, owing to limitations in the quality of the micrometeorite spectra, this study identified the first evidence of hydroxyl-group absorption bands at NIR wavelengths in Veritas family asteroids, suggesting the presence of intact phyllosilicates on their surfaces and thereby adding support to the genetic link between fine-grained micrometeorites and C-type asteroids.

Mid-IR spectroscopy revealed how micrometeorite mineralogy evolves during flash heating in the upper atmosphere, demonstrating that solid state recrystallization preserves pre-atmospheric textures, despite major changes in the mineralogy (Chapt.4). Spatially resolved Raman spectroscopy was used to investigate thermal gradients within micrometeorites during atmospheric entry and revealed that most micrometeorite cores preserve low-temperature (<300°C) carbonaceous phases inherited from their parent asteroid (Chapt.5). The development of secondary interconnected porosity was described for the first time, detailing how the growth and expansion of dehydration cracks driven by the out-gassing of volatiles leads to the formation of branching and sinuous channels (Chapt.7). These channels play an important role in the efficient heating of micrometeorite cores resulting in partial melting as scoriaceous micrometeorites are formed. In addition, the development

of secondary porosity significantly lowers the mechanical strength of micrometeoroids, promoting their disruption in the atmosphere.

Finally, a small-scale study, attempting to retrieve fine-grained micrometeorites preserved in ancient sedimentary rocks was trailed (Chapt.9). This led to the recovery of a new collection of fossil micrometeorites derived from Cretaceous chalk. Although no unmelted micrometeorites were discovered, the preserved cosmic spherules are found to have experienced complete diagenetic alteration, resulting in preserved micro-textures and replaced terrestrial mineralogies. A repeat study at a different time period and location also found cosmic spherules with identical preservation styles, suggesting that diagenetically altered micrometeorites most likely represent the most common form of cosmic dust on Earth.

Acknowledgements

I am most grateful to my primary supervisor Dr. Matt Genge who first encouraged me to take up a six-month research project in cosmic dust back in 2013 - as part of my master's programme. Dr. Matt Genge and Dr. Natasha Stephen would later suggest that a PhD in planetary sciences would be wise and thoroughly rewarding experience. Beyond all else, Matt has ensured that my time as a PhD student remained challenging, educational and interesting. I am proud to have been able to publish several components of my PhD thesis as journal articles, and this would not have been possible without his continued tuition and advice.

I would also like to thank Prof. Sara Russell, who has been a kind and helping voice throughout my study. Having welcomed me into the field, introduced me to many colleagues, as well as the dizzying array of meteorite specimens held at the museum and guided my research questions to some highly productive topics.

A huge thanks is given to Dr. Luigi Folco. I am not only grateful for the loan of TAM micrometeorites, and for the postage of a single curious micrometeorite (TAM37P-03) across the channel late into my PhD, but also for the many discussions by email and in person on the geochemistry, formation and alteration of Antarctic micrometeorites. Luigi has also provided me with comments, revisions and advice throughout my PhD. I am, therefore, looking forward to working with him next year as a post doc in Pisa!

There is also Dr. Matthias van Ginneken, who taught me how to identify and micro-manipulate cosmic dust under optical microscope and who pointed my research towards the enigmatic TAM collection. His instruction and willingness to answer any question - no matter how trivial - were much appreciated in the early stages of my PhD. Later, I met Jon Larsen and was introduced to his Project STARDUST mission, collecting micrometeorites from urban areas. I am grateful to have been a little part of this extraordinary operation and to have worked together with Jon when we first confirmed the extraterrestrial origin of some Norwegian rooftop particles. Today, I am working on more particles from Jon's collection, looking at how aerodynamic sculpting during atmospheric entry results in tailed and "twin-headed" cosmic spherules.

There are many technical staff at the NHM, Diamond Lightsource and Imperial College London, who also deserve a mention, having provided invaluable tuition and support as well as a large dose of patience during my study. I thank Tony Wighton and Callum Hatch for their sample preparation skills, generating many resin blocks of cosmic dust and polishing even the tiniest of particles under the most trying constraints. I also thank Dr. Natasha Almeida and Dr. Giles Miller for loan of samples and Dr. Tobias Salge, Dr. Tomasz Góral and Dr. Chris Jones for their expertise and support, whilst using EMMA lab equipment. John Spratt, in particular, must be thanked for the many hours he has spent sitting in front of an SEM with me explaining technical and theoretical details or fixing errors thrown up by the whimsical EVO. While, Dr. Tina Geraki at Diamond and Dr. Jens Najorka at the NHM are thanked for their time spent training me in mid-IR and μXRD techniques respectively.

I also thank Dr. Vincent Baeten at the Walloon Agricultural Research Centre and Dr. Alessandro Maturilli the German Aerospace Centre, both of whom kindly allowed me to use their near-IR spectrometers for a week's data collection. Although the NIR spectra from micrometeorites were

ultimately disappointing their willingness to support my research was highly encouraging and greatly appreciated.

In addition, I would like to thank my mum, dad, two brothers and girlfriend – Fiona – who listened endlessly to tales of cosmic dust, attended several talks I gave on the same topic and helped to collect material from rooftops, chalk cliffs or even Antarctica(!) to aid my research in the hunt for micrometeorites. Their motivation when times were low, and their guidance throughout cannot be overstated.

Finally, I thank Dr. Gareth Collins and Prof. Martin Lee, for their time spent examining this thesis and providing corrections and advice.

This thesis was funded by a training grant (#ST/M503526/1) from the Science and Technology Facilities Council (**STFC**) and in association with Imperial College London as a direct funder and the NHM as a joint research centre and awesome place to work!

Fig.0. The author, after collecting chalk blocks from the North Downs, part of the search for fossil micrometeorites in Cretaceous chalk.

Declaration of orginality

I declare that the work submitted in this thesis is my own, except where otherwise stated.

Signed: …… Date: **04-2018**

Copyright declaration

Contents

Chapter 1: Introduction

1.1 What are micrometeorites?

Micrometeorites are defined by Genge et al., (2008) as sub-millimetre extraterrestrial dust particles which have survived atmospheric entry and are recovered from the Earth's surface. By contrast, Rubin and Grossman (2010) define (micro-)meteorites as natural solid objects (between 10µm-2mm in size), which were derived from a celestial body, transported outside the dominant gravitational influence of that body and that later collided with a body larger than itself. This broader definition allows all extraterrestrial dust grains, even those that fall on Mars or other asteroids, to be defined as micrometeorites. In practice, however, the field of micrometeoritics is limited to the analysis of cosmic dust, using laboratory microanalysis techniques.

Micrometeorites form a continuum between smaller (<50µm) inter-planetary dust particles (IDPs) and larger (>2000µm) meteorites which, when combined represent the complete flux of extraterrestrial material arriving on Earth (Zolensky et al., 2006). This distinction between classes, based upon size, reflects differences in the parent body sources and consequently, differences in the petrology of materials (Zolensky et al., 2006). Micrometeorites are known to sample both asteroids and comets (Genge et al., 1997; Nesvorný et al., 2003; 2006; Noguchi et al., 2015) and it is this diversity, representing a significantly larger number of objects but also a different composition of parent bodies – including many which would otherwise remain unsampled – that make micrometeorites such an attractive research area. Furthermore, micrometeorites are abundant, relatively easy to recover and significantly understudied, in comparison to their larger meteorite counterparts.

This thesis focuses on the most abundant class of unmelted micrometeorites, most likely derived from C-type asteroids (Brownlee et al., 1997; Nesvorný et al., 2006; Vernazza et al., 2015). This group shares many petrographic similarities to the hydrated CM, CR and CI carbonaceous chondrites (Kurat et al., 1994; Noguchi et al., 2002; Genge et al., 2008; Suavet et al., 2010; Taylor et al., 2012; van Ginneken et al., 2012). However, previous analyses have also suggested that fine-grained micrometeorites may be derived from a distinct chondrite group, related to the hydrated carbonaceous chondrites (Engrand et al., 1998; Battandier et al., 2018). As such, debate on the origin and petrography of fine-grained micrometeorites continues.

1.2 Solar system formation and evolution

Models of the early solar system (0-150Ma) are constrained by the current distribution of planets and small bodies (DeMeo and Carry, 2014; Izidoro et al., 2015), by comparison with distant star systems (Fogg and Nelson, 2007; Carrasco-González et a., 2016), through dynamical simulations (Levison et al., 2009) and from empirical data obtained from extraterrestrial materials, including fireballs, meteorites and cosmic dust (McKeegan and Davis, 2003; Kunihiro et al., 2004; Palme et al., 2015; Greenwood et al., 2016).

The *Solar-Nebula-Disk-Model* (SNDM), describes the current consensus hypothesis for the origin and evolution of the solar system (Woolfson, 1993; Montmerle et al., 2006). In this scenario the partial collapse a giant molecular cloud, approximately 4.6Ga ago (McKeegan and Davis, 2003), resulted in the formation of a hot dense nebula characterised by a rapidly accreting central protostar, surrounded by a sphere of gas and dust. This nebula cloud progressively flattens into a protoplanetary disk as a result of angular momentum (Dullemond and Dominik, 2004; Montmerle et al., 2006; Brogan et al., 2014; Carrasco-González et al., 2016) and subsequently dissipates as gas is either consumed by the protosun, swept away by radiation pressure emitted from the sun or condenses and accretes into small porous dust clusters (Dullemond and Dominik, 2005; Blum, 2010).

The accretion of solid matter within the protoplanetary disk over the size range 1µm-1km remains problematic, as neither electrostatic nor gravitational forces can adequately explain growth (Blum, 2010). Instead, streaming instabilities or high-density dust regions are required to facilitate growth (Chambers, 2004; Blum, 2010). However, once objects reach >1km diameter, runaway growth, driven by collisional events leads to the development of several thousand planetary embryos (~500km diameter), termed planetesimals (Kleine et al., 2002; Bizzarro et al., 2005; Walsh et al., 2012). The majority of these objects did not survive the later turbulent collisional period, termed the giant impact era (Charnoz and Morbidelli, 2003; Dawson et al., 2016), and were either ejected from the solar system (Charnoz and Morbidelli, 2003; Walsh et al., 2012) or incorporated into larger bodies that ultimately grew to form planets (Chambers, 2004). However, the giant impact era also left a residual population of highly deformed planetesimal fragments, which now reside within the asteroid belt (Asphaug et al., 2006). Among these, the two largest objects [1] Ceres and [4] Vesta are the last surviving intact planetesimals (Russell et al., 2012).

The current planetary configuration, broadly reflects a cosmochemical gradient, characterised by an inner solar system dominated by refractory-rich terrestrial planets and an outer solar system composed of volatile-rich gas giants, ice giants, and trans-Neptunian comets (Lewis, 1974). Similar thermal gradients are also observed in young, protoplanetary disks (van Boekel et al., 2004). Within our own solar system, the snowline - defined as the radial distance at which volatile compounds such as water, methane, carbon dioxide and ammonia condense from the gas phase - separates the inner and outer solar system (Lecar et al., 2006). Today, the snowline lies outside the asteroid belt, between Mars and Jupiter, however, the radial position of this line may have varied over time, dependent on the opacity of the disk and the output energy of our evolving sun (Lecar et al., 2006). Furthermore, computational modelling suggests that the presence of Jupiter may have interrupted the migration of volatile gases moving inwards during accretion and resulted in the *fossilization* of the snowline, thereby leaving the inner solar system depleted in volatile elements (Morbidelli et al., 2016).

The SNDM therefore provides a coherent explanation of the solar system's evolution, which is supported by abundant observational data (Brogan et al., 2014; Carrasco-González et al., 2016). However, this model is also incomplete, since multiple phenomena remain unexplained by a static solar system model, where planets form *in-situ*, at their current radial distances and relative positions.

For example, the presence of volatile-rich cometary objects found within the asteroid belt and, therefore, inside the snowline (DeMeo and Carry, 2014), the distribution and diversity of Jupiter's Trojan asteroids (Morbidelli et al., 2005), the origin of the Late Heavy Bombardment (LHB) (Gomes et al., 2005) and an apparent Martian mass deficit (Walsh et al., 2011; Izidoro et al., 2015) all imply a chaotic early history, dominated by radial mixing. Additionally, an increasing number of distant extrasolar systems have recently been discovered by the Kepler space telescope. Most of these systems are distinctly different from our own, containing unusual planetary configurations that cannot be explained by a static formation model. For instance, several extrasolar systems contain *hot Jupiters*, gas giants whose masses are greater than Jupiter's but orbit their host stars at 1AU or less (Fogg and Nelson, 2007). Collectively, this body of evidence strongly implies a post-accretion period of planetary migration in which planetesimals are scattered by gravitational perturbations arising as the gas giants Jupiter and Saturn undergo both inward and outward migration, lock into orbital resonances and potentially swap positions (Morbidelli et al., 2005; Walsh et al., 2011 and others).

Currently, two competing mechanisms of giant planet migration and radial mixing exist; the *Nice Model* (Morbidelli et al., 2005; Gomes et al., 2005; Tsiganis et al., 2005; Levison et al., 2007) and the *Grand Tack Model* (Walsh et al., 2011; 2012). The *Nice Model* proposes that approximately 400Ma after formation; Jupiter and Saturn enter a 2:1 orbital resonance. This generates significant gravitational perturbations, causing planets and planetesimals in the outer solar system to migrate further outwards (Tsiganis et al., 2005) and leading to the scattering and depletion of the Kuiper belt comets (Morbidelli et al., 2005; Levison et al., 2007). Meanwhile, inner solar system asteroids are transported further inwards resulting in the LHB and causing Jupiter's outward migration to slow and reverse (Gomes et al., 2005). By expanding and separating, the movement of the gas giants depletes the early solar system planetesimal population whilst also explaining the unusual distribution of Trojan asteroids, main belt comets and the intense cratering record preserved on the moon. Conversely, the *Grand Tack Model* attempts to explain the mass deficit of Mars by invoking a rapid, early inward migration of Jupiter, which interrupts the accretion of terrestrial planets. Jupiter moves inwards to ~1.5AU, consuming much of the condensed matter that would have otherwise built Mars. Later, Jupiter is pulled outwards again, to its current position, after establishing a mean motion resonance with Saturn (Walsh et al., 2011; 2012). Both planetary migration scenarios contain a component of inward and outward movement and both cause scattering, ejection and collisions between planetesimals, however, the timing and dynamics of each model are distinct and remain hotly debated. Alternatively, empirical data obtained from the analysis of meteorites and cosmic dust provides further clues to the formation and evolution of the early solar system.

1.3. The chondritic assemblage and early solar system

Chondrites are a large and diverse class of primitive, undifferentiated meteorites united by the presence of chondrules, spherical droplets with igneous textures, embedded within a matrix of finer-grained material (Weisberg et al., 2006). Chondrites are relicts left over from the early solar system; representing precursor materials to (Chambers, 2004; Alexander, 2005; Barrat et al., 2016) and/or by-products of planetary formation (Krot et al., 2005; Kleine et al., 2005; Asphaug et al., 2006; Sanders et

al., 2012). Because these meteorites have remained unaltered or only mildly reprocessed since the beginning of the solar system (Alexander, 2005; Bland et al., 2005; Krot et al., 2009), analysis of their geochemistry, mineralogy and textures provides empirical constraints on the timing, physical conditions and mechanisms of condensation, accretion and planetesimal growth.

The carbonaceous chondrite (sub)class contains eight groups and (many ungrouped individual meteorites) (Weisberg et al., 2006), all of which contain bulk chemical compositions closely aligned to solar values (Palme et al., 2015). The relative abundance of elements within these chondrites is, therefore, similar to the proportions of elements within the Sun's photosphere, and consequently, preserves the primordial chemical signature of the protoplanetary disk (Gounelle, 2011). The main structural components within carbonaceous chondrites include calcium-aluminium-rich inclusions (CAIs), chondrules and matrix, in variable proportions, both within and between chondrite subgroups (Weisberg et al., 2006). CAIs are refractory-rich condensates representing the first solar system solids (McKeegan and Davis, 2003; Alexander, 2005; Kita et al., 2005; Krot et al., 2009). The young ages of these inclusions provide the time-zero anchor for the start of the solar system (McKeegan and Davis, 2003; Krot et al., 2009). Furthermore, short-lived extinct radionuclide dating systems suggest that the CAIs formation window was short (<700Ka, Kita et al., 2005; Krot et al., 2009) while the presence of rare igneous textured CAIs requires that melting and thermal reprocessing of CAIs occurred during this window (Kita et al., 2005; Krot et al., 2009). By contrast, chondrule formation begins shortly after or simultaneously with CAI formation but lasts significantly longer, for up to 4Ma after time zero (Kita et al., 2005; Krot et al., 2009). Over this time period chondrules are repeatedly melted by an unknown transient, pulse heating event, and subsequently recrystallized at cooling rates between 10-1000Khr^{-1} (Desch and Connolly, 2002). The presence of concentric layered coarse and fine-grained rims adhered to some chondrules, and notably present in anhydrous CV chondrites, requires that the accretion of material and the heating of chondrules were coeval (Rubin, 1984; Rubin and Wasson, 1987). Later the chemically heterogeneous fine-grained and volatile-rich matrix accreted, forming chondrites (Palme et al., 2015).

Among all carbonaceous chondrite subgroups, a chemical complementarity exists between chondrules and matrix, such that chondrules are refractory-rich and volatile-poor, while the surrounding matrix is volatile-rich and refractory-poor (Bland et al., 2005; Palme et al., 2015). Despite differences in elemental partitioning between chondrules and matrix, differences in chondrule size and differences in the matrix-chondrule proportions between the eight carbonaceous chondrite subgroups, the bulk chemical composition of any carbonaceous chondrite, in any subgroup, sums to give approximately solar elemental abundances (Bland et al., 2005; Palme et al., 2015). This complementarity provides a significant constraint on the physical conditions and mechanisms of chondrite formation, demanding that each carbonaceous chondrite subgroup formed in a closed-system (Jones, 2012; Palme et al., 2015). As a result, any proposed mechanism for chondrite formation must provide a plausible model to maintain chemical complementarity. Current mechanisms tend to favour nebula-hosted rather than planetesimal-hosted mechanisms, in which shock waves (Desch and Connolly, 2002; Krot et al., 2009; Morris et al., 2012) or impact jetting (Salmeron and ireland, 2012;

Johnson et al., 2015) drive melting. This most likely requires a vertically stratified and/or annularly-separated disk (Boley et al., 2005; Salmeron and Ireland, 2012). However, planetesimal-hosted mechanisms such as the dirty-splash model (Krot et al., 2005; Sanders et al., 2012), and the fly-by model (Asphaug et al., 2006), in which chondrules are generated when accreted planetesimals collide, remain credible alternatives.

Since their formation, approximately 4.5Ga ago, the parent bodies of carbonaceous chondrites have remained largely unaltered. As a result, asteroids and comets are remnants of the early solar system. Their primitive geology provides a method of reconstructing the history and mechanisms of accretion, aqueous alteration, thermal metamorphism, shock deformation and differentiation during the first ~150Ma of the solar system's evolution (Krot et al., 2009; Tonui et al., 2014; Lindgren et al., 2015).

1.4. Dust in space

Both asteroids and comets continually produce dust through impacts (Nesvorný et al., 2003; Flynn et al., 2009), spontaneous disruption (Nesvorný et al., 2010), sublimation (Schulz et al., 2004) and mantle shedding events (Schulz et al., 2015). Collectively, this mass of dust forms the Zodiacal cloud, a diffuse spiral-shaped disc which, scatters and remits solar radiation in the infrared (Nesvorný et al., 2006; 2010).

Within the inner solar system, asteroids produce dust primarily through collisions. When a significant collision between two asteroids occurs and this results in the breakup of a large asteroid, a new asteroid family is born. This process is known as a catastrophic disruption. (Hirayama, 1918; Durda et al., 1998; Michel et al., 2004 and references therein). Asteroid families share a genetic origin, as part of a larger body, and often remain as a loose cluster, with similar proper orbital elements (Michel et al., 2004). Thus, the asteroid belt evolves over geological time through the collisional break up of its members (Nesvorný et al., 2002; 2003). Asteroids are also heavily affected by small-body, non-gravitational processes, such as Yarkovsky drift and the YORP [Yarkovsky–O'Keefe–Radzievskii–Paddack] effect (Bottke et al., 2001; 2006). Over geological time these processes cause the proper orbital elements of asteroids to vary, forcing asteroid families to gradually disperse (Nesvorný et al., 2002; Bottke et al., 2006). Similarly, cosmic dust is also affected by small body non-gravitational forces. Upon liberation from their parent body, cosmic dust particles rapidly (10^5-10^7 years) spiral into the inner solar system, losing angular momentum as radiation pressure exerts a force tangential to their orbit (Wyatt and Whipple 1950; Dohnanyi, 1972; 1976). Dust is then either captured by the terrestrial planets or consumed by the Sun (Dohnanyi, 1976; Love & Brownlee, 1991; Nishiizumi et al., 1995; Nesvorný et al., 2003). Since P-R drag is efficient, only recent (<10Ma) asteroid break up events are associated with dust bands (Nesvorný et al., 2003) and, therefore, dominate the supply micrometeorites to Earth. Figure 1.1 shows 3 prominent young asteroid families and their associated IRAS dust bands.

Fig.1.1. Map of the asteroid belt, displaying proper orbital elements (semi-major axis and inclination) for 50,000 asteroids. This plot is generated from a synthetic idealised population – produced by averaging the known proper orbital elements of multiple asteroids, thereby giving fewer total objects (a reduced dataset), which remains representative of the true asteroid population. This plot reveals the structure of the belt and the position of the Kirkwood Gaps (gravitationally unstable secular and mean motion resonance bands, from which Earth-crossing meteorites are sourced). Dense clusters of asteroids represent asteroid families, generated by the catastrophic disruption of a larger body. Upon this plot the 3 young, asteroid families are marked (Themis [green], Koronis [red] and Veritas [purple]) and their associated IRAS dust bands. These families are responsible for up to 50% of the micrometeorite flux. Figure modified after Nesvorný et al., 2003 (Fig.1), with raw data obtained from the AstDyS-2 (2016).

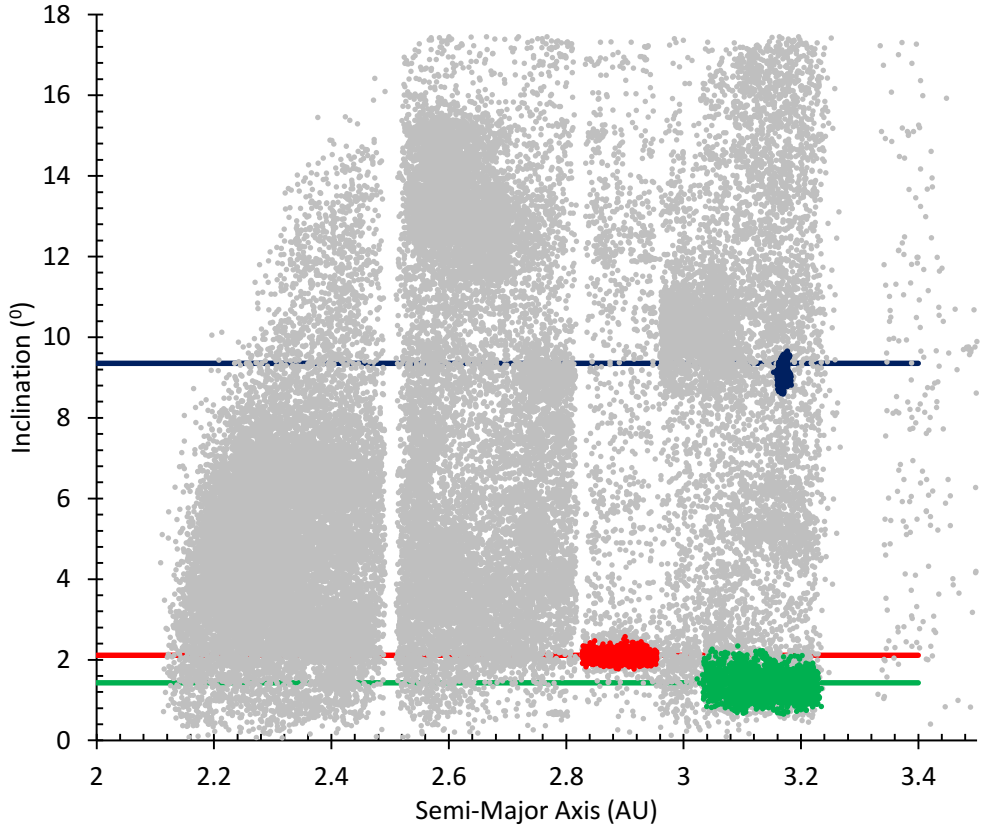

1.5. Transport to Earth

Meteorites are delivered to Earth, through impact events which disrupt their orbit and by the Yarkovsky effect, forcing small objects (<1km) to drift into secular resonance zones, known as the Kirkwood Gaps (Fig.1.1, Bottke, et al., 2001). The Kirkwood Gaps excite an object's orbital eccentricity, and this ultimately leads, either to ejection from the solar system or collision with a terrestrial planet (Vokrouhlický et al., 2000). The total number of parent bodies that meteorites sample is, therefore, heavily restricted (Burbine et al., 2002). By contrast, dust is always transported inwards. This means micrometeorites have the ability to sample a much larger proportion of the total asteroid population. Consequently, micrometeorites can provide a more comprehensive picture of solar system geology (Gounelle, et al., 2009; Noguchi et al., 2013).

In addition to a high diversity of parent bodies, micrometeorites add a significant quantity of material to Earth, with an estimated mass flux of 20,000-60,000tyr^{-1}(Love and Brownlee, 1993; Peucker-

Ehrenbrink, 1996; Zolensky et al., 2006). Global flux estimates use, either surface, atmospheric or space-based proxies (Carrillo-Sánchez et al., 2015). However, the total influx value varies by two orders of magnitude, dependent on the type of proxy used. Space based estimates, using satellite observations of the Zodiacal Cloud (Carrillo-Sánchez et al., 2015), meteor showers (Dohnanyi, 1972) or micrometeorite impacts into satellite panels (Love & Brownlee, 1993) produce the largest flux figures (20,000-60,000tyr^{-1}). Conversely, atmosphere and Earth-based estimates produce much lower flux values. Radar observations of the upper atmosphere, produce dust fluxes estimates between 1,600-2,300 tyr^{-1} (Matthews et al., 2001), while calculations, evaluating micrometeorite concentrations held in ice cores, or wholesale melted blue ice collections, typically arrive at values between 1,500-20,000 tyr^{-1}; with most calculations favouring the lower extreme of this range (Maurette et al 1986; Yiou and Raisbeck 1989; Taylor et al., 2000). Finally, deep sea flux calculations, which measure the concentrations of extraterrestrial trace elements (such as Os and Ir) in marine sediments arrive at median values of 37,000±13,000tyr^{-1} (Peucker-Ehrenbrink, 1996).

This disparity in flux estimates is a result of atmospheric entry heating. Extraterrestrial dust enters the Earth's atmosphere at high velocity, typically between 11 to 72 kms^{-1} (Love and Brownlee, 1991). Rapid deceleration results in intense flash heating with many micrometeorites being vapourised. Modelling suggest that up to 90% of dust entering the Earth's atmosphere does not survive (Love and Brownlee 1991; Taylor et al., 1998). Consequently, space-based fluxes or surface chemical analogues (using deep sea Os and Ir concentrations) sample the total dust flux, while Antarctic ice collections sample only those particles which have survived entry (Prasad & Rudraswami, 2013).

1.6. Atmospheric entry

The Earth's atmosphere acts as an effective barrier to incoming extraterrestrial dust; the majority of high velocity (>16kms^{-1}) cometary particles are vapourised, while lower velocity (~11kms^{-1}) asteroidal particles are much more likely to survive (Love and Brownlee, 1991). Therefore, although cometary particles have been recovered (Dobrică et al., 2012; Noguchi et al., 2015), asteroidal micrometeorites dominate collections (Taylor et al., 2012).

During entry, flash heating begins at altitudes of 85-90km, within the Earth's Mesosphere. Heating lasts between 2-10 seconds and peak temperatures reach up to ~1700°C (Fig.1.2 and Love and Brownlee, 1991). Detailed modelling of micrometeoroids during atmospheric entry can be found in Love and Brownlee, (1991), Carrillo-Sánchez et al., (2015) and Genge (2016a). The effects of entry heating are so significant that micrometeorite classification groups particles based on the degree of thermal reprocessing experienced. The majority of dust particles which reach the Earth's surface, have completely melted and recrystallized. These melted micrometeorites are termed cosmic spherules and represent the largest fraction of extraterrestrial dust. Whilst in a molten state, micrometeorites form spherical droplets, pulled in by surface tension (Genge, 2016b). Components begin to separate as a result of immiscibility (Genge and Grady, 1998) and density contrasts (Taylor et al., 2000), leading to metal bead formation and separation (Bi et al., 1993; Genge et al., 2016a) cumulate layering (Genge et al., 2016b) and vesicle migration (Genge, 2016b). As peak temperatures rise, Langmuir evaporation

results in the loss of volatile and moderately volatile elements (notably Na, S, P, Cl and Mn). Consequently, the bulk compositions of cosmic spherules deviate from chondritic abundances, with the most severely heated spherules showing the greatest loss of volatile elements (Toppani et al., 2001; Cordier et al., 2011). Lower in the atmosphere, quench cooling results in the growth of distinctive dendritic crystals on the particle exteriors and interiors (Genge et al., 2016c; Khisina et al., 2016).

Fig.1.2. A temperature-time plot demonstrating the typical heating profiles experienced by asteroidal micrometeoroids. The model parameter inputs are as follows: a 100µm diameter particle, impinging at 12kms^{-1} with a variable entry angle (with respect to the Earth's surface, such that the 90° model represents a "vertical" trajectory orientated normal to the Earth's surface). Angles of 20°, 45° and 90° are shown. The duration of heating varies with entry angle, while peak temperature is dependent on angle, speed and particle size. Reproduced from Love and Brownlee (1991).

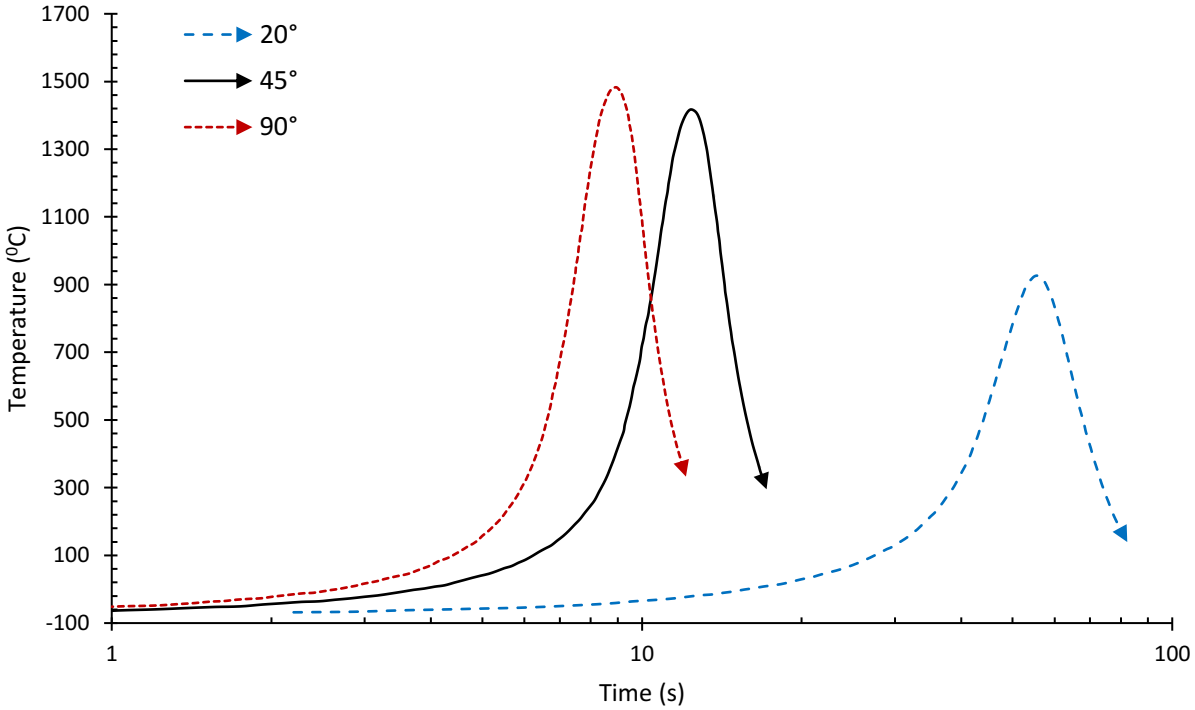

Cosmic spherules are divided into 3 compositional types: silicate dominated, S-types, representing ~95% of all spherules, metallic iron-dominated, I-types (~4%) and rare (<1%) mixed composition (Fe-rich silicate bearing) G-type spherules (Taylor et al., 2000). S-type cosmic spherules are further subdivided into porphyritic (PO), barred olivine (BO) cryptocrystalline (CC), and glassy or vitreous (V) dependent on their mesostasis textures (Fig.1.3). These subdivisions reflect a progressive sequence of increasing peak temperature attained during entry (PO<BO<CC<V) (Genge et al., 2008; Taylor et al., 2012). However, recent oxygen isotope analysis suggests that the S-type subdivisions, may in part, also reflect different parent body sources; with the majority of PO and CC cosmic spherules showing isotopic signatures associated with ordinary chondrite parents, while BO and V type spherules are related to carbonaceous chondrite parents (Suavet et al., 2010; 2011a; van Ginneken et al., 2017).

Fig.1.3. Cosmic spherules from the Larkman Nunatak micrometeorite collection. This selection illustrates the diversity of petrologic types and the range of textures commonly found. Using a broad compositional classification, particles can be classed as S-type, [silicate dominated] (A-I), I-type [metal-rich] (J and K) and G-type [intermediate FeSi-rich composition] (L). Within the S-type class spherules are sub-classified into scoriaceous (A), porphyritic [relict-bearing] (PO-RGB as in B and C), porphyritic [mesostasis] (PO as in D and E), Barred Olivine (BO as in F and G), Cryptocrystalline (CC as in H) and Vitreous [or glassy] (V as in I). This sequence (ScMM<PO-RGB<PO<BO<CC<V) reflects an increasing peak temperature attained during atmospheric entry heating. Within the I-type class particles are sub-divided into metal-bearing (MET as in J) or oxidised (OX as in K), dependent upon the degree of oxidation as determined by the presence of absence of a reduced Fe-Ni bead. G-type spherules are exceedingly rare (<1% of CS), consequently, these spherules are not subdivided further, but are identified by the presence of cruciform magnetite dendrites suspended within an Fe-rich silicate glass. All scale bars are 100µm. Classification system follows that outlined in Genge et al., (2008; 2017a).

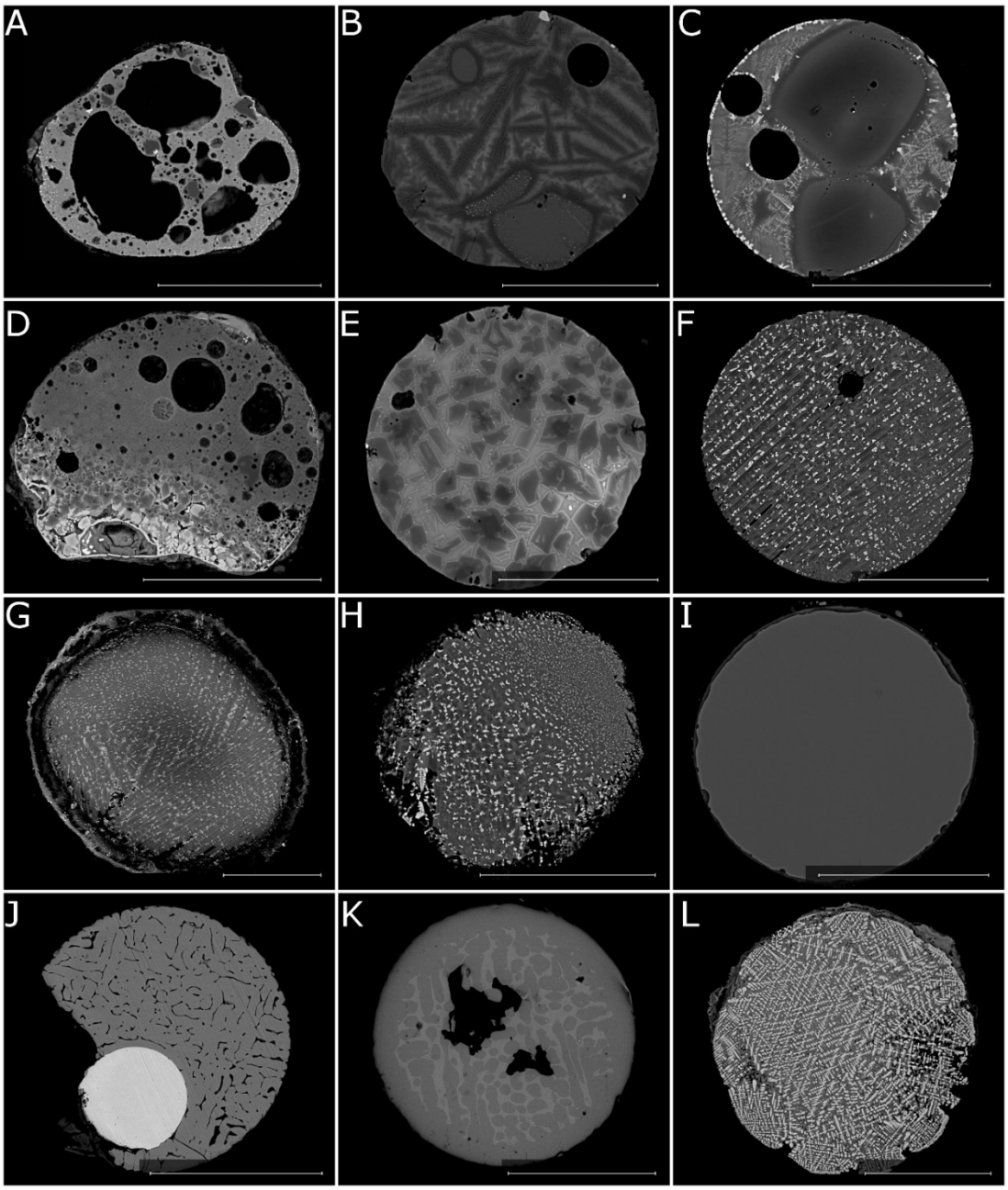

A small fraction of micrometeorites survive entry as unmelted or partially melted (scoriaceous) particles. For unmelted micrometeorites peak temperatures do not exceed 1350°C, the solidus temperature for chondritic matrix (Toppani et al., 2001), while the peak temperatures of scoriaceous micrometeorites range from 1350-1500°C (Toppani et al., 2001). In both unmelted and scoriaceous micrometeorites pre-atmospheric textures (Genge et al., 1997; Engrand and Maurette, 1998), organic matter (Suzuki et al., 2010; Dobrică et al., 2011), mineralogy (Gounelle et al., 2009) and geochemical signatures (Steele et al., 1992; Kurat et al., 1994) from their parent body asteroid can be discerned. As a result, these particles have the ability to constrain local solar system geology.

Despite lower peak temperatures, both unmelted and scoriaceous micrometeorites are heavily altered by atmospheric entry effects. Low temperature phases such as carbonaceous phases, sulphides and phyllosilicates thermally decompose or partially melt (Nozaki et al., 2006; Court and Tan, 2016), resulting in the release of volatile gases and the formation of vesicles (Taylor et al., 2011). Simultaneously, the interaction between decomposition gases results in complex secondary phases forming. In particular, the carbothermic decomposition of organic matter drives the production of sulphur dioxide at subsolidus temperatures (Court and Tan, 2016). At a particle's perimeter entry heating is most severe, here melting occurs, leading to the formation of outer spinel-magnetite rims (Toppani and Libourel, 2003) and inner igneous rims (Genge, 2006 and Fig.1.4). This produces zoned micrometeorites with distinct cores and rims. In scoriaceous micrometeorites partial melting results in changes in the particle's shape and volume. Scoriaceous micrometeorites are characterised by smooth, rounded particle edges and abundant vesicles (often comprising >50% volume). The sudden formation of vesicles can result in rapid expansion in volume, referred to as the *parachute effect*, which, causes dramatic deceleration of the micrometeoroid and may be important in preventing further rises in peak temperatures, thereby inhibiting complete melting in some scoriaceous micrometeorites (Genge, 2017).

In unmelted micrometeorites entry heating is, by definition, modest. Since peak temperatures remain below the solidus of chondritic matrix, any thermal evolution occurs in the solid state. Although volatile gases are released, and thermal decomposition reactions occur, the particle's original parent body texture is preserved (Genge et al., 1997). Unmelted micrometeorites are, therefore, grouped into two compositional classes based on their parent body characteristics. Micrometeorites composed predominately of large (>4μm) anhydrous crystals, single crystal particles and those rich in plagioclase are classed as coarse-grained micrometeorites. Alternatively, micrometeorites with smaller (<4μm) crystal sizes and rich in phyllosilicate minerals are classed as fine-grained micrometeorites. An additional class of micrometeorites containing both coarse and fine-grained domains are referred to as composite micrometeorites (Genge et al., 2008). The following sections discuss both unmelted micrometeorite types.

Fig.1.4. (A) An example of a small micrometeorite (CP94-050-054) containing a well-developed [inner] igneous rim (7µm thick) and outer magnetite rim. This particle supported a zoned core-to-rim thermal gradient. (B). The boundary between the igneous rim and the less heated core is a sudden sharp contact. (C) Modelling from Genge et al., (2017b) suggests that igneous rims like these require high thermal gradients (>200µmK^{-1}) and arise only where hydrated phyllosilicates thermally decomposed and then melt, providing a sink to absorb the abundant heat energy generated during atmospheric entry. As a result, hydrated particles can maintain relatively low internal temperatures (~600-1100°C, Chapt.4) and consequently preserve unmelted and dehydroxylated phyllosilicates or recrystalized anhydrous olivine at their core. This study suggests that core-to-rim thermal gradients maintained by thermal conduction are overprinted in larger particles once secondary pore space and branching channels develop.

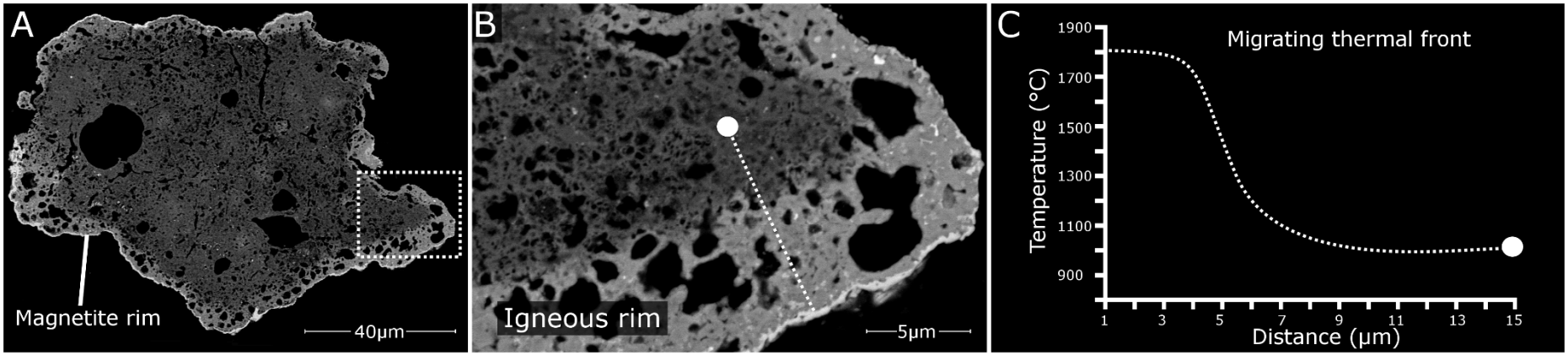

1.7. Coarse-grained micrometeorites

Coarse-grained micrometeorites have igneous textures and are dominated by large (<4µm) anhydrous olivine and pyroxene crystals. Mesostasis glass is common, while sulphides, Fe-oxides, and metal may also occur (Genge et al., 2005; 2008). The majority of coarse-grained micrometeorites have chondritic abundances, although, rare achondritic examples are known. These achondritic micrometeorites typically contain Ca-rich plagioclase and represent fragments of extraterrestrial basalts, derived from differentiated asteroids, most likely from the Vesta family (Gounelle et al., 2009).

The igneous textures in coarse-grained micrometeorites attest to melting and recrystallization in space. The presence of interstitial glass in many particles requires rapid cooling rates. Furthermore, the textures of coarse-grained micrometeorites, which include porphyritic, granular, radiating (pyroxene) and barred (olivine), are consistent with high cooling rates (Genge et al., 2005). Trace element analysis demonstrates that the majority of coarse-grained micrometeorites fall within the compositional field of chondrites (Steele, 1992; Genge, et al., 2005). In addition, the presence of composite micrometeorites, containing both coarse and fine-grained domains, implies that both micrometeorite classes are derived from the same parent bodies (Genge et al., 2005; Genge, 2006). Therefore, on the basis of textural and geochemical evidence, coarse-grained micrometeorites are considered fragments of chondrules derived from impact-disrupted primitive asteroids.

Both ordinary chondrite and carbonaceous chondrite parents send coarse-grained micrometeorites to Earth (Steele, 1992; Suavet et al., 2010; 2011a; Imae et al., 2013). Several studies have revealed, on the basis of trace element data (Genge, 2008; van Ginneken et al., 2012) or mineralogy (Prasad et al., 2015), the presence of unmelted ordinary chondrite-like micrometeorites (Fig.1.5). Estimates for the contribution of ordinary chondrite-like micrometeorites vary, from 10-30% of the total micrometeorite flux (Suavet et al., 2010; Taylor et al., 2012). However, with increasing particle size, ordinary chondrite-like micrometeorites become increasingly more common (Suavet et al., 2010). This suggests that, on disruption, different asteroid parents produce different size-distributions of dust. Light gas gun experiments confirm this hypothesis, demonstrating that hydrated carbonaceous chondrites produce abundant small dust (<100µm, Durda and Flynn, 1999; Flynn et al., 2009), while anhydrous carbonaceous chondrites and ordinary chondrites produce larger fragments (<300µm, van Ginneken et al., 2012).

In 2008 Genge suggested that up to 70% of coarse-grained micrometeorites are derived from an ordinary chondrite parent body. A single asteroid family – the Koronis complex - is the most likely candidate for these micrometeorites (Genge, 2008a). This family is a major group within the asteroid belt and includes >300 members (Zappala et al., 1995). Furthermore, the Koronis family contains the Karin subcluster, a tight collection of young asteroids formed by a recent (5.8Ma, Nesvorný et al., 2002; 2003; 2006) secondary break up event. Observations from the IRAS all sky survey show the Koronis family and in particular the Karin subcluster are linked to the prominent 2.1° (inclination) dust band (Fig.1.1. and Nesvorný et al., 2002; 2003; 2006). Current estimates suggest that the Karin subcluster contributes approximately 15-25% of the micrometeorite flux to Earth (Nesvorný et al.,

2006). Given this evidence, which pairs laboratory microanalysis with telescope observations and dynamical simulations, the flux of coarse-grained micrometeorites is relatively well constrained. Conversely, fine-grained micrometeorites are more abundant and could derive from a much larger range of parent bodies.

Fig.1.5. An ordinary chondrite-like coarse-grained micrometeorites, derived from the TAM micrometeorite collection. This giant micrometeorite contains a complete chondrule as well as a fragmented chondrule at the particle margin. The abundance of metal and the distinct chondrule outline classifies this grain as a H4 ordinary chondrite. Several additional chondrule-bearing micrometeorites are described in van Ginneken et al., (2012).

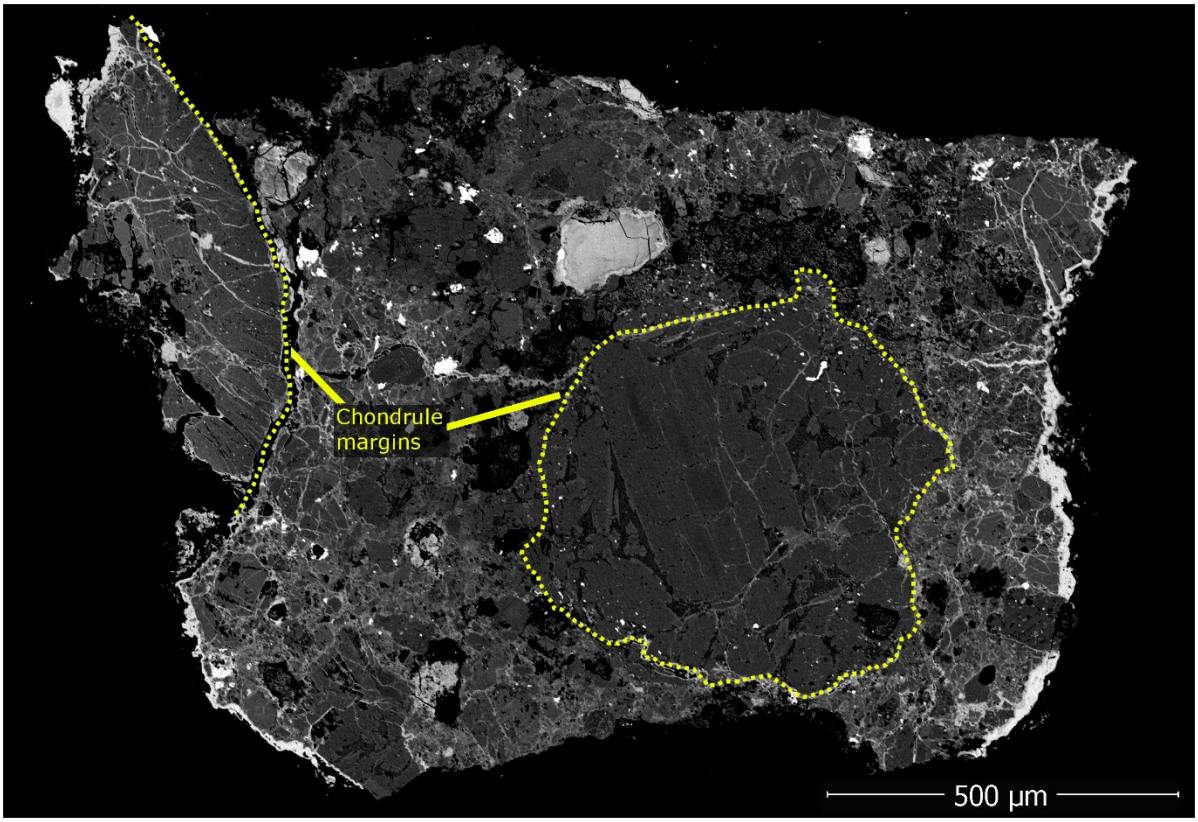

1.8. Fine-grained micrometeorites

Analysis of over 5500 micrometeorites collected at the South Pole Water Well suggest that up to 75% of the micrometeorite flux is composed of friable, fine-grained, carbonaceous material (Taylor et al., 2012). These particles are referred to as fine-grained micrometeorites and represent the focus of the present work. Fine-grained micrometeorites are dominated by extraterrestrial phyllosilicates. Both serpentine and saponite have been identified (Genge et al., 2001; Noguchi et al., 2002). These phyllosilicates are typically short stacked or misorientated clusters (Noguchi et al., 2002 and Fig.1.6.), rich in Mg and Fe, which replace the more common, Al and Si found in terrestrial phyllosilicates (Taylor et al., 2012). Accessory phases common in fine-grained micrometeorites include Fe-sulphides such as tochilinite (Genge et al., 1997), troilite and pyrrhotite (Dobrică et al., 2009), small anhydrous forsterite and enstatite crystals (Kurat et al., 1994; Genge et al., 1997; 2008), framboidal and platelet magnetite (Genge et al., 2008), carbonaceous phases (Suzuki et al., 2010; Dobrică et al 2011) and in rare instances

carbonates (Noguchi et al., 2002). The mineralogy of fine-grained micrometeorites is, therefore, similar to the primitive, hydrated CM, CR CI carbonaceous chondrites and the ungrouped C2 tagish Lake meteorite (Genge et al., 1997; 2008; Noguchi et al., 2002). This link is further strengthened through petrologic (Kurat et al., 1994; Genge et al., 2005), geochemical (Steele, 1992; van Ginneken et al., 2012), isotopic (Engrand et al., 1999; Alexander et al., 2002; Suavet et al., 2010; van Ginneken etal., 2017), textural (Genge et al., 1997) and organic matter analyses (Suzuki et al., 2010; Dobrică et al., 2011).

Fig.1.6. High magnification SEM-BSE image of a large CI-like fine-grained micrometeorite recovered from the TAM micrometeorite collection. This particle was analysed in van Ginneken et al., (2012) and is included in this thesis under the particle designation TAM-2.1c. This particle contains framboidal and platelet magnetite crystallites suspended in a matrix of Mg-rich saponite. Phyllosilicate clusters in this particle are well-formed and their pseudo-hexagonal stacked and misorientated structure can be clearly seen. Scale bar is 20µm.

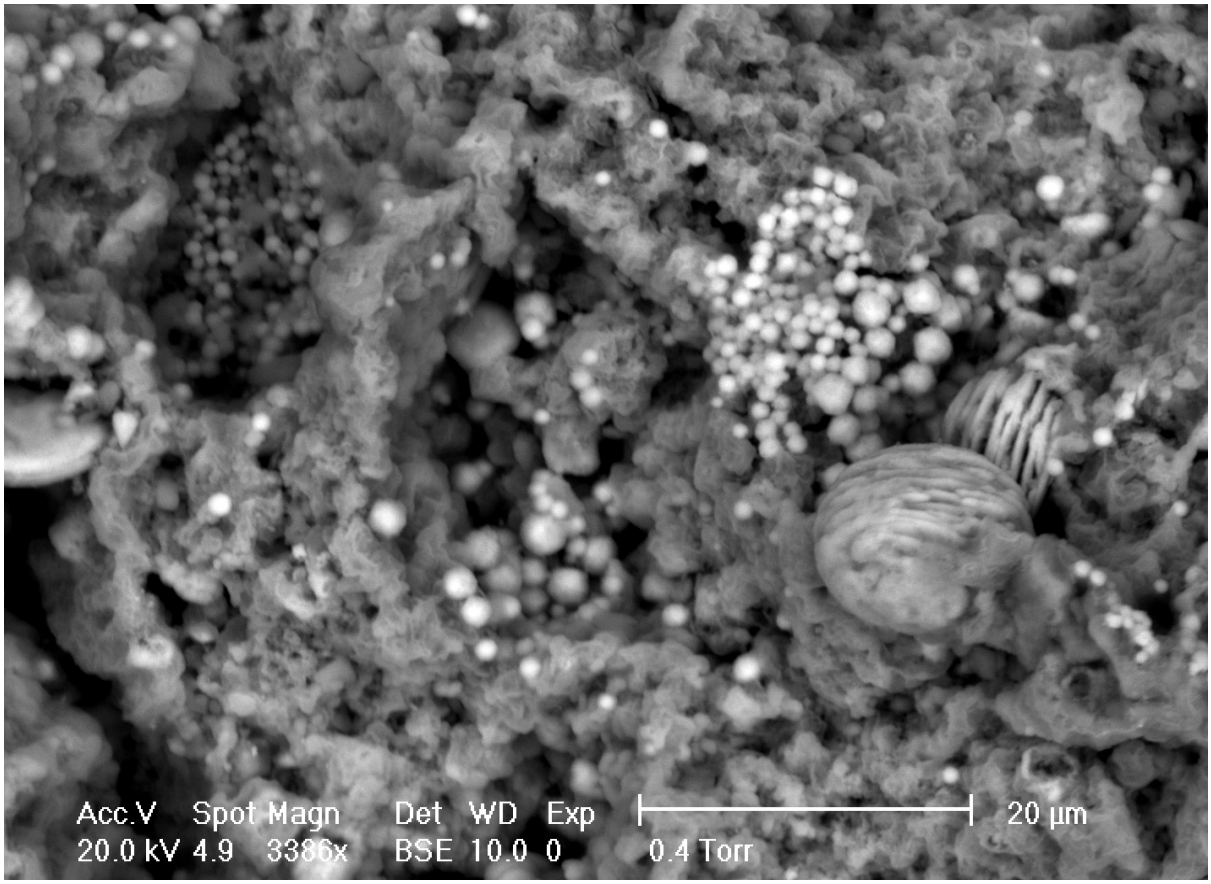

Fine-grained micrometeorites can be sub-classified into C1, C2 and C3 subtypes based on the analysis of their microtextures, observable under BSE (Genge et al., 1997; 2008). C1 particles have homogenous textures, similar to CI chondrites, contain Mg-rich phyllosilicates, typically saponite and abundant magnetite (van Ginneken et al., 2012). C2 particles are similar to CM chondrites and consequently, share similar, less aqueously altered petrographies. C2 particles preserve a heterogeneous matrix containing anhydrous olivine and pyroxene crystals which may be collected into chondrule fragments (Genge et al., 2005; van Ginneken et al., 2012). C3 Fine-grained micrometeorites

are anhydrous and highly porous, these particles are rare and not analysed in this thesis. The relative proportions of C1, C2 and C3 particles are not accurately known, but C1 and C2 subtypes are much more common than C3 particles (Genge et al., 2008).

Fine-grained micrometeorites enter the Earth's atmosphere with hydrated phyllosilicates (Noguchi et al., 2002; Genge, 2006; Nozaki et al., 2006; Genge et al., 2017b). During entry heating, thermal decomposition results in the loss of water from phyllosilicate minerals and the formation of dehydration cracks (Genge, 2006; Nozaki et al., 2006; Genge et al., 2008). It has been suggested that the development of cracks could promote the fragmentation of micrometeorites during passage through the atmosphere (Genge, 2006; 2008b). Simultaneously, igneous (Genge, 2006) and magnetite (Toppani and Libourel, 2003) rims form through melting, evaporation and recrystallization at the particle exterior. Large anhydrous crystals located at the micrometeorite's perimeter may fracture due to thermal stress, arising from high thermal gradients (>200Kμm^{-1}, Genge et al., 2017b). Despite these terrestrial overprints fine-grained micrometeorites retain valuable information from their parent bodies. Given the similarities between fine-grained micrometeorites and CM, CR and CI chondrites, both materials are likely sourced from the same parent asteroids. However, linking micrometeorites to specific parent asteroids is difficult because of the alteration that affects both bodies.

1.9. Asteroid parent bodies of fine-grained micrometeorites

Asteroid classification is based upon visible and near-IR spectral profiles, collected from ground-based telescopes (Chapman et al., 1971; 1975; Tholen, 1984; Bus and Binzel, 2002; DeMeo et al., 2009). Asteroid spectra are dependent on the surface composition; the asteroid's age, grain size and thickness of the surface regolith, angle of observation and Earth's atmospheric conditions during observation all affect the final spectra (Clark et al., 2002; Chapman et al., 2011). To the first order, asteroids are classified into 3 classes: S-type, C-type and X-type (Chapman et al., 1975), with additional groups and subgroups assigned over time to reflect the increasing diversity and complexity of the asteroid population (Tholen, 1984; Bus and Binzel, 2002; DeMeo et al., 2009).

S-type asteroids have red-sloped spectra (defined as increasing reflectance with increasing wavelength) over visible wavelengths and two wide absorption bands (reflectance minima associated with asymmetric covalent bonds in mineral structures) centred at approximately 1µm and 2µm (Chapman et al., 1975; Chapman, 1996 and Fig1.7). These features indicate the presence of anhydrous olivine and pyroxene on the asteroid's surface (Gaffey et al., 2002). S-type asteroids are associated with ordinary chondrites on the basis of similar spectral profiles (Chapman, 1996). This link was confirmed in 2010, when the Hayabusa sample return mission recovered material for analysis from the S-type asteroid [25143] Itokawa. Spectral analysis in the laboratory demonstrated that Itokawa was composed of low-total-iron, low metal (LL) type 4 equilibrated ordinary chondrite (Nakamura et al., 2011). By contrast, C-type asteroids are associated with carbonaceous chondrite parents (Fornasier et al., 2014).

C-type asteroids are characterised by low albedos, shallow red-sloped, flat or blue-sloped spectral profiles, which lack strong absorption bands (Fig1.7). Weak hydration features are observed in >50% of C-type asteroids (Rivkin et al., 2002; Kaluna et al., 2015) and include minor absorption bands in the 0.7µm region (Fornasier et al., 2014; McAdam et al., 2015) and the 3µm region (Feierberg et al., 1985; Campins et al., 2010). These bands are associated with water-ice and structural water held within phyllosilicate crystal lattices (O-H and Si-OH bonds). Owing to their small size, typically <300km diameter, C-type asteroids were unable to retain initial heat, generated from radioactive decay of short-lived isotopes (Kunihiro et al., 2004). Alternatively, some planetesimals could have formed relatively late in the solar system's evolution (>10Ma), after the decay of most short-lived radioisotopes and, therefore, lacked sufficient heat to melt and differentiate (Kunihiro et al., 2004; Kleine et al., 2005). Therefore, C-type asteroids most likely retain chondritic compositions, and today, exist as relicts representing precursor material to planets or late-accreting material, formed after the planet building episode (Kunhiro et al., 2004; Bizzarro et al., 2005; Kleine et al., 2005). Although melting did not occur, evidence from CM and CI chondrites requires that internal temperatures were between 0°C and 350°C (Bunch & Chang, 1980; Clayton & Mayeda, 1999; Verdier-Paoletti et al., 2016), which led to the melting of water-ice and the reaction of this water with anhydrous and amorphous components, resulting in aqueously altered petrographies (McSween, 1979; Rubin et al., 2007).

Fig.1.7. Example near-IR spectra (over the wavelength range 0.8-2.5µm) collected from an S-type asteroid (25143 Itokawa, shown in red) and C-type asteroid (41 Daphne, shown in purple). S-type asteroids are characterised by two prominent absorption bands, centred at approximately 1µm and 2µm, these features indicate the presence of anhydrous crystalline olivine and pyroxene at the surface. [25143] Itokawa was visited by the Hayabusa sample return mission between 2003-2010 and confirmed the suspected spectroscopic link between S-type asteroids and ordinary chondrites (Nakamura et al., 2011). By contrast, C-type spectra are characterised by shallow, featureless spectra which may show a slight red (increasing reflectance with increasing wavelength) or blue (decreasing reflectance with increasing wavelength) profiles. Weak absorption features, located at 0.7µm (not visible), are present in approximately 50% of C-type asteroids (Rivkin et al., 2002; Kaluna et al., 2015). The spectrum of 41 Daphne was obtained from the IRTF Near-IR Spectroscopy of Asteroids V2.0 (Bus, 2011) and the spectra of Itokawa from the Hayabusa NIRS Calibrated Spectra V1.0 (Abe et al., 2011).

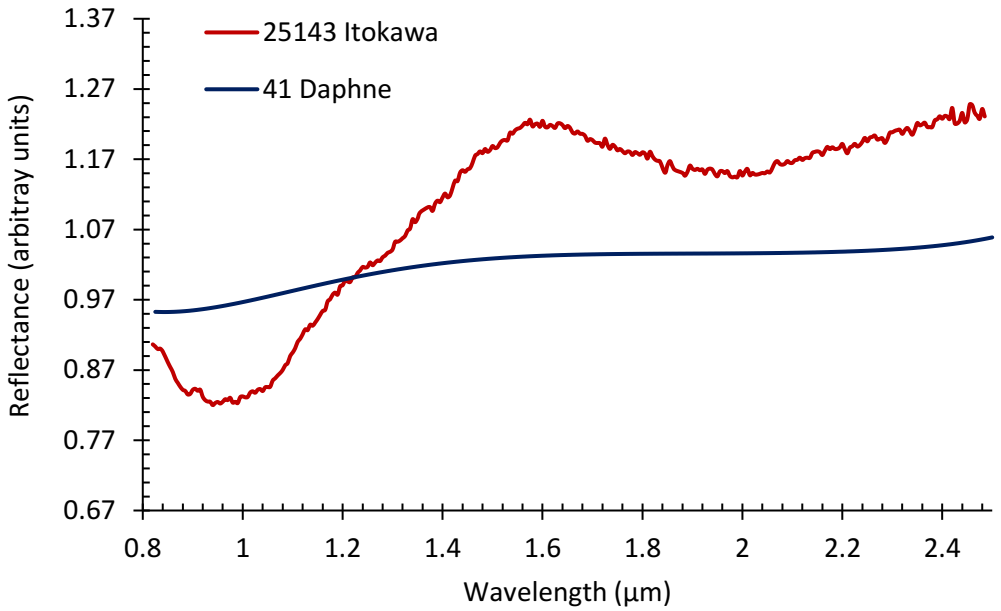

Deriving compositional information from the near-IR spectra of asteroid surfaces is hindered by space weathering. Atmosphere-free bodies are damaged by micrometeorite bombardment and solar irradiation (Chapman, 1996; Sasaki et al., 2001). Over geological time space weathering results in the amorphization of surface minerals, loss of spectral features, drops in albedo, changes in spectral slope (spectral reddening and bluing) and a loss of distinction between spectral classes (Chapman, 1996; Clark et al., 2002; Kaluna et al., 2015). Studies analysing age-spectral slope relationships show that space weathering can remove compositional signatures from S-type asteroids in <10Ma (Jedicke et al., 2004). Consequently, only young asteroid families with fresh surfaces remain unaffected.

Two major C-type families are of interest to the present study, the ancient Themis family (>2.5Ga, Broz et al. 2013) and the young (8.3Ma, Nesvorný et al., 2003; 2006) Veritas family. Both are associated with major IRAS dust bands (at 1.8° and 9.35° inclination respectively as in Fig.1.1) and accordingly, are potential sources of the current flux of primitive hydrated Fine-grained micrometeorites (Nesvorný et al., 2003; 2006). The Veritas family is a particularly attractive target for spectroscopic study, given its young age. This family is composed of ~300 members, with diameters >1km (Nesvorný et al., 2003). Prior to disruption the original parent body would have been ~100km in diameter (Nesvorný et al.,

2003; Michel et al., 2011; Novakovi, 2012). This makes the pre-family Vertias asteroid a medium-sized planetesimal. By contrast, the Themis family contains >550 members (each >1km diameter, Zappala et al., 1995), requiring an initial parent body between 270km and 400km in diameter (Durda et al., 2007; Broz et al., 2013). Although the Themis family formed over a billion years ago, the Beagle subcluster within this group, represents a recent secondary break up event, with an estimated formation age of <10Ma (Nesvorný et al., 2008). Both families contain a variety of spectral types (Di Martino et al., 1997; Kaluna et al., 2016), which could indicate compositional differences between the core and outer layers of the original asteroid, which would imply a partially differentiated interior (Di Martino et al., 1997). Fine-grained micrometeorites originating from the Veritas and Themis families may, therefore, span a range of compositional types.

1.10. Fossil micrometeorites

Micrometeorites have also been recovered from the rock record. Preserved, fossil micrometeorites, and larger fossil meteorites, are the only available Earth-based proxies with which to study the asteroid belt's geological evolution. Fossil collections can provide constraints on the past dust flux (Onoue et al., 2011), empirical evidence supporting the timing of asteroid family formation (Heck et al., 2008) and were crucial in revealing an oxygen-rich Archaean upper atmosphere (Tomkins et al., 2016).

Since the theoretical and empirically constrained upper maximum residence time for individual dust particles in the local solar system is <10Ma (Nishiizumi et al., 1995; Nesvorny et al., 2003), any (fossil) micrometeorites derived from sediments older than this will sample the dust flux prior to the *present era*. For these fossil collections it is reasonable to expect different proportions, accretion rates and source bodies to contribute to the palaeo-dust flux. To date, only 8 collections of fossil micrometeorites exist (Table 1.1). Although these collections span Archaean (~2.5Ga, Tomkins et al., 2016) to Miocene (Meier et al., 2016) sediments, the vast majority of the geological record is unsampled. Instead, isolated and random time periods have been searched. Two prominent studies involving fossil meteoritic material demonstrate the importance of this rapidly expanding field:

(1) Fossil meteorites and micrometeorites from the Lower Ordovician (~470Ma) have revealed a significantly increased extraterrestrial mass flux, over two orders of magnitude greater than today (Schmitz, 1997; Schmitz et al., 2001). This flux increase is associated with the formation of the Flora (S-type) asteroid family and delivery of ordinary (L) chondrites to Earth. Collisional modelling of the asteroid belt by Nesvorný et al., (2007) identified the Flora family as the most probable source, with the collisional age of the family, the shock ages of many L-chondrites and the age of the host limestones all dating to approximately 470Ma (Korochantseva et al., 2007; Nesvorný et al., 2007; Heck et al., 2008).

(2) The only systematic study to recover fossil micrometeorites from an extended sequence of sedimentary beds, over a 10Ma period, revealed the first and only fossil coarse-grained micrometeorites (Onoue et al., 2011). This study also demonstrated that during the Triassic (246-237Ma) the Earth received a comparable extraterrestrial dust flux to today, albeit with an anomalously

high abundance of micrometeorites contained within a single bed and suggesting a sudden spike in the dust flux, potentially related to the breakup of a small asteroid (Onoue et al., 2011).

These recent successes, combined with a relatively unexplored geological record make fossil micrometeorites an attractive area of research, with the potential to discover new and highly significant conclusions regarding the geological history of the solar system.

Table.1.1 Inventory of all published fossil micrometeorite collections recovered to date.

	Approximate age	Geologic Period	Collection Name	N=?	Location	Sediment	Separation method	Authors
1	~2.5Ga	Archaean	Archaea Spherules	60	Australia	Limestones	Dissolution (ND)	Tomkins et al., 2016
2	478-466Ma	Ordovician	Durness Group Collection	10	UK	Limestones	Dissolution (20% HCl)	Dredge et al., 2010
3	480-460Ma	Ordovician	Argentinian Spherules	237	Argentina	Limestones	Dissolution (10% Acetic)	Voldman et al., 2013
4	~470Ma	Ordovician	Lynna River Chromite Grains	50*	Russia	Limestones	Dissolution (20% HCl)	Meier et al., 2014
5	240Ma	Triassic	Triassic deep sea MMS	258	Japan	Chert	Mechanical	Onoue et al., 2011
6	185Ma	Triassic	Halite MMs	>100	UK	Halite	Dissolution (water)	Davidson et al., 2007
7	170-166Ma	Jurassic	Hardgrounds Southern Alps	12	Italy	Limestones	ND	Jehanno et al., 1988
8	40-30Ma	Eocene	Mt. Hillaby Collection	28	Barbados	ND	Mechanical	Taylor & Brownlee, 1991
	0Ma	*Anthropocene*	*South Pole Water Well (SPWW)*	*>1000*	*Antarctica*	*Water ice*	*Melting & filtering*	*Taylor et al., 1998*

1.11. Aims of this thesis

Meteoritics aims to better understand the geology of the solar system, including aspects such as the formation mechanisms, chronology and geochemical constraints of the early solar system, during the "*planet-building*" phase. Pragmatically, this is achieved through the laboratory analysis of extraterrestrial samples brought to Earth by space missions or as meteorites, micrometeorites and interplanetary dust. The related discipline of astronomy commonly employs spectroscopic techniques to analyse distant objects, such as asteroids and comets, revealing information on their temperature, composition and surface regolith. In this thesis, a combined study using both petrologic and spectroscopic techniques is employed, with the aim of better understanding the parent body geological properties and source asteroid families of fine-grained micrometeorites. Thus, this thesis is of relevance to researchers of cosmic dust in the fields of both meteoritics and asteroid spectroscopy.

The primary objective, to further constrain the physical characteristics of the fine-grained micrometeorite parent asteroids, will be achieved through petrologic analysis of a large population of Antarctic micrometeorites, derived from 2 distinct collections. This will include conventional laboratory microanalysis techniques (SEM-EDS, EMPA, EDX-mapping, µXRD and µCT) as well as micro-spectroscopic data (mid-IR, near-IR and Raman spectroscopy). The spectroscopic techniques will complement the geochemical data, revealing information on particle mineralogies and allowing investigation of the carbonaceous phases within samples. Thus, it is expected that a multi-element approach, generating datasets where each individual micrometeorite has been analysed by multiple techniques, will allow a greater understanding of the particle's provenance and geological history.

In addition, the collection of near-IR spectra from micrometeorites will also allow a direct comparison against existing spectra, obtained from C-type asteroids. Although current consensus links several meteorite and micrometeorite groups to general asteroid spectral classes (Gaffey et al., 2002; Imae et al., 2013) and, in some cases to specific asteroid families (Genge, 2008; Heck et al., 2008), the link between fine-grained micrometeorites and specific C-type asteroid families requires further support. To this end, the secondary objective of this thesis is to test the recently proposed Veritas hypothesis that: "*the current flux of fine-grained micrometeorites are sourced, primarily from the Veritas asteroid family*" (Nesvorný et al., 2002; 2003; 2006). The Veritas hypothesis will be investigated through the comparison of near-IR spectra (collected in the lab) from fine-grained micrometeorites against near-IR spectra of Veritas family members, previously collected via ground-based telescopes (Chapman et al., 2011).

The action of atmospheric entry reprocessing on unmelted (and scoriaceous) micrometeorites will also be investigated. This is because atmospheric entry heating affects all micrometeorite samples, even unmelted particles, and can prevent the unambiguous analysis of their parent body features. It is, therefore, essential that the two geological processes can be identified, and their effects understood separately. Although many previous works have studied entry heating in micrometeorites, most focus on high temperature, late-stage melting, evaporation and the formation of cosmic spherules (Love and Brownlee et al., 1991; Toppani et al., 2001; Toppani and Libourel, 2003; Cordier

et al., 2011). Instead, this study will analyse how thermal decomposition in the solid state affects a micrometeorite's petrography; ensuring that terrestrial overprints are not erroneously interpreted as parent body signatures.

Finally, a section of the geological column will be searched for fossil micrometeorites. An essential component of this research will be understanding how diagenesis effects the long-term preservation of cosmic dust. Ancient micrometeorites provide a means of studying different asteroid parent bodies to those currently sourcing micrometeorites to Earth and represent parent bodies that were catastrophically disrupted in the distant geological past. This thesis aims to make a useful contribution to the topic of fossil micrometeorites – a rapidly expanding area of research. Although the probability of recovering the first fine-grained fossil micrometeorites is low, owing to their friable nature, such a success would provide unique material for comparison with Antarctic collections.

This thesis, therefore, carries four principal aims; (1) to better constrain the geology of fine-grained micrometeorite parent asteroids – investigating topics such as as their aqueous alteration and impact histories, (2) to test the Veritas hypothesis – regarding their probable parent asteroid families (3) to analyse the early stages of atmospheric entry heating and (4) to recover fossil micrometeorites from an unstudied time period. These aims are linked by the desire to better understand the provenance, petrology and subsequent alteration of extraterrestrial dust both now and in the geological past. The study of micrometeorites by several generations of the planetary scientists have improved humanity's knowledge and appreciation of the solar system, the diversity of small bodies and the chaotic early evolution. This thesis aims to further expand our collection of planetary and small body knowledge through the study of unmelted micrometeorites.

.

Chapter 2: Methods and Materials

2.0 Overview This chapter outlines all samples used and experimental techniques employed in the current study. The origin, collection, analytical history and format of all Antarctic micrometeorites and carbonaceous chondrites are detailed. For each experimental technique, the laboratory where the data were collected, the instruments, operating conditions, data processing and analytical or experimental limitations are described.

2.1 Antarctic Micrometeorites

Although modern micrometeorites have been recovered from Greenland lakes (Maurette et al., 1986), deep-sea sediments (Taylor and Brownlee, 1991; Prasad et al., 2013), and even urban rooftops (Genge et al., 2016b), the least biased collections, containing the most friable material (fine-grained and cometary micrometeorites) are found in Antarctica (Taylor et al., 2000). To date, micrometeorites have been collected from blue ice (Taylor et al., 2000), snow (Duprat et al., 2007; Noguchi et al., 2015), moraine (Harvey and Maurette, 1991; Suttle et al., 2015; Genge et al., 2018) and rock traps (Rochette et al., 2008; Suavet et al., 2009) on the Antarctic plateau. Among these collections unmelted fine-grained micrometeorites remain relatively rare. Owing to their friable mineralogies, particles are easily damaged during collection, mounting and sectioning. However, uncompressed snow and lightly compacted rock traps contain the highest yields of friable micrometeorites (Duprat et al., 2007; Rochette et al., 2008).

Due to the stable environment, Antarctic micrometeorite collections can accumulate extraterrestrial dust over significant periods of time, potentially exceeding 3Ma (Suavet et al., 2011b). Such long exposure times sample the cosmic flux over the late Quaternary, providing low-bias collections, which include large and rare micrometeorites (Suavet et al., 2009). However, long residence times in the Antarctic environment also result in terrestrial weathering. Micrometeorites are altered by the etching of glass and replacement by palagonite, the corrosion and hydration of Fe-Ni metal, the dissolution of anhydrous phases and replacement by terrestrial secondary minerals (van Ginneken et al., 2016). Na- and K-bearing jarosite, halite and calcite are all common encrustation minerals found on micrometeorite surfaces. Antarctic micrometeorite collections, therefore, benefit from long accumulation periods but may also contain abundant highly weathered particles of limited scientific value to this study.

Micrometeorites used in this thesis are derived from 2 Antarctic collections: Cap Prud'homme (CP94) and the Transantarctic Mountains (TAM). Data from the Larkman Nunatak micrometeorite collection, recovered from moraine sediments is also used in this study for context.

2.1.1. Micrometeorites from Cap Prud'homme

Two resin blocks, containing approximately 100 Antarctic micrometeorites, were studied. These blocks contain both coarse and fine-grained micrometeorites which had previously been collected during the 1994 field season at the French Antarctic research dome, Cap Prud'homme [66°41'31"S,

139°53'46"E] (Maurette et al., 1991). Particles were collected by melting and filtering of blue ice at this site. The resulting residues were then analysed under binocular microscope and potential extraterrestrial particles picked, mounted in resin, sectioned and polished; these stages were performed by Dr. Matt Genge. Some of the Cap Prud'homme micrometeorites used in this thesis have previously been included in the following publications: Genge (2006; 2008a; 2008b) and Genge et al., (2005; 2008).

The Cap Prud'homme collection includes unmelted coarse-grained, fine-grained and partially melted scoriaceous micrometeorites as well as completely melted cosmic spherules. However, only the scoriaceous and fine-grained micrometeorites from this site are analysed in the present study. Micrometeorites accumulate primarily by aeolian processes on the icesheet surface before being buried by snow and becoming ice-stored. Sorting (most likely via winnowing) and subsequent removal of larger micrometeorites occurs. This is because only small micrometeorites (typically <100µm and never exceeding 300µm) are found within the Larkman Nunatak sediment. The estimated accumulation period for this collection is ~50Ka (Maurette et al., 1994).

Research suggests that ice-storage leads to high quality preservation of micrometeorites (Taylor et al., 2000). Despite being held in ice, the lack of encrustation rims on most Cap Prud'homme micrometeorites attests to the absence of abundant liquid water in contact with the particle surface for significant periods of time (van Ginneken et al., 2016).

Micrometeorites from this collection are denoted by the prefix: CP94-, followed by their classification number, in the format: CP94-50-*XXX*. The first 2 digits (-50-) relate to the particle's approximate size (that is <100µm) and the final 3 digits give the particle's unique identification number. This convention was designed by Dr. Matt Genge and applied to all Cap Prud'homme micrometeorites analysed by the micrometeoritics research group at Imperial College London. All micrometeorite IDs and corresponding petrographic information for the Cap Prud'homme collection are stored on the Imperial College Micrometeorite database, accessible at - https://wwwf.imperial.ac.uk/earthscienceandengineering/rocklibrary/mmindex.php.

2.1.2. Micrometeorites from the Transantarctic Mountains

The TAM micrometeorites were provided on loan by Dr. Luigi Folco. This included 10 resin blocks containing approximately 30 micrometeorites in total (both coarse and fine-grained, of which only the fine-grained are analysed in this study). These particles were originally picked by Dr. Matthias van Ginneken and Dr. Luigi Folco between 2008 and 2010. Some of these micrometeorites have previously been described by van Ginneken et al., (2012).

The TAM particles were recovered from exposed rock traps in Victoria Land in the Transantarctic mountains at Frontier Mountain [72°58'S, 160°30'E] and Miller Butte [72°42'S, 160°15'E] (Rochette et al., 2008). In their study, the term rock trap is used to refer to decimetre-scale weathering joints found on the surface of flat, glacially eroded granite nunataks (Rochette et al., 2008). The accumulated sediment within these rock traps was extracted and searched for micrometeorites.

Rock traps in the Transantarctic mountains accumulate micrometeorites primarily by direct infall (Suavet et al., 2009). Three independent dating methods attest to a significant accumulation period for this collection. The presence of Australasian microtektites (Folco et al., 2008) requires this site to have been actively collecting cosmic dust for least 0.78Ma (the age of the tektite strewnfield), while, the presence of cosmic spherules with a thermal remnant magnetization signature acquired during the Earth's reversed polarity field, also requires a minimum accumulation period of 0.78Ma (the end of the Matuyama Chron, Suavet et al., 2011b). In addition, ^{10}Be, cosmogenic exposure ages, measured on the terrestrial collection surface approach 3Ma (Welten et al., 2008). Thus, the total accumulation window could be up to 3Ma (Suavet et al., 2011b). With such long periods of time many of the TAM micrometeorites are heavily weathered (van Ginneken et al., 2016). However, it is this long accumulation period that has allowed the TAM site to collect an abundance of large micrometeorites, making this collection unique (Folco, 2015). To date the TAM collection includes several thousand micrometeorites with diameters <100µm to >2000µm (Folco, 2015).

Micrometeorites from the TAM collection are denoted by the prefix: TAM-, followed by their unique identification code, which may include both letters and numbers, for example: TAM-19B-17 or TAM-2.1c. This classification system was adopted from the owner's and ensures that data relating to any given particle can easily be traced beyond this study.

2.1.3. Micrometeorites from Larkman Nunatak

The Larkman Nunatak micrometeorite collection is an evolving project developed and curated by the micrometeoritics research group at Imperial College London. During the 2006-2007 ANSMET meteorite hunting expedition, approximately 10kg of supraglacial moraine sediment were collected from Larkman Nunatak [86°46'S, 179°20'E], an exposed crescent-shaped mountain, forming the southernmost nunatak of the Shackelton Glacier drainage basin, located within the Grosvenor Mountains, Antarctica.

After analysis of the moraine sediment under binocular microscope and subsequent washing and sieving, samples were searched for extraterrestrial dust by optical picking and magnetic separation. Abundances in excess of 600 cosmic spherules per kilogram of moraine sediment were recovered and include a near-complete collection of micrometeorite types, similar to the statistics observed from blue ice and rock trap collections (Suttle et al., 2015). Additionally, approximately 50 Australasian microtektites were also discovered, the presence of these spherules requires the Larkman site to have been actively accumulating extraterrestrial dust for at least ~0.78Ma (Folco et al., 2008).

Accumulation of micrometeorites at Larkman Nunatak most likely occurs by direct infall, aeolian transport and by ablation of overriding blue ice by katabatic winds and deposition of the host ice-bound partciles. Winnowing is suspected to affect the collection, acting to remove larger (>100µm) particles, and resulting in a biased size distribution (Suttle et al., 2015). Terrestrial weathering is significant, with many particles exhibiting surface encrustations, etching and replacement (van

Ginneken et al., 2016). As a result, fine-grained micrometeorites are exceedingly rare in this collection.

Although Larkman fine-grained micrometeorites are not analysed in this study, textural and geochemical data from Larkman cosmic spherules are employed to provide context and comparisons with the unmelted fine-grained micrometeorites and fossil micrometeorites studied.

Several MSci students, (E. Rosenthal, W. Cheah and B. Davies), as well as post-graduate (*this author*) and post-doctoral researchers (M. Ginneken) have contributed to the development of the Larkman collection. Dr. Matt Genge is the principal investigator for this project. Petrographic data for all Larkman particles are accessible on the Imperial College Micrometeorite database. Further details of the Larkman Nunatak collection, accumulation mechanisms and site characterisation can be found in Genge et al., (2018).

2.2. Carbonaceous chondrites

In addition to the micrometeorites, carbonaceous chondrites were included in the present study to act as reference materials and to represent the closest analogues to fine-grained micrometeorites (Genge et al., 1997). A suite of 11 carbonaceous chondrites, consisting of CM and CI classes, thermally metamorphosed CM chondrites and C2-ungrouped meteorites were obtained from the NHM, from ANSMET research loans and from Dr. Matt Genge's personal collection. By including several CM chondrites, a range of thermal histories are represented. Jbilet Winselwan, PCA 02012 and EET 96029 have experienced moderate-high grade thermal metamorphism, outside the range typically observed among the CM family (Lee et al., 2016; Zolensky et al., 2016), consequently, these samples may represent more appropriate analogue materials for comparison against heated fine-grained micrometeorites, altered by atmospheric entry or parent body heating. The two ANSMET meteorite samples (PCA 02012 and EET 96029) and the NHM sample (Jbilet Winselwan) had previously been analysed by Lee et al., (2016) and Dr. Ashley King using position sensitive – X-ray diffraction (PSD-XRD) to quantify their modal mineralogy (Howard et al., 2009; 2011). This technique requires the meteorite to be crushed to a fine powder, this study therefore received these samples as powders. However, Jbilet Winselwan was analysed in both the powder and polished resin block format. Table 2.1. outlines all carbonaceous chondrite samples analysed in this study, their corresponding datasets and respective sources.

Table 2.1. Carbonaceous chondrite samples analysed in this thesis. This table outlines the datasets collected, origin and format of each sample. Note: samples marked with a cross (†), delineate chips containing a fusion crust edge and are therefore affected by atmospheric entry heating. For most of these samples both unheated and heavily altered material are present in each chip allowing investigation of entry heating affects in known C2 chondritic materials.

No.	Stub ID	Sample	Format	Classification	SEM-BSE	EMPA-Bulk	EMPA-Anhydrous	X-ray element map	µXRD	Fabric analysis	Raman Spectroscopy	Mid-IR spectroscopy	NIR Spectroscopy
1	NHM - P16384	Ivuna	Resin block	CI	•	•					•	•	•
2	Genge personal	Alais†	Resin block	CI	•	•						•	•
3	Genge personal	Orgueil†	Resin block	CI	•	•						•	•
4	NHM - P10918	ALH81002	Resin block	CM2	•	•					•	•	•
5	NHM - P20501	Cold Bokkeveld	Resin block	CM2	•	•				•	•	•	•
6	NHM - P20492	Mighei	Resin block	CM2	•	•					•	•	•
7	NHM - P20501	Murray	Resin block	CM2	•	•					•	•	•
8	Genge personal	Murchison†	Resin block	CM2	•	•						•	•
9	Genge personal	Nogoya†	Resin block	CM2	•	•						•	•
10	NHM - P18927, ANSMET & Genge personal	Jiblet Winselwan	Block & powder	TM-CM	•	•				•	•	•	•
11	ANSMET -	PCA 02012	Powder	TM-CM							•		
12	ANSMET	EET 96029	Powder	TM-CM							•		
13	Genge personal	Renazzo†	Resin block	CR3	•	•						•	
14	NHM - P11243	Tagish Lake	Resin block	C2 ungrouped	•	•					•	•	•
15	NHM - P9530	Bells	Resin block	C2 ungrouped	•	•						•	•

2.3. Experimental techniques

This thesis uses a multi-element approach, analysing a large population of Antarctic fine-grained micrometeorites with a variety of geochemical and spectroscopic techniques. Therefore, each individual micrometeorite has a wide array of associated data (Table 2.2). This section outlines each experimental technique, the facilities where the data were collected, and the operating conditions applied.

2.3.1. SEM-BSE, SEI and EMPA

All SEM data were collected at the Natural History Museum (NHM), London in the Imaging and analysis centre. In total, 3 SEMs were used in this study.

(1) A Zeiss scanning electron microscope (SEM) EVO 15LS fitted with an Oxford Instruments' 80mm^2 X-Max silicon drift detector (SSD) energy dispersive spectrometer (EDS) provided standard-based quantitative geochemical assays. All analyses were performed under accelerating voltages of 20kV, beam currents of 3nA and a focused beam spot (~1µm diameter). Prior to analysis, instrumental gain calibrations were performed against an elemental cobalt standard. This generated a clean single-element spectrum with widely separated energy peaks, suitable for accurate peak position and intensity validation. During analysis an optimal fixed working distance was maintained to maximise count rates. Additionally, beam current, count deadtimes and acceleration voltages were carefully monitored. Raw data were processed using the Oxford Instruments' INCA software, with weight totals determined using "*oxygen by stoichiometry*". Under these analytical parameters quantitative SEM-EDS analyses are capable of producing high-accuracy results. Detection limits are on the order of 0.2wt% and analytical uncertainties vary between 0.1-0.5wt%. However, analyses which contain overlap (that is, multi-phase analyses), analyses of high porosity samples, hydrated and carbonaceous materials (composed of light elements) will all lower the accuracy significantly, leading to weight totals substantially below 100%.

All loaned resin blocks containing Antarctic micrometeorites were analysed by this SEM to identify fine-grained micrometeorites of further interest and to collect low resolution BSE images of all particles. The EVO is optimised for rapid identification of unknown mineral phases found, using stoichiometric analysis.

(2) A Cameca SX100 electron microprobe (EMPA) equipped with five wave dispersive spectrometers (WDS) was also used in this study. This instrument is ideal for high-resolution geochemical and trace element analysis. Under ideal conditions detection limits (and analytical uncertainties) are as follows: Mg 0.02wt% (0.60wt%), Si 0.02wt% (0.70wt%), Al 0.02wt% (0.10wt%), Ca 0.01wt% (0.10wt%), K 0.02wt% (0.01wt%), Na 0.04wt% (0.04wt%), P 0.01wt% (0.02wt%), S 0.03wt% (0.07wt%), Fe 0.03wt% (1.50wt%), Ni 0.03wt% (0.06wt%), Mn 0.02wt% (0.02wt%), Cr 0.01wt% (0.04wt%) and Co 0.01wt% (0.01wt%). The EMPA was used primarily for the collection of bulk geochemical data, although single phase analysis of metal, sulphide and anhydrous minerals in some grains were also conducted.

Prior to operation, the Cameca was calibrated using a suite of mineral standards, specific for each element under detection. Standards included, but were not limited to: forsterite (Mg_2SiO_4) (San Carlos olivine) for calibration of Mg, hematite (Fe_2O_3) for Fe calibration, Wollastonite ($CaSiO_3$) for calibration of Si and Ca and corundum (Al_2O_3) for Al calibration. All analyses were conducted under acceleration voltages of 20kV, beam currents of 10nA and a focused beam spot of ~1µm diameter. Standard ZAF corrections were applied.

A bulk composition for each individual micrometeorite was acquired by collecting a minimum of 8 (and up to 40) randomly selected spot analyses located within a particle's fine-grained matrix. Each spot analysis was then evaluated for accuracy on the basis of weight totals; totals below 70% (an arbitrary cut-off threshold) were rejected. The mean average spot analysis was then calculated and taken as a bulk composition. By their nature matrix analyses are multiphase since the interaction volume within the sample unequally excites a mixed submicron mineral assemblage and the resulting X-rays produce a biased sample of the elemental composition (Fig.2.6 and Rinaldi & Llovet, 2015). Hydrated minerals or carbonaceous phases lower totals further since hydrogen and carbon are not detectable by EMPA. Consequently, chondritic, hydrated matrix always results in low analytical totals (Noguchi et al., 2002; Rubin et al., 2007).

Although detection limits for trace elements in a single WDS analysis are typically on the order of 0.02-0.04wt%, by acquiring and averaging multiple analyses, several of which record the presence of a trace element at or near the detection limit, it is possible to derive a value for the concentration of a trace element, which is below the analytical detection limit but remains meaningful. However, these values should be treated as qualitative indications, not quantitative values.

Despite the known drawbacks and analytical limitations associated with EMPA of fine-grained matrix, this technique is routinely employed in the study of hydrated chondrites (Mcsween, 1987; Tomeoka & Buseck, 1988; Rubin et al., 2007) and micrometeorites (van Ginneken et al., 2012). In this study the EMPA data was a useful tool, which when combined with other analytical techniques aided the interpretation of petrography and mineralogy.

(3) A FEI Quanta 650 field emission gun SEM was also used in this study. Field emission guns provide a more stable electron beam than conventional tungsten filament SEMs and therefore, allow higher resolution imaging (Goldstein et al., 2012). The Quanta is capable of extremely high magnification, resolving submicron compositional and topographic features. This SEM was employed to collect BSE images of several fine-grained micrometeorites and to highlight micron-scale textures of interest to this study.

In addition, the Quanta 650 at the NHM is also equipped with a retractable Bruker Flat Quad 5060F EDS detector capable of ultra-fast and shadow-free semi-quantitative elemental analysis via the production of hyperspectral maps. This function was employed on several fine-grained micrometeorites with complex mineralogy and an extremely fine-grained, heterogeneous matrix. Operating conditions for these particles typically employed a 9kV electron beam which rastered

over the micrometeorite's exposed surface area for approximately 10-20 hours. A count rate output of 27.7kcps and a deadtime of 5-10% was maintained throughout acquisition, providing approximate pixel resolutions of 0.2µm, estimated interaction radii of 0.3µm and interaction depths of 0.6µm.

Table 2.2. Antarctic micrometeorites analysed in this thesis and corresponding data types collected on each particle.

No.	Stub ID	Particle ID	Classification	SEM-BSE	EMPA-Bulk	EMPA-Anhydrous	X-ray element map	µXRD	Fabric analysis	Raman Spectroscopy	Mid-IR spectroscopy	NIR Spectroscopy
1	UMM94-01-02	CP94-050-044	ScMM	•	•							
2	UMM94-01-06	CP94-050-047	FgMM	•	•	•					•	
3	UMM94-01-07	CP94-050-048	Fg-ScMM	•	•				•	•	•	•
4	UMM94-01-08	CP94-050-049	ScMM	•	•	•						•
5	UMM94-01-12	CP94-050-051	C2-FgMM	•	•	•						
6	UMM94-01-13	CP94-050-052	C2-FgMM	•	•	•	•	•		•	•	•
7	UMM94-01-14	CP94-050-053	ScMM	•	•	•					•	
8	UMM94-01-15	CP94-050-054	C1-FgMM	•	•				•	•	•	
9	UMM94-01-22	CP94-050-060	C2-FgMM	•	•	•					•	•
10	UMM94-01-27	CP94-050-063	ScMM	•		•				•	•	
11	UMM94-01-28	CP94-050-064	C1-FgMM	•	•			•			•	•
12	UMM94-01-32	CP94-050-067	C1-FgMM	•	•					•	•	•
13	UMM94-01-33	CP94-050-068	C3-FgMM	•	•							
14	UMM94-01-37	CP94-050-070	ScMM	•								
15	UMM94-01-38	CP94-050-071	ScMM	•	•	•					•	
16	UMM94-01-41	CP94-050-073	ScMM	•	•	•						•
17	UMM94-01-42	CP94-050-074	C1-FgMM	•	•				•	•	•	•
18	UMM94-01-43	CP94-050-075	C2-FgMM	•	•					•		
19	UMM94-01-50	CP94-050-079	ScMM	•	•				•	•	•	
20	UMM94-01-51	CP94-050-081	C1-FgMM	•	•	•				•	•	
21	UMM94-01-52	CP94-050-082	C2-FgMM	•	•							
22	UMM94-01-54	CP94-050-080	C2-FgMM	•	•						•	
23	UMM94-01-55	CP94-050-084	ScMM	•		•					•	
24	UMM94-01-63	CP94-050-090	ScMM	•	•					•	•	
25	UMM94-01-81	CP94-050-096	C2-FgMM	•	•	•			•		•	
26	UMM94-01-82	CP94-050-097	C2-FgMM	•	•					•		
27	UMM94-01-83	CP94-050-099	C2-FgMM	•	•							
28	UMM94-01-84	CP94-050-100	C2-FgMM	•	•					•		

Table 2.2. *Continued*.

No.	Stub ID	Particle ID	Classification	SEM-BSE	EMPA-Bulk	EMPA-Anhydrous	X-ray element map	µXRD	Fabric analysis	Raman Spectroscopy	Mid-IR spectroscopy	NIR Spectroscopy
29	UMM94-01-85	CP94-050-101	ScMM	•	•	•						
30	UMM94-01-93	CP94-050-105	C2-FgMM	•	•						•	•
31	UMM94-01-94	CP94-050-106	C2-FgMM	•	•							
32	UMM94-01-97	CP94-050-109	C2-FgMM	•	•		•		•	•	•	•
33	UMM94-01-98	CP94-050-110	C2-FgMM	•	•			•	•			
34	UMM94-02-04	CP94-050-113	C2-FgMM	•	•	•				•	•	
35	UMM94-02-07	CP94-050-115	C2-FgMM	•	•	•				•	•	
36	UMM94-02-12	CP94-050-182	C2-FgMM	•	•		•				•	
37	UMM94-02-13	CP94-050-183	C1-FgMM	•	•					•	•	
38	UMM94-02-15	CP94-050-185	ScMM	•								
39	UMM94-02-16	CP94-050-256	C1-FgMM	•	•					•	•	
40	UMM94-02-25	CP94-050-122	ScMM	•	•						•	
41	UMM94-02-26	CP94-050-123	C2-FgMM	•	•	•			•	•	•	
42	UMM94-02-31	CP94-050-127	C2-FgMM	•	•	•			•	•	•	
43	UMM94-02-33	CP94-050-128	C1-FgMM	•	•				•			
44	UMM94-02-35	CP94-050-129	C1-FgMM	•	•					•	•	
45	UMM94-02-35a	CP94-050-130	C2-FgMM	•	•					•	•	
46	UMM94-02-38	CP94-050-132	C1-FgMM	•	•							
47	UMM94-02-43	CP94-050-136	C2-FgMM	•	•	•			•	•	•	
48	UMM94-02-44	CP94-050-137	C3-FgMM	•	•	•						
49	UMM94-02-48	CP94-050-139	C1-FgMM	•	•				•	•	•	
50	UMM94-02-49	CP94-050-140	C1-FgMM	•	•	•			•	•	•	
51	UMM94-02-51	CP94-050-142	C2-FgMM	•	•	•			•	•	•	
52	UMM94-02-62	CP94-050-150	ScMM	•	•							
53	UMM94-02-64	CP94-050-152	C2-FgMM	•	•	•			•	•	•	
54	UMM94-02-65	CP94-050-153	C2-FgMM	•	•	•				•	•	
55	UMM94-02-71	CP94-050-158	Fg-ScMM	•	•						•	
56	UMM94-02-72	CP94-050-159	C2-FgMM	•	•					•	•	

Table 2.2. *Continued*.

No.	Stub ID	Particle ID	Classification	SEM-BSE	EMPA-Bulk	EMPA-Anhydrous	X-ray element map	µXRD	Fabric analysis	Raman Spectroscopy	Mid-IR spectroscopy	NIR Spectroscopy
57	UMM94-02-72A	CP94-050-160	C2-FgMM	•	•		•		•	•	•	
58	UMM94-02-73	CP94-050-161	C1-FgMM	•	•							
59	UMM94-02-76	CP94-050-163	C2-FgMM	•	•	•			•	•	•	
60	UMM94-02-80	CP94-050-167	C2-FgMM	•	•	•			•		•	
61	UMM94-02-81	CP94-050-168	C2-FgMM	•	•				•		•	
62	UMM94-02-82	CP94-050-169	C1-FgMM	•	•					•	•	
63	UMM94-02-84	CP94-050-170	C2-FgMM	•	•					•	•	
64	UMM94-02-93	CP94-050-176	C1-FgMM	•	•					•	•	
65	UMM94-02-95	CP94-050-178	ScMM	•								
66	UMM94-02-97	CP94-050-180	C1-FgMM	•	•					•	•	
67	TAM-M1	19B-7	Chondrule-bearing - CM2.0	•	•		•		•		•	
68	TAM-M4	4-16.	C2-FgMM	•						•	•	•
69	TAM-M4	4-27.	C2-FgMM	•						•	•	•
70	TAM-M5	4-14.	Chondrule bearing - CV-like	•						•	•	•
71	TAM-M5	5-30.	Chondrule bearing - C2 ungrouped	•	•					•	•	•
72	TAM-M5	15-11.	C1-FgMM	•	•					•	•	
73	TAM-M6	5-18.	C2-FgMM	•	•			•			•	
74	TAM-M6	19-7.	C1-Fg-ScMM	•	•		•	•		•	•	•
75	TAM-M6	19B-17.	C2-FgMM	•	•		•	•		•	•	
76	TAM-M7	18C-12.	FgMM	•	•			•		•	•	•
77	TAM-M7	19B-18.	C2-FgMM	•	•			•		•	•	•
78	TAM-B2	2.1C.	CI chondritic (C1)	•	•						•	
79	TAM-B2	2.1Q.	C2-FgMM	•	•		•				•	
80	TAM-B2	2.1T.	FgMM	•	•						•	
81	N/A	37P-03	C1-FgMM	•				•				

Figure 2.6. SEM-EDS analysis of a mixed phase sample. This schematic displays a 20KeV beam centred directly over a grain boundary between forsterite [Mg_2SiO_4] (left) and kamacite [Fe_9Ni] (right). Electron travel path and penetration depth are illustrated using density shading. Due to differences in composition and density, the excitation of inner shell electrons and subsequent emission of X-rays is biased towards the overproduction of counts from the kamacite. The resulting spectrum will therefore give an overestimate of Fe and Ni concentration. This simulation was performed in the CASINO software (v.2.42), modelling 6000 electron paths.

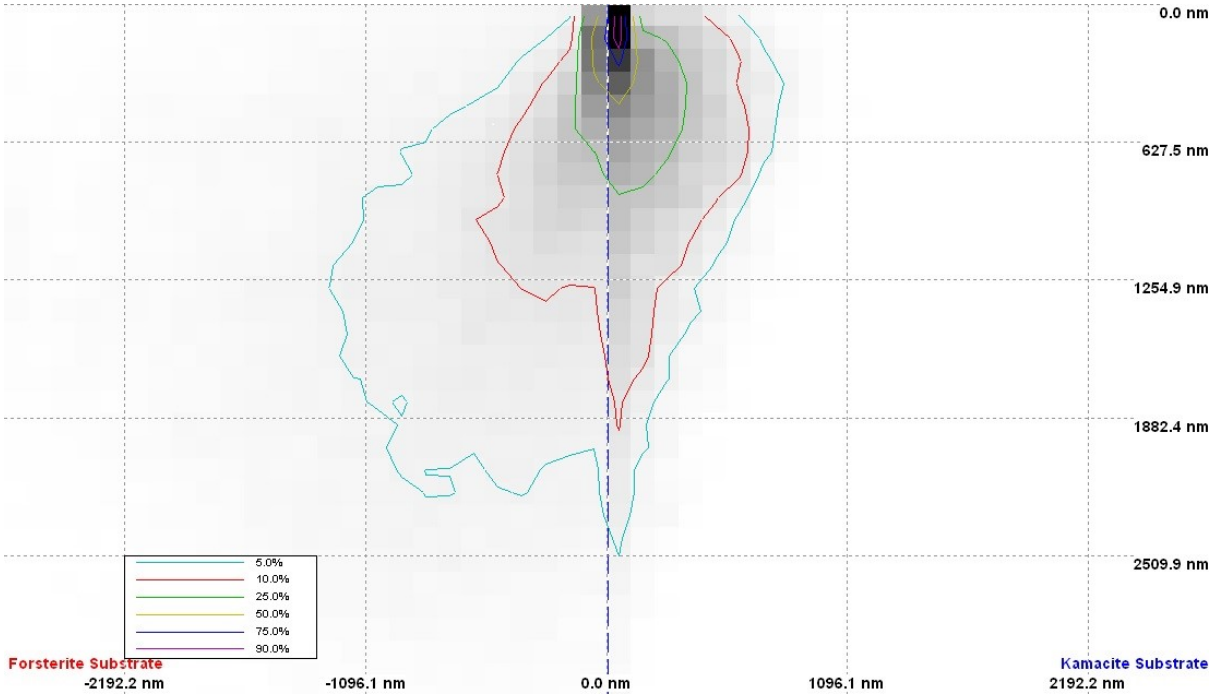

2.3.2. Micro-X-ray diffraction

Whole particle phase identification was conducted in the micro-X-ray diffraction (µXRD) laboratory at the NHM, London. A Rigaku Rapid II micro-diffraction system, equipped with a 2D curved imaging plate detector was employed to collect diffraction pattern data from several selected micrometeorites. The large-area, curved detector subtends a 2θ range, allowing rapid collection of data and inclusion of diffraction peaks at low and high angles.

A Cu X-ray source was selected for analysis and fitted to an incident beam monochromator, providing a clean, continuous Cu-Kα source with a voltage and current of approximately, 40kV and 36 mA respectively. This was focused through a choice of 50µm, 100µm or 300µm diameter collimators, selected based on the particle size of the micrometeorite under analysis. To maximise the number of absolute counts and grain orientations, the stage was set to continuous in-plane (ϕ) rotation. Each micrometeorite analysis ran for approximately 24hours. Pattern data were analysed using the in-house Rigaku 2DP image processing software. The 2D diffraction images were converted to 1D XRD pattern data following automated removal of the background signal and integration of the Debye rings over reflection angles between 20-80°2θ. Low-angle (<20°2θ) diffraction data could not be collected, because the resin block which holds the micrometeorites, prevented the stage from rotation out-of-plane (Ω) below 20°2θ, cutting off low-

angle reflections. Peak positions in the converted 1D pattern were identified by comparison against the PDF-4 database, this includes an extensive mineral database (held by International Centre for Diffraction Data (ICDD)).

The success of the µXRD technique was highly dependent on the size of the micrometeorites. Data collected from the smaller Cap Prud'homme micrometeorite suffered from artefacts arising from the epoxy resin in which the micrometeorites were mounted. This produced a large, broad peak, which spanned the range ~20-50°2θ. Conversely, the larger TAM micrometeorites produced diffraction patterns with clear peaks associated with inorganic minerals.

2.3.3. Micro-computed tomography

Within Earth Sciences, the use of non-invasive, high-resolution µCT has found a wide range of applications visualising the internal structure of small, rare and complex materials (Ketcham and Carlson, 2001; Landis and Keane, 2010; Lin et al., 2016). A laboratory-based Zeiss Xradia 510 Versa X-ray microscope, located in the Earth Science and Engineering Department at Imperial College London was used to analyse a single micrometeorite: TAM37P-03.

A total analysis volume of approximately 500x500x500µm (0.125mm^3) was investigated, which included the entire micrometeorite's volume (~0.04mm^3). The sample was scanned using a cone-beam setup and sealed transmission X-ray source, at high energy (50keV) and with a 20x magnification lens. This generated a high-resolution scan, with a voxel size of just 0.64µm. A 3D model of the particle could then be created using the 871 tomographic slices - acquired at a rotation rate of ~0.2° per projection. Before processing these images, the raw reconstructed scan was filtered using a nonlocal means edge preserving filter (Buades et al., 2008) that reduced image noise arising from beam attenuation, beam hardening and ring artefacts (Ketcham and Carlson, 2001). Pore space within this micrometeorite was then segmented using a histogram-based thresholding method (Tsai, 1985) as shown in Fig.7.S1. In the final dataset (Fig.7.4), as with standard SEM-BEI data, black regions represent void space, while grey-scale values are used to show the average atomic weight of the sample, with white areas representing the highest average weight materials.

2.3.4. Mid-IR spectroscopy

Mid-IR spectroscopic data were collected at Diamond Lightsource, located within the Harwell science and innovation campus in Didcot, Oxfordshire, UK. A Thermo scientific FT-IR spectrometer equipped with a Nicolet continuum microscope attachment collected spectra from all micrometeorite samples. Mid-IR spectra were collected in percentage reflectance mode. Each spectrum combined 120 integrated scans with a 4cm^{-1} resolution. A reference background spectrum, collected upon a clean, polished gold standard (and resampled every hour), was subtracted from the raw data. Data were collected in air and corrections for atmospheric suppression were not applied. Preliminary experiments using a nitrogen purge system demonstrated that these fine-grained micrometeorites did not contain any absorption bands in the wavelength regions affected by atmospheric absorption (approximately 3-8µm), instead, only

vibrations in the silicate fingerprint region (approximately 8-15µm wavelengths) were observed. No baseline correction of spectra was necessary.

A global Mid-IR spectrum was obtained for each Cap Prud'homme micrometeorite by altering the aperture on microscope to fit the size of the particle being analysed. For the TAM micrometeorites several spectra were collected, ensuring that the entire exposed surface area of the particle was analysed. These spectra were then averaged to give a global spectrum. For the carbonaceous chondrite samples, spectra were collected through a 100µm^2 grid.

2.3.5. Near-IR spectroscopy

Near-IR spectroscopic data were collected at the Walloon Agricultural Research Centre (in French: *Centre de recherche agricole, wallon* and abbreviated to CRA-W). Data were collected in the Maurice Henseval building, located on Chée de Namur 24, 5030 Gembloux, in Wallonia, Belgium. After discussion of the thesis' aims with the Head of the Food and Feed Quality at CRA-W Unit, Dr. Vincent Baeten kindly allowed the required spectroscopic data to be collected, at their site over the period of a week, from 26-30th, Oct, 2015.

Data were collected on a Bruker 3000 Hyperion NIR microscope. The microscope used a 15x objective lens, a CaF_2 beamsplitter, TE-InGAs detector and 10kHz scanning velocity, providing an optimised setup for the measurement of spectra over NIR wavelengths. A reference spectrum was collected on a white, teflon background and resampled between each measurement. Spectra were collected as absolute absorbance values and then converted to reflectance values for comparison with asteroid spectra. Each spectrum integrated 8 scans and used a sampling resolution of 16cm^{-1}. Spectra cover the wavelength range ~0.8-2.5µm (~12,500-4000cm^{-1} wavenumbers). Despite optimised conditions, at low wavelengths (approximately 0.8-1.0µm) data quality is affected by poor signal-to-noise.

For each sample, the aperture on the microscope was adjusted to fit the size of the micrometeorite, avoiding the epoxy resin holding the particles. Micrometeorites were scanned in a 4-by-4 grid, producing a data block of 16 spectra. This method provided spatially resolved spectra which could either be combined to give a single, bulk NIR spectrum or analysed independently to compare components within a single micrometeorite.

In addition to data collection at CRA-W, data collect was also attempted at the German Aerospace Centre (in German*: Deutsches Zentrum für Luft- und Raumfahrt* abbreviated to DLR), in Aldershof, Berlin. Dr. Alessandro Maturilli, granted access to the lab for the week 12-16th Dec, 2016. Data were collected on a commercial Bruker IFS,125HR FTIR spectrometer. However, the lack of a microscope attachment for this instrument prevented any meaningful data from being acquired. During trial experiments all spectra collected from micrometeorite surfaces were dominated by the signal of the epoxy resin. Despite best efforts this problem could not be overcome with the experimental setup available. Therefore, the spectra from DLR are not included in this thesis.

2.3.6. Raman Spectroscopy

Raman spectra were also collected at Diamond Lightsource, in the spectroscopy and support lab 91. A Renishaw inVia Raman Microscope was used, with a 473nm green Ar+ laser. Excitation radiation was focused through a 50x objective lens, providing a spot size of ~6µm diameter. Laser power was kept below 80µW and acquisition times below 30 seconds, this prevented sample degradation through heating and graphitisation of organic matter (Kagi et al., 1994). Repeated measurements upon the same region of CM2 Cold Bokkeveld, were performed to ensure sample alteration did not occur during analysis. Raman spectra were collected from randomly selected points within the matrix of each sample. Repeat analyses reduced analytical uncertainty by allowing rejection of unreliable and noisy spectra and determination of sample heterogeneity.

Except when specified, spot measurements were collected from within the matrix of fine-grained micrometeorites in those areas interpreted to be the least altered, for example avoiding igneous rims, vesicles and mesostasis identified through BSE imaging. Additionally, line transects were performed on 8 micrometeorites and a section of CM2 Murchison. Transects spanned the entire length of the particle and were collected to investigate the spatial relationship between each particle's core and rim. For each line transect a step size of 5µm was chosen. All other analytical parameters including acquisition times, laser power and spot size were kept identical to the point analyses.

Chapter 3: Chemistry, Mineralogy and Petrography of Antarctic Micrometeorites

3.0. Overview – This chapter explores the petrography of fine-grained micrometeorites using SEM-BSE, EMPA, X-ray element mapping and µXRD. Particles are shown to have chondritic compositions, overprinted by characteristic depletions and enrichments relating to their terrestrial collection sites. Bulk mineralogy, as determined by µXRD, reveals a low-degree of crystallinity with anhydrous olivine and pyroxene, sulfides and magnetite as the only minerals detected. This suggests that atmospheric entry has resulted in the complete loss of hydrated sheet silicate phases. The extent of aqueous alteration among fine-grained micrometeorites is evaluated using criteria developed for CM chondrites. Most particles show moderate-severe alteration and contain only residual anhydrous silicates. A single micrometeorite, containing a relict pseudomorphic chondrule, was also identified and assigned a CM2.0 petrologic subtype. In agreement with previous studies, the current flux of fine-grained micrometeorites appears to be chondrule-poor, even when the contribution from coarse-grained micrometeorites (interpreted as chondrule fragments) are considered. This study, therefore, proposes that the source asteroids of the micrometeorite flux are primarily intensely altered, hydrated, CM-like bodies.

3.1. Aqueous alteration in carbonaceous chondrites

Hydrated C1 and C2 carbonaceous chondrites contain abundant water, between 2-20wt% (Tonui et al., 2003; Rubin et al., 2007). This requires a significant episode of aqueous alteration on the parent asteroid (Vebel et al., 2001; Rubin et al., 2007; Velbel and Palmer, 2011). Among CM and CI chondrites, phyllosilicate phases have replaced anhydrous minerals, amorphous condensates and mesostasis glass (Browning et al., 1996; Rubin et al., 2007; Vebel and Palmer, 2011), resulting in high phyllosilicate concentrations, >60%vol (Howard et al., 2009; 2011). The matrix of hydrated carbonaceous chondrites is, therefore, dominated by sub-micron short stacked and misorientated phyllosilicate clusters, intermixed with hydrated sulphides, primarily tochilinite (Fig.1.6, McSween, 1979; 1987; Rubin et al., 2007). Consequently, the CM and CI matrix is highly porous, exhibits a low degree of crystallinity and is extremely fine-grained (Rubin et al., 2007).

Aqueous alteration occurred under low-temperature (0-300°C) oxidising conditions (Bunch and Chang, 1980; Johnson and Prinz, 1993; Keil, 2000; Busemann et al., 2007; Guo and Eiler, 2007). With high water-to-rock ratios (Lee et al., 2012) and under relatively short durations (Rubin, 2012). Probable sources of heat include radiogenic decay (Keil, 2000; Kunihiro et al., 2004; Šrámek et al., 2012), impact events (Rubin, 2012; Hanna et al., 2015; Lindgren et al., 2015) and tidal heating (Mizuno and Boss, 1985). For the CM chondrites aqueous alteration was moderate. Within this subgroup, individual meteorites are assigned a petrologic subtype, reflecting the degree of aqueous alteration (McSween, 1979; 1987; Browning et al., 1996; Trigo-Rodriguez et al., 2006; Rubin et al., 2007; Vebel and Palmer, 2011). Serpentization progresses by the replacement of anhydrous phases with phyllosilicates. Initially Fe-rich cronstedtite forms, later this is reprocessed to generate Mg-rich serpentine (Tomeoka et al., 1989; Howard et al., 2009; 2011; Vebel and Palmer, 2011). In low petrologic subtype chondrites

(CM1/CM2.0), such as Kaidun (Zolensky et al., 1996a), EET 83334, ALH 88045 (Zolensky et al., 1997), LAP 02273 and MET 01070 (Rubin et al., 2007), all anhydrous phases are lost and even chondrules are replaced by phyllosilicate (Hanowski and Brearley, 2001; Trigo-Rodriguez et al., 2006; Rubin et al., 2007). Among these meteorites, relict textures record the outlines of former chondrules. At such high degrees of alteration, chemical and isotopic homogenisation occurs, as a result of cation diffusion (Zega and Buseck, 2003; Lee et al., 2012). However, the most intensely altered chondrite group is the CI class, which lack chondrules and refractory phases completely. In addition, the matrix is homogenous and composed of Mg-rich saponite (Tomeoka and Buseck, 1988). Framboidal and platelet magnetite are present, most likely representing the oxidation of FeNi metal during aqueous alteration (Tomeoka and Buseck, 1988).

The similarity between CM and CI chondrites and fine-grained micrometeorites is well-documented (Steele, 1992; Genge et al., 1997; Taylor et al., 2012; van Ginneken et al., 2012). This implies a genetic relationship between micrometeorites and C2 chondrites. As a result, studies on C2 hydrated chondrites directly inform fine-grained micrometeorite research and vice versa. However, since micrometeorites sample many more individual asteroids than meteorites, by virtue of the P-R drag delivery mechanism (Poynting, 1904; Dohnanyi, 1976; Nishiizumi et al., 1995; Nesvorný et al., 2003; 2006), research on fine-grained micrometeorites has the potential to greatly expand our collective knowledge of C-type asteroids. In this chapter, the petrography of the Antarctic micrometeorite population is explored through the use of SEM-BSE to analyse textures, EMPA to investigate bulk and trace geochemistry and through µXRD to resolve mineralogy.

3.2. Results: multi-element microanalysis of Antarctic micrometeorites

In total eighty-one unmelted micrometeorites are analysed in this thesis (64 fine-grained and 17 scoriaceous micrometeorites, Table.2.2). Several particles were selected for a more in-depth analysis, using elemental mapping and µXRD.

3.2.1. Bulk geochemistry from EMPA

Bulk compositions were determined for 74 (~91%) of the Antarctic micrometeorites analysed in this thesis (Table 2.2 and Sect.2.4.1). All particles have chondritic elemental abundances (Fig.3.1, Table.3.1), calculated relative to CI Ivuna. Major elements vary between Mg 0.1-1.3x (1.4-16.1wt%), Al 0.5-8.0x (0.5-9.0wt%), Si 0.5-1.5x (7.4-21.8wt%) and Fe 0.7-3.0x (10.3-45.4wt%). Despite chondritic compositions, all the micrometeorites are depleted in Ni 0.04-0.80x (b.d.l-1.2wt%) and Co 0.0-1.0x (b.d.l, ~0.07wt%). In addition, subtle differences are observed between collection sites. For example, S is heavily depleted among the Cap Prud'homme micrometeorites 0.08-1.16 (b.d.l-0.4wt%) while the TAM particles have chondritic concentrations 0.29-1.93 (0.8-5.5wt%), though this may reflect the later addition of S by terrestrial weathering products (van Ginneken et al., 2016). Conversely, the TAM particles are enriched in K up to 2.76 times above chondritic values. Variations in composition between collection sites most likely represent differences in the geochemical environment, age and mechanisms of terrestrial weathering.

3.2.2. Bulk mineralogy from µXRD

In total, µXRD pattern data were collected from nine micrometeorites. The success of this technique was dependent entirely on the size of the micrometeorites analysed. The TAM particles were sufficiently large to remain centred under the radiation beam during analysis, while the smaller Cap Prud'homme particles rotated in and out of the beam during data acquisition. This resulted in the collection of diffraction signals from the epoxy resin holding the micrometeorites. Even when the smallest aperture on the beam collimator (50µm diameter) was used and the particle held stable and the data collection time extended (>50 hours), the only detectable signal from the Cap Prud'homme micrometeorites were magnetite peaks, found in particle CP94-050-052. By contrast, all the TAM particles produced X-ray patterns containing inorganic mineral peaks, an example of which is shown in figure 3.2. Forsterite, enstatite and troilite were detected in every TAM particle, while jarosite and magnetite were also present in most particles. Conversely, chromite, pyrrhotite, akaganéite, calcite, halite and goethite were detected in individual micrometeorites (Table 3.1). Diffraction peaks associated with hydrated phyllosilicates were not detected.

Fig.3.1. Spider diagrams illustrating the bulk chemical composition of the Antarctic micrometeorite population. Values are normalized against solar composition [CI Ivuna, P16384, Table.2.1]. Each micrometeorite is plotted as a grey line. The population is split into (A) Cap Prud'homme and (B) TAM samples, allowing distinct differences to be observed in the composition of micrometeorites recovered from each site. Primarily this reflects differences in preservation and weathering artefacts as a result of different storage sites and ages. However, all particles show depletions in Co and Ni, as a result of leaching and interaction with terrestrial water.

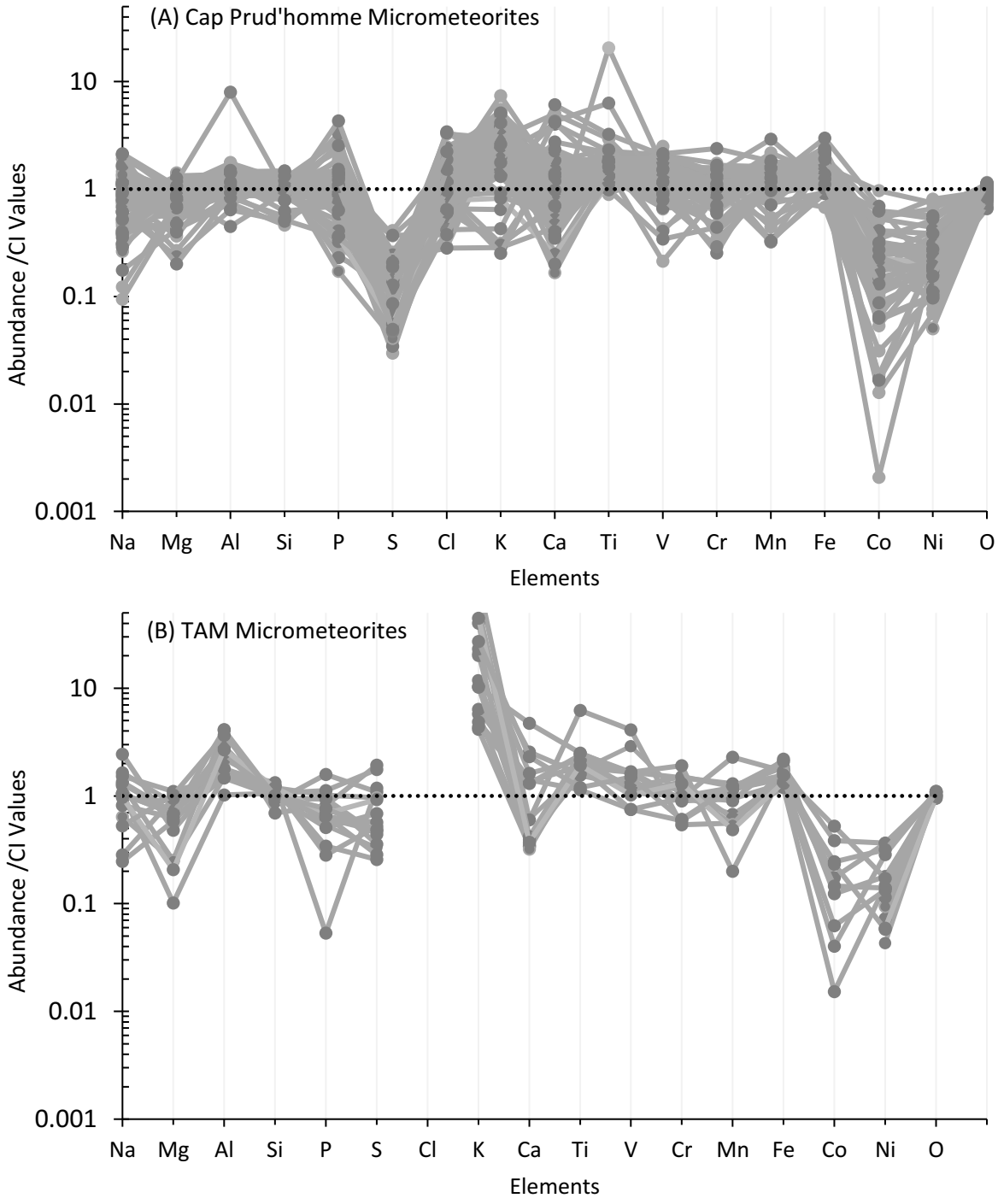

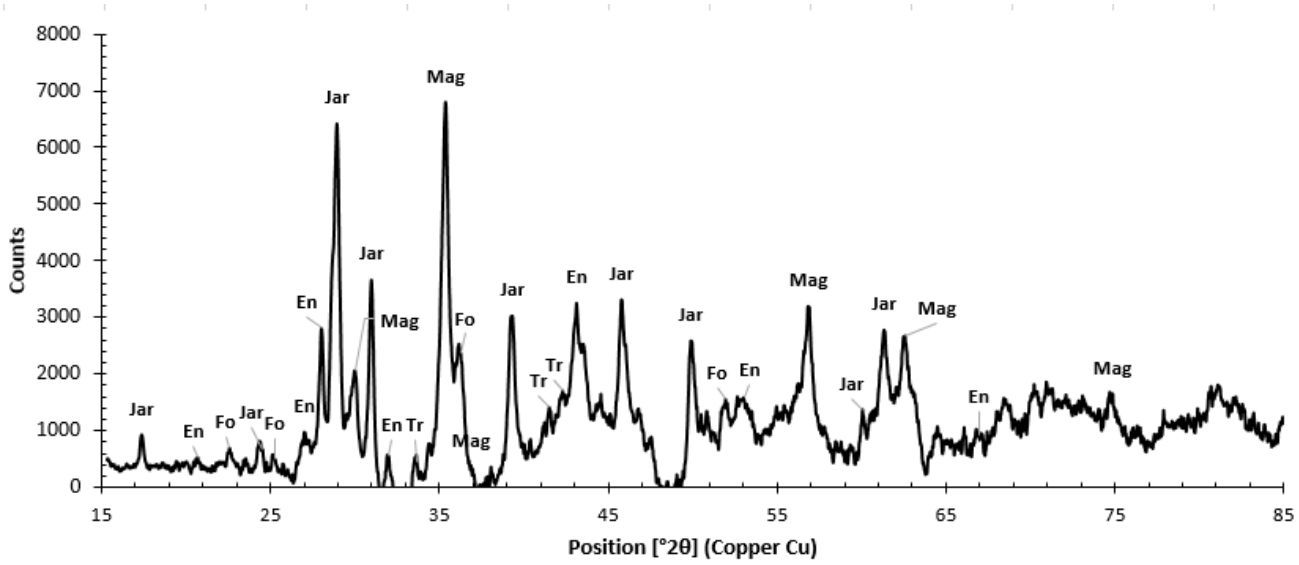

Fig.3.2. Micro-XRD pattern data from particle TAM19-7. Data were collected over the diffraction angles 15-85° (2θ). Low angle peaks (including the primary peaks associated with phyllosilicates ~10°) could not be imaged, owing to limitations in the experimental setup (see section 2.4.2). Several significant diffraction peaks associated with each mineral are labelled using the following abbreviations: Fo=forsterite, En=enstatite, Tr=troilite, Mag=magnetite and Jar=jarosite.

Particle	Forsterite	Enstatite	Magnetite	Chromite	Troilite	Pyrrhotite	Akaganéite	Halite	Calcite	Goethite	Jarosite
CP94-050-052			•								
CP94-050-064											
CP94-050-110											
TAM19-7	•	•	•		•						•
TAM18C-12	•	•	•	•	•					•	•
TAM19B-17	•	•			•			•	•		•
TAM19B-18	•	•	•		•						•
TAM5-18	•	•			•	•					
TAM19B-7			•				•				•
TAM37.P03	•	•	•								

Table 3.1 Qualitative assessment of micrometeorite mineralogy for the ten particles analysed, as determined by µXRD. All TAM particles contain anhydrous Mg-rich silicates and most particles contain magnetite. Chromite and Fe-sulfides are also detected in several grains while halite, calcite, goethite and jarosite are interpreted as terrestrial weathering products (see van Ginneken et al., 2016).

3.2.3. Fine-grained matrix: textures and geochemistry

Fine-grained micrometeorites have a complex, mixed mineral assemblage composed of extremely small crystals <<10µm, commonly embedded in an amorphous silica glass. As a result, even under high magnification SEM, it is often not possible to distinguish individual crystals. Similarly, EMPA obtained from fine-grained micrometeorite matrix always contains overlap and, therefore, produces non-stoichiometric atomic ratios (Fig.3.3, Table.3.1). Most analyses have O/Si ratios between 3.0 and 4.5, while the ideal ratio for serpentine is 4.5, for olivine 4.0 and for enstatite and saponite 3.0. The variable analysis ratios derived from micrometeorite matrix imply a mixed assemblage most likely composed of these four silicate phases. The dominant cations are Fe and Mg (totalling ~33wt%, ~22at%), which display a negative correlation in elemental abundance, such that a micrometeorite's matrix is typically either Mg-rich, Fe-poor or Fe-rich, Mg-poor.

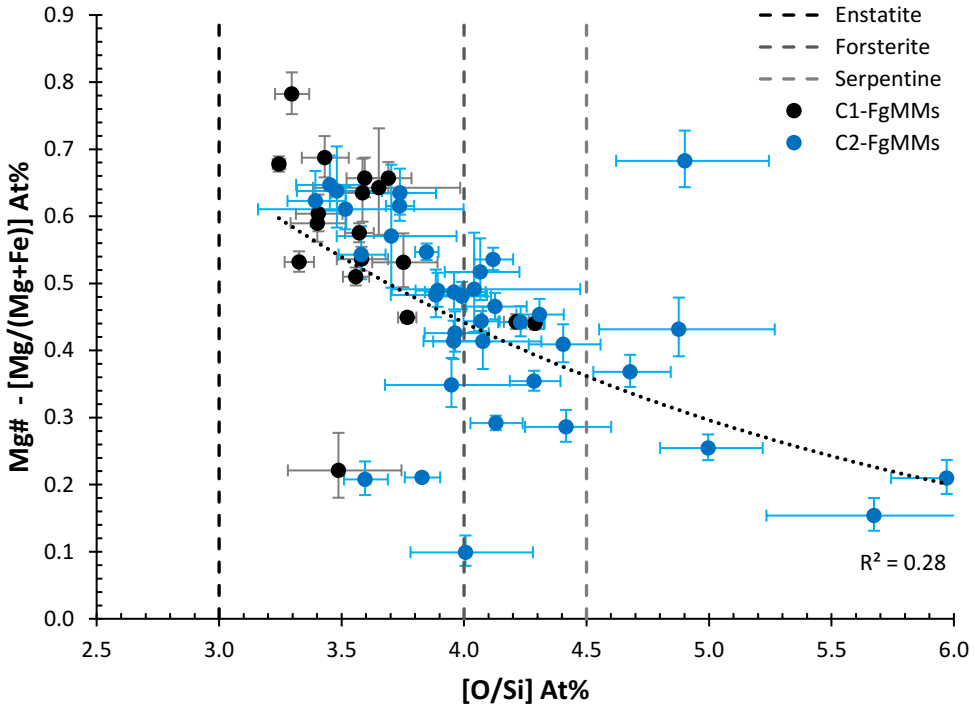

Fig.3.3. Average EMPA data obtained from the matrix of fifty-five micrometeorites (fine-grained and scoriaceous). Atomic ratios of O/Si and their Mg# (Mg/[Mg+Fe]) are displayed. This allows the dominant matrix mineral to be inferred from silicate stoichiometry (O/Si) and the cation composition of to be evaluated via the Mg#. The stoichiometric compositions for enstatite (and saponite), olivine, and serpentine are plotted as dashed black, dark grey and light grey lines respectively. The majority of micrometeorite matrix compositions fall within this compositional range 3.0<[O/Si]<4.5, suggesting that most micrometeorites are composed of a mixed mineral assemblage of anhydrous framework and chain silicates and hydrated sheet silicates. In addition, this plot reveals a weak negative correlation (R^2=0.35) between silicate stoichiometry and Mg#; demonstrating that enstatite/saponite compositions tend to be Mg-enriched while micrometeorites with a serpentine-bearing matrix tend to be Fe-enriched. A few micrometeorites contain an anomalous matrix composition with high O/Si ratios (>4.5) these silica-poor micrometeorites are oxidised. It is possible that some of these micrometeorites contain Fe-oxides produced during atmospheric entry heating from Fe-sulfides. Alternatively, their matrix may contain small spinels or other oxides. In this chart C1-FgMMs are plotted as solid black circles and C2-FgMMs plotted as solid blue circles. Error bars show one standard error of the mean away from the average atomic ratio. These values were calcualted using the quoted analytical uncertainties for each element (shown in Sect.2.3.1, Cameca SX100). Because the graph plots At% ratios, the min and max error bars represent a combined error calculation, for example min error is determined as: [the smallest possible value / the largest possible value], while max error is the reverse.

The pre-atmospheric mineralogy of fine-grained micrometeorites is dominated by phyllosilicates (Genge et al., 2001; 2008; Nakamura et al., 2001; Noguchi et al., 2002). Micrometeorites analysed here contain some relict coarse-grained phyllosilicate clusters, which can be tentatively identified in some particles under SEM-BSE (Fig.3.4D-G). These appear as dense, lens-shaped, radiating or irregular masses, containing fibrous, acicular or sheet-like morphologies (Rubin et al., 2007). However, in most instances, chondritic phyllosilicates are too small to confidently resolve with SEM-BSE techniques alone and, instead, require the use of a TEM to measure the interlayer basal spacing distances (Nakamura et al., 2001; Noguchi et al., 2002). Thus, the phyllosilicate matrix in most micrometeorites typically appears as an indistinct porous material, infilling the space between inclusions and vesicles. However, because micrometeorites are heated above 600°C during atmospheric entry, phyllosilicate dehydration products are common, and easily identified by the presence of dehydration cracks - linear voids, frequently <10µm in length and often found as subparallel clusters (Chapt.6, Genge et al., 2001; 2008). Using the above textural evidence, phyllosilicates represent the major phase in micrometeorite matrix (>65% vol), in both the C1 and C2 micrometeorites.

Two end-member phyllosilicate morphologies are recognised: (1) relatively coarse-grained Fe-rich (light-coloured) masses, which commonly have radiating or star-like morphologies, as in CP94-050-075 (Fig.3.4F [edge]) and CP94-050-105 (Fig.3.4G). Alternatively, (2) phyllosilicates may appear as Mg-rich finer-grained (dark-coloured) masses, typically with fewer and smaller dehydration cracks, as in CP94-050-067 (Fig.3.4), CP94-050-075 (Fig.3.4F [centre]) and CP94-050-140 (Fig.3.4H). However, phyllosilicates with intermediate characteristics as in CP94-050-0152 (Fig.3.4D) are also common. Occasionally, these two distinct morphologies may co-occur within a single micrometeorite, as seen in CP94-050-075 (Fig.3.4F), CP94-050-105 (Fig.3.4G), CP94-050-060 (not shown) and CP94-050-110 (Fig.3.6C). Within these particles, both phyllosilicate types are found inter-grown although boundaries phases remain distinct. Phyllosilicates are also commonly found mantling anhydrous silicates as in CP94-050-105 and CP94-050-110 (Fig.3.5C and 3.5D) or surrounding other accessory phases, as in CP94-050160 (Fig.3.4C) where coarse Fe-rich phyllosilicates coat a rare refractory Mg-Al spinel, suspected to be a hibonite-Fe ($[Fe,Mg]Al_{12}O_{19}$) grain (Sect.5.7).

Micrometeorites also contain non-silicate phases. Low concentrations of S (~0.8wt%,) are detected in all matrix analyses. Because S does not partition into the silicate crystal lattice, these contributions most likely represent small FeNi sulfide crystals, including tochilinite ($6Fe_{0.9}S{\cdot}5[Mg,Fe^{2+}][OH]_2$), troilite (FeS) or pyrrhotite ($Fe_{(1-x)}S_x$) (Table 3.1.). Furthermore, larger FeNi sulphide grains are identified in several micrometeorites and appear as either dispersed, rounded particles as in CP94-050-048 (Fig.3.4K) or as radiating, fibrous masses, ~5-10µm in size, as in CP94-050-160 (Fig.3.4C). Oxides are also common. Most unmelted micrometeorites have magnetite rims as well as internal magnetite crystals, with platelet or framboidal morphologies (Fig.3.4H and Fig.1.6). These are most common among the C1-FgMMs and are, therefore, typically found among a Mg-rich matrix with low O/Si ratios (~3.0). Accessory chromite and other refractory spinels were

also detected in some particles, and notably common in TAM2.1T (Fig.3.5) and CP94-050-182 (not shown).

Fourteen micrometeorites (~18%) have geochemically distinct internal clasts. These clasts identified as lithological inclusions within a micrometeorite, which are texturally and geochemically distinct, composed of multiple crystals and have a clearly defined boundary, separating the clast from the host lithology. In most cases, clasts are primarily composed of phyllosilicates (and their thermal decomposition products) and are composed of a different but related chondritic lithology to their host particle. For example, particle CP94-050-0142 (Fig.3.4I) contains a diamond-shaped clast with an Fe-enriched composition relative to the host matrix. This clast also contains significantly more and larger dehydration cracks, suggesting a coarser grain size and a more heat-sensitive phyllosilicate species than the host matrix. Conversely, particle CP94-050-123 (Fig.3.4J) contains a dark clast with Mg-enriched composition relative to the host matrix and small magnetite grains. Likewise, TAM2.1T (Fig.3.5) also contains a Mg-rich dark clast consisting of 30% of the particle's exposed surface area and hosting several rounded magnetite grains as well as a single magnetite platelet. In TAM2.1T both the C1 and C2 lithologies are exposed at the particle perimeter, allowing a comparison to be made between the response of both lithologies to (approximately) the same peak temperature. In this case the magnetite rim coating the C1 lithology is approximately half the thickness of the rim on the C2 lithology, while the C2 lithology also contains significantly more dehydration cracks.

Fig.3.4. (Overleaf) Image panel illustrating the range of matrix textures observed within the Antarctic micrometeorite population. Particles are grouped such that similar textures appear together and ordered to reflect an increasing atmospheric entry overprint. Panels A-C show micrometeorites containing intact phyllosilicates. Particles CP94-050-052 (A) and TAM19B-17 (B) have a heterogeneous matrix, composed of well-defined isolated micron-scale silicates. Anhydrous forsterite and enstatite crystals are common and appear as small rounded grains. Conversely, particle CP94-050-160 (C) contains a relatively homogenous matrix composed of Mg-rich serpentine in which fibrous, radiating tochilinite is suspended. Additionally, this micrometeorite contains a rare refractory phase (identified as hibonite, [$Ca(Al,Ti,Mg)_{12}O_{19}$]) mantled by coarser Fe-rich phyllosilicates. Panels D-G show particles containing dehydrated phyllosilicates, as evidenced by the abundance of dehydration cracks within their matrix. In particles CP94-050-152 (D) and CP94-050-067 (E) cracks are present within a fine-grained Mg-rich matrix, while particles CP94-050-075 (F) and CP94-050-105 (G) contain a mixed coarse-grained Fe-rich and fine-grained Mg-rich matrix, in which dehydration cracks are more common among the Fe-rich phase. Particle CP94-050-140 (H) is a C1-FgMM, containing a homogenous Mg-rich matrix and abundant magnetite (both framboid and platelet morphologies). Magnetite grains contain rounded submicron vesicles and thin Fe-enriched rims. Particles CP94-050-142 (I) and CP94-050-123 (J) contain geochemically distinct clasts, which is CP94-050142 are discernible as a result of grain size contrasts, while in CP94-050-123 the clast boundary is defined by a sudden transition in bulk chemistry. Particles CP94-050-048 (K) and CP94-050-053 (L) are scoriaceous micrometeorites whose matrix contains abundant rounded vesicles up to 50% vol. Dispersed, nano-scale Fe-sulphides are visible in CP94-050-048 while partially melted anhydrous silicates are coated by Fe-rich mesostasis in CP94-050-053. All scale bars are 10μm.

Fig.3.4. Micrometeorite matrix textures

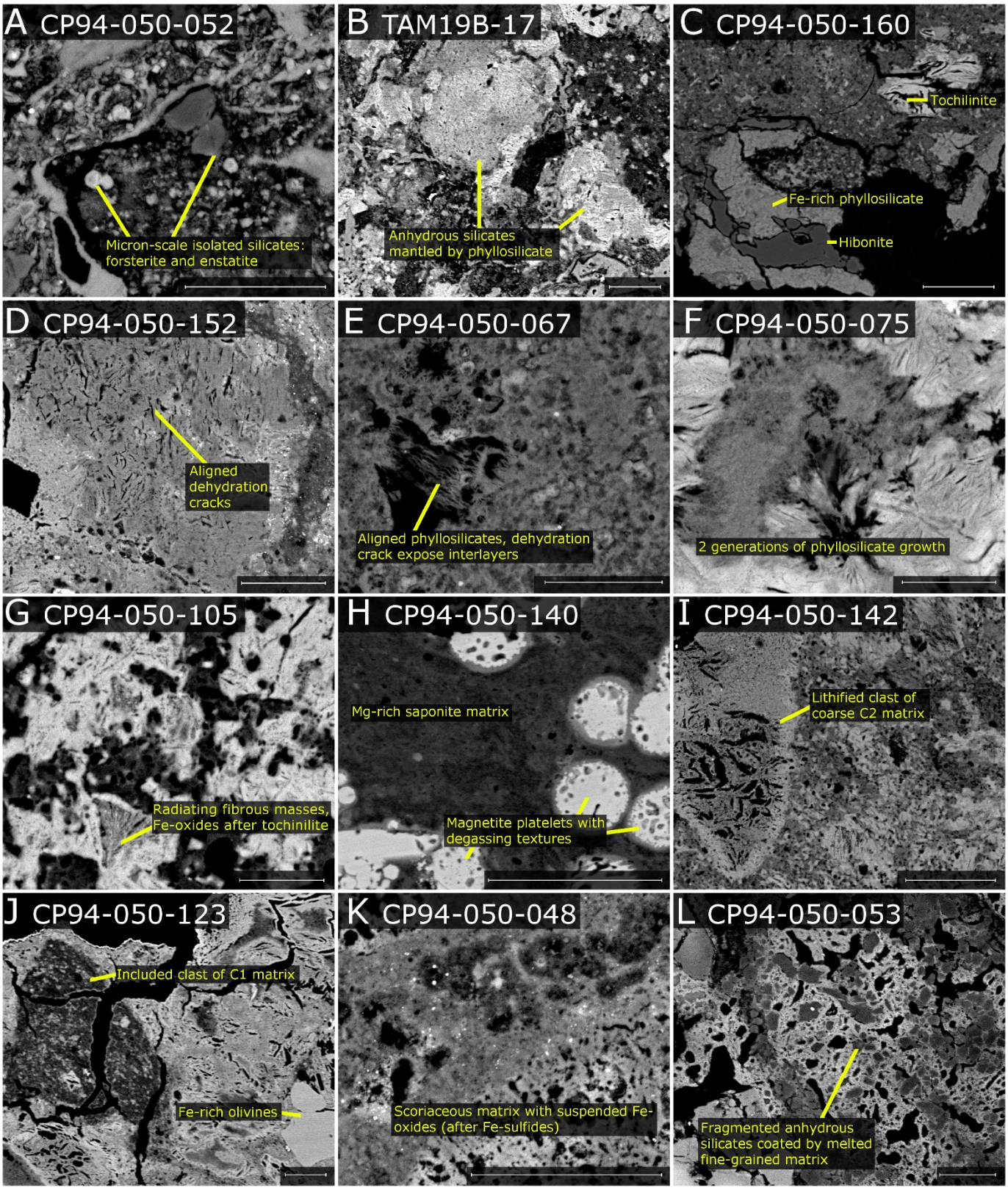

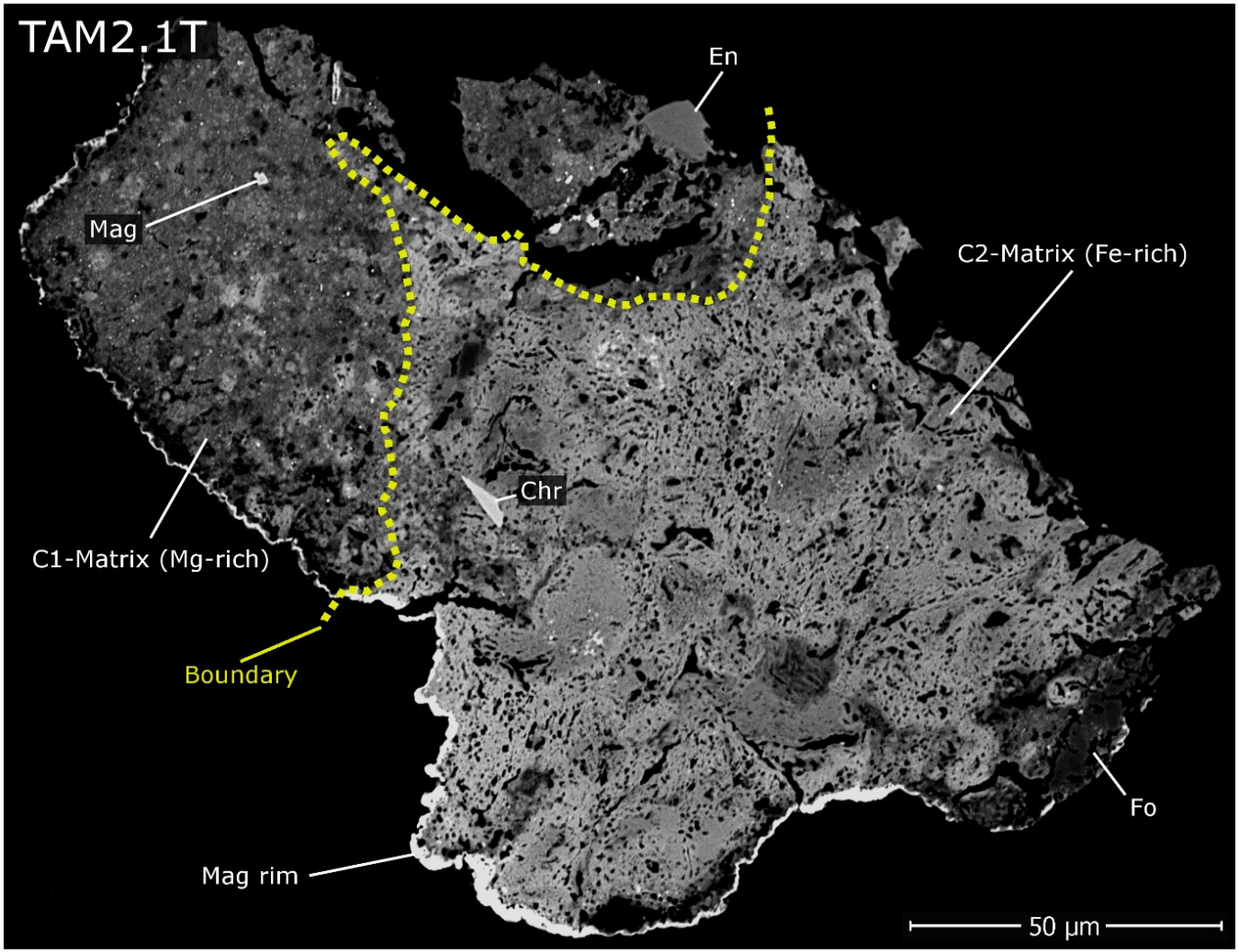

Fig.3.5. TAM2.1T a C2-FgMM containing a large clast of C1 fine-grained matrix (upper left). This particle therefore shares characteristics of both micrometeorite types. The boundary between lithologies is clearly defined and traced by a dashed yellow line. The C2 matrix (~70% area) contains relatively coarse Fe-rich phyllosilicates with abundant dehydration cracks, forming clustered subparallel void sets. Fragmented chromite spinels (Chr) reaching up to 10µm in length and forsterite (Fo) are present within the matrix. The C1 matrix is characterised by an absence of dehydration cracks, fewer anhydrous silicates and the presence of rare magnetite grains and a single enstatite crystal. (En) Note the difference in magnetite rim thickness between the two lithologies.

Fig.3.6. Anhydrous silicates (forsterite and enstatite) common in fine-grained micrometeorites. Three textural types are identified (A and B) fragmented, angular grains or grain clusters (C and D) isolated anhedral grains and grain clusters mantled by Fe-rich coarse-grained phyllosilicates and (E) large fragmented silicates, located at particle perimeters and containing Fe-oxide melt veins. All scale bars are 10µm.

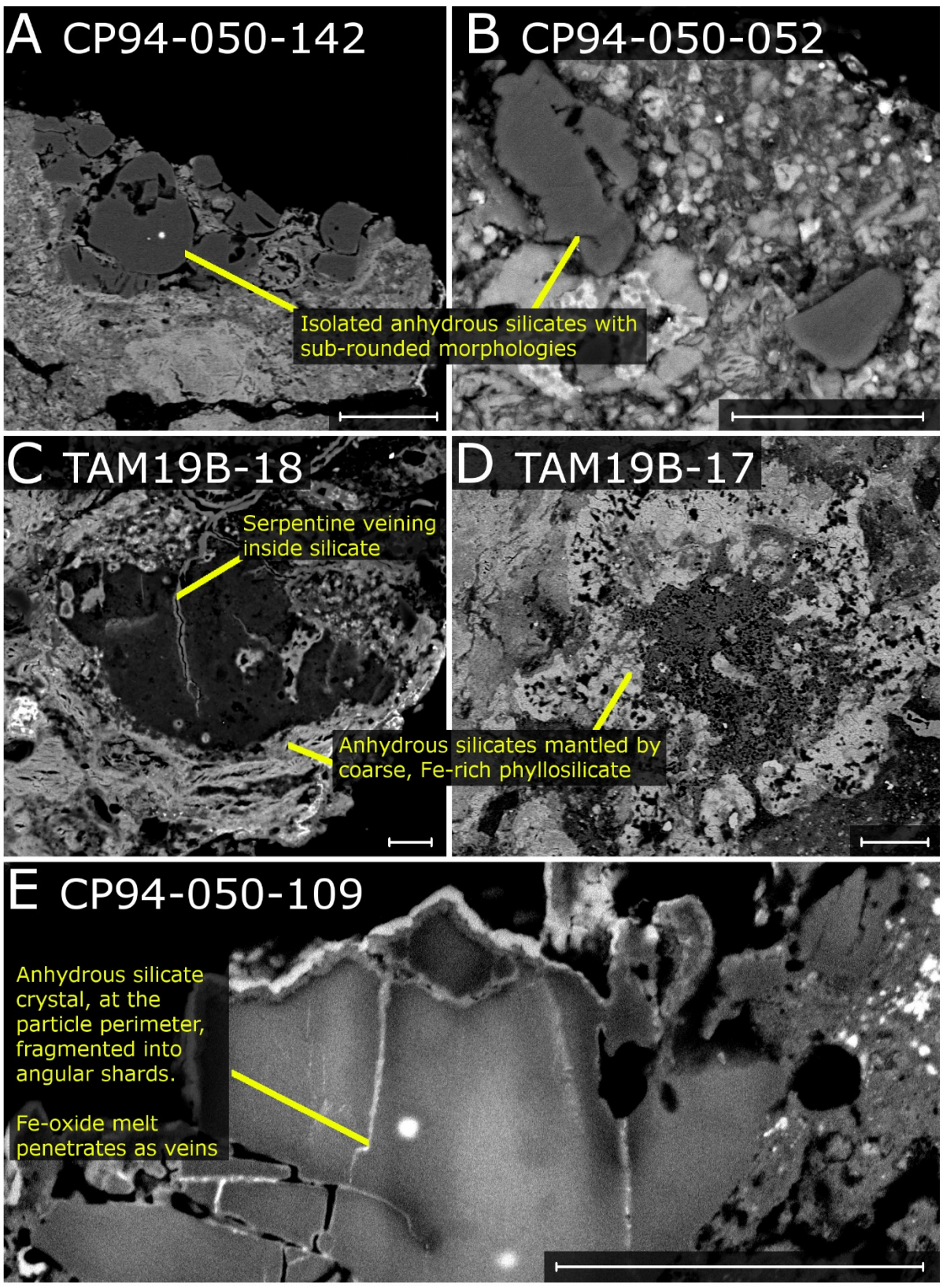

3.2.4. Anhydrous silicates: geochemistry and morphology

Most fine-grained C2 micrometeorites have anhydrous silicate crystals exposed in their cross-section. These particles generally have fragmented and angular or rounded and residual morphologies (CP94-050-142 and CP94-050-052, Figs.3.6A and B), and are commonly <4µm in size. Alternatively, several anhedral grains form clusters and are mantled by Fe-rich phyllosilicates (CP94-050-105 and CP94-050-110, Figs.3.6C and D). A third morphology, common among the scoriaceous micrometeorites and, only present at a micrometeorite's perimeter, are tight clusters of highly fragmented silicates, whose fracture planes are filled by Fe-oxides, most probably wüstite or magnetite (CP94-050-107, Fig.3.6E).

The chemical composition of micrometeorite mafic silicates was analysed (Fig.3.8 and Fig.3.9). In total, thirty-one olivine grains and twenty-six pyroxene grains were investigated. All olivine grains are forsteritic and most pyroxenes (85%) are low-Ca (CaO<9.0wt%) enstatite; although, four high-Ca (CaO>11.0wt%) diopside crystals were found. Anhydrous silicates within the fine-grained micrometeorites are, therefore, Mg-rich; containing Mg#>52% [Mg/(Mg+Fe) mol%] and typically >80%. In addition, their cation compositions show a bimodal distribution – as either low-Fe (Fo>88%, En>92%) or high-Fe (Fo<72%, En<72%) crystals. Intermediate compositions with Mg# between 73-87% were entirely absent (Fig.3.8).

Most anhydrous silicates also have significant minor and trace element contamination, with MnO (<2.2wt%), Cr_2O_5 (2.7wt%), Al_2O_5 (<5.6wt%), NiO (<0.9wt%), P_2O_5 (<0.2wt%), NaO (<0.5wt%) and TiO_2 (0.8wt%) all detected in varying quantities. The compositional range of the trace element contamination in the micrometeorite population was compared against the observed ranges found among CM2, CV3, CO3 and UOCs (Fig.3.9). However, because there is significant overlap in the ranges of the carbonaceous and unequilibrated ordinary chondrite groups, this analysis cannot unambiguously assign a given micrometeorite to a specific chondrite parent body, but instead, provides an assessment of the probable chondrite clan.

The majority of silicate grains within the Antarctic micrometeorite population fall within the compositional field of CM2 chondrites (as well as other chondrite groups). However, a significant number of grains also plot outside the chondritic range. In particular, several silicates show low-Fe concentrations (FeO<3wt%), and relatively high MnO (0.5-2.2wt%) or Cr_2O_5 (0.5-2.7wt%) concentrations. These silicates are similar to the (low-iron-manganese-enriched) LIME and (low-iron-chromium-enriched) LICE silicates reported from IDP collections (Klöck et al., 1989), cometary micrometeorites (Noguchi et al., 2015), highly primitive carbonaceous chondrites (e.g. CO3.0, Klöck et al., 1989) and rarely in asteroidal micrometeorites (Dobrică et al., 2009).

Fig.3.8. Histograms showing cation compositions [Mg/(Mg+Fe) At%] of anhydrous (A) olivine and (B) pyroxene grains found within the matrix of Cap Prud'homme micrometeorites. Silicates show bimodal compositions, with either low-Fe (Fo>88%, En>92%) or high-Fe (Fo<72%, En<72%) grains. Grains with intermediate compositions are absent.

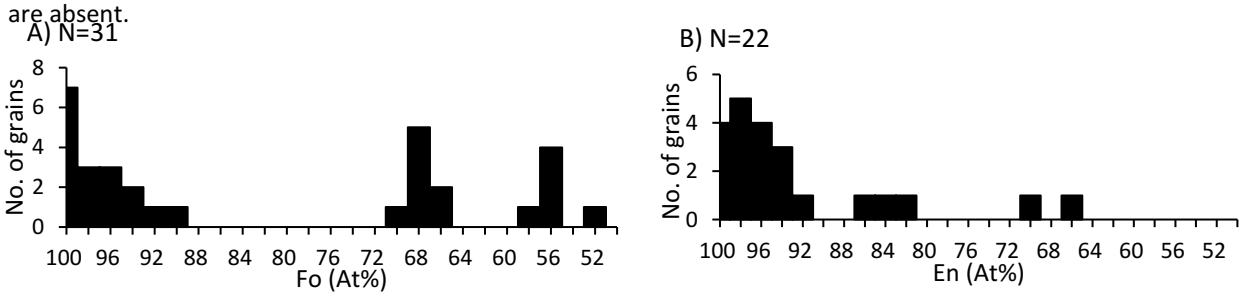

Fig.3.9. Trace element data collected from isolated anhydrous (A-C) olivine and (D-F) pyroxene grains present within the Cap Prud'homme micrometeorites. The compositional ranges of anhydrous silicates from CM2 (solid black line), CV3 (dashed dark grey line), CO3 (thin dotted grey line) and UOC (black dotted line) chondrites are also plotted. Although the majority of grain analyses plot within the composition field for CM2 chondrites, this range overlaps significantly with other chondrite classes. In addition, a large number of grains plot outside the compositional ranges commonly observed for any chondrite group; demonstrating that micrometeorites sample a more diverse suite of parent bodies than the larger meteorite population. Several grains show affinities to the highly primitive LIME and LICE silicates reported from IDPs, cometary Stardust samples and primitive chondrites. Compositional field data were taken from Bearley and Jones, (1998) and references therein.

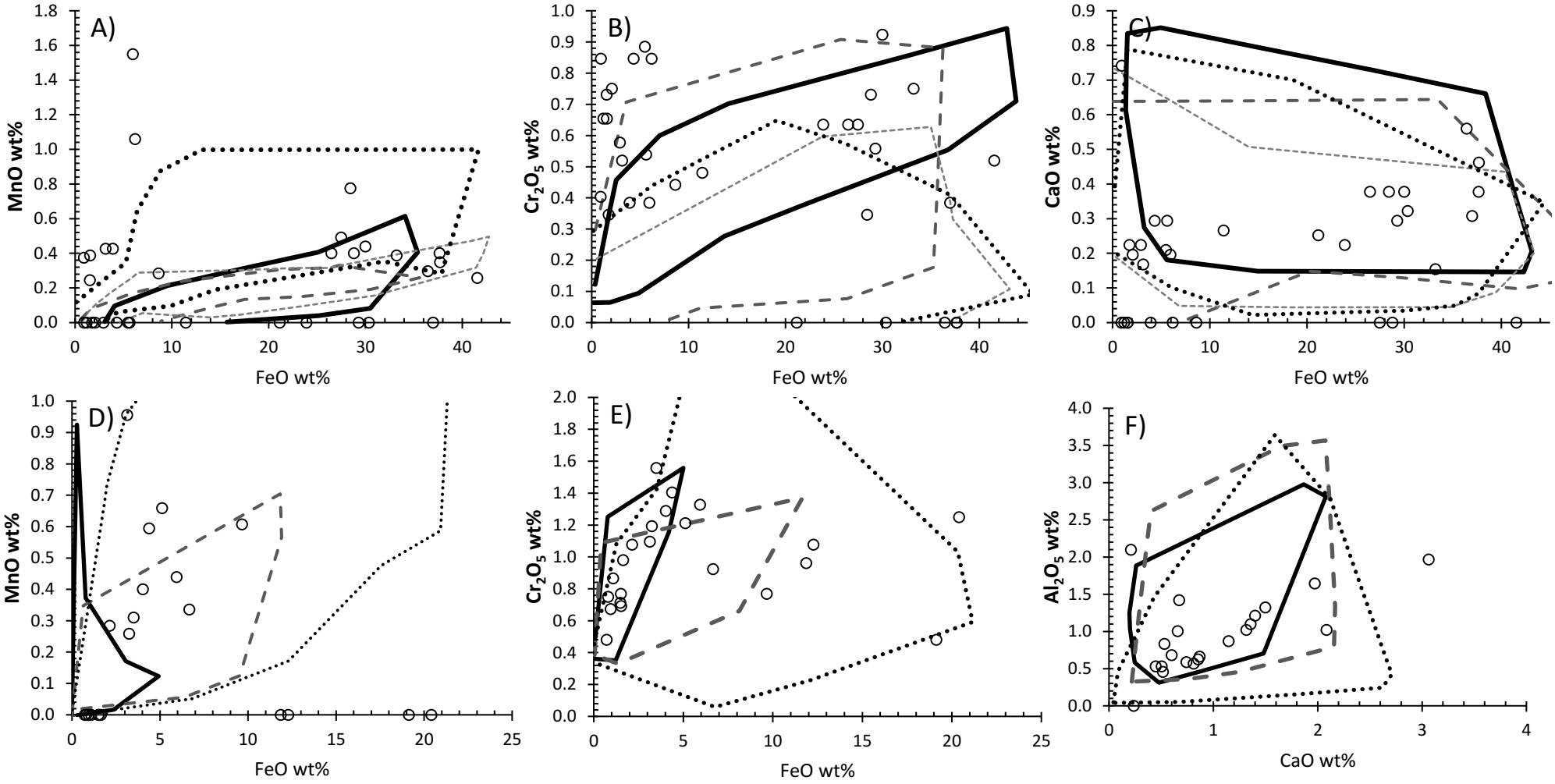

3.2.5. Giant TAM micrometeorites with more representative petrographies

3.2.5.1. TAM19B-7

This micrometeorite has a rectangular cross-section, with dimensions of ~830x950µm (Fig.3.10A). The matrix is highly vesicular, suggesting that this micrometeorite is transitional between the fine-grained and scoriaceous classes. However, relict textures show that the pre-atmospheric matrix was compact, dense and predominantly fine-grained, being composed of Fe-rich phyllosilicates and with minimal coarse-grained tochilite-rich clumps (formerly described as PCP clumps). The most distinctive feature of this particle is the presence of two geochemically distinct domains, separated by a relatively sharp compositional contact (with a boundary thickness of ~5µm). The lower left portion of the micrometeorite, contains Mg at concentrations between 4.1-8.2wt% and Fe at concentrations between 12.4-20.9wt%, while the upper right domain is heavily depleted in Mg, with concentrations below 3.0wt%. However, Fe concentrations in this region is high, varying between 16.0wt% and 31.9wt%. These two domains are, therefore, Mg-poor (Mg#26-60) and Fe-rich (Mg#0-36) respectively. In the upper right portion, the majority of large voids (vesicles, dehydration cracks and interconnected channels [Chapt.7]) have Fe-rich linings, while Fe-rich linings are less pronounced in the Mg-bearing domain.

Within the Fe-rich domain a rounded, oblate region of matrix with dimensions of approximately 180x140µm and an average diameter of ~160µm is present (Fig.3.10B, aspect ratio of ~1.3). This component is geochemically indistinguishable from the host micrometeorite, but clearly identifiable under BEI, as a result of distinctive matrix textures. This object is mantled by a fine-grained, weakly layered and compact rim with variable thickness, between 10-25µm. The inclusion core has an abundance of rounded voids (<20µm diameter), which results in a high porosity. Several of these voids are coated with Fe-rich rims.

3.2.5.2. TAM19B-17

This micrometeorite has a triangular cross-section, with maximum dimensions of 460x480µm (Fig.3.11A.). The phyllosilicate matrix is heterogenous, fine-grained, Fe-rich (avg Mg#18) and dense, containing limited pore space. Significant variations in back scatter potential (between Mg#3-38) produce a complex texture of intergrown or amorphous phases. For example, dark, poorly defined and dense regions of relatively Mg-rich matrix (Mg>6wt%) are sparse and mantled or cross-cut by large clusters of lighter, Fe-enriched (Mg<3wt%, Fe>20wt%) and coarser-grain material, which may contain several small dehydration cracks. Micron scale veins and infilled pores are also common (Fig.3.11E).

Anhydrous silicates in TAM19B-17 are relatively common and appear as large (>80x100µm) crystal clusters with anhedral or skeletal morphologies. Grains may enclose small (<4µm diameter) Fe-Ni metal droplets or are surrounded by thin (<5µm) Fe-Ni sulfide linings. Most silicate crystals are heavily altered and replaced, as evidenced by their rounded outlines (Fig.3.11E). Several grains have broken into a series of smaller residual silicate crystals or contain fractures. Silicate margins are also surrounded by thick (>20µm) Fe-rich growths. In Fig.3.11A the

outlines of three prominent refractory crystal clusters have been traced. They have rounded, elongate and oval-shaped morphologies. These regions typically have darker (low-Z values), Mg-enriched matrix in between the crystal fragments.

TAM19B-17 also has several combined Ca, Al and Ti hotspots (Fig.3.11C). Four such zones of enrichment are identified, the largest of which is shown in Fig.3.11D and exceeds 100µm in diameter. The core of this hotspot contains small Al-spinels embedded within a porous material, which is tentatively identified as bridgmanite - a silicate perovskite composed of ferromagnesian silicates [$(Mg,Fe)SiO_3$] and calclium silicate [wollastonite, $CaSiO_3$], and whose combined stoichiometry approaches $(Mg,Fe,Ca)(Al,Si)O_3$). The core of this inclusion is surrounded by a thick and equally porous margin of more Fe-enriched material with a stoichiometry closer to that of an Al-rich pyroxene.

3.2.5.3. TAM19B-18

This micrometeorite has an elongated and irregular cross-section, with dimensions of 870x530µm (Fig.3.12A). The particle is dominated by large (>80µm) clusters of coarse, Fe-rich phyllosilicates (Mg#20-44, ~3-9wt% Mg) which are identified by their prominent internal and subparallel dehydration crack sets. These coarse phyllosilicate clumps represent up to 85% of the particle's exposed surface area. The remaining regions are either pore space; which is primarily in the form of large and interconnected cracks (Chapt.7), or isolated anhydrous silicates (Fig.3.12B and 3.12C). The compositions of olivines vary over a wide range between Fo22-98 and crystals vary in size from <5µm to approximately 120µm. Most silicate grains contain penetrating fracture sets that are infilled by thin serpentine veins (Fig.3.12C). Thick phyllosilicate mantles also wrap around most crystals (Fig.3.12B), producing overgrowth rims that have a weakly foliated texture.

This micrometeorite also contains an embedded clast (~130x180µm, Fig.3.12A) characterised by a compact, mildly Mg-enriched matrix (Mg#39-49, ~7-9wt% Mg) and containing a single large (35x40µm) olivine crystal. Sub-spherical micron-scale Fe-oxide beads are also present in the matrix, prior to atmospheric entry, these were most likely tochilinite grains.

3.3. Discussion: evidence for aqueous alteration in fine-grained micrometeorites

In the original classification scheme of Genge et al., (2008) fine-grained micrometeorites are subdivided into C1 and C2 types dependent on their matrix textures and geochemistry. Here >50% of the micrometeorites analysed are C2 fine-grained micrometeorites, containing a hydrated matrix with embedded anhydrous silicates and accessory minerals such as spinel, sulfides and Fe-oxides. These particles, therefore, share petrographic affinities with the CM2 chondrites (Kurat et al., 1994; Genge et al., 2001; 2008; Taylor et al., 2012).

The presence of dehydration cracks in >95% of the micrometeorites analysed (Fig.3.4), as well as matrix EMPA showing silicate stoichiometries (O/Si at%) between 3.0-4.5 (Fig.3.3), strongly imply phyllosilicates are the dominant (pre-atmospheric) matrix minerals. In most particles, this matrix is

composed of intermixed clumps of coarse Fe-rich and finer-grained Mg-rich zones, which overlap and cross-cut each other – these are interpreted as cronstedtite and saponite respectively. Here, the inferred presence of 2 different phyllosilicate species is necessary to explain the observed correlation seen in Fig.3.3; where Mg-rich spot analyses have O/Si ratios approaching 3 and imply the former existence of saponite, while Fe-rich spot analyses have O/Si ratios of approximately 4-4.5 and imply the former existence of serpentine. This combined mineralogy and cation chemistry trend is consistent with observations from CM chondrites, that suggest progressive aqueous alteration proceeds by the successive replacement of Fe-bearing phyllosilicate with Mg-bearing phyllosilicates (McSween, 1979; Tomeoka et al., 1989), and this is likewise coupled with a transition from serpentine-dominated matrix to saponite-dominated matrix (Howard et al., 2009; 2011).

Anhydrous silicates (both olivine and pyroxene) are found in fine-grained micrometeorites but typically represent <<30% of the matrix by volume and commonly have anhedral, skeletal or residual morphologies with thick overgrowth rims of phyllosilicate, infilled fractures and rounded edges. These textures and inferred mineralogies also attest to a significant episode of post-accretion, parent body aqueous alteration (Mcsween, 1979; 1987; Noughi et al., 2017), in which mafic silicates are consumed as source material for phyllosilicate growth.

In TAM19B-17 and TAM19B-18, variations in the back-scatter signal of the matrix (between Mg#3-38 and Mg#20-44 respectively), coupled with a complex intergrown texture, imply multiple generations of phyllosilicate growth during aqueous alteration (Tomeoka et al., 1985; Vebel et al., 2012). This conclusion is supported by micro-scale observations of serpentine veins that cross cut thick phyllosilicate rims around olivine grains (Fig.3.12B) and penetrate the silicate crystal cores. Here, a stratigraphic relationship can be established: the phyllosilicate overgrowths on silicate crystals must predate the internal serpentine veining. This requires that aqueous alteration progressed initially by the growth of hydrated phyllosilicate mantles that grew around the anhydrous silicates, initially using these crystals as a substrate and replacing the original matrix, which was probably a porous mixture of amorphous silica (Noguchi et al., 2017). Furthermore, because these rims are layered, this implies successive periods of growth, to develop a concentric layered texture. However, during a later alteration period serpentine veins grew through the rim and began to consume the olivine (and pyroxene) host crystals. This is clearly seen in TAM19B-18 (Fig.3.12B). Similar chronologies, where anhydrous silicates are first used as substrates and then as source material for secondary phyllosilicate growth, are characteristic alteration mechanisms found in hydrated chondrites as detailed in Greenwood et al. (1994).

Additionally, Lee and Lindgren (2016) described near identical veinlet growth features to those observed in TAM19B-17 and TAM19B-18 within the CM chondrite Murchison. They noted that narrow veinlets of Fe-rich serpentine form first by filling pre-existing fractures - potentially generated by thermal contraction cooling. The serpentine veinlets then widened, expanding out into the host crystal's core, forming phyllosilicate patches and generating skeletal olivine textures. The growth of serpentine outwards from the veinlets is crystallographically controlled and determined by the

orientation of the serpentine lattice with respect to the olivine host crystal (Lee and Lindgren, 2016). In Fig.3B (TAM19B-18) the veinlets have formed but have yet to expand in width, while in Fig.3.11A and 3.11E from TAM19B-17 vein expansion has resulted in the significant internal replacement of some large anhydrous silicates, suggesting that the extent of alteration in TAM19B-17 is further progressed than in TAM19B-18.

In TAM19B-17, several large (~100µm diameter) inclusions were identified (Fig.3.11A, 3.11C) that may be interpreted as aqueously altered refractory phases. They contain elevated abundances of refractory elements, including Ca, Al and Ti, which are collected into small bright spots, most likely representing residual mineral grains that survived aqueous alteration. The largest refractory inclusion, shown in Fig.3.11D, is zoned irregular-shaped, with a porous core and radiating Fe-rich rim. Chemical analysis of the inclusion's core suggest bridgmanite – a refractory silicate perovskite - is present while the outer rim is dense, Fe-enriched (Fig.3.11B) and of variable thickness. Although the inclusion core retains some refractory material, the margin has been entirely replaced with secondary phyllosilicates (cronstedtite) which grew outwards from the host inclusion. These observations are, therefore, very similar to the altered CAIs described from C2 Tagish Lake by Takayama and Tomeoka (2012, Fig.10). They observe large (~300µm diameter) zoned refractory assemblages, mantled by thick Fe-rich phyllosilicate rims and whose dark cores have higher porosities, as well as residual refractory minerals (perovskite and Al-spinel). The biggest difference between these two assemblages is the presence of abundant carbonate in the Tagish Lake CAIs, which are not present in the TAM micrometeorite inclusion. This is most likely because carbonates in micrometeorites are lost during atmospheric entry heating even at modest peak temperatures (<600°C, Nozaki et al., 2006). However, their removal by thermal decomposition, along with the dehydration of phyllosilicate explains the presence of rounded voids within the Fe-rich rim surrounding this inclusion (Fig.3.11D). Thus, the Ca-Al-Ti hotspots within TAM19B-17 are interpreted as heavily replaced, "ghost" CAIs and altered olivine clusters formed by intense aqueous alteration.

Fig.3.10. A) Particle TAM19B-7, a giant TAM micrometeorite with dimensions 830x950µm. This particle contains a well-defined geochemical boundary, separating two zones of distinct matrix, the larger "left hand" zone is Mg-bearing (4.1-8.2wt%), while the "right hand" portion is Mg depleted, with Mg concentrations below 3.0wt%. This region contains a circular inclusion, interpreted as a chondrule pseudomorph and highlighted by a dashed white square (B). The inclusion has a high porosity and oblate or crushed shape and is composed of phyllosilicate decomposition products. (C) A compact, fine-grained rim, approximately 15µm thick and containing Fe-Ni oxide nuggets surrounds the inclusion. Whole particle, major element (Mg, Si, Fe) and weathering (S, K) maps are shown in (D) and (E) respectively.

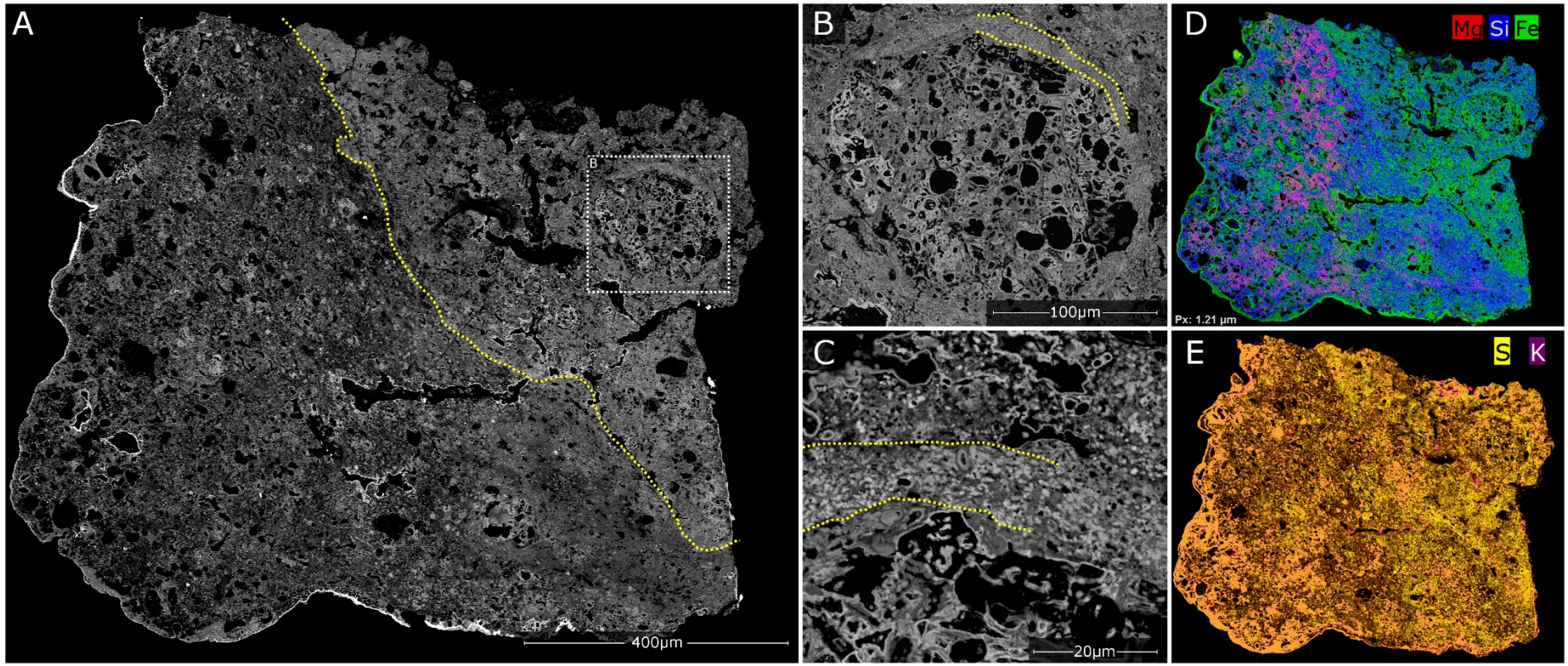

Fig.3.11. Particle TAM19B-17, has a triangular cross-section. This micrometeorite has a compact, low-porosity and intensely aqueous altered internal texture. A thick jarosite encrustation rim surrounds the particle attesting to a significant period of terrestrial weathering. Inside the weathering rim is a magnetite rim, produced by atmospheric entry heating. The matrix contains a complex intermix of lighter (Fe-rich) and darker (Mg-rich) zones that are intergrown and cross cut by later periods of veining and pore-filling. Three regions are highlighted by a dashed yellow line, these indicate where refractory phases (silicates and oxides) have been partially altered and replaced, these zones are interpreted as ghost CAIs. Element maps (B and C) reveal the major element and trace refractory element distributions, and these aid in the identification of hydrated and partially replaced CAIs (D) and altered isolated anhydrous silicates (E).

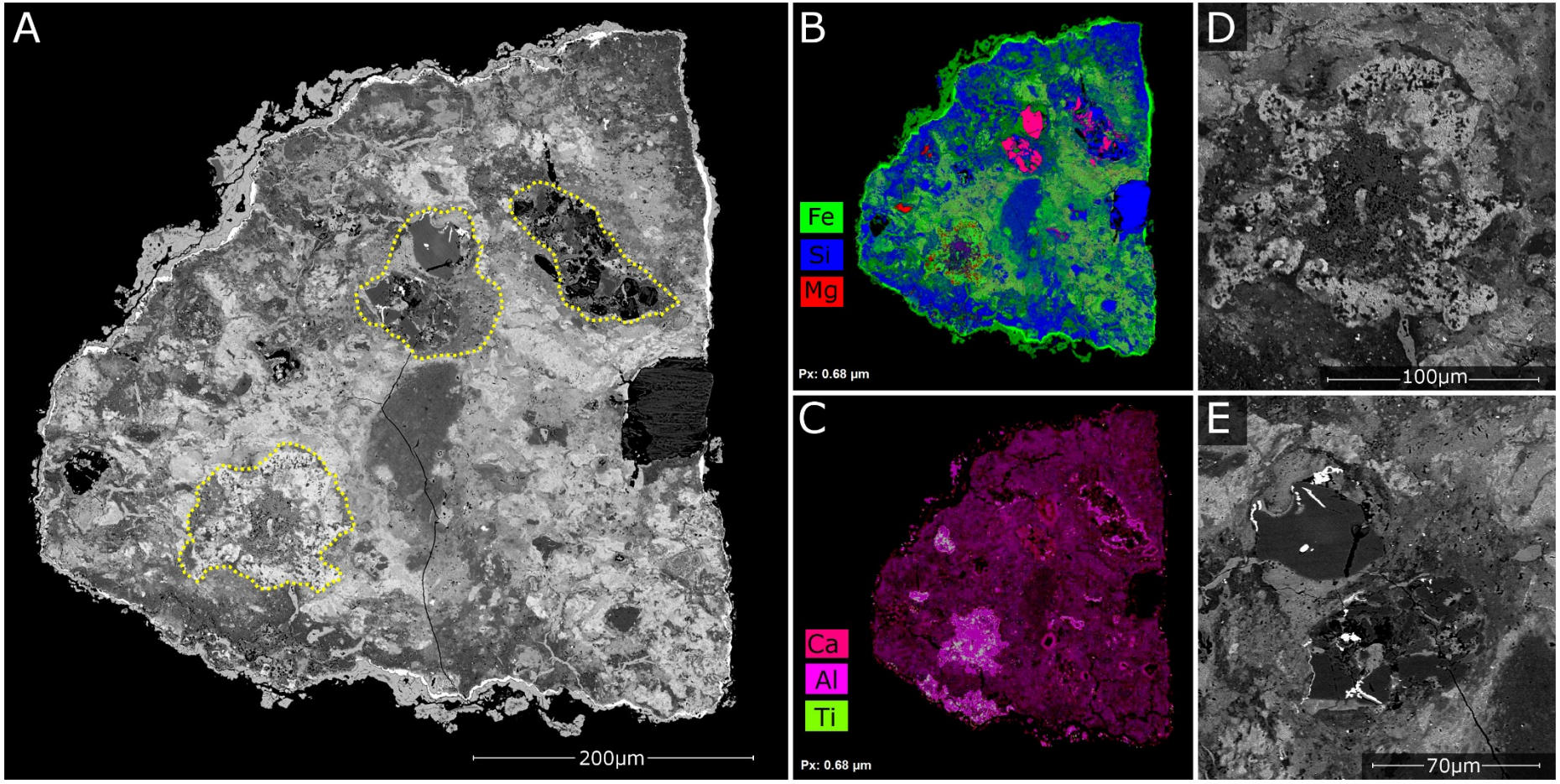

Fig.3.12. Particle TAM19B-18. This micrometeorite is composed of >85% matrix and is dominated by coarse, Fe-rich phyllosilicate decomposition products, which prior to atmospheric entry would have been cronstedtite (serpentine) clusters - equivalent to the PCP clumps described in previous studies of CM chondrites (Rubin et al., 2007). A lithic clast, composed of compact, Mg-rich matrix and containing a single large olivine crystal is found in the bottom right corner. (B and C) Anhydrous silicates are relatively rare and have anhedral or skeletal morphologies, containing abundant fractures, filled with serpentine alteration products, or are broken into a series of smaller, rounded and residual crystal relicts. Large phyllosilicate overgrowths mantle most grains, and in places generate a foliation texture, wrapping around larger crystals. Note: the view shown in (C) is from a higher plane of section and, therefore, cannot be located on the whole particle image, seen in (A).

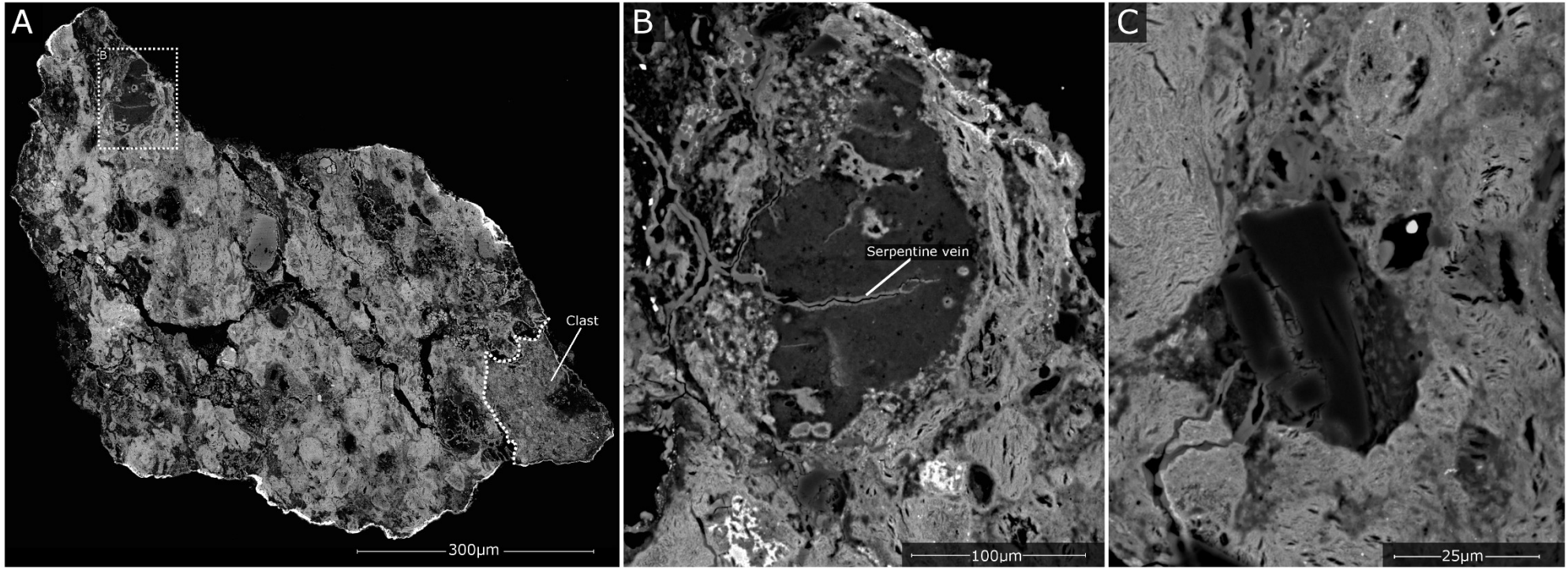

3.4. Discussion: evaluating the extent of aqueous alteration in fine-grained micrometeorites

Variability in the degree of aqueous alteration among CM chondrites is well-documented and has been extensively investigated using textural features (Vebel et al., 2012; Lee and Lindgren, 2016), elemental ratios (Rubin et al., 2007), modal mineralogy (Howard et al., 2009; King et al., 2017), spectroscopy (Takir et al., 2013) and isotopic signatures (Lee et al., 2012; 2013). Therefore, several CM chondrites now have an assigned petrologic subtype, however, this remains <10% of the total CM chondrites, currently listed on the Meteoritical Bulletin (2017). The numerical subclassification of Rubin et al., (2007) ranges between CM2.0 to CM2.7 (and theoretically up to an entirely unaltered CM3.0). In this scale, lower subtypes represent meteorites more intensely altered by fluid interaction.

Until now, the degree of aqueous alteration affecting fine-grained micrometeorites has not been explicitly investigated nor quantified. This is most likely because micrometeorites, are by definition, small and, therefore, the total analysis area is greatly restricted, preventing many of the conventional assessment criteria from being applied. In spite of these limitations, this study assigned approximate petrologic subtypes to the (CM-like) C2 fine-grained micrometeorites using a reduced set of alteration criteria, adapted from Rubin et al., (2007), which are applicable to studying alteration in smaller samples.

The following metrics are used: (1) the percentage of metallic FeNi [varying between <0.02%-1% by volume], (2) the (estimated) degree of replacement affecting anhydrous silicates [0-100%], (3) The abundance of large phyllosilicate clumps [varying between 2-40%vol] and (4) the elemental FeO/SiO_2 ratio of phyllosilicate [varying between 1.0-3.3]. These criteria are chosen as they can be applied to all thirty-seven particles and focus on major mineralogy and/or their heat-resistant phases. The remaining metrics which analyse accessory phases, such as sulfides or carbonates, are rarely preserved owing to the effects unrepresentative sampling and atmospheric entry flash heating.

The most informative of these criteria are the abundance and morphology of anhydrous silicates and the abundance of PCP clumps, both of which can be readily assessed from BSE images. Conversely, the abundance of FeNi metal is difficult to determine, given the low total abundances expected, while the FeO/SiO_2 ratios vary hugely between extremes of 0.28 to 3.34 (Fig.3.13). This range exceeds that measured from CM chondrites by Rubin et al., (2007) and could suggest a later period of geochemical alteration, either during atmospheric entry or terrestrial weathering, that subsequently modified the FeO/SiO_2 ratios, making this criteria less reliable. The petrologic subtypes from the C2 fine-grained micrometeorite population are shown in Table.3.2 and Fig.3.14.

Three C2 micrometeorites contain clearly defined, isolated anhydrous silicates which appear to have avoided main-stage aqueous alteration (e.g. CP94-050-0652, Fig.3.6B), these micrometeorites were, therefore, assigned the petrologic subtype, ranging between CM2.6-2.4. By contrast, ten micrometeorites (27%) are assigned a CM2.3 petrologic subtype, based on the presence of minimally altered anhydrous silicates (2-15%). These micrometeorites may contain thin phyllosilicate rims surrounding olivine and pyroxene crystals or weakly embayed crystal margins. The modal petrologic subtype of the C2 fine-grained micrometeorite population is CM2.2, with 43% (Fig.3.14) of the

particles showing significant replacement of their anhydrous silicates. In these micrometeorites, anhydrous silicates are small, anhedral, mantled by thick phyllosilicate growths and contain alteration veins that penetrate deeply into the crystal cores, as described from CP94-050-105 and CP94-050-110 (Fig.3.6C and 3.6D) and TAM19B-17, TAM19B-18 (Figs. 3.11 and 3.12). Seven C2 fine-grained micrometeorites are classified with a petrologic subtype of CM2.1 and contain only residual anhydrous silicate crystals, typically <2µm in size, which are geochemically indistinct from the surrounding matrix. CP94-050-075 (Fig.3.4F) is an example of a highly altered CM2.1 micrometeorite. Completely altered CM2.0 particles are rare, with only one particle assigned this grade. TAM19B-7 (discussed in detail below [Sect.3.5]) entirely lacks olivine or pyroxene crystals, and also has low concentrations of Fe-rich serpentine clumps, as these have since been replaced by Mg-bearing, finer-grained phyllosilicate.

The remaining unmelted micrometeorites (totalling seventeen) are C1 fine-grained micrometeorites, whose petrography is similar to CI chondrites (Kurat et al., 1992; Genge et al., 1997; 2008; van Ginneken et al., 2012). However, owing to the small number of CI chondrite specimens currently known (<10, Meteoritical Bulletin, 2017), high-precision petrologic subtypes are not assigned to members of this meteorite class. C1 fine-grained micrometeorites have extremely fine-grained, homogenous Mg-rich phyllosilicates, most likely dominated by saponite (~90 vol%) interspersed with magnetite and ferrihydrite grains. In hydrated carbonaceous chondrites magnetite forms by the oxidation of precursor FeNi metal or Fe-sulphides, and, therefore, requires oxidising fluids (Kerridge et al., 1979; Weisberg et al., 1993; Zolensky et al., 1996a; Zolotov, 2012). Two distinct magnetite morphologies were recognised; framboidal and platelet (or plaquettes) types. While framboids are common in CI, CM, CR and CV chondrites (Kerridge et al., 1979; Weisberg et al., 1993; Keller et al., 1994; Rubin et al., 2007), platelets are found only in CI and CR2 chondrites and the C2 Tagish Lake meteorite (Kerridge et al., 1979; Weisberg et al., 1993; Takayama and Tomeoka, 2012) and may, therefore, indicate lower petrologic subtypes, more intense alteration and the growth of secondary phases after primary alteration products.

Collectively, the fine-grained micrometeorite population included in this thesis covers the complete range of aqueously altered petrologic subtypes observed in within CM2.7-CM2.0 and CI chondrites. The modal alteration state of the C2 fine-grained micrometeorites is CM2.2, while the alteration state of C1 fine-grained micrometeorites is more intense and reflects a sustained period of alteration, sufficient to induce complete secondary replacement of alteration phases. On the basis of this study, the current parent asteroids of the fine-grained micrometeorites flux are, therefore, expected to be heavily altered bodies (>80% volume phyllosilicates), which may contain observable hydration features in their NIR spectra (Chapt.8).

3.5. A chondrule pseudomorph preserved in TAM19B-7

The most unusual feature found in TAM19B-7 is an oblate inclusion (Fig.3.11B) whose size, shape and textures are reminiscent of those of chondrules. This inclusion measures ~160µm in diameter and is, therefore, within the size range for chondrules found in both CM and CO chondrites (typically 100-300µm) but significantly smaller than chondrules found in CR chondrites (~700µm) (Rubin and

Wasson, 1986; Jones, 2012). Additionally, the presence of a fine-grained rim with a uniform thickness of ~15µm mantles the inclusion (Fig.3.11B). This closely resembles the compact, low-porosity phyllosilicate-rich dark rims that surround chondrules in CM chondrites. Such rims imply formation by compaction and aqueous alteration on the parent asteroid (Trigo-Rodriguez et al., 2006; Wasson and Rubin, 2014).

However, despite these initial similarities, the inclusion's internal mineralogy and texture is distinct from that of chondrules. The mineralogy of this inclusion is dominated by amorphous, dehydroxylated phyllosilicate and Fe-oxides, and thus differs from the igneous assemblage of anhydrous silicates, FeNi metal, silicate glass and sulfides that are found in chondrules (Jones, 2012). While the texture of the inclusion is also different to that of chondrules, being dominated by rounded voids set within a fine-grained porous groundmass. In contrast, vesicles are extremely rare in chondrules (Maharaj and Hewins, 1994). Variations in backscattered signal also suggest some regions are Fe-enriched, notably towards the inclusion's margin but within the fine-grained rim. The inclusion in TAM19B-7 cannot, therefore, be classified as a chondrule in the strict sense. It is, however, a sub-spherical object with a chondritic composition surrounded by a fine-grained rim. These three criteria are more consistent with chondrules than any other objects found in meteorites.

Fig.3.13. Estimated petrologic grade of the C2 fine-grained micrometeorite population, inferred using FeO/SiO_2 ratios calculated from the average matrix EMPA data. The thin dashed blue lines represent the minimum and maximum values, while the thick dashed blue line shows the mean average value. A calibration curve was established using an exponential line-of-best-fit [$y=0.88x^{3.7}$, $R^2=0.76$], plotted through the CM chondrite data from Rubin et al., (2007) and shown here in dark grey (wash-out effect). This curve was then used to approximate the positions of micrometeorites and thus assign petrologic subtypes. However, the FeO/SiO_2 ratios of most micrometeorites are lower than any CM chondrite analysed by Rubin et al., (2007), implying these particles either experienced a later process that affected their FeO/SiO2 ratios, this could be during atmospheric entry or terrestrial weathering.

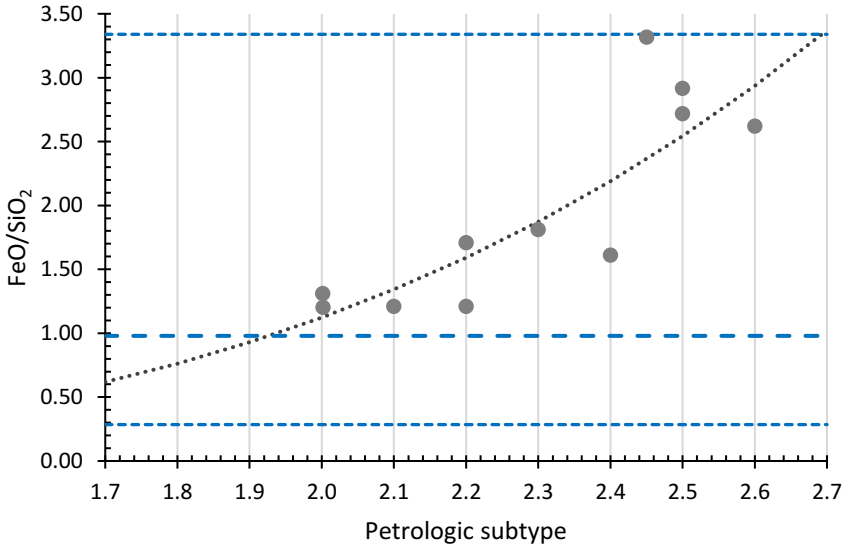

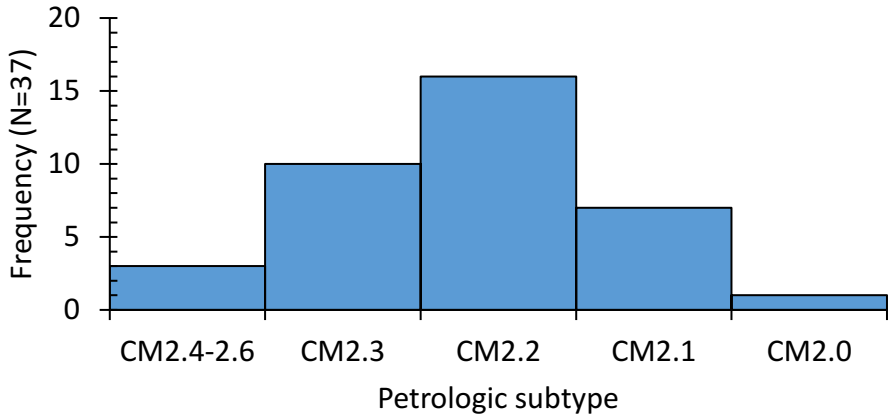

Fig.3.14. Histogram showing the petrologic subtype of 37 C2-FgMMs. The modal value is CM2.2., representing a highly altered lithology containing abundant Mg-rich phyllosilicates and few intact anhydrous silicates.

In the most highly altered CM chondrites, (CM2.0), anhydrous silicates are absent. Instead, chondrules have been entirely replaced by phyllosilicates, resulting in pseudomorphic relict inclusions that imperfectly preserve former textures, including rim morphologies (Zolensky et al., 1997; Rubin et al., 2007; Vebel et al., 2012; Lee and Lindgren, 2016). Partially replaced chondrules are also found in the ungrouped C2 meteorite Tagish Lake (Takayama and Tomeoka, 2012) and some CR chondrites, such as GRO 95577 (Weisberg and Huber, 2007). In TAM19B-7, the lack of significant geochemical variation between the chondrule-like inclusion, its rim and the surrounding matrix, as well as a pre-atmospheric phyllosilicate-bearing mineralogy suggest that this inclusion represents a thermally altered, chondrule pseudomorph.

Likewise, the texture of this inclusion is consistent with an aqueously altered chondrule pseudomorph that experienced later dehydration during atmospheric entry. Relict chondrules within CM2 and CR2 chondrites preserve partial outlines of phenocrysts, mesostasis and pore space, through subtle differences in the composition and mineralogy of their secondary phases (Weisberg and Huber, 2007; Vebel et al., 2012; Lee and Lindgren, 2016). By contrast, the minor geochemical variations observed in TAM19B-7's inclusion, result from the degassing and decomposition of different low-temperature phases during entry heating. For example, tochilinite, which is common within CM2 chondrites, begins to degas at 300°C (Nozaki et al., 2006), while serpentine group minerals decompose at higher temperatures (400-600°C, Nozaki et al., 2006). Thus, the breakdown of secondary alteration phases could explain the abundance voids, while the occurrence of different secondary phases - with different decomposition temperatures – suggesting that outlines of the former chondrule's mineralogy may be preserved. Therefore, the resemblance of the void distribution to that of a porphyritic texture is not coincidental and instead, reflects the pre-atmospheric, pseudomorphic texture.

The petrography of TAM19B-7 is, therefore, comparable to those observed in EET 83334, ALH 88045 (Zolensky et al., 1997), MET 01070 and LAP 02277 (Rubin et al., 2007) and other highly altered CM chondrites, which contain >90% matrix by volume and minimal anhydrous silicates. Consequently, the

degree of aqueous alteration affecting TAM19B-7 is equivalent to CM2.0 in the scheme of Rubin et al., (2007) or a CM1 under the alternative alteration scheme (Zolensky et al., 1997).

Similar alteration textures, detailing the replacement of chondrules in fine-grained micrometeorites were previously described by Genge (2002) from four small (<100µm) particles of the Cap Prudhomme micrometeorite collection. This included partially altered micrometeorites, containing equant olivine crystals within phyllosilicate, as well as completely pseudomorphed textures, where pre-existing phenocrysts are traced by subtle differences in mineralogy and composition. In addition, chondrule fragments set within fine-grained groundmass have also been described (Genge et al., 2005) and demonstrate that fragmented chondrules can be found, even among small micrometeorites. Genge (2006) also noted that thermal decomposition and melting of small selvages of fine-grained matrix on the exterior of chondrule fragments in micrometeorites leads to coarse-grained micrometeorites with igneous rims (Genge et al., 2005). This body of evidence demonstrates that chondrule fragments, associated with hydrated C2 lithologies, are present within the fine-grained micrometeorite population although some fraction are affected by intense aqueous alteration.

3.6. Discussion: embedded clasts within fine-grained micrometeorites

Fourteen micrometeorites were identified which contain geochemically or texturally distinct clasts (Sect.3.2.3 and Figs. 3.4I, 3.4J, 3.5, 3.10, 3.12). In most cases, these clasts are either C1 matrix held within a C2 fine-grained micrometeorite, or the reverse; a C1 fine-grained micrometeorite containing a C2 clast. However, occurrences are also observed in which a micrometeorite contained a clast of a similar lithology were identified, as in CP94-050-160 (Fig.3.4I [C2-FgMM hosting 2xC2 clasts]). Because the embedded clasts show different aqueous alteration textures and degrees of alteration to their host particle, this requires that the included clasts have a different alteration history. Most hydrated carbonaceous chondrites show significant local variations in the degree and style of alteration (Zolensky et al., 2002; Hewins et al., 2014). This has led to disparate or contradictory petrographic classifications, where multiple studies have analysed different slices of the same meteorite. In such cases, variations in the extent of alteration are typically observed over significantly larger length-scales (millimetre-scale distances), rather than the micron length scale variations reported here and are explained either as a result of brecciated samples (Brearley, 1995;) or heterogeneous aqueous alteration, perhaps arising where water availability was highly limited (Hewins et al., 2014). However, because the differences in aqueous alteration among clast and host in micrometeorites occur over very small distances, they are best explained by brecciation scenario – in which included clasts were derived by collisional disruption of an already hydrated asteroid and subsequently captured onto another accreting body (Zolensky et al., 1996b).

Impact experiments demonstrate that CM and CI lithologies produce abundant small dust (<100µm, Flynn et al., 2009) within the size range observed for the embedded clasts. Additionally, several previous studies have reported hydrated, carbonaceous fossil micrometeorite clasts or dark lithic inclusions within CR chondrites (Weisberg et al., 1993) C2 Tagish Lake (Zolensky et al., 2002), ordinary chondrites (Nakashima et al., 2003; Briani et al., 2012) HED meteorites and lunar soils (Wasson et al.,

1975; Zolensky et al., 1996b; Gounelle et al., 2003). Since micron-scale hydrated C2 dust fragments are common contaminants among other extraterrestrial materials it is unsurprising that micrometeorites also preserve captured fragments of hydrated dust (palaeo-micrometeorites). Furthermore, these observations demonstrate that the early inner solar system dust flux, or at leat the region in which these micrometeorite parent bodies formed, was dominated by hydrated fine-grained chondritic material and was, therefore, similar to the current micrometeorite flux.

In all instances, the boundary between a clast and matrix, although well-defined, is transitional over several microns; suggesting that these clasts were incorporated into the host micrometeorites and later lithified by geochemical exchange. Aqueous fluids provide an effective method of transferring ions via dissolution and precipitation reactions, aqueous alteration is, thus, the most likely process driving clast integration. (McSween 1987; Hanoswki et al., 2001; Zega et al., 2003). Alternatively, thermal metamorphism (Tonui et al., 2003; Lee et al., 2016) or impact-heating could have triggered recrystallization and ion exchange (Nakashima et al., 2003). Several studies have suggested that aqueous alteration on hydrated asteroids may have been driven by impact heating (Trigo-Rodriguez et al., 2006; Lee and Ellen, 2008; Furukawa et al., 2001; Rubin, 2012; Lindgren et al., 2015). This is supported by an increasing number of CM chondrites, which show evidence of both aqueous alteration and shock processing (Hanna et al., 2015; Lindgren et al., 2015). As a result, it is probable that both impacts and aqueous alteration combined were responsible for the geochemical integration of clasts into the host micrometeorites.

3.7. Discussion: Anhydrous silicates, origin and formation

Anhydrous silicates are common components of unmelted fine-grained micrometeorites and, in this study, were identified in both the C1 and C2 particles. Most crystals are 1-4µm in size, form loose clusters, have Mg-rich compositions (Mg#>80 mol%) with relatively high concentrations of trace elements (mean=1.1wt%, max=6.4wt%) and, where phyllosilicate replacement has not affected crystal margins, show sharp angular morphologies.

Mg-rich anhydrous silicates form at high-temperatures (~1300K, Grossman, 1972). In micrometeorites, the presence of significant trace element substitution into the silicate crystal lattice impies that these crystals formed in geochemical environments where other phases with higher partition coefficients (e.g. oxides), were not also crystallizing at the same time. Thus, the presence of included Ca, Al, Ti, Cr, Mn and Ni in olivine and pyroxene crystals requires that those elements were more incompatible in the reservoir fluid than in the host silicate phase (Beattie, 1994). Additionally, because micromeoteorite olivine (and pyroxene) have low volatile element concentrations (e.g. Cl and Na) and moderate concentrations of refractory elements (Ca, Al, Ti) further supports a high-temperature origin (Steele, 1986) and may indicate thier crystallization by condensation from the solar nebula (Steele, 1986; Klöck et al., 1989) as opposed to an igneous formation history, by crystallization from a melt.

The trace element budgets of most anhydrous silicate grains fall within the compositional fields commonly observed for carbonaceous or ordinary chondrites, however, crystal grains were identified

with distinct compositions (Fig.3.9). Notably, several anhydrous silicates containing unusually high Mn and high Cr concentrations (>0.5wt%) were observed. In these silicates, Mn and Cr concentrations are comparable to their Fe concentrations and are, therefore, classified as refractory LIME and LICE silicates (Klöck et al., 1989; Ebel et al., 2012). Such silicates are relatively rare among carbonaceous chondrites, being absent from (most) chondrules, but found in low numbers as isolated matrix grains (Klöck et al., 1989; Frank et al., 2014). Conversely, LIME and LICE silicates are relatively common in IDPs (Klöck et al., 1989), cometary micrometeorites (Dobrică et al., 2009; Noguchi et al., 2015) and WILD 2 dust samples (Ebel et al., 2012). These silicates represent early condensate products, which formed under reducing conditions, in the absence of water-ice and at high dust densities (Ebel et al., 2012). Their preservation in some asteroidal fine-grained micrometeorites further expands the inventory of host extraterrestrial materials in which they are found and implies that LIME and LICE silicates may have been common components of the early solar system. However, the current rarity of LIME and LICE silicates, especially among inner solar system samples, suggests that few of these primitive refractory silicates survive later nebula and parent bodies geological processing (Ebel et al., 2012).

In addition to the LIME and LICE silicates, anhydrous silicate grains in micrometeorites segregated into two geochemically distinct populations; either low-Fe (Mg#>88%) or high-Fe (Mg#<72%) crystals, with intermediate compositions being absent. This relationship reflects similar observations from carbonaceous and ordinary chondrites. Among these meteorites chondrules are classified as either type I or type II, dependent on the Mg# of their host olivine and pyroxene grains. Type I chondrules have Mg-rich compositions (Mg#>90%) and are generally considered reduced early-formed chondrules and precursor material to the more oxidized, later generation, ferroan type II chondrules (Mg#<90%) (Hewins, 1997; Frank et al., 2014; Jacquet et al., 2015; Villeneuve et al., 2017). Recent experimental studies have shown how transient heating events, under oxidising conditions can efficiently transform type I chondrule analogues into type II chondrules, via the melting and dissolution of FeNi metal blebs and subsequent inclusion of this Fe into the olivine crystal structure (Villeneuve et al., 2017). However, the source of these heating events, the astrophysical environment of formation and how closed system conditions are maintained remain problematic. Regardless of their exact formation mechanism, the type I and type II silicates observed here within micrometeorite matrix are most likely derived by the same mechanisms. Indeed, their small size, angular morphologies (when unaltered by aqueous fluid), bimodal compositional ranges and close geochemical affinities to anhydrous silicates from a range of known extraterrestrial materials strongly suggest that the matrix-hosted anhydrous silicate crystals found in fine-grained micrometeorites are small chondrule shards from disrupted and fragmented chondrules, which were acquired by accretion during the solar nebula stage (McSween, H.Y., 1977; Alexander et al., 1989; Nelson et al., 2002; Wasson et al., 2003).

3.8. Discussion: chondrule-poor CM-like micrometeorites

The apparent paucity of recognisable, whole chondrules among Antarctic micrometeorites, <<1% among the SPWW collection (Taylor et al., 2012) and <3% within the Larkman Nunatak collection (Genge et al., 2017, Fig.8) has previously been taken as evidence that fine-grained micrometeorites

sample a chondrule-poor, matrix-rich parent body, related to, but distinct from, the CM chondrite group (Engrand and Maurette, 1998; Reshma et al., 2013). However, the small size (<100µm) of most Antarctic micrometeorites prevents individual grains from sampling whole chondrules, whose diameters typically exceed 250µm (Jones, 2012). Instead, chondrules are present in Antarctic micrometeorite collections as fragmented shards and classified as coarse-grained or composite micrometeorites (Genge, et al., 2005; 2008; van Ginneken et al., 2017). Estimates for the abundance of coarse and composite micrometeorites are, at present, poorly constrained but likely represent between 10-30% of the total micrometeorite flux (Kurat et al., 1994; Taylor et al., 2012). However, up to 70% of this material is geochemically related to ordinary chondrite precursors (Genge, 2008), leaving little remaining material to account for the CM chondrule budget (perhaps as little as 2% of the total flux). For comparison, CM chondrites are composed of approximately 20% chondrules and 70% matrix by volume (Weisberg, et al., 2006). Thus, it appears that hydrated fine-grained micrometeorites, like those analysed in this study, are moderately-to-severely underrepresented in C2 chondrule material, potentially by up to 1 order of magnitude.

The evidence from this thesis supports the suggestion that fine-grained micrometeorites are chondrule-poor, rarely containing intact and unaltered chondrules. Despite analysis of 81 particles, no unaltered chondrules were found, instead, a single chondrule pseudomorph was identified in TAM19B-7, as well as highly altered refractory CAIs from TAM19B-17 and CP94-050-160. Likewise, the extent of aqueous alteration among the fine-grained micrometeorite population confirmed that most particles are intensely altered, with petrologic subtypes of CM2.2 or less. It therefore seems probable that a significant fraction of micrometeorite flux reaching the Earth today, originates from intensely aqueously altered CM-like asteroids. This would explain the reduced flux of recognisable C2 chondrules, owing to removal by aqueous alteration, whilst also supporting the well-documented genetic match between (most) fine-grained micrometeorites and fine-grained CM2 matrix.

3.9. Conclusions from microanalysis techniques

The mineralogy, petrography and geochemistry of 81 fine-grained and scoriaceous micrometeorites were analysed in this chapter. All unmelted, fine-grained micrometeorites have chondritic bulk compositions and, therefore, preserve primordial geochemical signatures, reflecting the condensation and accretion of material from the protoplanetary disk. However, particle mineralogy and textures also record later geological processes operating on their host asteroids. Since micrometeorites are composed primarily of hydrated phases, aqueous alteration is the fundamental geological process preserved in fine-grained micrometeorites.

Petrologic subtypes (between CM2.6-CM2.0) were assigned to the moderately altered CM-like (C2) micrometeorites, reflecting the extent of aqueous alteration experienced. This was achieved by evaluating the abundance and morphology of matrix-hosted anhydrous silicates, as well as the FeO/SiO_2 ratio of micrometeorite matrix and the (estimated) abundance of FeNi metal and PCP clumps. Because aqueous alteration progresses by the replacement of anhydrous phases with hydrated phases, this metric provides an adequate, if low-resolution, proxy for alteration extent. A

single micrometeorite (TAM19B-7) was found to contain a pseudomorphic microchondrule and therefore classed as a CM2.0, while the majority of micrometeorites were assigned a C2.2 grade. Only three micrometeorites have unaltered anhydrous silicates and were classed as CM2.6-2.4 (least altered).

Seventeen percent of the micrometeorites studied have internal clasts, typically these are C2 fine-grained micrometeorites hosting C1 matrix clasts (or vice versa). In all cases the embedded clasts show evidence of petrographic integration into host micrometeorite, suggesting that these clasts were captured prior to aqueous alteration and were later geochemically integrated (lithified). Consequently, embedded clasts were most likely derived as impact debris from neighbouring disrupted hydrated asteroids.

In addition to a phyllosilicate matrix and clastic material, fine-grained micrometeorites have residual anhydrous silicates, which survived aqueous alteration. Geochemical analysis of these silicates revealed the presence of three geochemically distinct populations. Although most grains are compositionally similar to type I or type II chondrule olivines (and pyroxenes), highly refractory LIME/LICE silicates were also identified, which represent some of the earliest solids formed in the solar system. The observed compositional range of micrometeorite olivine is also greater than that of CM chondrites. This finding is consistent with previous studies of olivine in micrometeorites and can only be explained if micrometeorites sample a more diverse population of C-type asteroids than the larger meteorite population. This also implies that the compositional range found in micrometeorite olivine most likely reflects the true range of the CM chondrite family, which has otherwise yet to be adequately represented by meteorites.

Finally, as with previous studies, this chapter observed a significant paucity of chondrule material among the fine-grained micrometeorite population. Although some fraction of the coarse-grained micrometeorite population is known to represent chondrule fragments from carbonaceous chondrites, even when this contribution is included, the ratio of chondrules to matrix among hydrated, carbonaceous micrometeorites remains low. This is demonstrated clearly in the petrography of the larger TAM micrometeorites, which despite sampling a significant area of matrix (>500μm^2), entirely lack chondrules (as in TAM19-7, TAM18C-12, TAM15.11, TAM19B-17 and TAM19B-18).

Based on this petrographic study, the current flux of fine-grained micrometeorites appears to be sampling primitive chondrule-poor, intensely aqueously altered (CM2.2-CM2.0) CM-like asteroids that collected abundant fragments of other hydrated and disintegrated neighbouring C-type asteroids during their accretionary history.

Table.3.1 Bulk WD-EMPA data from the micrometeorite population. Elements Na to O are shown in wt%, while FeO/SiO_2 ratios are expressed as weight percent oxide and O/Si and Mg# are given as At% ratios. [Average standard error of the mean values for each element are as follows: Na 0.04wt%, Mg 0.72wt%, Al 0.20wt%, Si 0.80wt%, P 0.02wt%, S 0.12wt%, Cl 0.02wt%, K 0.04wt%, Ca 0.14wt%, Ti 0.02wt%, V 0.01wt%, Cr 0.04wt%, Mn 0.02wt%, Fe 0.87wt%, Co <0.01wt%, Ni 0.06wt%, Cu 0.03wt%, Zn 0.06wt%, and O 0.94wt%.]

No.	Particle ID	N	Na	Mg	Al	Si	P	S	Cl	K	Ca	Ti	V	Cr	Mn	Fe	Co	Ni	Cu	Zn	O	Total	FeO/SiO_2	O/Si [At%]	Mg# [At%]
1	CP94-050-047	9	0.34	12.50	1.64	20.18	0.09	0.36	0.17	0.08	0.36	0.07	0.01	0.30	0.13	17.40	0.02	0.23	0.09	0.32	39.00	93.30	0.52	3.39	62.5
2	CP94-050-048	8	0.31	14.14	1.02	18.73	0.17	0.43	0.08	0.06	1.72	0.09	0.01	0.43	0.21	18.33	0.03	0.46	0.08	0.31	39.03	95.64	0.59	3.66	64.2
3	CP94-050-052	12	0.17	2.86	0.73	7.39	0.16	0.49	0.36	0.03	1.17	0.09	0.00	0.44	0.18	36.14	0.00	0.33	1.05	1.79	23.90	77.29	2.94	5.67	15.5
4	CP94-050-053	7	0.09	14.56	0.80	19.13	0.14	0.10	0.10	0.02	2.60	0.13	0.01	0.48	0.40	16.48	0.02	0.14	0.10	0.31	38.79	94.40	0.52	3.56	67.3
5	CP94-050-054	13	0.47	10.17	1.46	17.52	0.10	0.20	0.27	0.13	0.25	0.07	0.01	0.36	0.17	16.26	0.00	0.22	0.46	0.67	33.95	82.74	0.56	3.40	59.2
6	CP94-050-060	7	0.19	9.76	1.40	15.79	0.17	0.36	0.10	0.09	0.16	0.07	0.01	0.24	0.19	30.24	0.00	0.19	0.15	0.49	35.65	95.23	1.15	3.96	42.9
7	CP94-050-064	11	0.22	10.56	1.48	15.32	0.15	0.69	0.06	0.09	0.51	0.06	0.00	0.55	0.22	30.55	0.04	0.79	0.23	0.51	36.77	98.81	1.20	4.21	44.5
8	CP94-050-067	15	0.33	9.80	1.17	17.26	0.04	0.40	0.14	0.06	0.21	0.09	0.01	0.40	0.14	21.64	0.00	0.15	0.73	1.06	34.99	88.60	0.75	3.56	51.3
9	CP94-050-068	7	0.39	10.06	1.52	17.51	0.11	0.62	0.22	0.13	0.81	0.06	0.01	0.30	0.22	20.32	0.00	0.18	0.31	0.83	35.89	89.50	0.70	3.60	53.5
10	CP94-050-071	6	0.48	8.14	1.69	16.86	0.24	0.52	0.18	0.14	0.79	0.08	0.01	0.30	0.17	20.78	0.00	0.22	0.81	0.94	34.36	86.72	0.74	3.58	47.7
11	CP94-050-073	6	0.05	5.16	0.95	8.18	0.14	0.14	0.10	0.01	0.31	0.04	0.00	0.15	0.17	45.44	0.05	0.26	0.29	1.05	27.68	90.17	3.34	5.94	20.9
12	CP94-050-074	9	0.32	12.63	1.64	21.83	0.16	0.46	0.09	0.15	0.16	0.09	0.00	0.44	0.05	13.80	0.00	0.42	0.30	0.71	40.34	93.58	0.38	3.24	68.0
13	CP94-050-075	7	0.12	10.68	1.35	14.51	0.06	0.50	0.13	0.04	0.09	0.05	0.00	0.23	0.18	30.96	-0.01	0.17	0.38	0.44	34.98	94.85	1.28	4.23	44.5
14	CP94-050-079	10	0.31	12.66	1.20	15.88	0.12	0.51	0.09	0.09	0.22	0.06	0.01	0.29	0.21	25.91	0.01	0.31	0.22	0.38	36.53	95.02	0.98	4.04	53.2
15	CP94-050-081	7	0.08	10.56	0.51	13.80	0.22	0.40	0.13	0.01	0.97	0.05	0.01	0.28	0.19	30.90	0.01	0.30	0.16	0.38	33.73	92.69	1.35	4.29	44.3
16	CP94-050-082	12	0.11	14.29	9.03	14.41	0.52	0.13	0.06	0.01	1.83	0.25	0.00	0.10	0.17	15.26	0.00	0.31	0.02	0.05	40.23	96.79	0.64	4.90	68.5
17	CP94-050-080	7	0.25	10.06	1.08	14.43	0.40	0.42	0.21	0.07	1.00	0.06	0.00	0.33	0.23	23.92	0.00	0.17	0.45	1.13	33.23	87.44	1.00	4.04	49.4
18	CP94-050-090	7	0.31	14.77	1.25	18.85	0.21	1.05	0.06	0.11	0.42	0.07	0.01	0.44	0.23	17.98	0.04	0.84	0.14	0.39	40.30	97.46	0.57	3.75	65.6
19	CP94-050-096	13	0.18	9.67	1.58	13.65	0.12	0.55	0.12	0.07	0.32	0.05	0.00	0.27	0.20	32.12	0.03	0.57	0.22	0.43	34.26	94.42	1.41	4.41	41.2
20	CP94-050-097	9	0.11	8.48	1.05	11.69	0.20	0.36	0.13	0.03	0.30	0.07	0.01	0.38	0.16	33.46	0.02	0.40	0.39	1.16	31.15	89.55	1.72	4.68	37.1
21	CP94-050-099	9	0.32	10.71	1.37	15.42	0.16	0.40	0.18	0.09	0.15	0.07	0.01	0.46	0.21	25.92	0.02	0.36	0.10	0.24	34.79	90.99	1.01	3.96	49.0
22	CP94-050-100	13	0.60	4.86	1.33	9.20	0.11	0.34	0.50	0.08	0.56	0.09	0.01	0.51	0.14	32.72	-0.01	0.15	0.41	1.51	26.19	79.31	2.14	5.00	25.7
23	CP94-050-101	8	0.15	10.12	1.21	13.36	0.06	0.38	0.14	0.04	0.18	0.06	0.01	0.21	0.18	28.76	0.02	0.41	0.06	0.23	32.35	87.93	1.29	4.25	45.0
24	CP94-050-105	7	0.11	5.89	1.48	11.58	0.17	0.14	0.23	0.04	0.17	0.07	0.01	0.37	0.16	33.78	0.00	0.16	0.19	0.67	29.14	84.36	1.75	4.42	28.8
25	CP94-050-106	7	0.26	14.38	1.28	17.79	0.19	0.24	0.09	0.11	0.30	0.06	0.01	0.79	0.25	19.02	0.01	0.26	0.23	0.40	37.88	93.56	0.64	3.74	63.7
26	CP94-050-109	9	0.61	12.94	1.31	19.62	0.10	0.59	0.10	0.12	0.59	0.06	0.01	0.44	0.22	16.88	0.01	0.23	0.08	0.61	38.91	93.42	0.52	3.48	64.0
27	CP94-050-110	7	0.11	10.93	1.28	14.14	0.04	0.65	0.12	0.02	0.14	0.07	0.01	0.28	0.20	30.24	-0.01	0.53	0.10	0.28	34.71	93.86	1.29	4.31	45.6
28	CP94-050-113	7	0.45	8.77	2.00	15.35	0.28	0.73	0.20	0.21	0.57	0.07	0.01	0.30	0.15	21.61	0.04	1.20	0.16	0.97	33.97	87.04	0.85	3.89	48.5
29	CP94-050-115	6	0.36	6.00	1.18	13.18	0.30	0.47	0.49	0.09	0.53	0.09	0.01	0.50	0.10	25.76	-0.01	0.07	0.77	1.11	29.65	80.66	1.18	3.95	35.1
30	CP94-050-183	7	0.12	8.27	1.25	15.07	0.20	0.47	0.30	0.07	0.31	0.08	0.01	0.37	0.13	23.30	-0.01	0.13	0.74	1.30	32.35	84.46	0.93	3.77	45.2
31	CP94-050-256	6	0.28	12.64	1.53	18.50	0.44	0.50	0.23	0.16	0.33	0.08	0.01	0.41	0.15	16.69	-0.01	0.20	0.48	0.86	37.79	91.26	0.54	3.59	63.8
32	CP94-050-123	6	0.15	11.07	1.02	14.98	0.22	0.46	0.13	0.05	0.16	0.09	0.00	0.27	0.21	29.22	0.00	0.32	0.16	0.48	35.23	94.23	1.17	4.13	46.8
33	CP94-050-127	7	0.28	12.22	1.42	17.19	0.23	0.63	0.07	0.12	0.36	0.08	0.01	0.46	0.23	23.28	0.02	0.41	0.18	0.47	37.67	95.31	0.81	3.85	55.0

Table.3.1 *continued.*

No.	Particle ID	N	Na	Mg	Al	Si	P	S	Cl	K	Ca	Ti	V	Cr	Mn	Fe	Co	Ni	Cu	Zn	O	Total	FeO/SiO_2	O/Si [At%]	Mg# [At%]
34	CP94-050-128	7	0.26	8.84	1.40	18.05	0.05	0.30	0.25	0.13	0.35	0.07	0.00	0.32	0.15	17.87	0.00	0.32	0.41	1.00	34.19	83.96	0.60	3.33	53.5
35	CP94-050-129	7	0.28	9.70	1.18	16.17	0.15	0.34	0.29	0.07	0.45	0.08	0.01	0.39	0.18	19.29	0.00	0.20	0.28	0.83	32.98	82.84	0.72	3.58	53.9
36	CP94-050-130	3	0.14	7.22	1.01	12.38	0.41	0.38	0.32	0.06	0.47	0.07	0.01	0.37	0.15	23.53	0.00	0.16	1.35	1.05	28.75	77.83	1.14	4.08	41.6
37	CP94-050-132	7	0.17	12.65	1.25	17.13	0.36	0.31	0.29	0.05	0.28	0.05	0.01	0.42	0.06	15.19	0.02	0.41	0.20	1.03	35.08	84.95	0.53	3.60	65.9
38	CP94-050-136	7	0.28	10.94	1.62	16.15	0.09	0.71	0.04	0.10	0.15	0.08	0.01	0.36	0.25	27.14	0.02	0.45	0.05	0.43	36.73	95.61	1.01	3.99	48.4
39	CP94-050-137	7	0.28	7.34	1.26	14.20	0.16	0.45	0.32	0.11	0.56	0.08	0.01	0.41	0.15	26.05	0.01	0.55	0.32	1.27	31.67	85.21	1.10	3.92	39.6
40	CP94-050-139	7	0.13	9.64	1.32	16.69	0.22	0.33	0.32	0.08	0.22	0.06	0.01	0.58	0.08	14.54	0.00	0.34	0.35	0.89	32.37	78.18	0.52	3.41	60.6
41	CP94-050-140	7	0.22	16.16	1.56	21.83	0.12	0.28	0.10	0.08	0.17	0.06	0.01	0.33	0.12	10.34	0.00	0.15	0.13	0.43	40.99	93.06	0.28	3.30	78.4
42	CP94-050-142	7	0.14	10.14	1.26	15.09	0.21	0.46	0.08	0.05	0.16	0.07	0.01	0.40	0.20	29.25	0.01	0.27	0.11	0.60	34.99	93.49	1.17	4.07	44.6
43	CP94-050-150	6	0.03	9.01	1.83	12.36	0.10	0.08	0.14	0.01	0.29	0.05	0.00	0.16	0.20	34.91	0.02	0.43	0.06	0.13	32.36	92.18	1.70	4.60	37.5
44	CP94-050-152	7	0.33	14.95	1.41	18.44	0.04	0.30	0.06	0.08	0.11	0.06	0.01	0.22	0.21	21.46	0.00	0.15	0.03	0.32	39.27	97.46	0.70	3.74	61.8
45	CP94-050-153	7	0.38	11.35	1.43	15.06	0.21	0.40	0.15	0.09	0.64	0.06	0.01	0.44	0.26	24.35	0.03	0.68	0.17	0.71	34.89	91.30	0.97	4.07	52.0
46	CP94-050-158	7	0.26	13.79	1.00	17.08	0.19	0.45	0.17	0.10	0.72	0.08	0.01	0.37	0.19	18.12	0.05	0.42	0.16	0.31	36.47	89.94	0.64	3.75	63.9
47	CP94-050-159	3	0.59	11.10	1.27	17.05	0.19	0.33	0.31	0.16	0.48	0.08	0.01	0.38	0.15	16.27	0.00	0.13	0.15	0.41	34.14	83.18	0.57	3.52	61.3
48	CP94-050-160	7	0.24	4.45	1.82	12.45	0.08	1.16	0.28	0.08	0.74	0.08	0.00	0.31	0.07	24.81	0.07	1.11	0.55	2.18	29.28	79.76	1.20	4.13	29.4
49	CP94-050-161	8	0.19	11.05	1.28	17.40	0.24	0.33	0.29	0.07	0.20	0.08	0.01	0.48	0.13	18.76	0.01	0.47	0.53	0.99	35.40	87.91	0.65	3.57	57.8
50	CP94-050-163	7	0.41	12.18	1.66	19.00	0.10	0.44	0.20	0.11	0.71	0.08	0.01	0.42	0.20	15.27	0.01	0.27	0.28	0.58	37.35	89.28	0.48	3.45	64.9
51	CP94-050-167	8	0.09	9.85	0.94	13.93	0.06	0.13	0.25	0.02	0.24	0.06	0.01	0.11	0.14	23.62	0.00	0.10	0.26	1.15	30.89	81.87	1.02	3.89	49.2
52	CP94-050-168	2	0.25	3.26	1.15	12.70	0.22	0.49	0.37	0.13	0.38	0.06	0.00	0.38	0.04	28.05	0.01	0.26	0.45	1.30	27.70	77.21	1.33	3.83	21.3
53	CP94-050-169	7	0.22	13.40	1.37	18.23	0.18	0.44	0.12	0.06	0.20	0.83	0.01	0.41	0.14	17.15	0.02	0.47	0.15	0.74	37.93	92.08	0.57	3.65	64.5
54	CP94-050-170	12	0.22	13.18	1.40	15.75	0.10	0.48	0.10	0.05	0.45	0.07	0.01	0.26	0.22	26.22	0.01	0.35	0.16	0.40	36.97	96.40	1.00	4.12	53.9
55	CP94-050-176	8	0.21	13.65	1.71	19.85	0.09	0.42	0.12	0.08	0.25	0.05	0.01	0.42	0.10	14.27	0.02	0.77	0.10	0.60	38.80	91.53	0.43	3.43	69.0
56	CP94-050-180	7	0.28	13.85	1.60	18.64	0.13	1.04	0.16	0.07	0.18	0.07	0.01	0.36	0.12	16.63	0.04	0.98	0.32	0.50	39.19	94.17	0.54	3.69	65.9
57	5-30.	22	0.08	11.53	2.03	18.28	0.10	0.81	ND	0.29	2.03	0.10	0.01	0.30	0.13	19.96	0.02	0.47	0.01	0.01	38.57	94.73	0.66	3.70	57.0
58	15-11.	11	0.28	2.53	3.04	17.70	0.11	2.62	ND	1.29	0.16	0.08	0.01	0.43	0.07	20.43	0.00	0.09	0.02	0.01	35.17	84.01	0.69	3.49	22.1
59	5-18.	5	0.38	8.57	2.84	13.04	0.25	3.08	ND	0.18	0.60	0.05	0.00	0.32	0.32	25.96	0.01	0.54	0.02	0.01	36.24	92.42	1.20	4.88	43.1
60	19-7.	19	0.70	5.88	1.96	19.67	0.01	3.35	ND	1.16	0.15	0.08	0.01	0.45	0.09	18.31	0.00	0.22	0.04	0.00	39.20	91.25	0.56	3.50	42.5
61	19B-7	20	0.40	2.10	1.92	17.66	0.18	2.37	ND	0.40	0.07	0.00	0.00	0.58	0.00	21.92	0.00	0.43	0.00	0.00	36.76	85.58	0.75	3.65	18.1
62	19B-17.	25	0.18	3.04	1.68	17.56	0.16	2.72	ND	0.61	0.14	0.09	0.01	0.39	0.08	26.67	0.00	0.14	0.01	0.02	35.97	89.45	0.91	3.60	20.8
63	18C-12.	18	0.30	1.24	1.16	15.67	0.18	4.98	ND	1.59	0.18	0.10	0.01	0.63	0.03	25.91	0.00	0.21	0.02	0.03	35.75	87.99	0.99	4.01	9.9
64	19B-18.	20	0.23	7.65	1.66	14.77	0.08	1.94	ND	0.30	0.17	0.06	0.01	0.33	0.17	32.03	0.01	0.27	0.01	0.02	36.06	95.75	1.30	4.29	35.4
65	2.1C.	18	0.47	10.44	2.51	18.16	0.04	1.47	ND	0.12	0.15	0.07	0.01	0.49	0.18	21.14	0.00	0.42	0.01	0.03	38.82	94.53	0.70	3.75	53.2
66	2.1Q.	15	0.36	3.06	4.68	10.27	0.13	5.45	ND	2.76	0.26	0.25	0.02	0.18	0.08	26.51	0.00	0.11	0.02	0.03	34.93	89.09	1.55	5.97	21.0
67	2.1T.	14	0.37	8.64	1.96	16.45	0.10	1.34	ND	0.17	0.15	0.08	0.01	0.50	0.17	28.11	0.03	0.54	0.01	0.01	37.08	95.70	1.03	3.96	41.4

Table.3.2. Petrologic subtypes for thirty-seven C2-FgMMs. Classifications are established on the basis of the abundance and alteration state of matrix-hosted anhydrous silicates

No	Stub ID	Particle ID	Classification	Matrix Phyllosilicates	Anhydr. silicates [alteration]	Anhydrous silicates Mg#	Accessory phases	Clasts, chondrules?	Grade (CM2.6-2.0)
1	UMM94-01-12	CP94-050-051	C2-FgMM	Mg-rich, compact, homogenous	<2%	68-70%			2.4-2.6
2	UMM94-01-13	CP94-050-052	C2-FgMM	Nuggets and ribbon morphologies	<2%	67-97%	magnetite, sulphides, spinel	C2 clast	2.4-2.6
3	UMM94-01-22	CP94-050-060	C2-FgMM	Mixed, coarse Fe-rich and fine Mg-rich	15-85%	97%	magnetite		2.2
4	UMM94-01-43	CP94-050-075	C2-FgMM	Mixed, coarse Fe-rich and fine Mg-rich	85-99%				2.1
5	UMM94-01-52	CP94-050-082	C2-FgMM	Fine, Fe-rich, homogenous	15-85%				2.2
6	UMM94-01-54	CP94-050-080	C2-FgMM	Fe-rich nuggets	2-15%				2.3
7	UMM94-01-81	CP94-050-096	C2-FgMM	Coarse, Fe-rich clumps	2-15%	94-99%		C1 clast	2.3
8	UMM94-01-82	CP94-050-097	C2-FgMM	Mixed, coarse Fe-rich and fine Mg-rich	15-85%		FeNi sulphides	C1 clast	2.2
9	UMM94-01-83	CP94-050-099	C2-FgMM	Mg-rich, porous, fine grained	15-85%		magnetite	C2 clast	2.2
10	UMM94-01-84	CP94-050-100	C2-FgMM	Nuggets and ribbon morphologies	<2%	83-85%	magnetite		2.4-2.6
11	UMM94-01-93	CP94-050-105	C2-FgMM	Mixed, coarse Fe-rich and fine Mg-rich	15-85%				2.2
12	UMM94-01-94	CP94-050-106	C2-FgMM	Coarse, Fe-rich clumps	15-85%				2.2
13	UMM94-01-97	CP94-050-109	C2-FgMM	Mg-rich fine-grained & Fe-rich nuggets	2-15%	82-94%	magnetite, FeNi sulphides	C2 clast	2.3
14	UMM94-01-98	CP94-050-110	C2-FgMM	Primarily fibrous, coarse Fe-rich	15-85%		FeNi sulphides		2.2
15	UMM94-02-04	CP94-050-113	C2-FgMM	Fe-rich, homogenous	15-85%	94-98%			2.2
16	UMM94-02-07	CP94-050-115	C2-FgMM	Fe-rich nuggets in Mg-rich fine-grained	85-99%	94%	magnetite, sulphides, spinel		2.1
17	UMM94-02-12	CP94-050-182	C2-FgMM	Mixed, coarse Fe-rich and fine Mg-rich	15-85%	41-97%	Cr-spinels, FeNi sulphides	microchondrule	2.2
18	UMM94-02-26	CP94-050-123	C2-FgMM	Primarily fibrous, coarse Fe-rich	2-15%	52-56%	magnetite	C1 clasts (x2)	2.3
19	UMM94-02-31	CP94-050-127	C2-FgMM	Mixed, coarse Fe-rich and fine Mg-rich	15-85%	91-98%	spinel		2.2
20	UMM94-02-35a	CP94-050-130	C2-FgMM	Fe-rich nuggets in Mg-rich fine-grained	85-99%		magnetite		2.1
21	UMM94-02-43	CP94-050-136	C2-FgMM	Fe-rich nuggets in Mg-rich fine-grained	85-99%	55%	magnetite		2.1
22	UMM94-02-51	CP94-050-142	C2-FgMM	Coarse, Fe-rich clumps	2-15%	96-99%		C2 clasts (x2)	2.3
23	UMM94-02-64	CP94-050-152	C2-FgMM	Coarse, Fe-rich clumps	85-99%	65%	magnetite		2.1
24	UMM94-02-65	CP94-050-153	C2-FgMM	Mg-rich fine-grained & Fe-rich nuggets	2-15%	98%	magnetite, FeNi sulphides		2.3

Table.3.2. *Continued.*

No	Stub ID	Particle ID	Classification	Matrix Phyllosilicates	Anhydr. silicates [alteration]	Anhydrous silicates Mg#	Accessory phases	Clasts, chondrules?	Grade (CM2.6-2.0)
25	UMM94-02-72	CP94-050-159	C2-FgMM	Mg-rich, compact, homogenous	15-85%		magnetite		2.2
26	UMM94-02-72A	CP94-050-160	C2-FgMM	Mixed, coarse Fe-rich and fine Mg-rich	85-99%		pyrrhotite, spinel		2.1
27	UMM94-02-76	CP94-050-163	C2-FgMM	Fe-rich nuggets in Mg-rich fine-grained	15-85%	99%	magnetite		2.2
28	UMM94-02-80	CP94-050-167	C2-FgMM	Coarse, Fe-rich clumps	2-15%	55-67%	Fe-oxides		2.3
29	UMM94-02-81	CP94-050-168	C2-FgMM	Mixed, coarse Fe-rich and fine Mg-rich	15-85%				2.2
30	UMM94-02-84	CP94-050-170	C2-FgMM	Fe-rich, coarse, homogenous	85-99%		FeNi sulphides		2.1
31	TAM-M1	19B-7	C2-FgMM	homogenous, compact	>99%		magnetite, FeNi sulphides	Altered chondrule	2.0
32	TAM-M4	4-16.	C2-FgMM	Mixed, coarse Fe-rich and fine Mg-rich	2-15%		magnetite		2.3
33	TAM-M4	4-27.	C2-FgMM	Fe-rich, coarse, homogenous	2-15%		FeNi sulphides		2.3
34	TAM-M6	5-18.	C2-FgMM	Fe-rich, coarse, homogenous			FeNi sulphides		2.3
35	TAM-M6	19B-17.	C2-FgMM	Mixed, coarse Fe-rich and fine Mg-rich	15-85%		FeNi sulphides		2.2
36	TAM-M7	19B-18.	C2-FgMM	Coarse, Fe-rich clumps	15-85%		mag, FeNi sulphides, carbonates	Various clasts	2.2
37	TAM-B2	2.1Q.	C2-FgMM	Fe-rich, coarse, homogenous	15-85%		mag, FeNi sulphides		2.2

Chapter 4: Implications from mid-IR spectroscopy

4.0. Overview – This chapter reviews mid-IR (8-13µm) spectral data collected from the Antarctic micrometeorite population. Five distinct spectral groups are identified which correspond to a progressive thermal decomposition trend. During atmospheric entry phyllosilicate minerals in the matrix of fine-grained micrometeorites experience dehydration (loss of interlayer water) and dehydroxylation (loss of structural water) to form amorphous mineraloid phases. Subject to further heating the matrix anneals, recrystallizing as a hyperfine olivine groundmass. Continued heating results in melting (>1350°C) and the formation of mesostasis textures in cosmic spherules. The survival of fine-grained micrometeorites during atmospheric entry is shown to be dependent not only on dynamic entry parameters (e.g. speed and entry angle) but also on the cation composition of the matrix phyllosilicates and therefore, on the degree of parent body aqueous alteration. Additionally, a small population of anomalous micrometeorites are identified whose Raman spectroscopy, geochemical and textural data suggest these particles have experienced thermal processing in-space and may, therefore, represent regolith micrometeorites derived from the surfaces of heated C-type asteroids.

4.1. Mid-IR spectroscopy of extraterrestrial silicates

Mid-IR spectroscopy provides compositional information relating to the type of chemical bonds present within a sample and is therefore employed in planetary science to infer mineralogy in remote sensing and laboratory settings (Beck et al., 2010; 2014; Vernazza et al., 2010; 2012). When impinging electromagnetic radiation of a specific quantized wavelength is absorbed, asymmetric covalent bonds (e.g. C-H) within the molecule are excited and vibrate, stretching and bending. As this energy is dissipated the bond re-emits radiation in the mid-IR. Silicate minerals produce characteristic absorption bands in the silicate fingerprint region, between 8µm and 13µm primarily associated with Si-O stretching vibrations in silica tetrahedra (Kieffer, 1979). Common vibrational features occurring over this wavelength range include; the Christiansen minimum, the Reststrahlen bands and transparency features. These signatures provide diagnostic information relating to the mineral species, cation composition and the grain size of the sample (Salisbury et al., 1991; Salisbury and Wald, 1992; Vernazza et al., 2010; 2012). The Christiansen minimum is a reflectance low, or anomalous transmittance, typically located at ~8.5µm in silicate minerals. This feature arises when the index of refraction of the medium light is travelling through, and the index of refraction of the mineral are equal (Prost, 1973). The Reststrahlen bands are a mirror-like reflectance peaks formed by stretching vibrations in asymmetric covalent bonds and the subsequent emission of electromagnetic radiation (Salisbury et al., 1991; Salisbury and Wald, 1992). While transparency features are broad reflectance maxima, located in the wavelength range 12-18µm, which form in optically thin samples when small (<50µm) crystals cause the diffuse scattering of IR radiation (Salisbury and Wald, 1992; Vernazza et al., 2010). Transparency features migrate to shorter wavelengths (Vernazza et al., 2010) and the Reststrahlen peaks decrease in spectral contrast (Salisbury and Wald 1992) as particle size decreases, resulting in a loss of compositional information. Grain sizes <5µm are significantly affected by these

volume scattering effects. Subsequently, deriving compositional information from the spectra of C-type and Trojan asteroids, which are covered by highly porous, extremely fine-grained regolith, remains challenging (Vernazza et al., 2010; 2012; Hargrove et al., 2015). Despite these difficulties, the 8-13µm region is of growing interest to the planetary science community; as this spectral range is now observable from Earth, via air-borne telescopes, such as the SOFIA instrument (Herter et al., 2012) and retrievable from space, via instruments such as the Spitzer Space Telescope (Houck et al., 2004) and the future James Webb Telescope (Gardner et al., 2006). As a result, a significant and increasing number of mid-IR spectra exist for asteroids (Landsman et al., 2016) and comets (Harker et al., 2011).

Laboratory spectra, collected from meteorites, micrometeorites and IDPs, as well as synthetic analogue samples, provide important ground-truth experiments, which aid the interpretation of asteroid and comet spectra. Previous analysis of hydrated chondritic material demonstrated that both CM and CI chondrites produce smooth, asymmetric spectral profiles, which closely resemble the phyllosilicate mineral saponite (Beck et al., 2010; 2014). For CI chondrites this result is expected, since the dominant matrix mineral present in this chondrite class is saponite, or other, closely related 2:1 phyllosilicates (Tonui et al., 2003; Howard et al., 2010; Cloutis et al., 2011). Conversely, the modal mineralogy of CM chondrites is dominated by 1:1 phyllosilicates, commonly Mg-rich serpentine and Fe-rich cronsteditite (Howard et al., 2009; 2011). It is, therefore, surprising that saponite, and not serpentine spectral signatures, are the best match for CM chondrites. This discrepancy is attributed either to the low degree of crystallinity found in extraterrestrial serpentines or by the replacement of Al and Si cations (found in terrestrial phyllosilicates) with Fe and Mg cations, causing a broadening the primary peak and a shift to lower wavelengths (Beck et al., 2010; 2014).

Although mid-IR spectroscopic methods are commonly employed in the analysis of carbonaceous chondrites (Sanford, 1984; Sailsbury et al., 1991; Tonui et al., 2003; 2014; Beck et al., 2010; 2014) the application of this technique to micrometeorites is relatively rare. To date, two studies have collected mid-IR spectra from a large population of micrometeorites (Osawa et al., 2001; Susuki et al., 2010), both investigations focused on short wavelength (2.0-5.0µm) absorption features associated with the excitation of C-H, -OH stretching vibrations in organic molecules. By contrast, this investigation focuses on higher wavelength (8-13µm) features related to bulk mineralogy. In addition, spectra were collected in reflectance mode and the data used to reveal the thermal processing history of individual micrometeorites and combined with SEM petrographic observations.

4.2. Results: The Mid-IR spectra of Antarctic micrometeorites

All samples produced silicate fingerprint spectra, containing a Christiansen minimum and Reststrahlen bands. Transparency maxima were not observed over the wavelength range studied. The position of Reststrahlen reflectance peaks provides diagnostic information relating to a sample's mineralogy, these peaks were, therefore, used to separate the micrometeorite population into 5 distinct spectral groups, as shown in Figure 4.1.

The carbonaceous chondrites (CM, CI and C2-ungrouped) all share a broadly similar, simple spectral profile, defined by a smooth, asymmetric peak located at approximately 10µm. In samples C2 Bells,

CI1 Ivuna, C2 Tagish Lake and CM2 Cold Bokkeveld this peak lies at 9.89µm, 9.95µm, 10.01µm and 10.07µm respectively. By contrast, in the remaining samples, all CM chondrites, the primary reflectance peak is broader and the maxima shifted to higher wavelengths, approximately 10.5µm. Several chondrites also contain a small shoulder peak, located at 11.5µm. This feature is most clearly resolvable in C2 Tagish Lake and CM Jbilet Winselwan. Only two fine-grained micrometeorites contain similar spectral profiles; particles CP94-050-052 and CP94-050-160 both contain a single, smooth reflectance peak, centred at 10.2µm and both also lack the higher wavelength secondary peak. This smooth, single peak spectral profile is designated as group 1. The remaining micrometeorite population can be classified into 4 distinct spectral groups.

Group 2 spectra are characterised by a relatively sharp primary peak centred between 9.0µm and 9.5µm. At higher wavelengths (>9.5µm) spectral profiles downslope and several smaller shoulder peaks are observed, located at 10.01µm, 10.9µm, 11.3µm and 11.7µm. Group 2 contains only 5 members, all of which are micrometeorites from the TAM collection. Particles TAM-19-7 and TAM-4-27 contain the sharpest, most easily resolvable secondary reflectance peaks. By contrast, particle TAM-19B-17 contains smooth indistinct peaks and particles TAM-18C-12 and TAM-15-11 are featureless at wavelengths >9.5µm.

Group 3 spectra also contain a sharp reflectance peak located between 9.0µm and 9.5µm. In addition, a prominent reflectance maxima is located at 10.8µm. Smaller secondary peaks are seen at ~10µm and between 11.4µm and 11.8µm. Group 3 spectra are, therefore, similar to the group 2 profile, sharing the 9.0-9.5µm peak but also contain a series of well-defined additional peaks. Spectra from this group tend to have a higher signal-to-noise ratio and this may indicate a small grain size, at the limit of the wavelength of impinging light, and consequently, a volume scattering effect. This spectral group contains 6 fine-grained micrometeorites, predominantly from the Cap Prudhomme collection.

Group 4 spectra are characterised by red-sloped spectral profiles (increasing reflectance with increasing wavelength) and a prominent reflectance maximum at 11.5µm. Although the distinctive sharp 9.0-9.5µm peak, present in groups 2 and 3, is also found in group 4 this is a minor feature among this spectral class. Group 4 spectra, therefore, closely resemble group 3 spectra, containing the same reflectance peak positions but with different relative peak intensities. This spectral group includes 12 Fine-grained micrometeorites and two scoriaceous micrometeorites, with representatives from both the Cap Prudhomme and TAM micrometeorite collections.

Group 5 spectra are defined by a primary reflectance peak, located at 11.5µm, shouldered by parasitic peaks at 10.8µm and at 12.4µm and containing a secondary peak at 10.5µm. The Christiansen minimum for this group is wide, spanning 8.0-9.0µm. Minimal spectral variation between group 5 samples is observed. This is the most populous spectral group and includes 14 Fine-grained micrometeorites and 3 scoriaceous micrometeorites, with representatives from both the Cap Prudhomme and TAM collections.

By extracting reflectance values at 3 key wavelengths: 9.95µm, 10.7µm and 11.5µm, centred on the main reflectance peaks, the spectral profiles of the entire micrometeorite population can be summarised in a single 2D scatter plot (Fig.4.2). In this plot, spectral groups 1-3 occupy a similar position, forming a dispersed cloud, while groups 4 and 5 plot in distinct domains. Despite their unique positions, all five spectral groups form a single continuous trend in peak position space. This trend is accurately described by a 2nd order polynomial with an R^2 regression value of 0.9. The five spectral groups are, therefore, related; as the 11.5µm peak increases the 9.95µm decreases, while the presence of peaks at 9.0-9.5µm and at 10.7µm are intermediate stages in this progression.

Fig.4.1. Mid-IR spectra (8-13µm) of selected carbonaceous chondrites and fine-grained micrometeorites. The MM population was separated into five spectral groups, on the basis of their absorption peak positions, six plots (A-F) display the characteristic spectral profiles for each spectral group and example spectra of cosmic spherules from Larkman Nunatak.

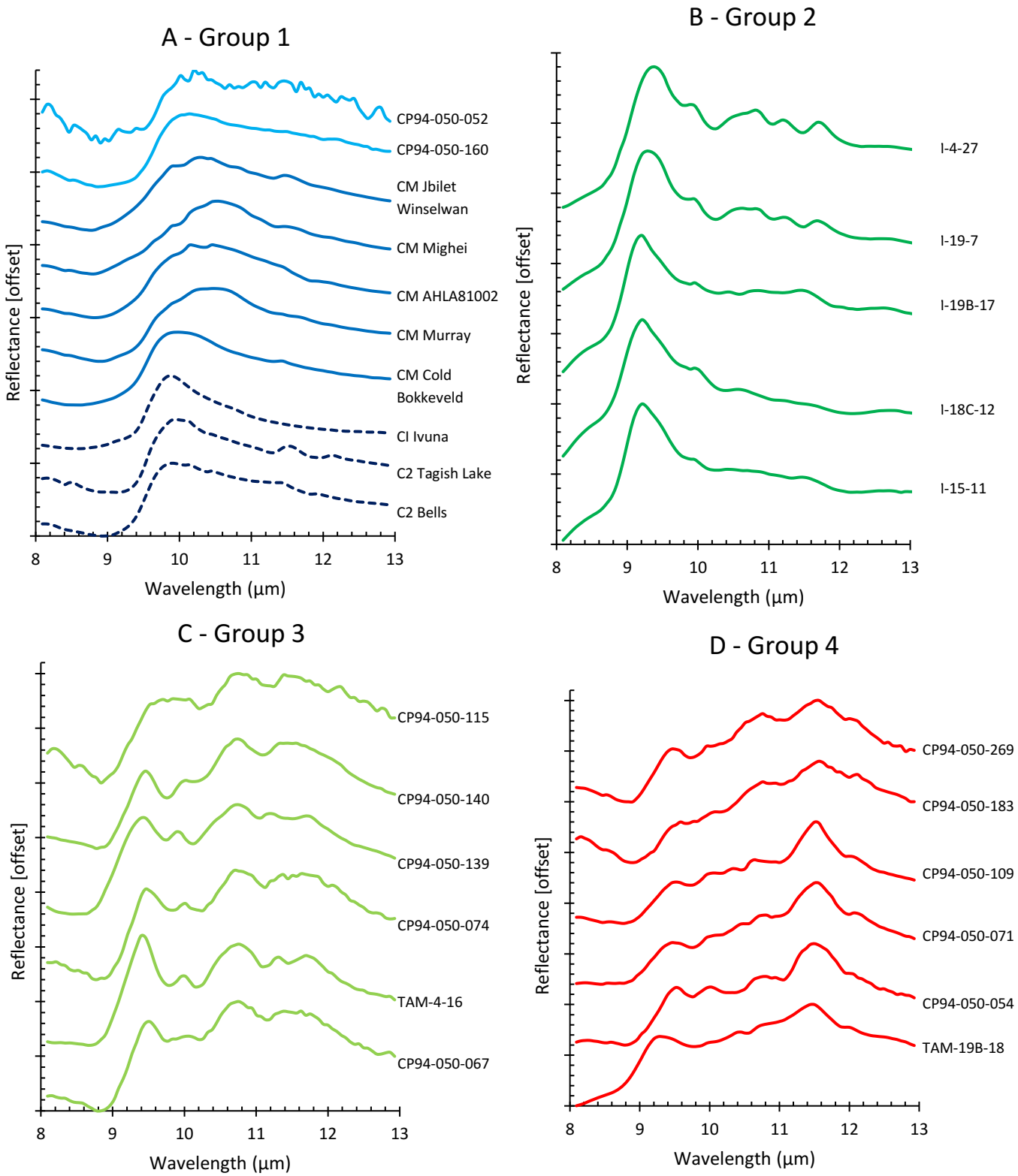

Fig.4.1. *Continued.*

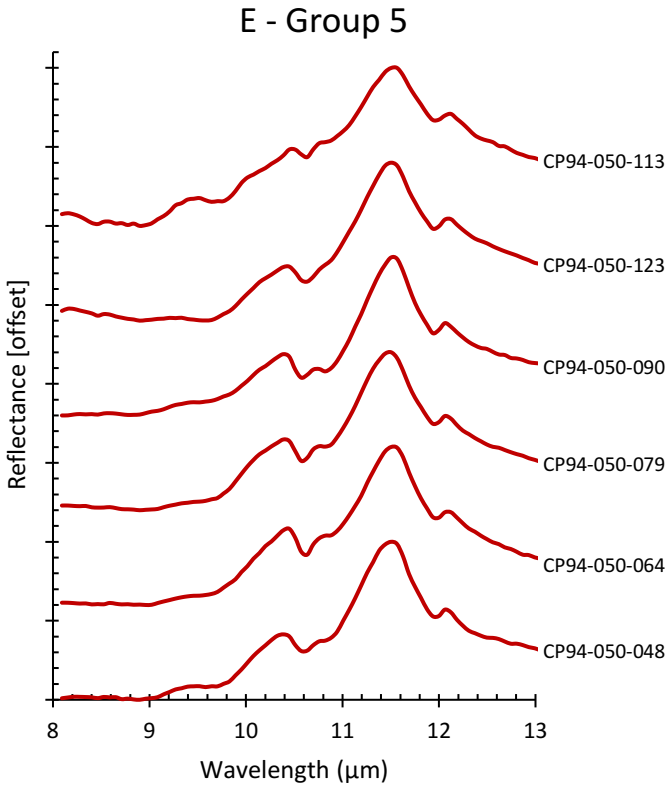

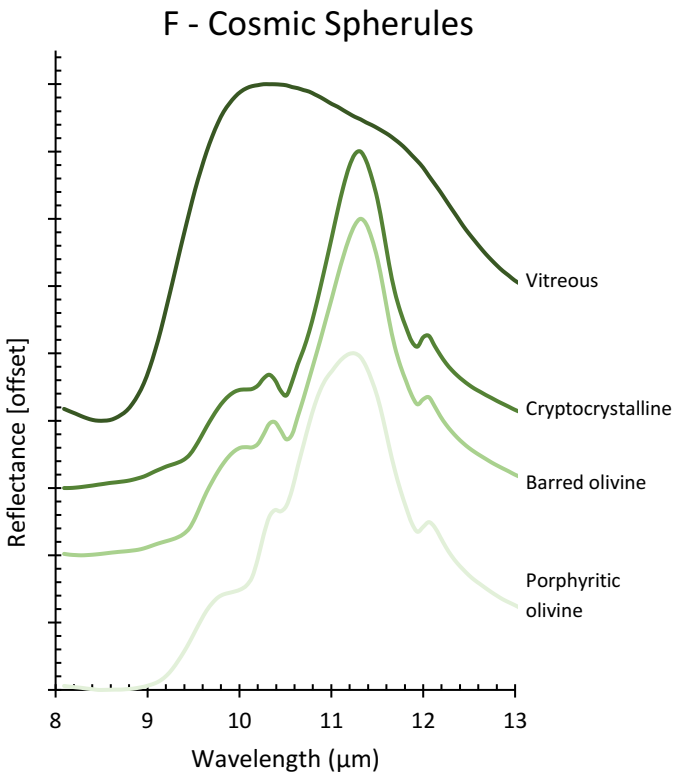

Fig.4.2. Deconvolved mid-IR spectra, using reflectance peak positions at three key wavelengths. The x-axis plots reflectance values at 9.95µm and the y-axis plots the ratio of reflectance values at 10.7µm/11.5µm. This plot illustrates the relationships between spectral groups and the carbonaceous chondrites. The entire fine-grained micrometeorite population can be described by a single (polynomial) trend-line with a negative correlation and R^2 value of 0.9, illustrating that, although distinct, the spectral groups form a continuous set of related profiles, with group 5 objects being most similar to group 4 objects and group1-3 sharing similar characteristics. In this plot spectral group are represented by different colours and shapes: blue crosses for group 1 micrometeorites, purple crosses for chondrites, dark green squares for group 2, light green diamonds for group 3, red circles for group 4 and dark red triangles for group 5. In addition, solid fill denote C2-fine-grained micrometeorites, open shapes denote C1-fine-grained micrometeorites and grey-infilled shapes are scoriaceous micrometeorites.

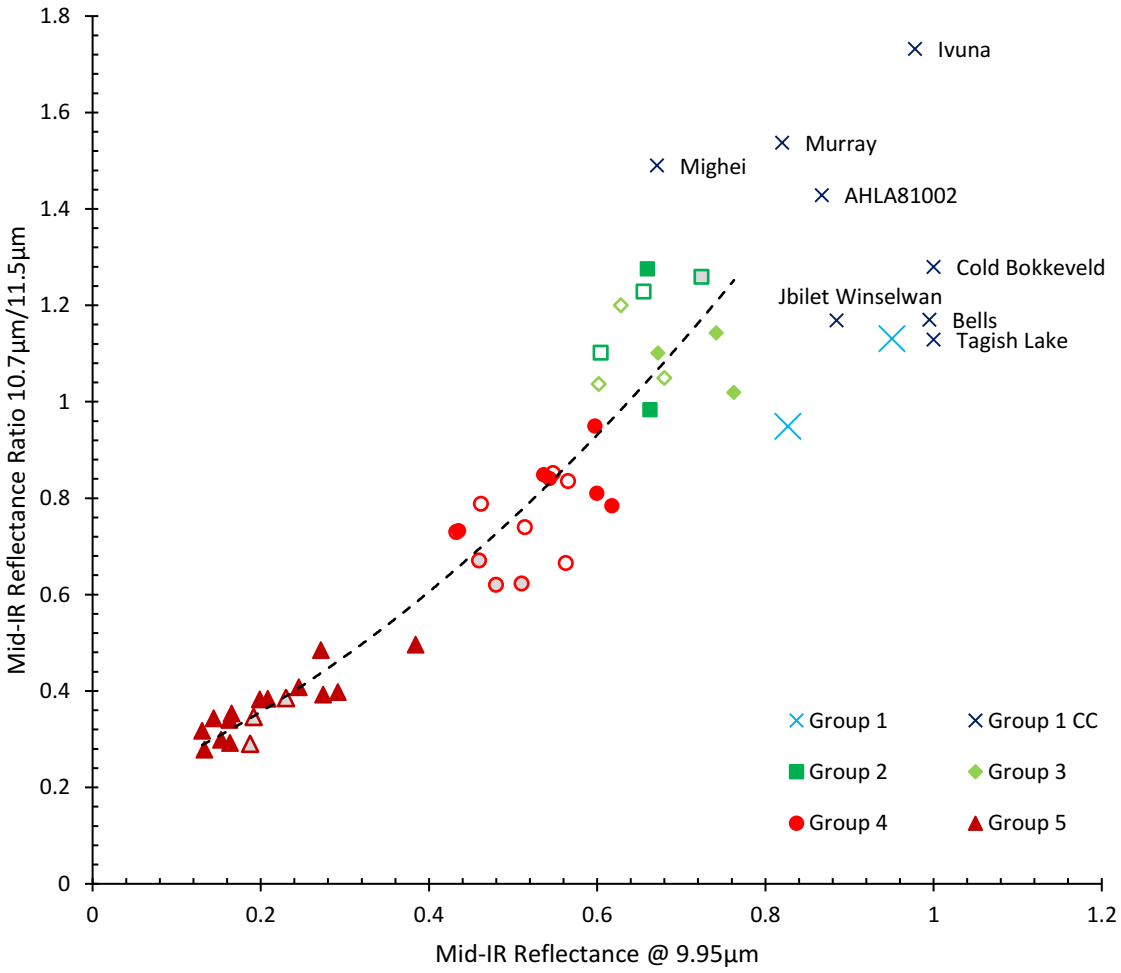

4.3. Results: Mid-IR spectral groups and matrix geochemistry

For each micrometeorite a bulk composition was determined by EMPA (see Chapt.3). Because the abundance of elements within a micrometeorite's matrix, relative to chondritic abundances, is dependent on post-accretion geochemical processes, analysis of elemental variations can provide indications of parent body processing (Bunch and Chang, 1980; Kurat et al., 1994; Browning et al., 1996; Grossman and Bearley, 2005) and/or terrestrial alteration (Cordier et al., 2011; van Ginneken et al., 2016). In this investigation correlations were identified between a micrometeorite's spectral group and the concentration of elements within the particle's matrix - dependent on elemental volatility.

The behaviour of refractory (Al), moderately refractory (Mg), moderately volatile (Mn) and highly volatile (Cl) elements (Fig.4.3) highlight these trends. For all spectral groups, Al concentrations varied between 0.5-2.0wt%, within the range observed for carbonaceous chondrites. Therefore, no correlation between Al concentration and spectral group variables exists. By contrast, a weak geochemical trend exists, between the concentration of Mg and a micrometeorite's spectral group. Groups 1-3 have concentrations between 2.8wt% and 16.1wt%, this range is restricted to 5.2-13.6wt% in group 4 micrometeorites and is further restricted to 8.7-14.9wt% among group 5 micrometeorites. Consequently, the average Mg concentration increases as spectral group increases, generating a weak negative correlation (R^2=0.30, Fig.4.3B). Moderately volatile elements, including Mn also demonstrate a similar trend. A moderate negative correlation (R^2=0.68, Fig.4.3C) is observed. Mn concentrations in group 1-3 range from 0.05wt% (near the limit of detection of 0.03wt%) up to 0.18wt%, however, this range is progressively reduced, and the average concentration increased in higher spectral groups. Conversely, a reverse trend, with a weak positive correlation (R^2=0.35, Fig.4.3D) is observed in the behaviour of the highly volatile element Cl. Groups 1-3 have the largest concentration range, from 0.1-0.5wt%, this decreases for group 4 to a more limited range between 0.09-0.35wt% and decreases further for group 5 from 0.03wt% (the detection limit) to 0.2wt%. The above geochemical trends can be collectively summarised by stating that micrometeorites in spectral groups 4 and 5 show progressive enrichment in moderately refractory elements and corresponding depletions in volatile components, while spectral groups 1-3 are enriched in volatile elements and show no correlation and, therefore, no apparent depletion in refractory elements.

4.4. Results: Mid-IR spectral groups and carbonaceous Raman data

Raman spectroscopy measures low-frequency vibrational and rotational modes arising from the excitation of symmetric covalent bonds (e.g. C-C). Inelastic scattering of monochromatic light over mid-IR wavelengths produces spectral signatures relating to both the mineralogy and organic components within a sample. Raman Spectroscopy on hydrated carbonaceous chondrites (el Amri et al., 2005; Quirco et al., 2005; 2014; Muirhead et al., 2012 and others), terrestrial shales (Rahl et al., 2005) and soot particles (Sheng, 2007) reveal the presence of prominent D and G bands, located at approximately 1350cm^{-1} and 1550cm^{-1} (Raman shift values) respectively. These features are products of vibrational modes in carbonaceous phases. These peak parameters can record both parent body signatures, relating to the composition of the carbonaceous phases present on their original asteroid (Busemann et al., 2007; Caro et al., 2008; Dobrică et al., 2011), and the peak metamorphic temperature (PMT) experienced over the lifetime of the sample (Rahl et al., 2005; Bonal et al., 2006; Busemann et al., 2007). Consequently, Raman spectroscopy provides a valuable metric for the reconstruction of thermal histories, independent of mineralogical criteria. Several studies focus on the R_1 peak height parameter, defined as: $R_1 = I_D/I_G$ (where I_x relates to a band parameter's intensity).

Fig.4.3. Comparisons between mid-IR spectral groups and bulk matrix geochemistry, with focus drawn to the behaviour of (A) refractory [Al], (B) moderately refractory [Mg], (C) moderately volatile [Mn] and (D) highly volatile [Cl]. In this plot spectral group are represented by different colours and shapes: blue crosses for group 1 micrometeorites, dark green squares for group 2, light green diamonds for group 3, red circles for group 4 and dark red triangles for group 5. In addition, solid fill denote C2-fine-grained micrometeorites, open shapes denote C1-fine-grained micrometeorites and grey-infilled shapes are scoriaceous micrometeorites.

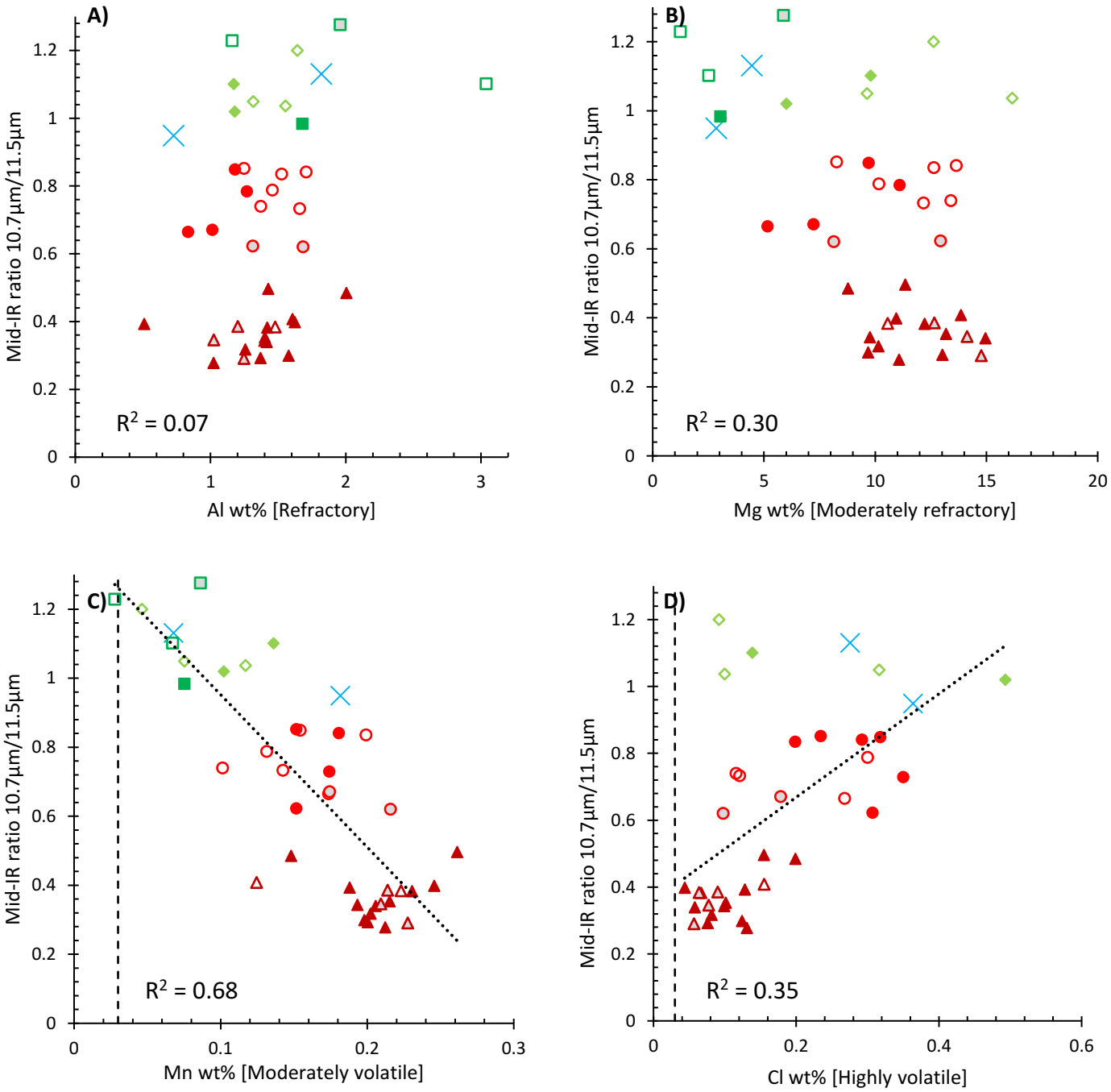

Fig.4.4. Comparisons between mid-IR spectral group and Raman R_1 peak parameter height ratios. A moderate negative correlation (with an R^2=0.62) is observed between a sample's mid-IR ratio (or spectral group) and R_1 values. A small population (5) of group 5 fine-grained micrometeorites show anomalous R_1 values, which do not match the observed trend, these are considered in the discussion (4.3). In this plot spectral group are represented by different colours and shapes: blue crosses for group 1 micrometeorites, purple crosses for chondrites, dark green squares for group 2, light green diamonds for group 3, red circles for group 4 and dark red triangles for group 5. In addition, solid fill denote C2-fine-grained micrometeorites, open shapes denote C1-fine-grained micrometeorites and grey-infilled shapes are scoriaceous micrometeorites.

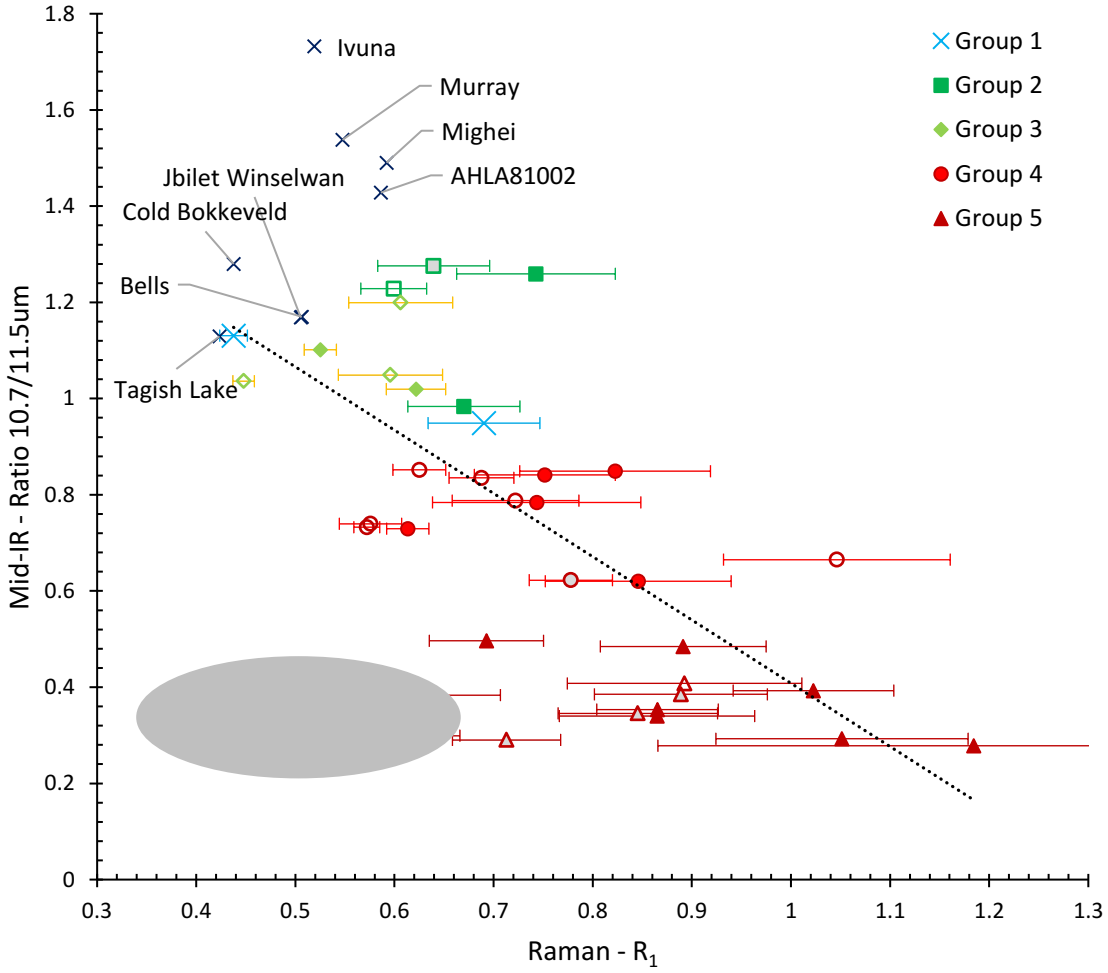

This parameter is known to closely relate to PMT (Ferrari and Robertson, 2000; Rahl et al., 2005; Bonal et al., 2006; Busemann et al., 2007). In addition, this variable carries the least analytical uncertainty associated with the data processing and extraction from raw Raman spectra. The relationship between Raman R_1 values and a micrometeorite's spectral groups is shown in figure 4.4. Collectively, the micrometeorite (and carbonaceous chondrite) population display a moderate negative correlation (R^2 = 0.60, Fig.4.4) between their R_1 peak height ratios and their mid-IR spectral group. As the reflectance peak ratio 10.7µm/11.5µm decreases, the R_1 peak height ratio increases. The carbonaceous chondrite R_1 values are restricted between 0.4-0.6, while the group 1 fine-grained micrometeorites plot marginally outside this range between 0.45 and 0.7. By contrast, the majority of group 2 and 3 micrometeorites extend to higher R_1 values, between 0.5 and 0.7. Spectral groups 4 and 5 have

progressively higher R_1 values, up to R_1=1.2. However, 6 Fine-grained micrometeorites from group 5, contain anomalous R_1 values, which do not fit the observed trend. These anomalous micrometeorites are all C2-fine-grained micrometeorites.

Note: Chapt.5 discusses, in detail, the Raman spectral data collected from the micrometeorite population, and illustrates the relationship between carbonaceous Raman peak parameters and a particle's thermal history; both as part of the asteroid parent body and during atmospheric entry heating. In Sect.5.3 all the Raman peak parameters are considered, this includes the G and D band peak positions, height, areas and widths. However, in this section (4.4) only a limited discussion of the Raman data is included, here a single Raman parameter (R_1) is considered. This is because the R_1 and subsequently the R_2 parameter, (not shown here) were found to most closely correlate with a particle's mid-IR spectral group, while other parameters exhibited no such correlation.

4.5. Discussion: Thermal decomposition of hydrous phases during atmospheric entry

The spectral profiles of group 1 members bear a strong resemblance to the spectra of unheated saponite. This suggests that the matrix mineralogy of the group 1 samples are dominated by hydrated extraterrestrial phyllosilicates. These samples have, therefore, avoided high temperature (>300°C, Bunch and Chang, 1980; Rubin et al., 2007; Busemann et al., 2007) processing (Beck et al., 2014). By contrast, the remaining 4 spectral groups contain unique spectral profiles which are distinct from the phyllosilicate signature. These micrometeorites have, instead, experienced an alternative processing history. Evidence outlined in this chapter's results section (4.2, 4.3 and 4.4) suggest that the remaining spectral groups (2, 3, 4 and 5) were subject to progressive thermal reprocessing, most likely during atmospheric entry. This is inferred from the progressive depletion in volatile elements (Fig.4.3) observed among higher spectral groups and increasing Raman R_1 values (suggestive of higher peak temperatures) observed among higher spectral groups (Fig.4.4).

Since phyllosilicates are the dominant mineral phase present in hydrated chondrites (and fine-grained micrometeorites), comprising up to 75% of the matrix by volume (Howard et al., 2009; 2011), the response of phyllosilicate minerals to flash heating will control the petrological evolution of micrometeoroids during atmospheric entry. Phyllosilicate minerals are members of sheet silicate class; at the molecular level, these minerals are composed of parallel, stacked sheets. Each layer is either a tetrahedral silicate sheet or an octahedral hydroxide sheet. Within these sheets, silica tetrahedra or octahedral cation complexes are covalently bonded at their anion corners, forming a repeating series of polymerised 4 or 6 member rings (Bailey, 1966; 1980; Fitzgerald et al., 1996). Between the silicate layers, metal cations balance the collective negative charge, whilst also acting as bridging atoms, holding layers together. Interlayer water (H_2O) molecules are also present in most phyllosilicate species (Bailey, 1966; 1980).

During the early stages of heating, phyllosilicate minerals contract as interlayer water is lost through evaporation, this process is referred to as dehydration (Drits and McCarty, 2007). Continued heating results in the loss of structural water and the collapse of the sheet silicate structure. This process is referred to as dehydroxylation and forms amorphous mineraloids (Wang et al., 2002; Zhang et al.,

2010; Che and Glotch, 2011; 2012). Structural water is held in M-OH bonds present in the octahedral subunits. (Here, the letter M represents a metal cation, typically Al^{3+} in terrestrial phyllosilicates, but substituted for Mg^{2+} or Fe^{2+} in extraterrestrial phyllosilicates (Che and Glotch, 2012)). Condensation reactions consume structural water, leaving isolated silica tetrahedra (Fitzgerald et al., 1996; Che and Glotch, 2011). Further heating will result in annealing of dehydroxlyates and the formation of anhydrous olivine and pyroxene (Che and Glotch 2011; 2012). These recrystallized anhydrous phases are easily distinguishable from primary anhydrous phases owing to their characteristic hyperfine (<1µm) grain sizes observable under SEM-BSE imaging (Greshake et al., 1998), and through the presence of broad, poorly defined reflection peaks in XRD patterns (Tonui et al., 2003; Nakamura, 2005).

Micrometeorites which have experienced phyllosilicate dehydration contain abundant dehydration cracks within their fine-grained matrix (Genge et al., 1997; 2008; Toppani et al., 2001). However, no mid-IR spectroscopic changes are associated with the loss of interlayer water (dehydration) over the 8-13µm wavelength region (Che and Glotch, 2012). Instead, changes are observed at lower wavelengths around 3µm (Feierberg et al., 1985; Campins et al., 2010). As a result, the first spectroscopic changes seen in heated phyllosilicates occurs during dehydroxylation (Che and Glotch, 2012). Once structural water is lost, a sudden change in the mid-IR spectra is observed, characterised by a shift in the primary reflectance peak from 9.5-10µm (present in intact phyllosilicates) to a new reflectance peak, located at 9.0-9.5µm and associated with amorphous dehydroxylates (Hallenbeck, 1998; Che and Glotch, 2012). Although dehydroxylates are amorphous, residual SiO_4 tetrahedra and Si-O-M linkages are retained, reflecting the former layered structure. These remnant bonds are responsible for the 9.0-9.5µm spectral signature (Wang et al., 2002; Madejová, 2003). The formation of a downshifted dehydroxylate peak is a common characteristic of all phyllosilicates species within the 1:1, 2:1 and 2:1:1 classes (Fig.4.6).

Micrometeorites in spectral groups 2 and 3 were found to contain a prominent reflectance peak located between 9.0µm and 9.5µm. Comparisons between the spectra of saponite dehydroxylates collected by Che and Glotch (2012) and the spectra of group 2 and 3 micrometeorites compare favourably (Fig.4.7), implying that the mineralogy of these particles is dominated by amorphous dehydroxylates. The presence of additional peaks located at 10.7µm, 11.5µm and 12.2µm among the group 3 micrometeorites implies that this population contains increased long-range order and a higher degree of crystallinity than the smooth, predominantly featureless spectra seen in the group 2 micrometeorites (Hallenbeck, 1998; Beck et al., 2010; Speck et al., 2011). Increased crystallinity could result from: (1) the group 3 micrometeorites containing more primary anhydrous silicates prior to atmospheric entry than the group 2 micrometeorites (a pre-atmospheric parent body signature). (2) Alternatively, the group 3 dehydroxylates may have begun to recrystallize, annealing into disordered anhydrous phases. (3) Conversely, these spectral differences may simply arise as a result of terrestrial weathering. Since the majority of the group 3 micrometeorites are collected from the Cap Prudhomme site, while all the group 2 micrometeorites are from the TAM collection, it is possible that the enhanced weathering affecting the TAM micrometeorites may have resulted in further breakdown

and amorphization of the dehydroxylate phases in these particles. Differences in peak temperature between the two spectral groups can, however, be ruled out. This is because the average R_1 Raman parameters for both groups are indistinguishable (at R_1=0.4-0.8), suggesting that both groups experienced similar peak temperatures.

The presence of magnetite and igneous rims enclosing a fine-grained matrix hosting abundant dehydration cracks provide textural evidence of atmospheric entry reprocessing in both group 2 and 3 micrometeorites. The combined average R_1 value for this population (R_1=0.61) is raised above the R_1 values of the unheated CM/CI chondrites (R_1=0.4-0.6); suggesting these micrometeorites have experienced additional high temperature processing, above the range associated with CM chondrites (>300°C, Bunch and Chang, 1980; Rubin et al., 2007; Busemann et al., 2007). Mild depletions in highly volatile Cl and corresponding enrichments in more refractory elements (such as Mg and Mn) support this conclusion. The temperature of dehydroxylation in experimentally heated phyllosilicate standards was empirically constrained between ~300°C (for 1:1 serpentine) and 700°C (for 2:1 saponite) (Che and Glotch, 2012). This temperature range agrees well with peak temperature estimates for dehydroxylation reactions in C2 chondrites (Tonui et al., 2003; 2014; Nozaki et al., 2006). As a result, the group 2 and 3 micrometeorites most likely experienced moderate thermal reprocessing during atmospheric entry, above the temperature range expected on their C-type parent body, but significantly below the melting solidus of chondritic matrix.

Fig.4.6. Mid-IR reflectance spectra comparing hydrated and dehydroxylated phyllosilicates taken from Che and Glotch (2012).

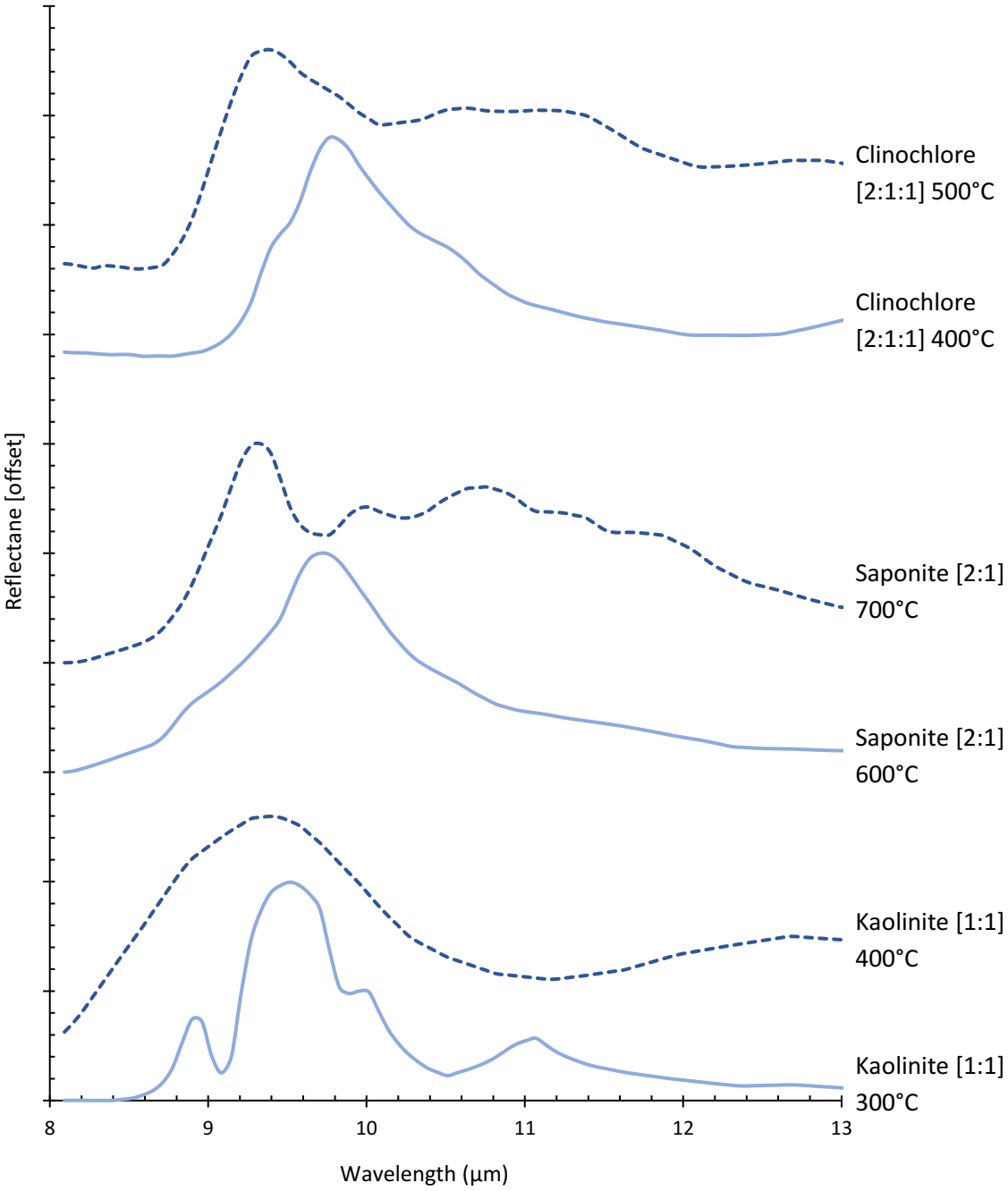

Fig.4.7. Mid-IR reflectance spectra comparing saponite dehydroxylates against group 2, 3 and 4 spectral classes.

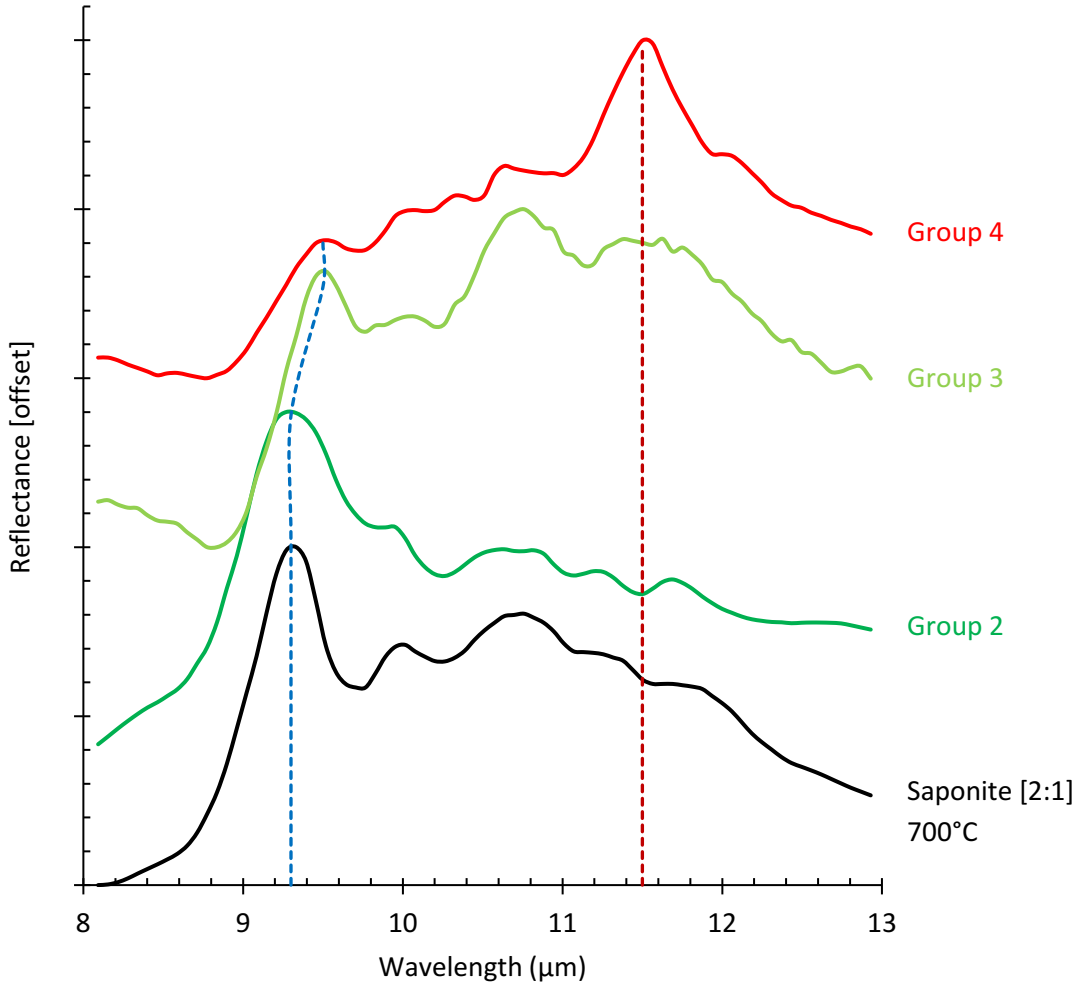

Group 4 micrometeorites also contained the dehydroxylate peak in their spectra; however this was a minor feature in their spectral profile. Instead, a red-slope and prominent reflectance peak at 11.5µm are the dominant features in this group. The position of this primary absorption band is identical to the primary peak seen in the spectra of olivine (Koike et al., 2006) and likewise is shouldered by peaks at 10.7µm and 12.2µm. The occurrence of anhydrous olivine and the simultaneous retention of dehydroxylates indicates that the group 4 micrometeorite population contain a partially recrystallized matrix. The relative heights of these peaks should reflect relative proportions of olivine and dehydroxylate remaining in the matrix (Thomson and Salisbury, 1993). For anhydrous olivine to form, the amorphous dehydroxylates must anneal (Hallenbeck, 1998; Tonui et al., 2003; Nakamura, 2005) and this requires higher peak temperatures or longer duration heating than the thermal reprocessing experienced by group 2 and 3 micrometeorites. Progressively higher R_1 values (0.5-1.0) and significant depletions in volatile Cl and corresponding enrichments in more refractory Mn and Mg confirm that group 4 micrometeorites have endured higher temperature atmospheric reprocessing. The onset of dehydroxylate recrystallization in hydrated chondrites occurs at ~700°C and therefore provides a minimum peak entry temperature for these micrometeorites (Akai, 1992; Nozaki et al., 2006).

The spectra of group 5 micrometeorites appear identical to the spectra of crystalline olivine (Koike et al., 2006). The lack of the distinctive dehydroxylate peak, seen in groups 2, 3 and 4, suggests that group 5 particles have experienced complete recrystallization of their matrix phyllosilicates into secondary anhydrous phases. Annealing in the solid-state has, therefore, produced a metamorphic olivine groundmass. This olivine is unlikely to be a primary constituent, inherited from the parent body, because group 5 micrometeorites show the greatest enrichment in Mn and Mg and reciprocal depletions in Cl; as well as the highest R_1 parameters. Correspondingly, geochemical and Raman evidence require a high temperature processing history.

Despite recrystallization, the majority of the micrometeorites in group 5 retain their pre-atmospheric parent body textures, allowing their classification as either C1 or C2 subtypes (see section 3.2). In addition, the retention of dehydration cracks in the majority of particles, despite the lack of phyllosilicates to host these cracks, ensures that earlier, lower grade thermal decomposition signatures are preserved. Furthermore, the presence of relict dehydration cracks in an anhydrous micrometeorite provides convincing textural evidence of a hydrated, phyllosilicate-rich precursor.

The ability to distinguish relict clasts, dehydration cracks and geochemical variations among the recrystallized groundmass of group 5 particles demonstrates that minimal diffusion or homogenisation occurs during annealing. Because atmospheric entry processes are rapid (<10 seconds, Love and Brownlee, 1991), kinetic effects prohibit the migration of elements over micron length scales by solid-state diffusion (Fabian et al., 2000; Grossman and Brearley, 2005). Therefore, phyllosilicate thermal decomposition during atmospheric entry does not entirely overprint parent body features. However, if entry temperatures are sustained above 700°C, continued annealing will result in a progressively increasing grains size and increasing crystallinity within the olivine groundmass (Hallenback, 1998; Fabian et al., 2000). Eventually pre-atmospheric textures will be entirely overprinted. Peak temperatures above 1350°C result in melting (Toppani et al., 2001) and the formation of partially melted scoriaceous micrometeorites. Higher temperatures (>1500°C, Toppani et al., 2001) lead to complete melting and the formation of igneous olivine in cosmic spherules. Mesostasis mineralogy in micrometeorites is dominated by olivine (Taylor et al., 2012) and consequently, mid-IR spectroscopy is no longer able to distinguish between the different classes of cosmic spherule and therefore, stages of entry reprocessing (Fig.4.1).

4.6. Discussion: micrometeorite survival and atmospheric entry biases

Phyllosilicate minerals are subdivided into classes, dependent on their sheet structure (Bailey, 1980). In 1:1 phyllosilicates, such as serpentine, repeating layers are formed by alternating tetrahedral silicate sheets and octahedral hydroxide sheets – these minerals lack interlayer water (Bailey, 1980; Che and Glotch, 2012). Conversely, in 2:1 phyllosilicates, such as saponite, a single octahedral sheet is sandwiched between 2 tetrahedral silicate sheets. In these minerals interlayer water is located between each 3-layer macro-sheet (Fig.4.5 and Bailey, 1980; Che and Glotch, 2012). This disparity in composition has important implications for the response of phyllosilicate minerals to entry heating.

Pyrolysis experiments on clay standards demonstrate that 2:1 phyllosilicates can withstand significantly higher peak temperatures than 1:1 phyllosilicates, before dehydroxylation occurs (Che and Glotch, 2011; 2012). This is because 2:1 phyllosilicates must first dehydrate (losing interlayer water) before they dehydroxylate (losing structural water) while, 1:1 phyllosilicates, which contain no interlayer water, begin thermal decomposition directly by dehydroxylation reactions at temperatures as low as 300°C (Che and Glotch, 2011; 2012). Therefore, the larger water reservoir in saponite minerals ensures that the same dehydroxylation reactions do not occur until peak temperatures >700°C are reached (Che and Glotch, 2011; 2012). This difference in temperature thresholds between 1:1 and 2:1 phyllosilicates was explored by Nozaki et al., (2006) and Akai, (1992) within the context of thermally metamorphosed and experimentally heated carbonaceous chondrites. Although the precise temperature thresholds of dehydroxylation vary between studies, a common observation is that CI chondrites, containing saponite, are significantly more heat resistant than CM chondrites, containing serpentine (Akai, 1992; Nozaki et al., 2006). Although CM chondrites (and C2-fine-grained micrometeorites) contain serpentine-like phyllosilicates (antigorite and greenalite) which do contain some interlayer water, this is significantly less than the water content found in true 2:1 phyllosilicates (Browning et al., 1996; Tomeoka et al., 1989; Velbel and Palmer, 2011) The presence of interlayer water in both C1 and C2 particles ensures that both can develop dehydration cracks during entry.

In addition to the phyllosilicate species, the cation chemistry of the host phyllosilicates is also important in defining how a micrometeoroid evolves during flight. Because solid-state diffusion is limited, recrystallized olivine in group 5 micrometeorites will inherit the cation composition of their former phyllosilicate parents. This means that Mg-rich phyllosilicates recrystallize as forsterite while Fe-rich phyllosilicates recrystallize as fayalite. Subsequently, with continued heating, these recrystallized group 5 micrometeorites will melt, forming igneous olivine. The onset of melting is defined by the solidus of the groundmass,[1] which itself is dependent on the cation chemistry of the host olivine. Fayalite end-members melt at ~1200°C, while the forsterite end-member melt at ~1900°C. The cation composition of the recrystallized metamorphic olivine will, therefore, control the peak temperature at which melting begins. Consequently, Mg-rich micrometeorites are significantly more likely to survive atmospheric entry unmelted than Fe-rich micrometeorites.

The degree of aqueous alteration on the parent asteroid controls both the phyllosilicate species and the cation chemistry of the minerals (McSween, 1979; 1987; Rubin et al., 2007; Howard et al., 2009; 2011). With increasing alteration phyllosilicates evolve from Fe-bearing serpentine towards Mg-rich saponite (Howard et al., 2009; 2011). Thus, the probability of survival as an unmelted particle is partially dependent on the parent body source. On the basis of these arguments, intensely aqueously altered CI-like, Mg-rich and saponite-bearing micrometeorites should be overrepresented among

[1] Since atmospheric entry heating is rapid, the onset of melting occurs under disequilibrium conditions, therefore the matrix solidus (a function of particle mineralogy and composition) only partially controls melting. Instead, the rate of heating transfer from the particle's exterior to the interior is also important. This factor is a function of grain density, conduction coefficients, the presence of water and the flow of volatile gases. Heat transfer and melting in micrometeorites is discussed in further detail in section 5.

micrometeorite collections. Conversely, mildly altered Fe-cronstedtite-bearing and CM-like micrometeorites should preferentially melt and form cosmic spherules. However, since C2 particles with genetic affinities to CM chondrites are significantly more abundant than C1 particles (Taylor et al., 2012), the present flux of micrometeorites must be dominated by CM-like parent sources. This conclusion is consistent with observations from larger size fractions of extraterrestrial material. The relative proportions of CM:CI chondrites recovered from the Earth's surface reveal that CM chondrites (representing ~43% of the total carbonaceous chondrite population) are significantly more abundant than CI chondrites (representing just 13% of the total carbonaceous chondrite population) (Burbine et al., 2002).

Fig.4.8. BSE image panel illustrating 5 of the anomalous fine-grained micrometeorites from spectral group 5. Magnetite rims form only a partial covering and igneous rims are absent. Dehydration cracks may be present, as in CP94-050-060 and variations in the Z value of the matrix reflect a variable Mg/Fe cation composition over short distances, this is characteristic of CM lithologies and C2 fine-grained micrometeorites. Anhydrous olivines are common and some grains contain reduced metal droplets. The spectral profiles of these particles suggest their matrix has experienced complete recrystallization and consists of hyper-fine anhydrous olivine crystallites, however the Raman R_1 values of these grains are characteristic of only modestly heated chondritic materials, retaining a disordered carbonaceous signature. These two observations are contradictory, and not immediately reconcilable, possible explanations for this disparity are considered in the discussion section 4.8.

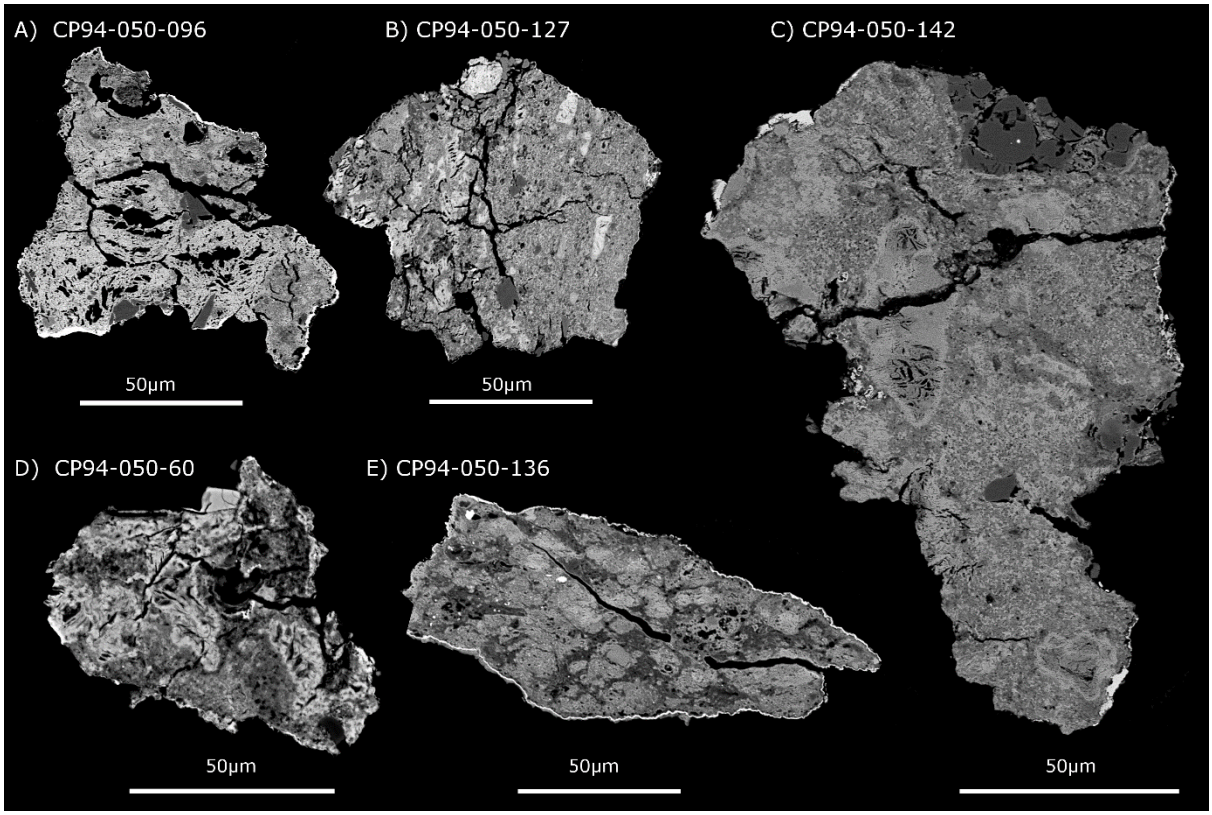

Fig.4.9. Bulk compositions (Mg vs. Fe abundances) of group 5 fine-grained micrometeorites, calculated by EMPA. The anomalous particles (larger dark black and labelled) tend to show higher Fe concentrations than their counterpart group 5 micrometeorites with higher R_1 values. This suggests that Fe-enriched micrometeorites are more susceptible to heating and will undergo annealing reactions at lower temperatures than Mg-rich particles. As with previous plots in this chapter symbols with solid fill denote C2-fine-grained micrometeorites, open symbols denote C1-fine-grained micrometeorites and grey-infilled symbols are scoriaceous micrometeorites.

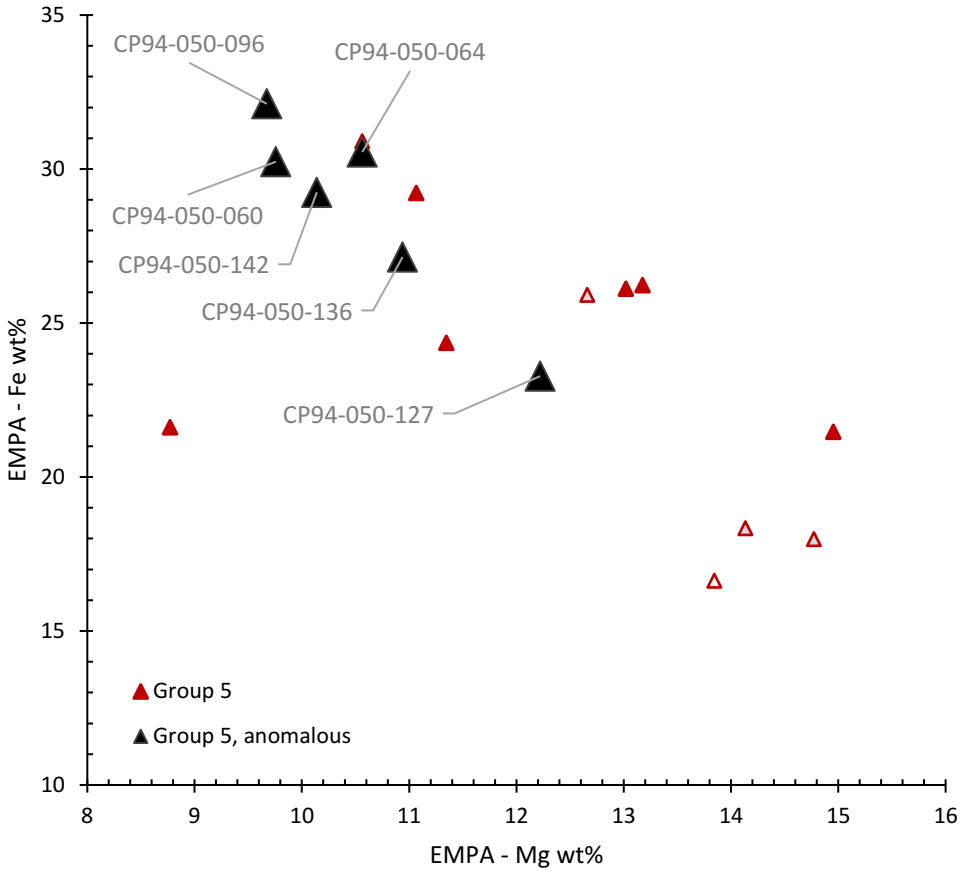

4.7. Discussion: dehydroxylation of micrometeorites in space

Six micrometeorites from group 5 were identified as anomalous (section 4.4). These particles have low R_1 Raman peak parameter values, inconsistent with their mid-IR spectra, which suggested high temperature processing during atmospheric entry, with peak temperatures >800°C and most likely >1350°C. At such high temperatures, disordered carbonaceous phases become intensely thermally reprocessed, forming ordered, carbonaceous macromolecules and ultimately crystalline graphite (Ferrari and Robertson, 2000). The Raman spectra of such high temperature materials often show high R_1 values characterised by sharp D and G bands (FWHM<100cm^{-1}) of approximately equal height (Rahl et al., 2005; Bonal et al., 2006 and others). However, the R_1 peak parameters for these 6 anomalous micrometeorites are relatively low (R_1<0.62) and have relatively wide bands (FWHM~110cm^{-1}) and are therefore, more similar to the Raman spectra of other less-heated micrometeorites, found in groups 2, 3 and 4. Under SEM-BSE imaging (Fig.4.8), these anomalous micrometeorites contain dehydration cracks. Partial magnetite rims mantle most particles, while igneous rims are absent. By contrast, the

majority of the main group 5 population have well-developed igneous rims, complete magnetite rims, and typically contain a vesicular matrix, hosting abundant micron-scale voids, formed by the degassing of volatiles (Taylor et al., 2011). Therefore, both the petrographic and Raman data suggest that the anomalous particles have experienced only moderate thermal reprocessing, at lower peak temperatures, than the main group 5 population. Despite this moderate heating, all of the group 5 micrometeorites are united by a common petrographic evolution; having originally contained phyllosilicates (shown by the presence of dehydration cracks) that later dehydroxylated and recrystallized as anhydrous phases.

During atmospheric entry the surface layers in hydrated, phyllosilicate-bearing micrometeorites melt. With continued heating, this melt layer expands, consuming the unmelted core (Genge, 2006; Genge et al., 2017b). The loss of water, both in dehydration and dehydroxylation reactions, expends much of the available incoming heat energy and results in significant thermal gradients (>200Kμm^{-1}, Genge et al., 2017b). The presence of hydrated minerals, therefore, slows the progress of the thermal front and can lead to the preservation of an unmelted core (section 5, see and Genge and Grady, 2000; Genge et al., 2017b). Conversely, small (<100µm diameter) anhydrous micrometeorites cannot maintain thermal gradients (Genge et al., 2017b) and instead, experience rapid, uniform heating (Love and Brownlee, 1991). Since all six of the anomalous micrometeorites lack igneous rims, these particles cannot have contained hydrated phyllosilicates when they entered the Earth's atmosphere. Instead, the anomalous population must have experienced in-space dehydroxylation, forming anhydrous particles prior to entry.

Although igneous rims are absent, magnetite rims are found on all the anomalous particles. Since magnetite rims develop by the melting, evaporation, oxidation and subsequent recrystallization of the refractory-enriched melt at low altitude (Toppani et al., 2001), magnetite rims do not require the presence of hydrated phases and are commonly present on anhydrous coarse-grained micrometeorites (Genge et al., 2005; 2008). Therefore, the presence of magnetite rims on the anomalous particles confirms that these are true micrometeorites, dust particles in space, and were later subject to atmospheric entry heating, melting and oxidation.

In space dehydroxylation of the phyllosilicate matrix requires the anomalous micrometeorites to have a two-stage thermal history. The initial phase of heating would have been sufficient to cause phyllosilicate decomposition, and potentially, recrystallization. Such a heating event could have occurred either on the parent asteroid or during shock-induced liberation (Tomioka et al., 2007). Later, a second phase of heating resulted in the development of an oxygen-bearing magnetite rim and increased thermal processing. For this scenario to be viable, carbonaceous matter would have to survive both episodes of heating. In this study disordered carbonaceous matter was detected within the matrix of Jbilet Winselwan, a thermally metamorphosed CM chondrite (400°C<PMT<600°C), containing dehydrated phyllosilicates (Zolensky et al., 2016). Likewise, several high-temperature (>600°C) CM chondrites are now known (Tonui et al., 2003; 2014; Nakamura, 2005; 2006; Nakato et al., 2008; Lee et al., 2016), many of which contain detectable carbonaceous phases (Quirico et al.,

2003; Bonal et al., 2006). Therefore, the survival of disordered carbonaceous phases during moderate thermal metamorphism is a realistic scenario (Nakato et al., 2013). Subsequent flash heating as micrometeorites enter the atmosphere must also be modest, with low entry angles (<10°), low entry speeds (~11kms^{-1}) and entry directions with the rotation of the planet, in order to preserve peak temperatures <700°C (Love and Brownlee, 1991; Genge, 2016a). Since these entry conditions are rare, the number of in-space dehydroxylated micrometeorites that survive entry unmelted, must be small.

The six anomalous micrometeorites have higher Fe concentrations than most, but not all, of the main group 5 population (Fig.4.9). This suggests their original phyllosilicate species was Fe-cronstedtite. Since Fe-bearing 2:1 phyllosilicates are the most susceptible to thermal decomposition (~300-400°C) annealing and melting (700°C), the peak temperatures required for mineralogical evolution are low further promoting the probability of carbonaceous matter survival.

Given the evidence outlined: (1) unusually low R_1 Raman values - suggesting relatively low (<800°C) peak temperatures, (2) Fe-rich bulk compositions – resulting in an enhanced susceptibility to thermal decomposition and melting and (3) the absence of igneous rims – which implies the anomalous micrometeorites were anhydrous prior to atmospheric entry; it is highly likely that the anomalous group 5 particles represent dehydroxylated CM-like chondritic dust derived from the regolith of a C-type asteroid.

4.8. Conclusions from mid-IR spectroscopy

This chapter discussed the thermal decomposition of hydrous phases within Antarctic micrometeorites during atmospheric entry. By collecting mid-IR spectroscopic data from a large population of Antarctic micrometeorites and several carbonaceous chondrite "reference standards", the bulk matrix mineralogy of all samples could be resolved, revealing a progressive sequence of thermal decomposition (Fig.4.10) whose evolution is identical in both CM and CI-like micrometeorites. Despite this similarity, differences in the dominant phyllosilicate species (1:1 vs. 2:1) produce differences in the interlayer and structural water content, as well as the nature of their cation complement, between CM and CI-like particles. These factors prove critical in determining the threshold temperature of thermal decomposition. As a result, atmospheric entry should bias the survival of micrometeorites in favour of CI-like material. However, contrary to this hypothesis, empirical evidence demonstrates that C2/CM-like micrometeorites are considerably more abundant and must, therefore, dominate the current dust flux.

The presence of a distinctive, and to date unreported, dehydroxylate peak in 29% of unmelted micrometeorites emphasises how the conversion of matrix phyllosilicates to dehydroxylates is an important intermediate stage in the thermal evolution of all hydrated chondritic materials; whether this is during flash heating via atmospheric entry or during thermal metamorphism on the parent asteroid. Because dehydroxylates are metastable over a wide temperature range (~300°C-800°C), the early stages of thermal decomposition in hydrated micrometeorites are dominated by the geochemical behaviour of these understudied mineraloid phases. Furthermore, since the regolith

material covering the surfaces of C-type asteroids are expected to have endured significant heating (Ostrowski et al., 2010; Matsuoka et al., 2015) future spectroscopic investigations, over mid-IR wavelengths, may therefore, expect to identify absorption bands at 9.0-9.5µm in asteroid spectra, which are associated with dehydroxylated phyllosilicates.

Finally, although the majority of fine-grained micrometeorites enter the atmosphere as hydrated particles (Nakamura et al., 2001; Noguchi et al., 2002; Genge, 2006; 2017a) this study revealed that at least some micrometeorites are dehydroxylated in space. These rare, anomalous particles are most likely samples of C-type asteroid regolith, and therefore, complement the increasing collections of thermally metamorphosed C2 chondrites (Nakato et al., 2013; Zolensky et al., 2014; 2016).

Fig.4.10. Summary plot: The mid-IR spectral evolution of hydrated fine-grained micrometeorites during atmospheric entry. Despite compositional differences between CM and CI-like fine-grained micrometeorites both groups follow the same generic spectral decomposition pathway defined by the stability of phyllosilicate phases and dependent on their composition and cation chemistry. Dashed grey lines show the positions of the main Reststrahlen band reflectance peaks present in heated micrometeorites.

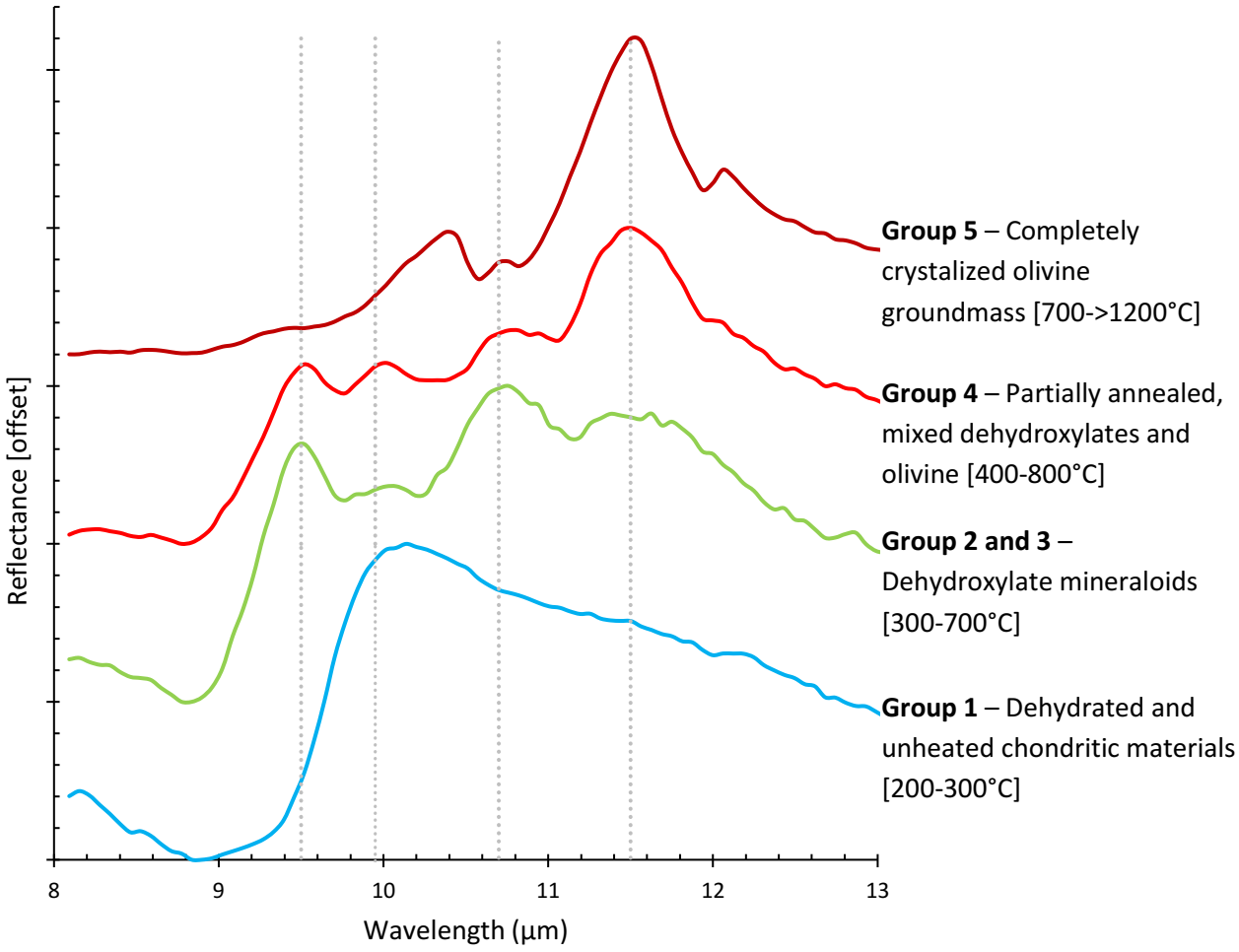

Chapter 5: Implications from Raman spectroscopy

5.0 Overview – Raman spectroscopy provides a means of investigating the thermal decomposition of fine-grained micrometeorites. This technique is ideal for the analysis of small samples and short duration heating and is, therefore, suitable for investigating atmospheric entry processes affecting cosmic dust. By combining textural data with spatially resolved Raman transects this study reveals how entry heating alters the carbonaceous phases within micrometeorites.

Previous studies argue that the migration of thermal gradients inwards, controlled by the dehydration and subsequent melting of phyllosilicates, is the primary mechanism by which micrometeorites are heated. In this study, spatially resolved Raman spectroscopy is used to analyse the disorder of carbonaceous matter and, thus, infer the peak temperatures attained across individual micrometeorites. The use of 1D transects allows thermal profiles through micrometeorites to be constructed. These data confirm that most micrometeorites support conduction-driven core-to-rim thermal gradients. However, some particles - notably those containing vesicular matrix – show erratic thermal gradients and, instead, contain graphitized carbon, indicating temperatures in some parts of the micrometeorite exceeded 900°C.

By contrast, several unmelted micrometeorites, with zoned Raman profiles, preserve unheated carbonaceous matter in their cores. These pre-atmospheric signatures suggest that fine-grained micrometeorites experienced low grade thermal metamorphism whilst on their parent asteroids, with peak temperatures <300°C; this is analogous to temperature estimates from unheated CM2 chondrites.

5.1 Raman spectroscopy as an analysis tool for extraterrestrial materials

Raman spectroscopy is non-destructive at low laser powers, independent of mineralogical context and provides micron-scale spatial resolution (Amri et al., 2005). Consequently, Raman is an attractive analytical technique for the study of small, valuable and mildly heated samples. Experimental pyrolysis studies on organic matter from the CM2 chondrite Murchison have demonstrated that Raman spectroscopy is most effective at tracing short duration, high temperature heating events and is, therefore, ideally suited to the analysis of flash heating effects during atmospheric entry (Muirhead et al., 2012).

However, relatively few previous studies have analysed the carbonaceous phases within micrometeorites using Raman spectroscopy (Suzuki et al., 2010; Dobrică et al., 2011). Dobrică et al., (2011) demonstrated a continuum in peak parameter space between fine-grained and ultra-carbonaceous micrometeorites, which implies that both asteroids and comets inherited similar organic matter. Their study also analysed partially melted scoriaceous micrometeorites, some of which retained residual carbonaceous matter that plotted outside the unmelted micrometeorite field. Since scoriaceous micrometeorites typically experience peak temperatures >1000°C (Toppani & Libourel, 2001) it is surprising that carbonaceous phases are preserved at all. However, the retention

of carbonaceous matter may allow the peak temperatures and spatial distribution of heating within affecting micrometeorites to be determined.

This thesis expands on the previous work using Raman spectroscopy to the study of fine-grained micrometeorites with complex thermal histories. Unmelted fine-grained micrometeorites may preserve both signals of parent body metamorphism and atmospheric entry flash heating in their Raman signatures. Micrometeorites are already known to support thermal gradients, evident from the presence of igneous rims, increasing Fe/Si and Mn/Si ratios towards particle rims (Toppani & Libourel, 2001; Genge, 2006) and thermally fractured Mg-silicate crystals, located at the particle margins (Genge et al., 2017b). Therefore, some unmelted fine-grained micrometeorites, with relict cores that experienced lower peak temperatures may retain organic matter, documenting their pre-atmospheric parent body metamorphic history, and this may be observable in their Raman spectra. To test this hypothesis, Raman spectra were collected from a large population of Antarctic micrometeorites and compared to CM2 chondrites. In addition, core-to-rim line transects through 8 micrometeorites were obtained, utilising the micron-scale resolution of Raman to record heating gradients and identify, where possible, parent body signals.

5.2 Data processing of raw Raman spectra

Carbonaceous Raman spectra are, to a first order approximation, composed of two bands, a 'G' and 'D' band. However, this doublet feature can be deconvolved into five smaller bands, $D_{1\text{-}4}$ and G_1, each associated with a different vibrational mode of the carbon skeleton, as outlined in Beyssac et al., (2003), Ivleva et al., (2007), Sheng, (2007) and Brunetto et al., (2009). In highly disordered carbonaceous materials, all five peaks are broad, overlapping and low intensity; therefore, reconstruction of all bands as independent features carries high uncertainties. In this study, only the most prominent bands: D_1 and G_1 are reconstructed. The fitting procedure is shown in figure 5.1.

Raw Raman spectra were reduced to their component spectral parameters. A baseline was subtracted using a 6th order polynomial, fitted to the fluorescence background between 700-2000cm^{-1}, omitting the central domain occupied by the absorption bands (1225-1725cm^{-1}). This baseline removal procedure is similar to other non-linear methods, such as the cubic splines or synthetic polynomial fits employed by Kostecki et al., (1997), Muñoz Caro et al., (2008) and Quirico et al., (2014). The signal to noise ratio was improved using an exponential smoothing function:

$$S_t = \alpha X_t + (1 - \alpha) S_{t-1} \qquad \text{- Eq.5.1}$$

Where:

- S_t = smoothed data point
- X_t = unsmoothed, original data point and,
- α = smoothing factor, in this study set to a value of 0.95

Smoothing had the effect of introducing a phase shift, moving the absolute peak positions to higher Raman shift values; this is an expected consequence of any smoothing function and is normally

corrected by shifting the smoothed spectrum down by half a window length for symmetric kernels. However, the necessary correction value for exponential smoothing functions remains a matter of debate (Nahmias & Olsen, 2015). Therefore, after comparing the peak positions of the smoothed and unsmoothed spectra and using a random sample of forty spectra, a downshift of 25cm^{-1} was selected. Since this study does not explicitly consider peak positions in the analysis of the Raman data, the smoothing artefact does not directly affect the conclusions of this study.

Figure 5.1 Processing Raman spectra with a LWBF fitting model. Raw Raman spectra carry a high degree of noise (top plot: black line) and, therefore, require processing before band parameters can be extracted. (1.) The baseline is removed with a 6th order polynomial (top plot: blue line), then (2.) the spectra is smoothed (bottom plot: black line) using an exponential smoothing algorithm with an alpha smoothing value of 0.95. The resulting profile (bottom plot: black line) is (3.) modelled by combined shape profiles (bottom plot: light and dark green lines for individual models, lorentzian and breit-wigner-fano model, respectively. The bold orange line represents the cumulative model). The residual is recorded below (as a dashed red line) and used to calculate the RSS fitting error. Spectra with RSS>2.5 or spectra whose fitting model did not converge were rejected. (4.) The band parameters are then recorded for each shape profile.

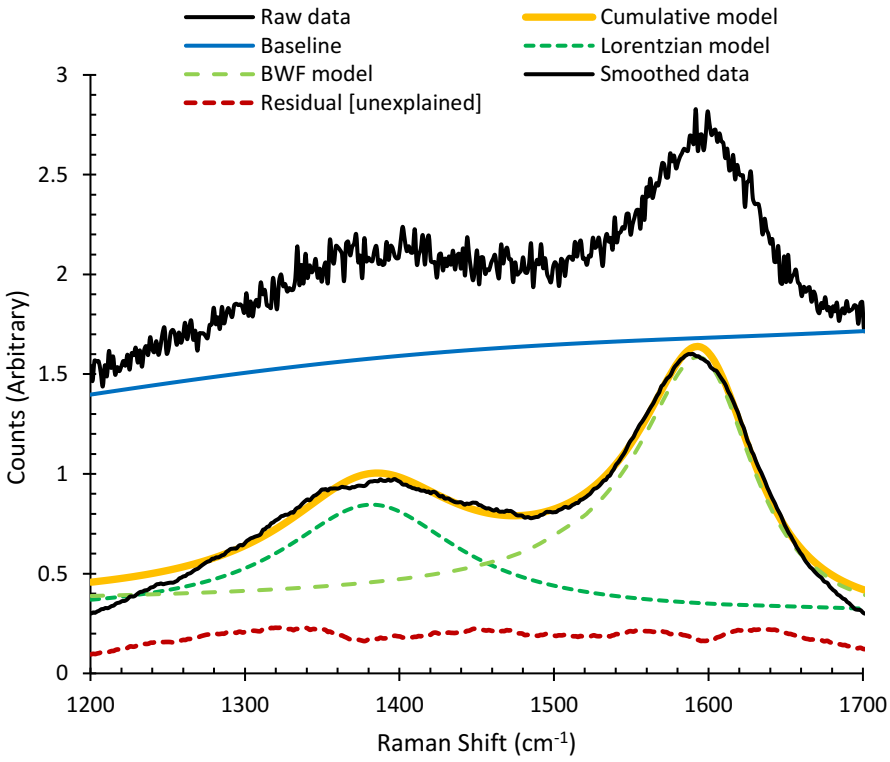

Peak deconvolution was performed using the conventional two-part Lorentzian-Breit-Wigner-Fano (LBWF) distribution, which is a common fitting model for the analysis of meteoritic carbonaceous Raman spectra. The base of modelled peaks was fixed such that peak area could not extend below the baseline. Levenberg-Marquardt algorithms were used in the fitting procedure to match the modelled shape profiles to the empirical spectra (Pujol, 2007). The reduced chi-squared statistic (obtained by dividing the residual sum of squares (RSS) by the degrees of freedom) was used as a fitting metric during modelling and required to converge in less than 500 iterations. Approximately 11% of models did not converge and the resulting spectra were rejected, on examination these were typically spectra

dominated by background florescence or contaminated by cosmic rays. The RSS error statistic was used as a measure to determine the goodness-of-fit and recorded for each spectrum. An arbitrary cut-off threshold of RSS>2.5 was chosen; models whose RSS was greater than this were rejected, which resulted in rejection of a further ~5% of spectra. Parameters from multiple analyses were averaged and the standard error of the mean calculated for each sample.

Because counting statistics and signal-to-noise ratios for individual spectra depend heavily on operating conditions, including laser intensity, laser wavelength, acquisition time, surface texture, focus, ambient (visible) light etc., this study employed comparative metrics (ratios, denoted by R_1 and R_2) to provide a fair comparison between and within samples. Both height and area ratios were calculated as outlined in Beyssac et al., (2002) and Rahl et al., (2005):

$$R_1 = I_{D1}/I_{G1} \quad \text{– Eq.5.2}$$

Where:
I_X = the height intensity of the band, specified by the subscript

$$R_1 = D_1/(G_1 + D_1) \quad \text{– Eq5.3}$$

Where:
All values are given as band areas

5.3 Results: The Raman spectra of Antarctic micrometeorites

5.3.1 Average peak parameters

All samples produced Raman spectra containing carbonaceous 'G' and 'D' bands, a selection of which are displayed in figure 5.2. The fluorescence background was highly variable, recording between 10^2-10^5 counts per sample. By fitting a 6th order polynomial to the fluorescence baselines, subtle peaks preserved in scoriaceous micrometeorites could be resolved. All spectra are asymmetric, with a sharper 'G' band and a lower, broader 'D' band (Figs. 5.1 and 5.2). For scoriaceous micrometeorites both bands are approximately equal height, while primitive chondrites and most fine-grained micrometeorites have taller 'G' bands than 'D' bands. As 'D' band height approaches the 'G' band height count statistics decrease, and higher signal-to-noise ratios were recorded, consequently, spectra with higher R_1 ratios tend to carry greater uncertainties.

A positive correlation exists between band height (R_1) and band area (R_2) ratios (Fig.5.3). This is described by a linear regression line for the carbonaceous chondrites and a 2nd order polynomial regression line for the fine-grained micrometeorites. Except PCA 02012, the entire carbonaceous chondrite population plots within a restricted region of R_1-R_2 space, with R_1<0.6 and R_2<0.4. Conversely, the thermally metamorphosed CM2 chondrite PCA 02012 is offset from the chondrite field to higher R ratios, at approximately R_1=0.9, R_2=0.45. The Raman peak parameters for the chondrite population, therefore, do not appear to correlate with either petrologic type or compositional class (e.g. CM2 versus CI). By contrast the micrometeorite population spans a wide range of R_1-R_2 space with the majority of fine-grained and scoriaceous particles plotting between

the chondrite field and the position of PCA 02012. A single micrometeorite, CP94-050-054 plots above PCA 02012 with higher R ratios at ~R_1=1.04, R_2=0.56. Interestingly, CP94-050-160, a C2-fine-grained micrometeorite also plots close to CM2 Cold Bokkeveld in both Fig. 5.3 and 5.4.

When band height ratio (R_1) is compared against the full width half maximum (FWHM) of the D band a similar relationship is observed. The carbonaceous chondrites plot as a relatively tight group, with a weak negative correlation (Fig.5.4). However, PCA 02012 remains separate from the carbonaceous chondrite group, owing to its high R_1 ratios, but demonstrates similar FWHM-D widths to other chondrites. Despite similar peak widths, the majority of the micrometeorite population, including all scoriaceous micrometeorites, are offset or *scattered* from the carbonaceous chondrite field, again resulting from higher R_1 ratios. The FWHM-D values for micrometeorites range from ~110-135cm^{-1}. The values presented in figures 5.3 and 5.4 are the average deconvolved spectral parameters for each sample, this data is displayed numerically in Table 5.1 (see Sect. 5.11, the chapter appendix).

Fig.5.2 Average Raman spectra for selected samples, illustrating the diversity in 'G' and 'D' band profiles. Spectra have been scaled between 0-1 and ordered by increasing 'D' band height. Error bars represent 1 standard deviation from the mean.

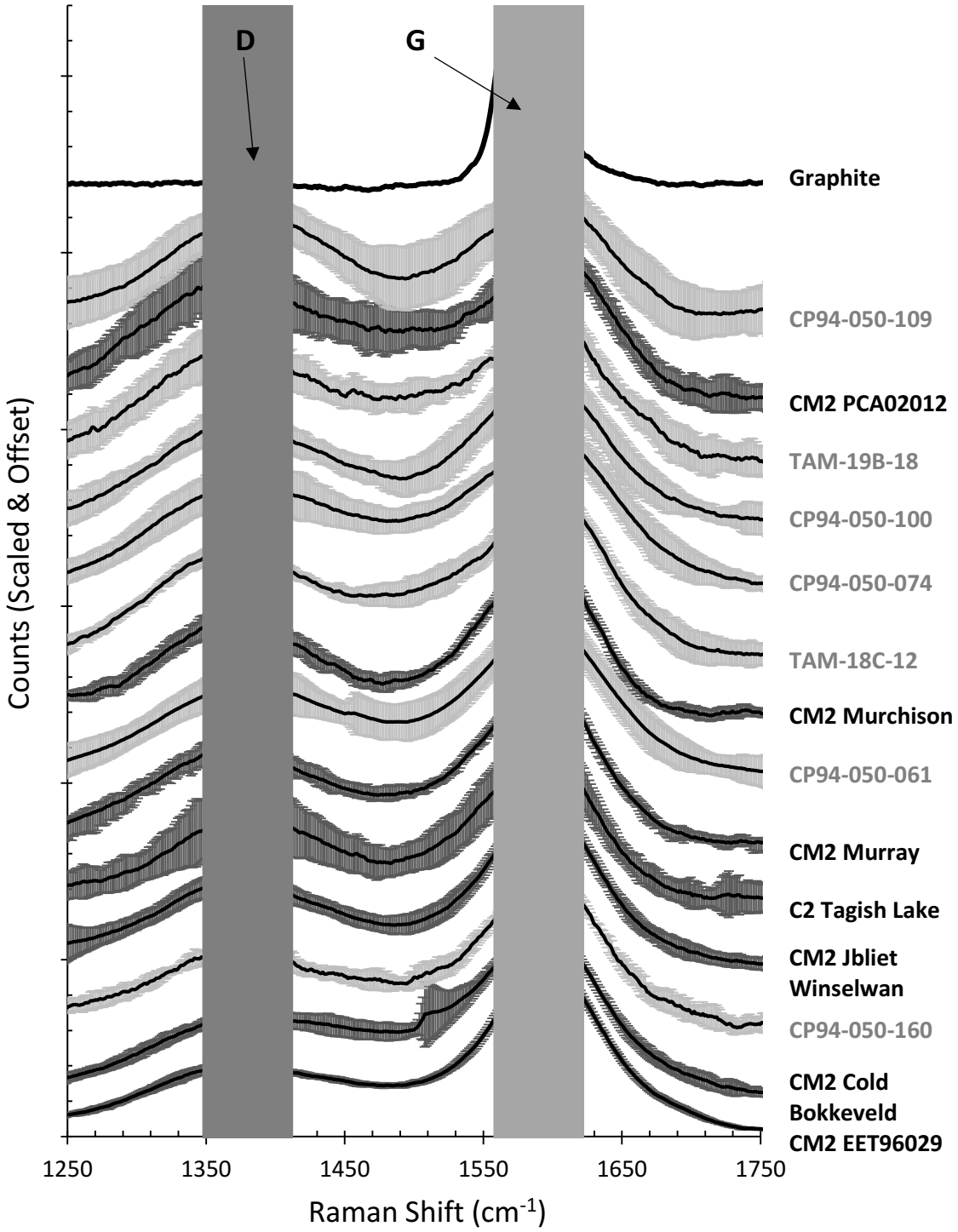

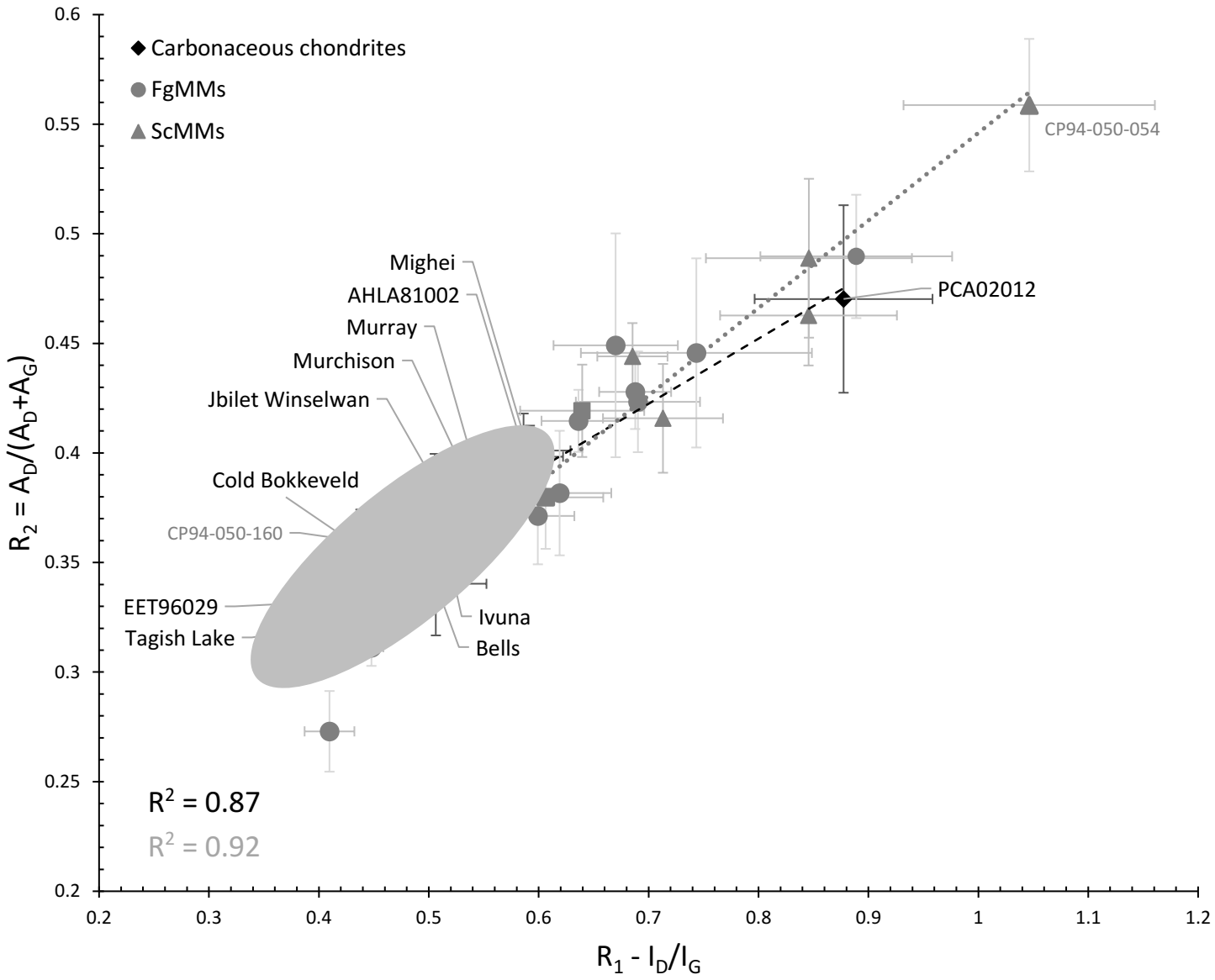

Fig.5.3 Average Raman spectral parameters – R_1 vs R_2.

The average spectral parameters for each sample are plotted, error bars show the standard error of the mean and reflect a sample's variance. Samples are distinguished by different symbols with diamonds representing chondrites, open circles for C1-FgMMs, solid circles for C2-FgMMs, squares for Fg-ScMMs and triangles for ScMMs. Both carbonaceous chondrites and FgMMs plot along similar linear regression lines, exhibiting a positive correlation between band height and area. Between 4 and 6 FgMMs plot within the chondrite domain (highlighted in grey) while the majority of the MMs have higher R_1 values, several grains show similar R_1 values as PCA02012.

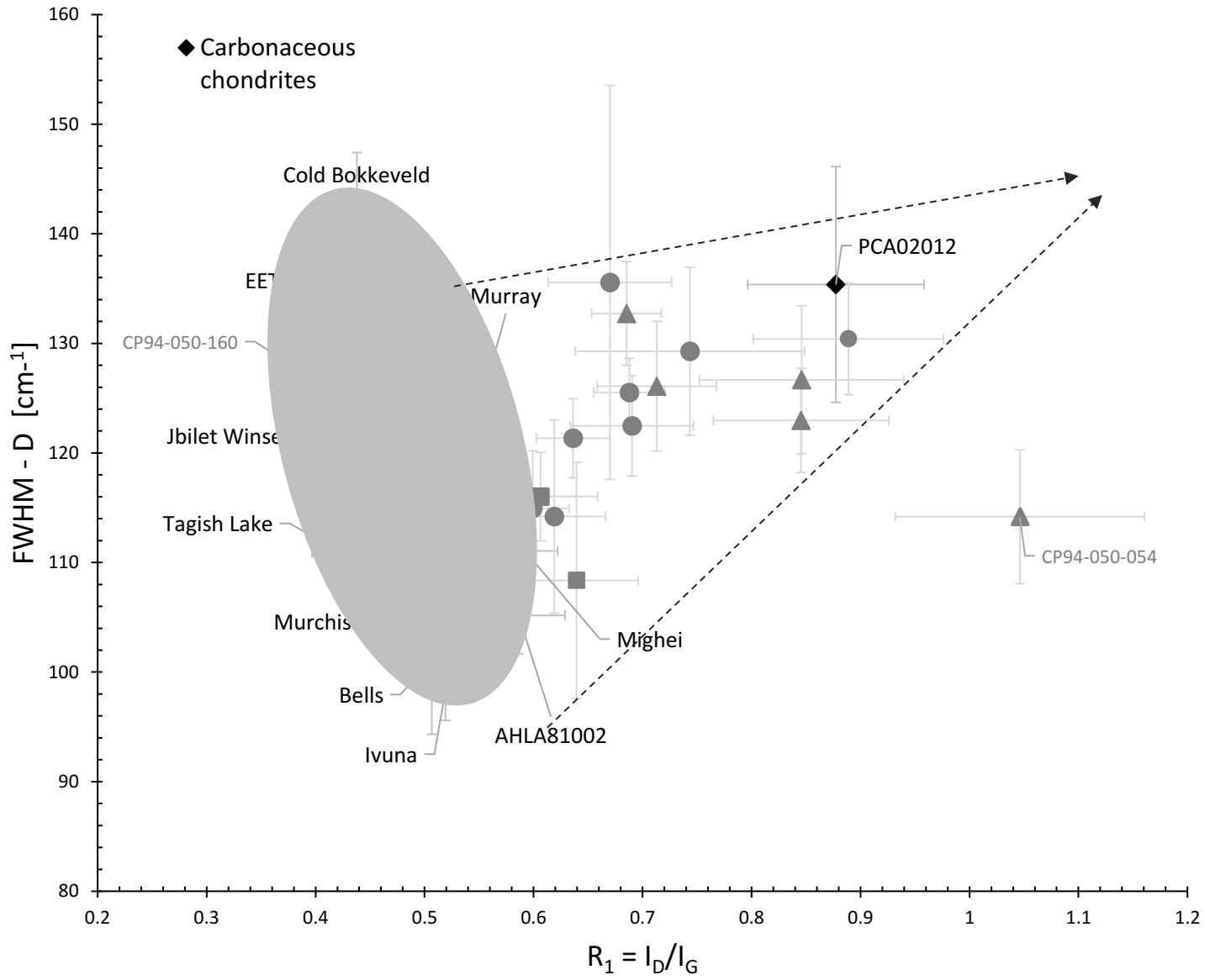

Fig.5.4. Average Raman spectral parameters – R_1 vs. FWHM-D.

The carbonaceous chondrite population (highlighted in grey) demonstrates a negative correlation between 'D' band width and peak height ratios. Several FgMMs plot within the carbonaceous chondrite field and close to individual meteorite specimens, notably Murray, Jbilet and Tagish Lake. However, many of the FgMMs are offset to higher R_1 values and demonstrate a decreasing FWHM –D range with increasing R_1 values, emphasized by the dashed black lines. This plot is commonly employed as a sensitive metric for tracing the degree of thermal metamorphism in carbonaceous samples. A narrowing 'D' band and increasing R_1 ratio are taken as evidence of thermal processing.

5.3.2 Raman line transects

Line transects were taken through sections of six fine-grained micrometeorites, two scoriaceous micrometeorites and the fusion crust of the CM2 chondrite Murchison. These are displayed in figure 5.5 and cross referenced to their spatial positions in figure 5.6. Transects are plotted with distance (in microns) on the x-axis and R_1 ratios on the y-axis. Band height ratios (R_1) were chosen over band area (R_2) or FWHM-D metrics as this parameter is considered sensitive to peak temperatures (Busemann et al., 2007) and can be reliably determined from spectra with the greatest confidence. Transects plotted using R_2 ratios demonstrate near identical profiles to the R_1 data, while transects plotted using FWHM-D values show similar but inverted profiles.

Particles CP94-050-067, CP94-050-061, CP94-050-074 and CP94-050-100 (Fig.5.5A-D) have low R_1 ratios and similar peak parameters across their particle width. The average R_1 ratio for CP94-050-061, CP94-050-067 and CP94-050-074 fall within the range observed for CM2 chondrites, while CP94-050-100 is just above this range. In addition, each of these micrometeorites have increasing R_1 values in the last ~10µm, at the particle margin. This is best demonstrated in CP94-050-061 (Fig.5.5B), where sudden increases up to R_1=1.3 are observed. These four micrometeorites, therefore, exhibit a simple zoning pattern with thin but resolvable rims and a corresponding uniform core. Particle CP94-050-048 (Fig.5.5G), also has a sharply zoned profile with a clearly resolvable core and rim, however, its profile is more complex, the rim is thick, and variable in width (~25-50µm), large variations in R_1 are observed over short distances and peak values at extreme edge on one side reach up to R_1=3.3. Conversely, the transects of CP94-050-054 and CP94-050-109 (Fig.5.5E and H) do not show discernible core-rim profiles and, instead, demonstrate an erratic or saw-tooth profile, with significant variations in R_1 over short (5µm) distances. In general, proximity to Fe-enrichment, igneous and/or magnetite rims, correlates with higher R_1 ratios. Likewise, the Murchison fusion crust demonstrates an increase in R_1 ratios towards the fusion edge. Initially, this is a shallow continuous increase, with R_1 ratios increasing from 0.4-0.6 over the first 0-85µm. This trend then becomes *saw-tooth* shaped, with significant variations over short distances. In the last 20µm from the fusion edge R_1 ratios peak at 2.7, and then decrease towards the rim, the last recorded spectra (within 5µm of the fragment's edge) is R_1=0.4.

Note that CP94-050-100 (Fig.5.5C) was previously sectioned in-situ by focused ion beam techniques for transmission electron microscope (TEM) study. As a result, the matrix adjacent to the section was deposited with gallium and exhibits an anomalously high R_1 ratio (~1.8). This correlates with the sample heating during analytical preparation and therefore the peak at 40µm should be ignored.

Fig.5.5 Raman line transects through eight micrometeorites and the fusion crust of Murchison.

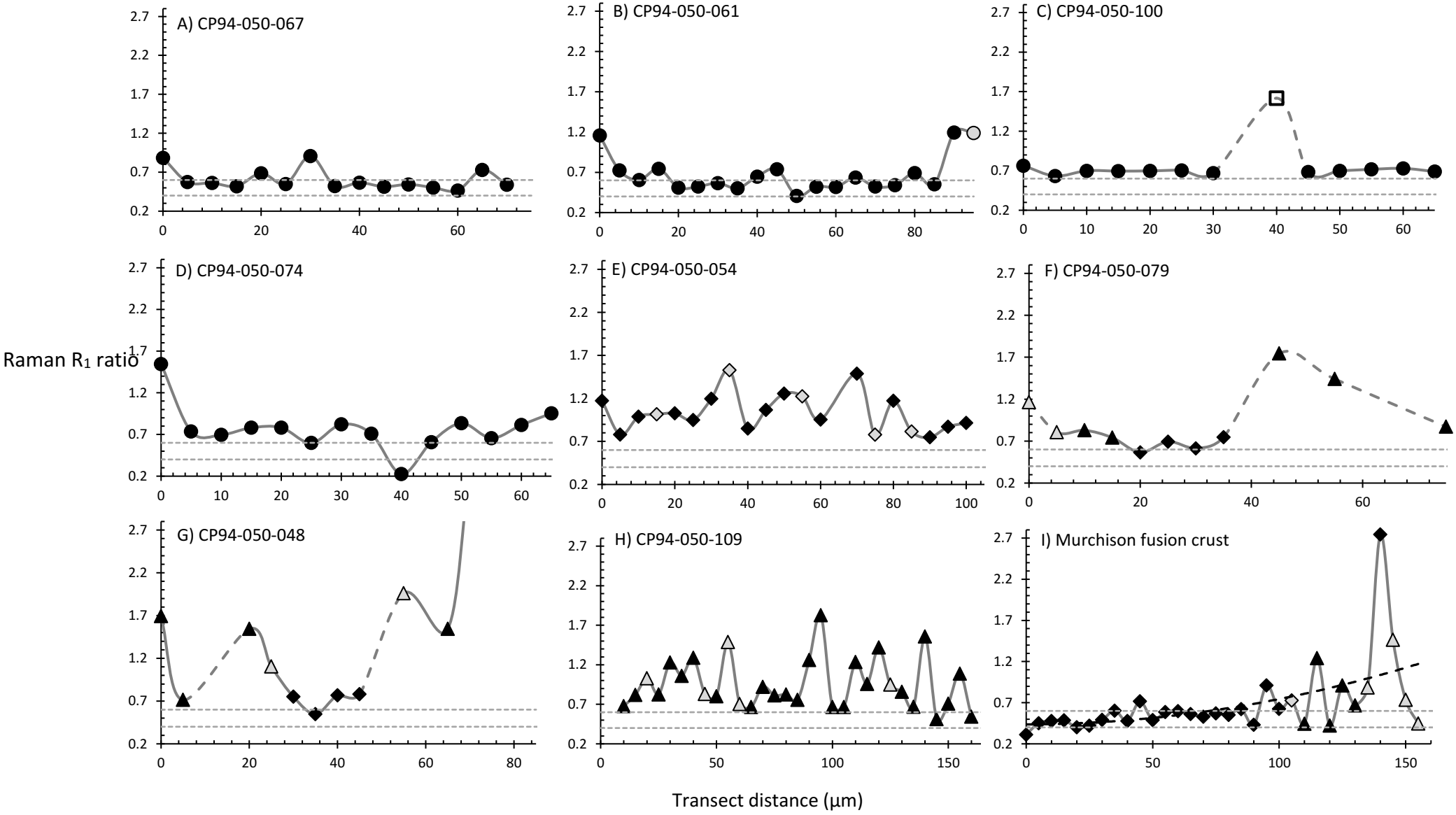

Fig.5.6. Image panel displaying the nineteen micrometeorites analysed in this chapter by Raman spectroscopy. White dashed lines are used to indicate the approximate positions of the line transects collected on eight of the micrometeorites (and the fusion crust of the carbonaceous chondrite Murchison). Rounded white dots indicate the starting points for these transects and correlate with the first point spectra shown on the left-hand side of each R_1 plots displayed in Fig.5.5.

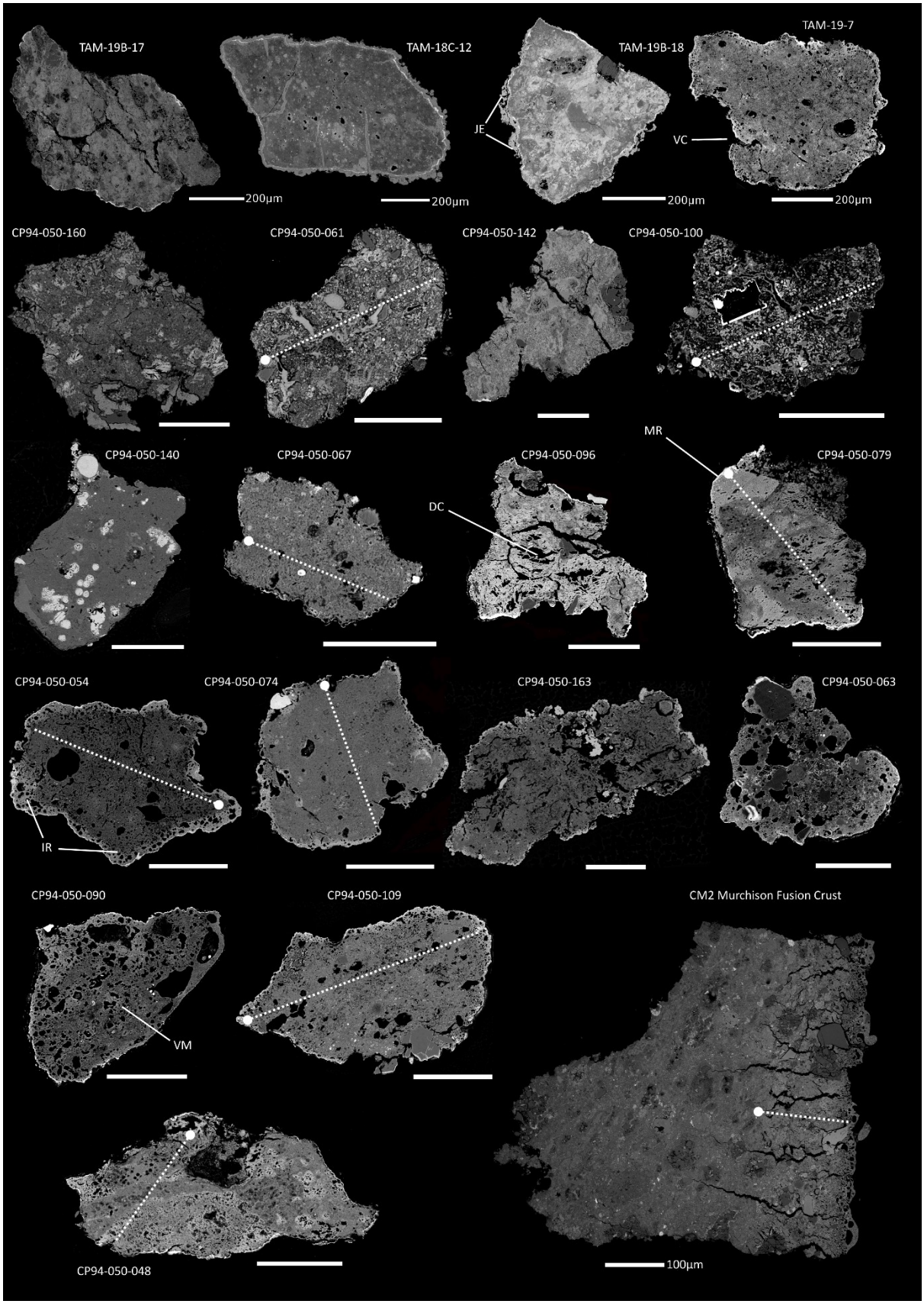

5.4. Discussion: evolution of carbonaceous Raman peak parameters

The 'G' or graphite band appears at ~1550-1610cm^{-1} and is a product of in-plane stretching motion of carbon-like (sp2) bonds. This peak is present in all organic matter (aliphatics and aromatics) and, therefore, relates to the complete carbon skeleton, being either, amorphous, nanocrystalline or polycrystalline. Conversely the 'D', referred to as the defect band, or the breathing mode, appears at ~1330-1410cm^{-1} and is associated with the presence of aromatic rings and sheet stacking. This spectral feature appears only with the imperfect arrangement of lattice layers and is not seen in graphitic specimens, as demonstrated in figure 5.7 and described in Ferrari & Robertson, (2000). The 'D' band is, therefore, an indication of disordered carbonaceous matter (Quirico et al., 2005; Bonal et al., 2006; Busemann et al., 2007).

With progressive heating carbonaceous phases evolve from amorphous carbon to nanocrystalline carbon and then to graphitic polycrystalline structures (Ferrari & Robertson, 2000). The R_1 ratio is dependent on aromatic ring cluster diameter and is, therefore, capable of tracing the degree of disorder. This value increases as an amorphous sample is heated and disorder is lost. However, the R_1 ratio demonstrates a two-fold response, dependent on the carbon environment (Fig.5.7); in an amorphous carbon setting an increasing R_1 ratio reflects an increase in cluster diameter and the growth of aromatic rings. However, once a threshold value - approximately R_1=2.5 - is breached, no more sp3 diamond-like bonds remain. With continued heating the R_1 ratio will then decrease as cluster diameter continues to grow and a polycrystalline, graphitic structure develops. This is displayed conceptually in figure 5.7 (Ferrari & Robertson, 2000; Kouketsu et al., 2014). For primitive meteoritic specimens, the carbonaceous matter is highly disordered and within the amorphous regime – as suggested by the wide FWHM-D bands (>100cm^{-1}), which are wider than both the nanocrystalline colloidal carbon standard (Table 5.1), whose FWHM-D was measured at 80cm^{-1} and the polycrystalline graphite standard which lacked a defects band entirely (Fig.5.2). Heating (both atmospheric entry and metamorphic) will increase the R_1 ratio of disordered carbonaceous matter, as aromatic ring clusters are formed. In the present study, this is observed where heated scoriaceous micrometeorites and the intensely thermally metamorphosed CM2 chondrite PCA02012 have higher R_1 ratios than the lower petrologic grade CM2 chondrites and most of the fine-grained micrometeorites. With continued heating the R_1 threshold is breached and graphitic polycrystalline carbon forms. Graphitic carbon is identified at the rim of CP94-050-048 (Fig.5.5G) and in the margin of the Murchison fusion crust (Fig.5.5I). Here, Raman peak parameters have either extremely high R_1 ratios (maximum R_1 ratios are 3.5 and 2.7 respectively) or low R_1 ratios and narrow 'D' bands (<100cm^{-1}), this is especially notable in the final three transect points from the Murchison crust, where one spectrum is deconvolved with a FWHM-D<16cm^{-1}. These observations are, therefore, consistent with the expected response of carbonaceous matter to progressive heating, as determined experimentally in Ferrari & Robertson, (2000).

The evolution of carbonaceous Raman spectra is also dependent on kinetic effects. The absolute temperature threshold at which carbonaceous matter transitions from the amorphous to the nanocrystalline regime is dependent on the duration of heating. In experimentally heated coke

samples this threshold occurs at ~1800°C (Kostecki et al., 1997) while in low grade metasediments from Japan this threshold occurs at significantly lower temperatures of just 300°C (Kouketsu et al., 1997). The coke samples of Kostecki et al., (1997) were heated over a matter of hours while the Japanses pelitic sediments were heated over geological timescales (10-100's of million years). Thus, the timeframe over which heating occurs must be considered. Carbonaceous CM2 chondrites are most likely to have experienced parent body heating via radioactive decay (Hevey & Sanders, 2006; ŠráMek et al., 2012) or successive impact events. Both of which could have lasted for significant timescales, potentially up to millions of years (Davison et al., 2012; Rubin, 2012), while fusion crusts and micrometeorites endure flash heating, lasting >10 seconds during atmospheric entry (Love & Brownlee, 1991). Experimental pyrolysis of organic matter in Murchison suggests that Raman is most reliable tracing short duration, high temperature heating events (Muirhead et al., 2012) and, therefore, entry heating signals should be more easily resolved than the lower temperature and longer duration parent body heating expected from carbonaceous chondrites.

Fig.5.7. Interpretation of Raman R_1 parameter evolution reproduced and modified from Ferrari & Robertson (2000) plot [figure 6]. Value L_a(Å) corresponds to the cluster diameter (of 6 ring carbon sheets) or in-plane correlation length in Angstroms. A higher L_a value therefore corresponds to increasing order of the carbon skeleton and building of a carbon framework. Two domains are defined within the plot, the amorphous carbon regime and the nanocrystalline regime. Within the amorphous regime an increasing R_1 value reflects the growth of clusters and an increase in order, once the R_1=2.5 threshold is breached the R_1 value then decreases as graphitisation proceeds.

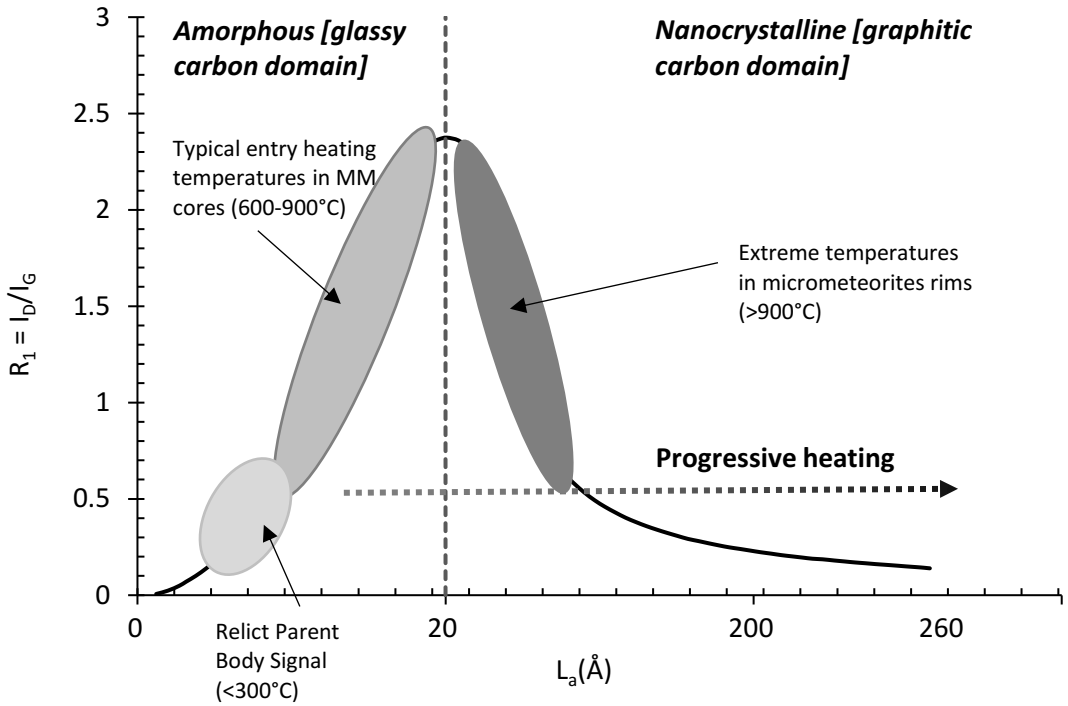

5.5. Discussion: Entry heating of carbonaceous phases in micrometeorites

Whilst on the parent asteroid, micrometeorite-sized volumes of fine-grained matrix will be heated uniformly and, therefore, inherit carbonaceous matter with similar Raman spectra and similar R_1 ratios throughout the particle. However, if a micrometeorite contains a variable R_1 ratio across the particle's width, this is most likely a product of later, non-uniform and short duration heating. Thus, zoned micrometeorites with higher R_1 ratios in the particle rim, and lower R_1 ratios in the particle core are strong evidence of thermal gradients within micrometeorites.

The Raman transects in figure 5.5, show that the majority of the micrometeorites analysed (five of eight) exhibit a zoned profile with higher R_1 ratios approaching (at least one of) the particle edges and, therefore, supported rim-to-core, U-shaped thermal gradients during atmospheric entry. Rims are present even in some particles which lack BSE evidence of heating (e.g. CP94-050-061 and CP94-050-067). Rim thicknesses are variable, both within and between particles, as is best demonstrated by comparing the rims of CP94-050-061 and CP94-050-048 (Fig.5.5B and G). Variation in rim thickness supports the idea of the high-temperature thermal front migrating inwards and suggests that entry reprocessing is more advanced in CP94-050-048 as compared to CP94-050-061. This is shown by the thicker rim and higher R_1 ratios. The presence of scoriaceous matrix and vesicles in CP94-050-048 (otherwise absent in CP94-050-061) are further petrographic evidence to suggest that this micrometeorite experienced higher peak temperatures or longer duration heating. Where a rim exists on only one side of the particle this may reflect a micrometeorite that broke apart during terrestrial residence. Alternatively, this could be explained by a late-stage fragmentation event during atmospheric entry (Chapt.7).

Although core-to-rim profiles exist in most micrometeorites, transects are not simple bimodal profiles with uniform cores and heated rims. Micrometeorites CP94-050-079 and CP94-050-054 (Fig.5.5E and F) have their highest peak temperatures near the particle's core, rather than at within their rims. For example, matrix adjacent to large vesicles, as seen in CP94-050-054 or in an expanded matrix, containing abundant small vesicles as dehydration cracks, as in CP94-050-079. Thus, a correlation is observed between R_1 ratios and the textures of micrometeorites (compare Figs.5.5 and 5.6) with higher R_1 ratios associated with areas containing scoriaceous textures and adjacent to dehydration cracks. Raman spectroscopy, therefore, can map internal peak temperature attained during entry heating and suggests that the flow of volatile gases may play a significant role in the heating of micrometeorite matrix.

The largest R_1 range is seen in CP94-050-048, a difference of ~2.9 between the lowest core value and the highest rim value (Fig.5.5G). This particle is transitional between fine-grained and scoriaceous micrometeorite and retains a central linear zone of unaltered relict matrix (~25µm wide) surrounded by a vesicular, heated mantle. Within the relict matrix submicron vesicles and spherical Fe-metal or Fe-sulphide grains are present, most likely resulting from the decomposition of tochilinite to troilite. Therefore, the BSE textural evidence suggests that the entire particle has been altered by entry heating and its pre-atmospheric mineralogy lost. Nevertheless, a single transect point, in the centre

of the core, retains a low R_1 ratio (0.6) which plots within the peak parameter space of the CM2 chondrites and may retain carbonaceous matter that survived entry relatively unheated.

Additional constraints on the evolution of Raman signatures can be obtained from the meteorite fusion crust. The fusion crust of Murchison can be split into two sections. The inner section, between 0µm and 80µm may be unaffected by entry heating because R_1 ratios consistently fall within the range of the CM2 chondrite population. Conversely, in the outer section, between 80µm-160µm, R_1 ratios are much higher, typically between 0.7 and 1.5 and large variations in R_1 over short distances are observed. This is similar to the Raman transect of the scoriaceous micrometeorite CP94-050-109 (Fig.5.5H).

Under BSE the Murchison fusion crust contains several large dehydration cracks (>300µm and up to 500µm), each of these is perpendicular to the fusion crust edge, composed of multiple interconnected cracks that form a branching series of channels and tends to decrease in width away from the external surface. By comparison CP94-050-109 has a vesicular matrix, composed of many micron-scale vesicles. Several larger vesicles are also present, and are presumed to form by coalescence (Genge, 2017). Both samples, therefore, share similar textures, characterized by an abundance of small voids (dehydration cracks and vesicles).

The Raman transects shown in this study can be split into two groups: (1) zoned U-shaped profiles with recognisable cores and rims or (2) *saw-tooth* profiles with erratic, highly variable R_1 ratios across their width, typically ranging from 0.6 to >1 and whose BSE data correlate with a vesicular matrix. The correlation between variable R_1 ratios over short length scales in saw-tooth transects and features such as dehydration cracks, igneous rims, decomposed Fe-sulfides and vesicles suggests that the decomposition of low-temperature phases and the migration of volatile gases may play a significant role in the heating of micrometeorites (and chondrite fusion crusts) during the advances stages of atmospheric entry. This could potentially act as an additional heating mechanism. Volatile gas-driven heating is explored further as the main focus of Chapter 7, using analysis of particle porosities, evaluating dehydration crack and vesicle interconnectivity and by elemental mapping to reveal localized heating of the micrometeorite matrix.

By contrast, those micrometeorites with U-shaped, core-to-rim thermal profiles, and low R_1 ratios and wide FHM-D bands at their particle cores may preserve parent body metamorphic signals. The average R_1 ratios in CP94-050-061, CP94-050-067, CP94-050-074, CP94-050-079 and CP94-050-048 are R_1=0.6 and this value is remarkably consistent between samples. Because the average R_1 ratios from the spot analyses on CM2 chondrites, shown in figure 5.3 and 5.4, range from 0.4-0.6, this suggests that the pre-atmospheric carbonaceous matter in fine-grained micrometeorites has experienced similar, low grade metamorphism (presumably <300°C) on similar, and potentially identical, asteroids as CM2 chondrites.

5.6 Discussion: thermal metamorphism in CM2 chondrites

Previous studies have shown that interclass petrologic subclassifications appear to correlate with Raman peak parameters, at least among the anhydrous chondrite groups. For example, CV oxidised, CV reduced, CO and ordinary chondrites all show distinct trends in their peak metamorphic temperature with increasing petrologic grade (Busseman et al., 2007). However, to date no relationship between carbonaceous phases observed with Raman spectroscopy and petrologic grade has been identified for the aqueously altered CM2 chondrites. Busseman et al., (2007) concluded that all meteorite classes most likely inherited a homogenous organic component and that the entire CM2 family has experienced only very mild thermal alteration, with peak temperatures <120°C (Busseman et al., 2007).

This study could not distinguish the Raman peak parameters of hydrated CM/CI, C2 ungrouped and moderately thermally metamorphosed CM2 chondrites. The only meteorite sample with distinct peak parameter data was the intensely metamorphosed chondrite PCA 02012. Based on a recrystallized olivine groundmass, and phyllosilicate volumes <5%, the peak temperature estimates for PCA 20102 are approximately 900°C, significantly higher than most CM chondrites (Nakato et al., 2013). The higher Raman R_1 ratios observed in this study, therefore, support previous petrographic studies. However, the thermally metamorphosed chondrites, Jbilet Winselwan and EET 96029, have also experienced mild heating, albeit at lower peak temperatures than PCA 02012. Their phyllosilicates are either dehydrated as in Jbilet Winselwan (Zolensky et al., 2016) or dehydroxylated as in EET 96029 (Lee et al., 2016). Estimated peak temperatures based on phyllosilicate decomposition are between 400-600°C. Despite experiencing higher peak temperatures than the unmetamorphosed CM2 population, both EET 96029 and Jbilet Winselwan plot among the other CM2 chondrites with similar R_1 ratios. Indeed, EET 96029 has the lowest R_1 ratio of any chondrite in the present study.

The lack of distinction between the mildly metamorphosed CM2 chondrites and the unheated CM2 population is unexpected and suggests that either: (1) the duration of parent body heating in CM2 chondrites was highly variable or that (2) Raman spectroscopy of carbonaceous phases is unsuitable for analysis of low grade thermal metamorphism or (3) that aqueous alteration can alter carbonaceous phases such that Raman is no longer a reliable thermal tracer. With the limited evidence in the present study it is, therefore, not possible to accurately reconstruct the peak metamorphic temperatures experienced by individual CM2 chondrites. Instead, this study can conclude only that PCA 02012 experienced significantly higher parent body temperatures than the rest of the CM2 group, likely around 900°C.

Since the Raman peak parameters for all chondrites are similar, and no clear distinction can be drawn between CM2, CI, ungrouped C2 chondrites and thermally metamorphosed CM2 chondrites. This supports Busemann et al., (2007)'s suggestion that hydrated primitive asteroids inherited a similar carbonaceous component and that this is largely unaffected by the low-grade thermal metamorphism expected to operate on C-type asteroids.

5.7. Discussion: a rare refractory, hydrated fine-grained micrometeorite

Although the majority of fine-grained micrometeorites plot outside the chondrite field, CP94-050-160 occupies a near identical R_1-R_2 space to that of Cold Bokkeveld. This micrometeorite was classified as only one of two micrometeorites in the G1 mid-IR spectral class (Chapt.4), which implies its matrix retains hydrated phyllosilicates, rather than containing decomposed dehydroxylates (Sect.4.5). In addition, element mapping was performed on this particle (Fig.5.8) and combined with SEM-EDS to determine mineral phases. This micrometeorite is composed of fine Mg-rich serpentines interspersed with Fe-Ni sulfides, coarse Fe-rich serpentine clusters, 10µm radiating fibrous tochilinite and occasional anhedral ~5µm olivines. The mineralogy (and bulk composition, Fig.3.1A) is, therefore, CM-like. Furthermore, CP94-050-160 contains a refractory inclusion; a single Mg-Al spinel sits at the particle perimeter (bottom left in Fig.5.8) and is mantled by Fe-rich phyllosilicates. This inclusion is, therefore, identical to the aqueously altered CAIs seen in CM2 chondrites and notably from Cold Bokkeveld (Greenwood et al., 1994). Finally, the retention of intact and abundant tochilinite also attests to an extremely low peak temperature, <245°C (Nazarov et al., 2009) and consequently minimal heating (both metamorphic and entry) over the lifetime of the particle.

The elemental distribution of S, Na, Mg and Al are shown in figure 5.8. The Na map illustrates slightly higher concentrations in the particle core than at the rim. In micrometeorites Na is a trace element and partitions into phyllosilicate phases, resulting in a near uniform distribution (Zolotov, 2012). Sodium is a volatile element and is, therefore, sensitive to heating and will readily move into the gas phase during atmospheric entry and be lost through evaporation (Taylor et al., 2007; Alexander et al., 2008). However, Na is also fluid-mobile and could be leached from the particle rim during weathering in the acidic Antarctic environment (Altheide et al., 2010; van Ginneken et al., 2016). As a result, Na depletions could be a product of either atmospheric entry or weathering. The observed depletion pattern cannot be used to distinguish between these two processes as both would progress from the rim inwards as observed in figure 5.8B. However, since the 50% condensation temperature of Na is ~685°C (Lodders, 2003) it is not possible for Na to be lost by evaporative heating whilst retaining tochilinite, therefore, depletions must result from terrestrial residence in the Antarctic ice.

Particle CP94-050-160 has, therefore, experienced negligible atmospheric entry heating, moderate weathering and retains an extensively hydrated mineralogy, including a rare altered refractory CAI; these features demonstrate a strong association to low petrologic subtype CM2 chondrites such as Cold Bokkeveld.

Fig.5.8 A) Particle CP94-050-160, a rare hydrated refractory micrometeorite. Characteristic atmospheric entry heating textures are absent, including an igneous and magnetite rim. The internal mineralogy is composed of radiating fibrous tochilinite masses sitting in a matrix of coarse Fe-rich and fine Mg-rich phyllosilicates. A hydrated spinel sits at the particle base (bottom left), mantled by Fe-rich phyllosilicates, this is highlighted with a dashed white circle. In addition to refractory phases being relative rare among micrometeorites, this feature is diagnostic of extensive aqueous alteration, and commonly found in low petrologic subtype chondrites, such as Cold Bokkeveld. B) Element maps display the distribution of S, Na, Mg and Al, these maps were chosen to highlight unusual petrologic features. Tochinilite masses are clearly visible in the S map, the retention of sulfide phases and presence of intact tochilinite, attests to minimal heating (<245°C). Mg and Al maps were included to emphasise the presence of the refractory CAI spinel while the zoned profile in the Na map, showing Na depletions in the particle rim is attributed to terrestrial weathering, resulting in the leaching fluid-mobile Na from the micrometeorite margins.

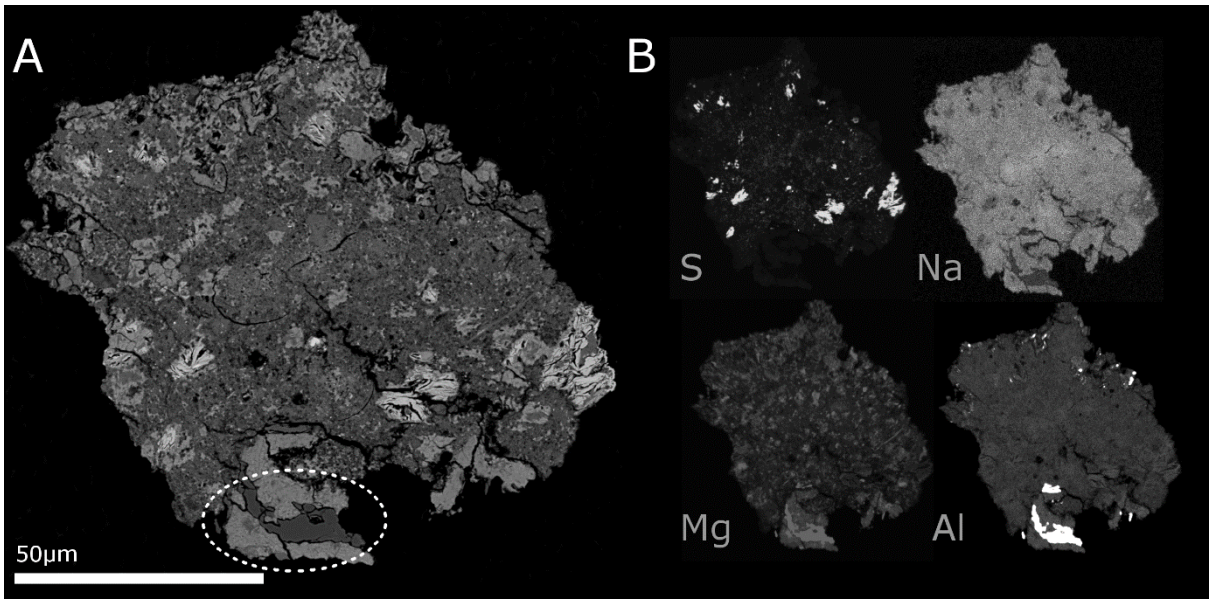

5.8. Implications of Raman spectroscopy

5.8.1 Estimating peak temperatures

The response of carbonaceous Raman spectra to heating is well-documented and follows a predictable evolutionary pathway in peak parameter space. Several previous studies have attempted to assign absolute temperature estimates to individual samples by establishing experimentally derived peak metamorphic temperature equations (Rahl et al., 2005; Bonal et al., 2006; Busemann et al., 2007). However, because Raman spectra are heavily dependent on the composition of carbonaceous phases, the peak temperature achieved and the duration of heating (Muirhead et al., 2012), each equation requires calibration to the specific heating scenario being investigated. As a result, the application of these equations to new investigations is ambiguous. In this study the R_1 peak height ratio was used as a proxy for peak temperatures, however, absolute temperature estimates were not assigned as this would be an over interpretation, given the variation in heating duration between the sample population.

5.8.2 Raman spatial analyses

Spot analyses and extracted insoluble organic residues can characterise the carbonaceous component with chondrites, however, additional spatial data is necessary in the analysis of smaller micrometeorites where entry heating significantly overprints pre-atmospheric information. In this study, Raman transects were paired with BSE imaging, allowing this investigation to differentiate between entry heating features, affecting the margins of most micrometeorites and probable parent body signatures, preserved in their cores. The inferred peak metamorphic temperatures inside these micrometeorites appear analogous to the R_1 range seen in CM2 chondrites, suggesting similar low grade (<300°C) peak metamorphic temperatures, potentially on the same asteroid parents.

5.8.3 Role of gas in entry heating

Four samples studied here (three micrometeorites and the Murchison fusion crust) showed no evidence of core-to-rim thermal gradients and, instead, their Raman line transects produced erratic, saw-tooth shaped profiles. In these samples a vesicular matrix and abundant dehydration cracks and vesicles are common. This could suggest that greater heating is experienced in matrix adjacent to pore space and that volatile gases are an important heat transfer mechanism in micrometeoroids. This hypothesis is explored in detail in Chapter 7.

5.8.4 Raman spectroscopy of CM2 chondrites

Raman spectroscopy was unable to distinguish between mildly (<500°C) thermally metamorphosed CM2 chondrites and unheated CM2 chondrites (with EET 96029 and Jbilet Winselwan plotting within the same peak parameter space as other CM2 chondrites). This was surprising given that the peak temperatures of the thermally metamorphosed chondrites are at least 200°C higher than their unheated counterparts. By contrast, the extensively heated PCA 02012 was clearly separated from the CM2 population and produced peak parameters expected of a high-temperature sample. This demonstrates that Raman spectroscopy struggles to unambiguously resolve low-grade thermal metamorphism (0-600°C) among the CM2 chondrites, where aqueous alteration and heating have occurred over significant and potentially disparate timescales (10^2-10^6 years). Despite these problems the similarity among carbonaceous phases in CM2/CI chondrites and unheated fine-grained micrometeorites supports the previous conclusions of Busemann et al., (2007) that meteorite parent bodies most likely acquired similar primitive assemblages of organic matter during early solar system accretion.

5.9 Conclusions from Raman spectroscopy

This study investigated the carbonaceous phases within fine-grained and scoriaceous micrometeorites using in-situ Raman microspectroscopy combined with SEM-BSE imaging, EMPA and quantitative element mapping. Line transects provided spatial context to the Raman data which proved crucial in resolving the complex thermal histories of individual micrometeorites.

Some unmelted micrometeorites record a two-stage thermal history, preserving signals of both parent body metamorphism and atmospheric entry flash heating. This was inferred on the basis of bimodal

transect profiles revealing heated rims and less-heated cores. Thermal gradients within these particles are steep, less than 20μm thick and are present even in particles which lack BSE evidence of entry heating (e.g. lack magnetite and igneous rims). Where relict cores are preserved, the Raman peak parameters were similar to those recorded in (unheated) CM2 chondrites, implying both groups experienced similar low grade thermal metamorphism (<300°C), potentially on the same parent bodies.

In addition, a single micrometeorite (CP94-050-160) was identified with a hydrated, refractory mineralogy and low Raman peak parameters similar to those in the low petrologic CM2 chondrite Cold Bokkeveld. Likewise, the presence of an aqueously altered CAI, the retention of heat-sensitive tochilinite and mid-IR spectral data suggest this particle retains phyllosilicates and have not been heated above 245°C – either during parent body heating or atmospheric entry heating.

5.10 Appendix: Peak parameter data for the micrometeorite and CM2 chondrite samples

Table 5.2 Each average value is accompanied by its standard error of the mean marked with the following symbol ($\sigma\bar{x}$) and shown in light grey.

Sample	Type	No. of Spectra	ω_G - (cm^{-1})	ω_G - ($\sigma\bar{x}$)	FWHM-G (cm^{-1})	FWHM-G ($\sigma\bar{x}$)	ω_D - (cm^{-1})	ω_D - ($\sigma\bar{x}$)	FWHM-D (cm^{-1})	FWHM-D ($\sigma\bar{x}$)	R_1 [Height]	R_1 ($\sigma\bar{x}$)	R_2 [Area]	R_2 ($\sigma\bar{x}$)
AHLA 81002	CM2	14	1593	0.67	82	2.19	1370	1.14	105	3.50	0.59	0.04	0.40	0.02
Mighei	CM2	7	1593	0.35	88	2.26	1372	0.97	111	3.70	0.59	0.03	0.40	0.01
Cold Bokkeveld	CM2.2	11	1592	0.57	97	1.42	1382	0.92	142	5.07	0.44	0.01	0.36	0.02
Murray	CM2.4/2.5	9	1593	0.77	93	1.74	1369	1.06	123	3.24	0.55	0.03	0.38	0.02
Murchison	CM2.6	9	1593	0.56	84	3.42	1368	0.68	104	5.28	0.54	0.04	0.38	0.02
EET 96029	CM2.7	9	1596	0.36	88	0.63	1376	0.94	133	2.78	0.38	0.01	0.33	0.01
Jbilet Winselwan	CM2.0-2.3	21	1595	0.25	85	1.43	1372	0.81	121	3.03	0.51	0.02	0.39	0.01
PCA 02012	CM2	10	1597	1.35	110	4.06	1375	1.87	135	10.76	0.88	0.08	0.47	0.04
Ivuna	CI1	11	1590	0.59	89	1.30	1374	0.90	98	2.82	0.52	0.02	0.35	0.01
Tagish Lake	C2	11	1592	0.61	88	2.23	1379	0.70	111	2.99	0.42	0.03	0.32	0.01
Bells	C2	11	1589	0.86	91	3.88	1375	1.85	101	6.85	0.51	0.05	0.34	0.02
CP94-050-061	C2-FgMM	26	1590	0.96	97	3.39	1370	1.70	122	4.58	0.69	0.06	0.42	0.02
CP94-050-067	C2-FgMM	17	1592	0.47	103	2.18	1372	1.59	127	4.53	0.53	0.02	0.36	0.01
CP94-050-079	FgMM	24	1591	1.97	98	5.09	1371	1.37	130	5.11	0.89	0.09	0.49	0.03
CP94-050-096	C2-FgMM	11	1591	1.15	103	6.77	1367	3.44	114	8.81	0.62	0.04	0.38	0.03
CP94-050-100	C2-FgMM	15	1588	0.57	96	1.82	1366	1.07	121	3.62	0.64	0.03	0.41	0.01
CP94-050-140	C1-FgMM	23	1591	0.49	113	1.20	1377	1.27	128	3.23	0.45	0.01	0.31	0.01
CP94-050-142	C2-FgMM	16	1587	0.86	116	2.53	1374	1.43	115	5.48	0.41	0.02	0.27	0.02
CP94-050-160	C2-FgMM	27	1594	0.36	85	1.34	1372	0.91	124	2.51	0.44	0.01	0.36	0.01
CP94-050-163	FgMM	40	1591	0.65	99	2.53	1367	1.21	126	3.10	0.69	0.03	0.43	0.02
TAM_19B-18	C2-FgMM	8	1595	1.37	100	2.26	1375	3.34	129	7.68	0.74	0.11	0.45	0.04
TAM_18C-12	C2-FgMM	6	1596	1.91	105	5.42	1371	1.35	115	5.27	0.60	0.03	0.37	0.02
TAM_19B-17	C2-FgMM	5	1595	1.39	94	2.87	1371	4.53	136	17.99	0.67	0.06	0.45	0.05
CP94-050-074	Fg-ScMM	16	1592	1.10	101	2.38	1371	1.68	116	4.04	0.61	0.05	0.38	0.02
TAM_19-7	Fg-ScMM	7	1594	1.33	87	8.05	1369	2.09	108	10.78	0.64	0.06	0.42	0.02
CP94-050-048	ScMM	16	1588	2.10	103	4.30	1373	1.78	123	4.76	0.85	0.08	0.46	0.02
CP94-050-054	ScMM	14	1587	1.91	79	3.49	1371	1.65	114	6.11	1.05	0.11	0.56	0.03
CP94-050-063	ScMM	16	1588	1.33	99	4.23	1368	2.35	133	4.74	0.69	0.03	0.44	0.02
CP94-050-090	ScMM	23	1590	1.25	108	2.85	1374	1.76	126	5.92	0.71	0.05	0.42	0.02
CP94-050-109	ScMM	17	1590	1.77	92	5.31	1372	1.66	127	6.76	0.85	0.09	0.49	0.04
Colloidal Carbon	Standard	3	1581	0.60	60	0.95	1362	1.07	83	8.38	0.50	0.02	0.40	0.03
Graphite	Standard	3	1573	0.59	39	0.10	-	-	-	-	-	-	-	-

Chapter 6: Shock fabrics in Antarctic micrometeorites

6.0 Overview – This chapter investigates unmelted, fine-grained micrometeorites for evidence of impact-induced shock deformation. The orientations of dehydration cracks and fracture networks are analysed in twenty-one micrometeorites via rose diagrams, circular statistics and entropy calculations. The growth of dehydration cracks and brittle fractures can reveal the presence of pre-existing anisotropies in the host matrix. Analysis of void orientations, therefore, provides a mechanism with which to study the subtle petrofabrics preserved within fine-grained and amorphous materials. Both uniaxial and biaxial fabrics are identified, often with a relatively large spread in orientations (40°-60°). Additionally, a single micrometeorite is found, which contains brittle deformation features, including cataclasis fabrics and localised domains of shear strain. This chapter concludes that both CM-like fine-grained micrometeorites and CM chondrites contain evidence of low-grade shock processing. When combined with anomalously low-density measurements for C-type asteroids and impact experiments suggesting that CM chondrites are highly prone to disruption, collectively these observations imply that the CM parent body asteroids are unlikely to have remained intact over the lifetime of the solar system. Instead, CM-like asteroids most likely exist as a collection of loosely aggregated rubble-pile asteroids, composed of primitive shocked clasts.

6.1. Impact events and shock deformation in the meteorite record

On small, primitive asteroids, residual heat from planetesimal formation and heat generated from radiogenic decay are rapidly lost to space (Kunihiro et al., 2004). Impact events, therefore, provide the main source of energy that drives geological processes (Rubin, 1995; Nakato et al., 2008; Davison et al., 2012). This includes; compaction, thermal metamorphism, fracturing, regolith gardening and aqueous alteration (Housen et al., 1979; Tomeoka et al., 1999; Rubin, 2012; Hanna et al., 2015).

Abundant evidence of past impact events can be found in the meteorite record (Gattacceca et al., 2005; Watt et al., 2006). In 1991 Stöffler et al., established a classification scheme to quantify the shock stage of individual meteorites. This system ranged between S1-S6 and relates to approximate shock pressures experienced by a sample. Shock stages are determined by the characteristic deformation response of index minerals, primarily olivine and plagioclase. Unshocked meteorites are classified as S1 [<5GPa]. These samples show no evidence of shock and therefore contain olivine grains with sharp optical extinction. As the shock pressure rises, weakly shocked S2 [5-10GPa] meteorites contain olivine with undulose extinction patterns and planar or irregular fractures. At higher shock stages S3 [15-20GPa] and S4 [30-35GPa], olivine grains develop abundant subparallel planar fractures and melt veins. The highest shock stages S5 [45-55GPa] and S6 [75-90GPa] are characterised by the recrystallization of olivine and plagioclase as ringwoodite and maskelynite (Stöffler et al., 1991).

Meteorite groups generally contain similar shock stages, the most heavily shocked carbonaceous chondrite groups are the anhydrous CV and CK chondrites, which are classified with S3-S4 shock stages, while the majority of CM chondrites are classified as S1, with only rare S2 and S3 members (Scott et al., 1992; Rubin, 2012). Despite their classification as unshocked, abundant textural evidence

of shock has been reported. This includes: aligned phyllosilicates (Fujimura et al., 1982; 1983; Rubin, 2012), crushed chondrules (Scott et al., 1992; Nakamura, 2006; Hanna et al., 2015), foliation fabrics (Zolensky et al., 1997; Gattacceca et al., 2005; Hanna et al., 2015; Lindgren et al., 2015), fracture melt veins (Zolensky et al., 2014a), and brecciated regolith samples, composed of several distinct CM lithologies (Metzler et al., 1992; Nakamura, 2006; Lee and Nicholson, 2009; Zolensky et al., 2014b; Zolensky et al., 2016). Additionally, at the microstructural scale, brittle deformation cataclasis fabrics within anhydrous chondrules (Hanna et al., 2015) have also been described.

Evidence of shock deformation within anhydrous, coarse-grained micrometeorites was previously identified by Genge (2007). However, to date, the shock stage of fine-grained micrometeorites has not been investigated. In this chapter, the internal textures in fine-grained micrometeorites are investigated using image analysis techniques, allowing the presence and strength of petrofabrics within hydrated cosmic dust to be evaluated.

6.2. Dehydration cracks as proxies for phyllosilicate orientation

Petrofabrics are formed by the alignment of fine-grained, platy minerals parallel to the σ3 stress axis (Fossen, 2010). Where equigranular objects are present within the matrix, elongate crystals wrap around these obstructions, generating foliation fabrics (Gattacceca et al., 2005; Hanna et al., 2015). In fine-grained micrometeorites, up to 95% of the matrix (by volume) is composed of fine-grained phyllosilicates (Chapt.3 and Howard et al., 2009; 2011 and others), petrofabrics in these samples will, therefore, be defined by the alignment of submicron crystals. However, the orientation of these crystals (and their cleavage planes) cannot be directly imaged using SEM-BSE techniques, owing to the small size of the features of interest. Therefore, this study required a new petrographic proxy for phyllosilicate orientation.

The SEM-BSE images of most unmelted and scoriaceous micrometeorites contain abundant, small, sublinear and elongate voids. The majority of these voids are dehydration cracks, formed by the thermal decomposition of phyllosilicates during atmospheric entry heating (Toppani and Libourel, 2001; Genge, 2006; Nozaki et al., 2006; Nakato et al., 2008). As phyllosilicates dehydrate, interlayer water is lost from between sheets and contraction occurs along the [001] crystal plane (Shen et al., 1990; Nozaki et al., 2006). This results in voids that are parallel to the basal cleavage plane (and long-axis) of the host crystals. The orientation of dehydration cracks, therefore, reveals the orientation of micron-scale crystals. This means that if dehydration cracks within a micrometeorite are aligned then the pre-atmospheric matrix phyllosilicates were also aligned and the micrometeorite, therefore, contains a petrofabric, inherited from its parent asteroid.

In Chapter 4, fine-grained micrometeorites were shown to follow a standard petrographic pathway during atmospheric entry (transition through mid-IR spectral groups 1-5). After phyllosilicate dehydroxylation, the amorphous matrix recrystallizes as an anhydrous metamorphic groundmass, composed of olivine. Crucially, these recrystallized micrometeorites (G4 & G5) were found to preserve both, previous stages of atmospheric entry heating (e.g. dehydration cracks) and pre-atmospheric parent body textures. Therefore, all unmelted micrometeorites can be evaluated for the existence of

petrofabrics and it is only in partially melted scoriaceous micrometeorites that pre-atmospheric phyllosilicate orientation can no longer be discerned.

6.3. Methods: Obtaining quantitative data from SEM-BSE images

6.3.1. Image analysis and void dataset extraction

Twenty-one micrometeorites are investigated in this chapter, for each particle, a high-resolution (between 49-192pxμm^{-2}) cross section SEM-BSE image acted as the raw dataset. The image analysis software, *ImageJ* (Schindelin et al., 2015) was used to resolve voids (dehydration cracks, fractures and sub-linear vesicles) from micrometeorite matrix. Brightness and contrast were manually altered, until a bimodal black-and-white image of the particle was generated, this separated matrix in white, from voids in black. The *particle analysis* function then identified each void and calculated its size, aspect ratio and orientation (angle with respect to an arbitrary *north*).

Voids with circularity values >0.7 were rejected (in most instances <<20% of the total number of voids). These highly circular voids do not demonstrate a clear elongation direction and, therefore, do not contribute significantly to the particle's petrofabric. In addition, small voids, <2µm in length or <1μm^2 were rejected. This arbitrary size threshold was chosen to reduce the noise in datasets and therefore improve reliability. This is because many of the smallest voids are products of the processing procedure and are, therefore, dependent on the exact threshold position chosen. Void space outlines, identified by the software, were cross-referenced against the original BSE images to ensure accurate extraction of data. Furthermore, repeat experiments were performed on each micrometeorite, in which the threshold position for dataset reduction was varied. This ensured that any trends in void orientation, obtained by the software, were true representations of the micrometeorite's texture. Figure 6.1 shows an example of the processed and raw images for a single micrometeorite (CP94-050-109).

6.3.2. Quantifying petrofabrics with conventional circular statistics

The extracted void datasets were investigated for evidence of preferred alignment. Void orientations were binned by 10° increments, creating circular histograms, referred to as rose diagrams. These plots were constructed in the *GeoRose* software (Yong Technology Inc., 2014) and standard circular statistics calculated using the *GEOrient* software (Holcombe, R., 2017). Several distinct statistical parameters were employed, which provide different approaches to the problem of evaluating clustering in circular data.

Circular kurtosis calculates the *peakedness* of a distribution, relative to a resultant vector; positive values indicate a sharp peak, while negative values indicate a flat peak and, therefore, a weaker fabric. The kappa coefficient (κ), also known as the von Mises concentration parameter, is a reciprocal measure of dispersion. When κ is small, the measured distribution approaches a uniform isotropic model (a distribution with no preferred orientation), while high values of κ reflect a distribution that is concentrated about a single (mean average) direction. By contrast, circular variance ranges between 0 and 1, with low values reflecting a narrow spread in voids and a strong

preferred orientation. Conversely, high variance values, close to 1, imply a random spread in orientations and a lack of preferred orientation.

Each of these circular statistics relies on an underlying assumption that the dataset under investigation can be accurately described by a von Mises distribution (the circular analogue of a normal distribution). As a result, these statistical parameters measure clustering with respect to a resultant vector and are, therefore, only suitable for the analysis of uniaxial distributions. Analysis of multimodal distributions (biaxial and triaxial etc.) will produce inaccurate and misleading values (Mardia and Jupp, 2000, p19-23 and 36-40; Berens, 2009). For example, a perfectly biaxial fabric that demonstrates a large spread in orientations (e.g. intersection angles of ~90°), will produce a high variance value, a low kappa value and a negative kurtosis value, suggesting a weak or absent fabric. However, in this instance, the circular statistics have significantly underestimated the true fabric, which contains clear evidence of alignment with two preferred orientations. This effect is most prominently when analysing equal-strength multimodal fabrics and less problematic for pseudo-uniaxial fabrics that contain a dominant orientation and weaker secondary orientation.

In Table 6.1. circular statistics are calculated for several idealised distributions, including a perfectly isotropic (no orientation) dataset, a perfectly uniaxial dataset and several biaxial datasets. This allows the suitability of conventional circular statistics to be evaluated.

Fig.6.1 Image processing and extraction of void datasets. The reduction of a 255-channel greyscale SEM-BSE image to a bimodal matrix-void dataset requires thresholding in the *imagej* software. The exact position of the threshold is subjective and results in different numbers of small voids being included in the extracted dataset. Repeat analyses were performed to ensure an accurate representation of void orientations was achieved. After processing the original BSE (A) was compared against the thresholded image (B).

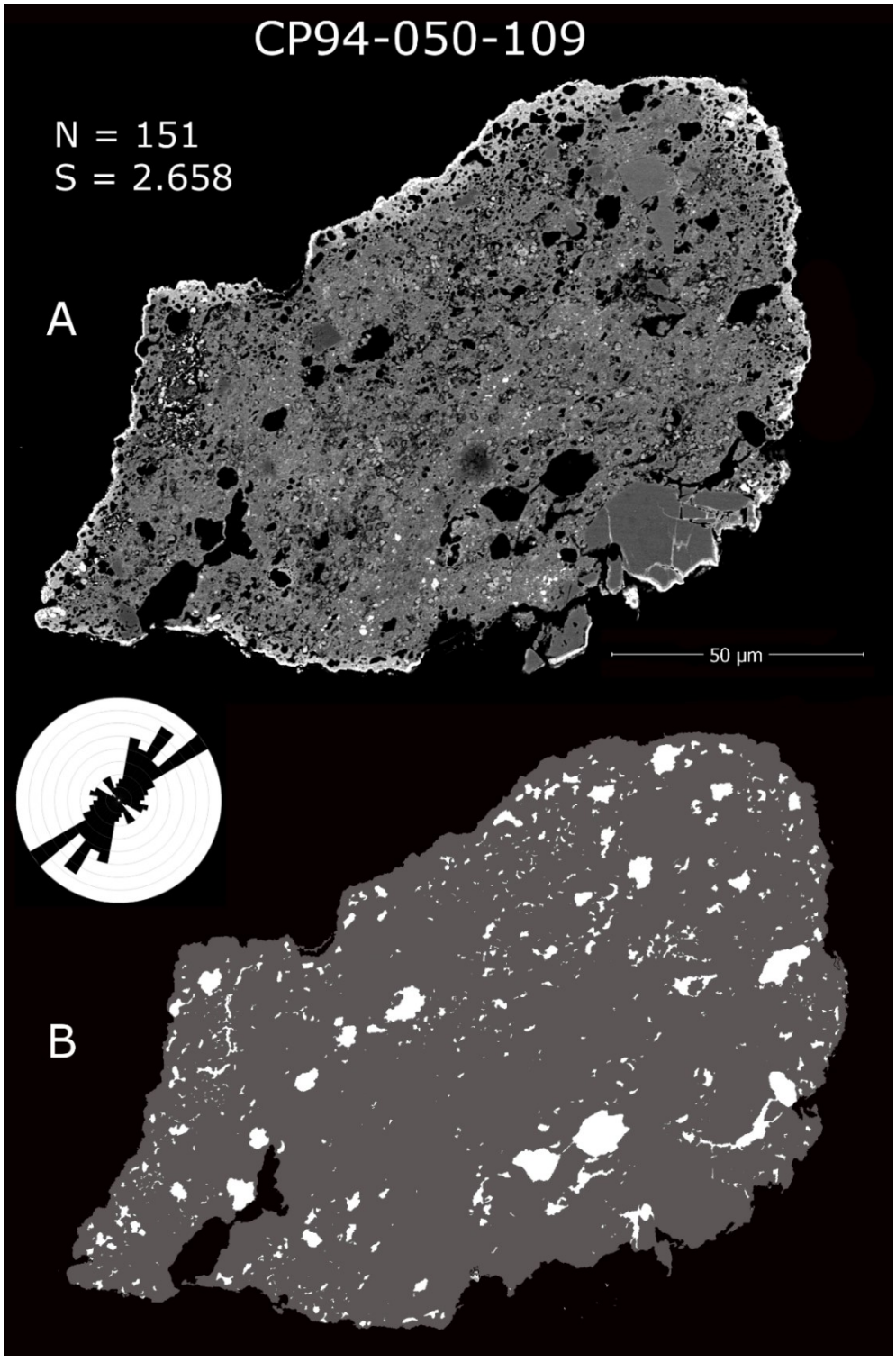

6.3.3. Quantifying petrofabrics using (statistical) entropy

Because multimodal fabrics are mistakenly interpreted as weak or non-existent, by conventional circular statistics, an additional statistical parameter, capable of analysing both uniaxial and multimodal distributions is required. Previously, Mohajeri and Gudmundsson, (2012) and Mohajeri et al., (2014) employed a simplified version of Shannon's (statistical) entropy. This was used to evaluate the degree of preferred orientation among street networks in urban settlements and fracture networks in Icelandic fault blocks. Using this equation, the void orientations in the fine-grained micrometeorite population were evaluated. A perfectly isotropic micrometeorite, with no preferred orientation, will produce a uniform circular rose diagram (Table 6.1). Conversely, a compacted micrometeorite, containing aligned voids will plot in a restricted arc (or, in the case of a multi-modal fabric, several arcs) on a rose diagram. This means that micrometeorites with low entropy rose diagrams contain a preferred orientation, while high entropy datasets are randomly orientated. The following entropy calculation was used:

$$S = -\alpha \sum_{i=1}^{t}(P_i \ln [P_i]) \qquad \text{-Eq.6.1}$$

Where: α is an arbitrary constant (in this case 1) that corrects for negative values, t is the number of bins on the rose diagram (in this case 18 bins of 10° each), and P_i is the percentage of voids aligned in each orientation. The natural logarithm of the entropy values (per bin) are summed to give a total, expressed as a dimensionless number. In this system maximum entropy, defined by an even distribution of voids in each bin (Table 6.1), gives a value of S_{MAX}=2.89. Entropy values calculated from the twenty-one micrometeorites range from S=2.17 to S=2.83.

Note: that the total number of bins, in this case 18, heavily affects the maximum entropy value (S_{MAX}=2.89) and, therefore, the absolute range in entropy values that a micrometoerite's petrofabrics can possibly occupy. By increasing the number of bins, the total entropy increases, which in turn allows greater distinction between similar rose diagrams. In this study, bins of 10° were selected as a compromise between a high entropy range and an appropriate sampling strategy for the density of the underlying data points (where N [the total number of voids considered] ranges from 31 to 1054).

The advantage of this entropy calculation is that no assumptions are made about the underlying distribution of the dataset, instead, the equation evaluates the degree of preferred alignment only on the basis of void partitioning. This calculation, therefore, provides a more robust assessment petrofabric that can evaluate both uniaxial and multimodal distributions together. In a low entropy system, and therefore a strong petrofabric, the majority of voids are concentrated into relatively few bins. This could be either as a single narrow arc or as multiple separate arcs. As long as the partitioning is the same, the clustering or location of the bins on the rose does not matter, the resulting entropy value will be the same. However, the entropy calculation does not provide an assessment of the fabric type; uniaxial fabrics cannot be distinguished from multimodal fabrics by their entropy values. Therefore, assessment of petrofabric type was performed subjectively by analysis of intersection angle between local maxima.

Table 6.1 Comparisons between standard direction statistics (reported from *GEOrient*) and entropy statistics (calculated using the method of Mohajeri and Gudmundsson, (2012) and Mohajeri et al., (2014)). An idealised set of void orientation datasets were constructed, which represent a range of uniaxial and multimodal distributions. The resulting circular statistics and entropy values are shown together for comparison. Attention is drawn to the disparity between the circ. variance and entropy values for multimodal fabrics. Because the entropy calculation does not weight fabric strength dependent on bin proximity, this statistic can accurately evaluate both uniaxial and multimodal petrofabrics.

No.	Fabric type, intersection angle (°)	Partitioned equally into X bins	Entropy (S)	Circ. Var (σ^2)	Circ. Kurtosis	Circ. Std. Dev. (°)	Kappa (κ)
1	Uniaxial, N/A	1	0.000	0.00	5.6295E+14	0.00	3.21686E+14
2	Uniaxial, N/A	2	0.693	0.00	-3091.86	5.01	32.91
3	Uniaxial, N/A	3	1.099	0.01	-1111.30	8.21	12.44
4	Uniaxial, N/A	4	1.386	0.02	-558.15	11.28	6.70
5	Biaxial, 90	2	0.693	1.00	0.94	237.11	0.00
6	Biaxial, 90	4	1.386	0.36	-8.27	53.84	0.35
7	Biaxial, 60	4	0.693	0.16	-39.50	33.73	1.15
8	Triaxial, 60	3	1.099	0.62	-0.10	80.13	0.04
9	Uniform/Isotropic, N/A	18	2.890	1.00	0.00	237.41	0.00

The entropy statistic, outlined above, was used to determine the presence and strength of petrofabrics in micrometeorites. Entropy values calculated for micrometeorites were compared against the entropy values calculated from two CM chondrites with known evidence of shock deformation: Cold Bokkeveld and Jbilet Winselwan. Both meteorites are classified as regolith breccias (Greenwood et al., 1993; 1994; Lee, 1993; Zolensky et al., 2016) and contain pervasive shock fabrics. Twinned calcite (Barber, 1981), elongated and flattened chondrules (Metzler et al., 1992), flattened CAIs (Greenwood et al., 1993; 1994) and fracture sets infilled by gypsum (Lee, 1993) are found in Cold Bokkeveld. Additionally, Jbilet Winselwan has experienced flash heating events, arising from intense impact and contains metal sulphide melt veins (Zolensky et al., 2016).

The entropy values for Cold Bokkeveld and Jbilet Winselwan are calculated at S=2.619 and S=2.783 respectively. These values provide context to the entropy statistics from the micrometeorites and therefore allow interpretation of petrofabric strength. An arbitrary cut-off value was set at S<2.78 (the value of Jbilet Winselwan). Any particles with entropy values greater than this threshold do not contain clear petrofabrics.

Because all the micrometeorites in this study were already set in resin, analysis of dehydration crack orientations is restricted only to the exposed 2D surface observable under SEM. *Plane of section* effects, therefore, prevent the direct measurement of voids which are orientated out of the plane of view. The rose diagram data are, therefore, only flattened two-dimensional approximations of a micrometeorite's true texture and thus any calculated petrofabric strengths are, at best, underestimates of the true fabric strength.

6.4. Results: Alignment of dehydration cracks in Antarctic micrometeorites

If the entropy value measured for Jbilet Wineselwan (S<2.783) is used as an arbitrary cut-off threshold, then 81% of micrometeorites (or seventeen out of twenty-one particles) show a preferred orientation in their alignment of voids (Table 6.2 and Figs 6.2 and 6.3). However, if the circular statistics (variance and kappa concentration factor), are also considered, then the number of micrometeorites with a well-defined petrofabric decreases and a clear split in the dataset is observed (Table 6.2 and Fig.6.4). Only ten micrometeorites (48%) contain combined low entropy values (S<2.78 [Jbilet Winselwan]), low variance values (σ^2<0.3) and high kappa values (κ>0.5). For these samples, there is a strong agreement between the conventional circular statistics and the entropy statistics. Among these micrometeorites, the null hypothesis (*that elongated voids within micrometeorites are randomly orientated)* can be rejected and, instead, it can be concluded that these samples contain well-developed petrofabrics.

For the remaining eleven micrometeorites (52%) their datasets contain greater dispersion and, therefore, evidence of preferred orientations is either weak or entirely absent. Three micrometeorites (CP94-050-110, CP94-050-127 and CP94-050-160) have low entropy values (S<2.619) but moderate variance (0.3<σ^2<0.45) and moderate kappa values (0.5>κ>0.41). The rose diagrams for these micrometeorites (Fig.6.3.5, 6.3.8 and 6.3.11) show voids concentrated into relatively few bins. However, since these bins are not clustered around a centroid, conventional circular statistics have underestimated the fabric strength. Each of these micrometeorites contains a multimodal fabric of moderate strength (biaxial in CP94-050-127 and CP94-050-160 and triaxial in CP94-050-110). In addition, eight micrometeorites have entropy values either S>2.75 or within error of this threshold (Fig.6.2:14-20 and Fig.6.3:14-20). For these micrometeorites, no obvious preferred orientation can be discerned from their rose diagrams and they are, therefore, classified as either possible fabrics or randomly orientated, and containing no fabric (see Table 6.2).

Among particles with a uniaxial fabric and a low entropy (S<2.78) more than 80% of voids plot in a narrow arc (40°-60°). However, as entropy increases, void orientations scatter and the dominant direction becomes less pronounced. Several micrometeorites contain biaxial fabrics with a small intersection angle (<40°) between void sets, this distribution is similar to conjugate fracture pairs formed in triaxial compression experiments (Wawersik and Fairhurst, 1970). Conversely, in CP94-050-127 (Fig.6.2.8 and Fig.6.3.8) void sets are perpendicular and present as a dominant and subordinate pair. Among 29% of the population (6/21 particles) the direction of the dominant void orientation is parallel to the elongation axis of the particle. This is clearly demonstrated by CP94-050-136, CP94-050-167 and CP94-050-109 (Fig.6.2.2, 6.2.3 and 6.2.7 and Fig.6.3.2, 6.3.3 and 6.3.7), which have well-defined fabrics and a clear particle elongation direction.

Both CM chondrites have biaxial fabrics (Fig.6.5), composed of a dominant and subordinate pair of voids. Although Cold Bokkeveld (S=2.619, σ^2=0.23, κ=0.75) has a stronger fabric than Jbilet Winselwan (S=2.783, σ^2=0.44, κ=0.20) both show similar intersection angles ~90° and 80-90° respectively. The

meteorite's intersection angles are, therefore, larger than those typically observed among the fine-grained micrometeorites.

For all samples, void length follows a power law distribution. This is shown in figure 6.6 (and calculated using data from CP94-050-109). A linear regression line (on a log-log plot) has been fitted to the data, demonstrating the power law relationship. During this investigation, a single micrometeorite (CP94-050-167, Fig.6.7), was identified which contains evidence of brittle deformation. This particle has a strong petrofabric (S=2.383, σ^2=0.11, κ=1.58) and an internal texture dominated by elongated and angular, olivine crystals. Crystals are tabular, compose approximately 50% of the particles exposed surface area, range in size from submicron to ~10µm in length and are geochemically homogenous. Particle CP94-050-167 is a member of mid-IR spectral group 5 (Chapt.4) and therefore the matrix is composed of submicron-scale, recrystallized olivine that replaced phyllosilicates during atmospheric entry. Iron-oxide grains are also present, most likely representing former Fe-sulphides phases (Taylor et al., 2012). However, the larger (pre-atmospheric) olivine crystals in CP94-050-167 are aligned with the elongation axis of the particle, creating a pervasive fabric. The clustered, Fe-oxides act as obstacles to alignment and force olivines to wrap around them, creating a weakly foliated texture. Abundant subparallel cracks are also present within the matrix and aligned parallel to the olivine crystals and elongation axis of the particle. In addition, two prominent shear fractures cut across the particle. These fractures intersect and split multiple olivine crystals, producing a distinctive cataclasis texture. The exposed jagged ends of the olivine crystals interlock and crystal grain size decreases notably towards the fracture plane. Adjacent to the shear fractures, olivine grains are rotated towards the fracture plane, allowing a dextral shear sense to be identified.

6.5. Discussion: The formation of petrofabrics in Antarctic micrometeorites

Petrofabrics were identified in up to 81% of the fine-grained micrometeorites analysed, ten particles contain strong evidence of well-defined uniaxial (and pseudo-uniaxial) fabrics, while three particles have multimodal fabrics. Other micrometeorites may be weakly aligned. Although these petrofabrics are defined by dehydration cracks, formed during atmospheric entry, their orientation is dependent on the pre-existing orientation of phyllosilicates, which is a parent body signature. Four potential formation mechanisms exist: (1) coarse-grained phyllosilicates aligned during aqueous alteration (2) crystals aligned by static compaction on a large planetesimal, analogous to burial of sediments on Earth, (3) alignment by compaction as a result of impact events, or (4) alignment by proto-sedimentary mechanisms such as accretion layering, fluidisation and liquefaction (Zolensky and Le, 2017).

(1) Coarse-grained phyllosilicate clusters are present in several of the C2 (CM-like) fine-grained micrometeorites (Chapt.3.2.3). These form by the replacement of anhydrous silicates and are typically found occupying cavities (vugs and veins) or infilling chondrules mesostasis (Tomeoka and Buseck, 1988; Zolensky et al., 1993). Crystals can reach several microns in length and commonly exhibit clearly defined cleavage planes. However, these components are highly localised and relatively rare components of the hydrated chondritic assemblage. Furthermore, several distinct coarse-grained

clusters are unlikely to be aligned in the same orientation, therefore, it is unlikely that aqueous alteration is responsible for the observed petrofabrics.

(2) Alternatively, terrestrial shales and mudstones are composed primarily of phyllosilicates. These rocks develop bedding-parallel fabrics during burial, as phyllosilicates align (and recrystallize) under confining pressure (Fossen, 2010). On Earth, the overburden necessary for phyllosilicate alignment is approximately 2400m (Ho et al., 1999; Day-Stirrat et al., 2008). However, the alignment of phyllosilicates in marine sediments also requires the loss of pore fluid, fluid overpressure and, potentially recrystallization during diagenesis (Ho et al., 1999; Day-Stirrat et al., 2008). However, if a simplistic scenario is assumed, in which pore fluid is negligible, the effective pressure at 2400m below the water-sediment interface will simply be a product of the entire vertical stress of the overlying sediment, transmitted by grain-to-grain stress bridges, plus the weight of the overlying water column. By using an average ocean water depth value of 2000m and a generic crustal sediment density ($2500 kgm^{-3}$) the effective pressure needed to generate aligned phyllosilicates in terrestrial shales is approximately 78.5MPa (see Chapt.6.11 [supplment]). Calculations for the core pressure in the four largest C-type asteroids (see Chapt.6.11 [supplment]) suggest that only asteroids >300km in diameter are able to support internal pressures sufficient to generate aligned phyllosilicates by static compaction. This strongly implies that the petrofabrics present in fine-grained micrometeorites did not form by compaction and, instead require an alternative process.

(3) Impact events were common in the early solar system (Melosh, 2011). Hydrated carbonaceous chondrites contain abundant pore space, which during an impact event, experiences compaction as the shock wave rapidly attenuates (Davison et al., 2012; Rubin, 2012; Lindgren et al., 2015). Shock deformation, therefore, primarily affects the outer layers of an asteroid. In these layers, shocked phyllosilicates align perpendicular to the local surface (Fossen, 2010, p41-46) as successive impact events, impinging over a range of random angles, result in non-coaxial shear. Initially, immature multimodal fabrics are produced, whose intersection results in the secondary lineation fabrics (Gattacceca et a., 2005; Smith et al., 2006; Hanna et al., 2015), however, with continued compaction, previous petrofabrics are progressively overprinted (Smith et al., 2006) and, ultimately develop into a single dominant, uniaxial petrofabrics (Fossen, 2010, p41-46; Smith et al., 2006; Lindgren et al., 2015). The range of petrofabrics observed within this fine-grained micrometeorite population is, therefore, consistent with an impact-processing origin.

(4) Finally, the alignment of platy minerals, such as phyllosilicate and elongate olivine grains, may also be possible through proto-sedimentary mechanisms. Zolensky and Le (2017) described layered olivine grains forming a lithic clast within the CV3 meteorite Vlgarano. They attribute the formation mechanism for this petrofabric to a sedimentation process involving [the flow] of "*large quantities of fluid*", resulting in features similar to the "*dish structures*" commonly found in terrestrial siltstones and sandstones. Such structures form by liquefaction and fluidsation of water-charged soft sediments. Likewise, the large flat areas observed on several asteroids, occasionally termed "*asteroid ponds*", are also preseumed to form by the same processes. Thus, it is also possible that the aligned phyllosilicate in fine-grained micrometeorites, observed in this study, could be a product of parent body sedimentary mechanisms operating in micro-gravity.

Table 6.2. Circular statistics and entropy data for the twenty-one micrometeorites analysed in this chapter. Data for CM chondrites (Cold Bokkeveld and Jbilet Winselwan) are also included as reference standards. Error margins for calculated entropy values vary by <0.12. Entries shown in black have low entropy values (S<2.78 [Jbilet Winselwan]), low variance values (σ^2<0.3) and high kappa concentration factors (κ>0.5) and, therefore, demonstrate well-defined preferred orientations and consequently strong petrofabrics. By contrast, entries shown in grey, have higher variance values and lower kappa concentration factors, although their entropy values may still be less than the entropy value for Cold Bokkeveld. The presence of petrofabrics in these particles carries a higher degree of uncertainty. Four micrometeorites were found to contain entropy values greater than Jbilet Winselwan and are considered as unaligned samples (no petrofabric).

No.	Sample	Type	N=?	No. of Fabrics (Subjective)	Fabric parallel to elongation axis	Entropy (S)	$S<S_{cutoff}$	Circ. Var (σ^2)	Circ. Kurtosis	Circ. Std. Dev. (°)	Kappa (κ)
1	CP94-050-079	ScMM	40	Biaxial	No - perpendicular	2.17	Positive	0.10	-40.74	26.84	1.71
2	CP94-050-136	FgMM	31	Uniaxial	Yes	2.31	Positive	0.13	-18.4	30.52	1.38
3	CP94-050-167	FgMM	175	Uniaxial	Yes	2.38	Positive	0.11	-29.4	28.14	1.58
4	CP94-050-140	FgMM	32	Biaxial	No - oblique	2.51	Positive	0.21	-7.93	39.78	0.82
5	TAM19B-7	FgMM	445	Uniaxial	No elongation direction	2.60	Positive	0.18	-11.25	36.41	1.00
6	CP94-050-110	FgMM	90	Triaxial	No - oblique	2.62	Probable	0.44	-0.89	62.08	0.19
7	CP94-050-170	FgMM	72	Uniaxial	No - oblique	2.64	Probable	0.23	-7.14	41.13	0.76
8	CP94-050-109	ScMM	151	Uniaxial	Yes	2.66	Probable	0.21	-5.67	38.85	0.87
9	CP94-050-127	FgMM	88	Biaxial	No - elongation axis	2.71	Probable	0.33	0.08	51.18	0.41
10	CP94-050-123	FgMM	121	Uniaxial	No - oblique	2.71	Probable	0.25	-3.78	43.07	0.68
11	CP94-050-096	FgMM	79	Uniaxial	Yes	2.73	Probable	0.24	-5.34	42.56	0.7
12	CP94-050-160	FgMM	107	Biaxial	No - perpendicular	2.73	Probable	0.37	-1.49	54.72	0.33
13	CP94-050-139	FgMM	90	Uniaxial	Yes	2.74	Probable	0.27	-3.19	45.69	0.58
14	CP94-050-163	FgMM	187	Biaxial	Yes	2.74	Probable	0.35	-0.74	53.3	0.36
15	CP94-050-142	FgMM	74	Uniaxial	No - perpendicular	2.75	Probable	0.36	-1.1	53.82	0.35
16	CP94-050-152	FgMM	78	Biaxial	No - oblique	2.75	Probable	0.41	-0.99	58.54	0.25
17	CP94-050-074	FgMM	66	Uniaxial	No - elongation axis	2.75	Probable	0.34	-1.17	51.95	0.39
18	CP94-050-270	FgMM	134	None	No fabric	2.80	Negative	0.34	-2.1	52.57	0.38
19	CP94-050-054	FgMM	155	None	No fabric	2.82	Negative	0.38	-0.89	56.29	0.29
20	CP94-050-048	ScMM	98	None	No fabric	2.82	Negative	0.52	-0.48	68.99	0.11
21	CP94-050-168	FgMM	214	None	No fabric	2.83	Negative	0.53	-0.05	70.9	0.09
22	Cold Bokkeveld	CM2.2	1054	Uniaxial	-	2.62	Positive	0.23	0.32	41.43	0.75
23	Jbilet Winsewlan	TM-CM	950	Biaxial	-	***2.78***	*Threshold value*	0.44	0.36	61.52	0.2

Fig.6.2. SEM-BSE Image panel of twenty unmelted fine-grained micrometeorites analysed for evidence of aligned voids. This figure should be cross-referenced with fig.6.4, which illustrates the extracted void orientation datasets for each micrometeorite, displayed as rose diagrams. Scale bars in this image panel are 50μm.

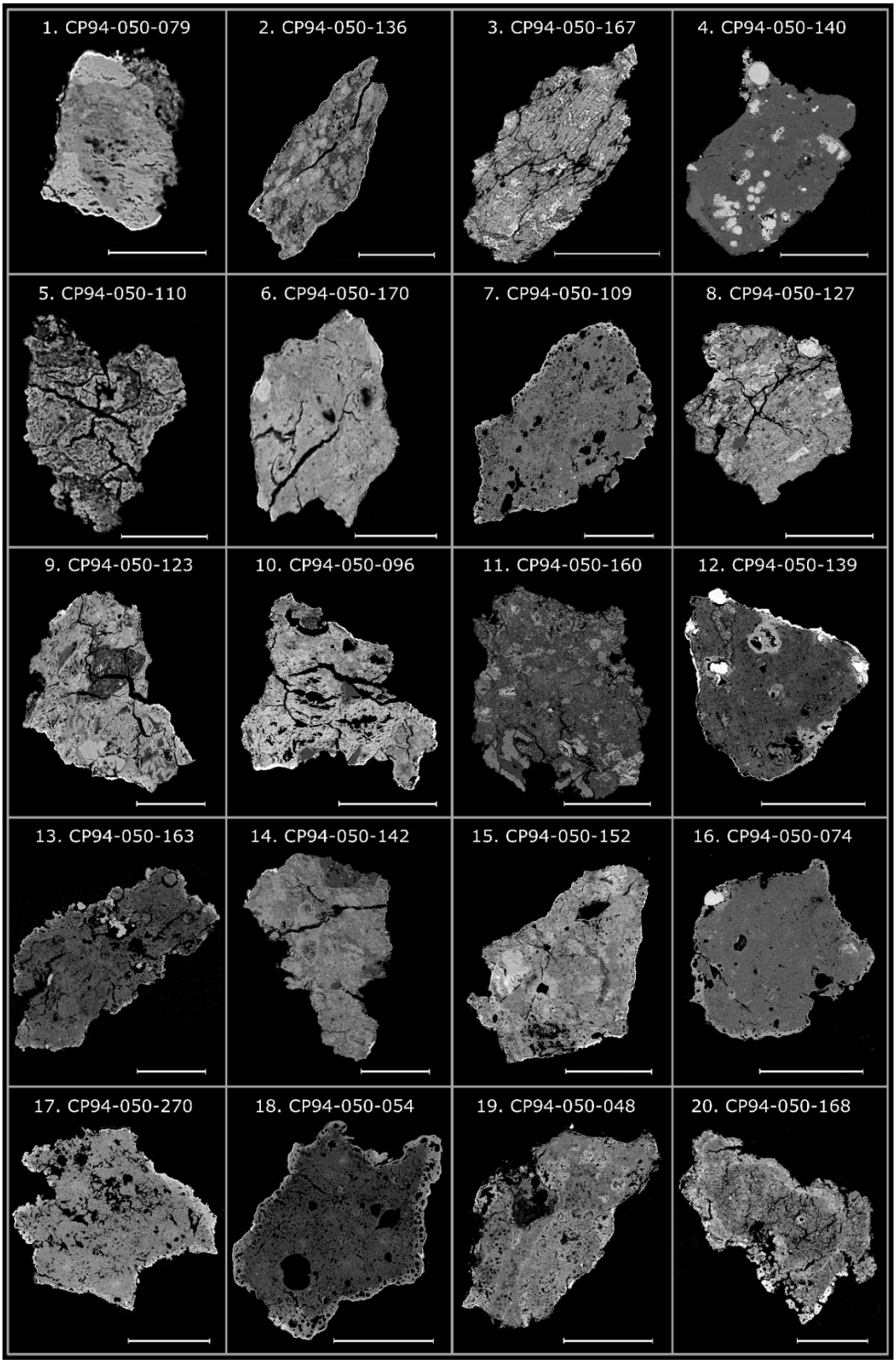

Fig.6.3. Rose diagrams, showing the orientation of elongated and sub-linear voids in twenty fine-grained micrometeorites. Petrofabric strength decreases with increasing frame number. The metadata for each rose is shown below and includes N the number of cracks analysed, S the entropy value and F the fabric type; either uniaxial (U), biaxial (B), triaxial (T) or absent (X).

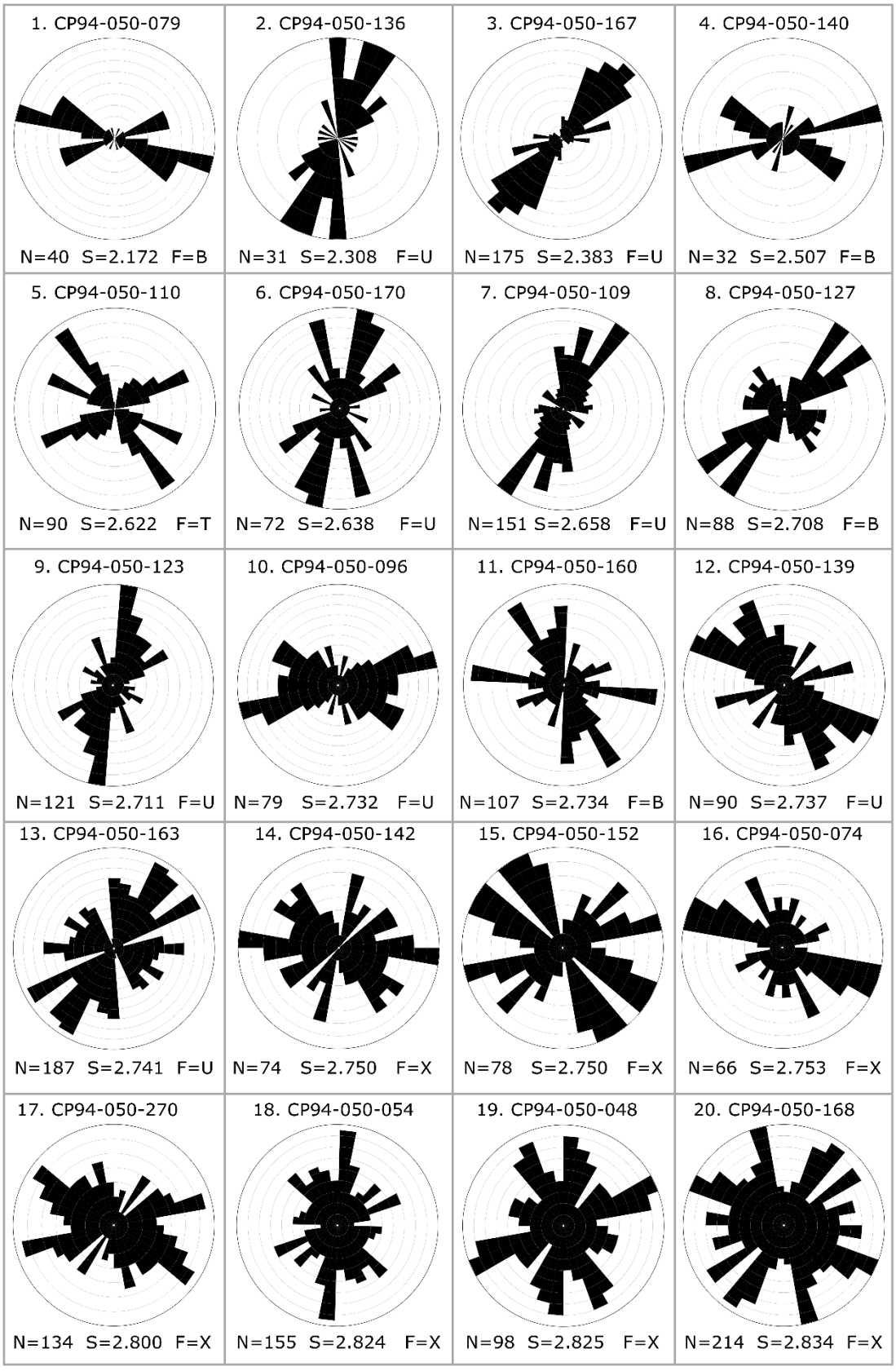

Fig.6.4. The relationship between conventional circular statistics and entropy statistics is investigated in these plots: (A) Entropy vs. circ. variance and (B) entropy vs. kappa concentration factor. Micrometeorites are plotted as black circles and CM chondrites as grey-infilled circles. 2nd order polynomial regression lines (R^2=0.61 and R^2=0.80) are fitted to the data, emphasising the close relationship between these two statistical analyses. The threshold values for entropy (S<2.62), circ. variance (σ^2<0.3) and kappa (κ>0.5) are illustrated by dashed grey lines.

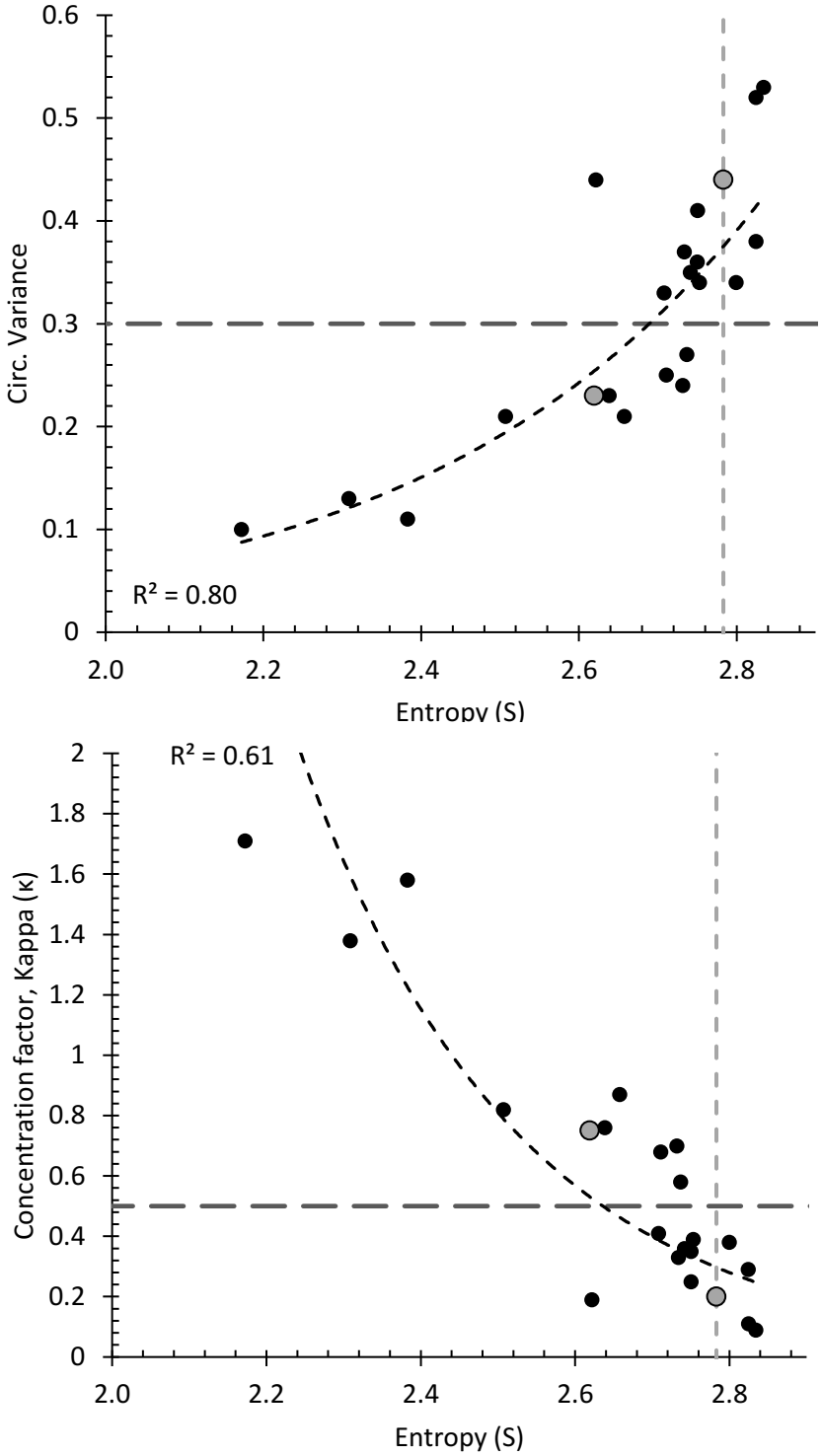

Fig. 6.5. Petrofabrics in Cold Bokkeveld and Jbilet Winselwan. SEM-BSE images of each chip shown with their rose diagram datasets. Both chondrites contain biaxial fabrics, characterised by a dominant and subordinate pair of orientations. Though these were not explicitly analysed in this study, both chondrites appear to contain flattened chondrules which are aligned with the dominant fracture orientation. Scale bars are 3000µm.

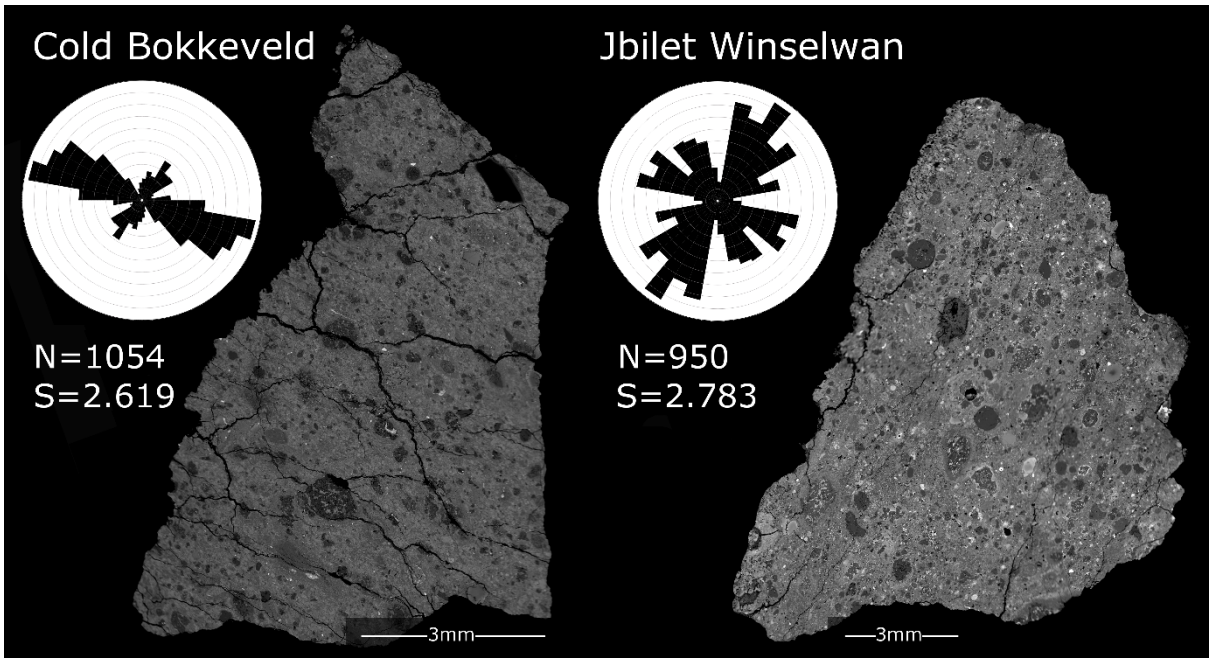

Fig.6.6. Log-Log plot showing the cumulative number (N) of cracks greater than length (L) in CP94-050-109. A linear regression line on a log-log plot indicates a power law relationship, this is the expected size distribution profile for all fracture networks.

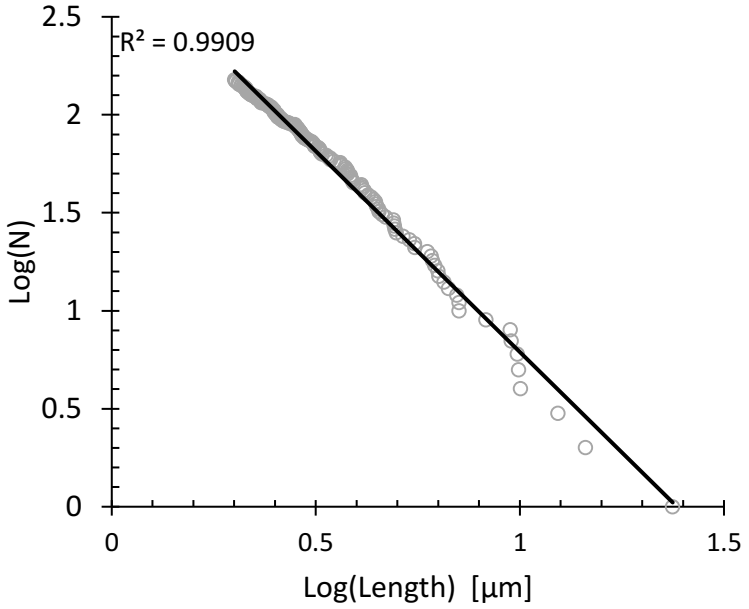

6.6. Discussion: Cataclasis fabric in CP94-050-167

Fine-grained micrometeorites containing brittle deformation features have not previously been described. However, in particle CP94-050-167, two grain-scale shear fractures were observed (Fig.6.7), these cut through olivine grains, generating a cataclasis texture, composed of crushed and rotated crystals. Brittle deformation features have been reported within the anhydrous chondrules of CM2 Murchison (Hanna et al., 2015), but, to date not within the hydrated matrix. This could be because rock samples with high phyllosilicate abundances (>15% volume), are likely to accommodate deformation by ductile plastic strain responses, primarily through the flow and rotation of grains (Fossen, 2010, p120-148). Conversely, in phyllosilicate-poor rocks or rocks with abundant cement, brittle failure and cataclastic flow tend to prevail. Since CM and CI lithologies are porous, hydrated and contain >60% volume phyllosilicates (Howard et al., 2009), deformation by phyllosilicate smearing and movement along ductile disaggregation bands is predicted (Fossen, 2010, p120-148).

However, the dominant deformation response in CP94-050-167 is a brittle cataclastic failure. For intragranular deformation to be the favoured strain response in a lithology prone to ductile deformation requires that this particle experienced relatively high strain rates during compaction. Niemeijer and Spiers (2005) empirically constrained the brittle response threshold for phyllosilicate-bearing rocks to slip velocities of >1µm s^{-1} (and whilst under a normal stress field of 5MPa). For terrestrial settings, such as within tectonic fault blocks, these slip velocities are high. However, for extraterrestrial impact scenarios, this slip rate is orders of magnitude less than the typical slip velocities experienced, where strain rates are typically between 10^2-10^3 s^{-1} and slip velocities may exceed ~150m s^{-1} (Kimberley and Ramesh, 2011). Thus, the brittle deformation of hydrated chondritic matrix during impact, therefore, seems probable under most impact conditions.

The brittle deformation response of hydrated chondrites was explored further by several research groups through light gas gun disruption experiments on meteorite targets (Durda and Flynn, 1999; Tomeoka et al., 1999 and Flynn et al., 2009). For example, Tomeoka et al., (1999) conducted experimental shock metamorphism tests on the CM chondrite Murchison. They were able to produce subparallel fractures, similar to those observed in CP94-050-167, within the phyllosilicate-rich matrix of CM2 Murchison, using a light-gas gun impact experiments and peak pressures >15GPa. However, at peak pressures lower than this threshold, they did not observe matrix hosted fractures. Assuming a fixed impactor size, a strain rate comparison is possible, and suggests that brittle deformation responses within the phyllosilicate-bearing matrix of CM chondrites requires a minimum impact pressure of approximately 15GPa, equivalent to an S3 shock stage, and correspondingly high strain rates, before the matrix will develop internal cataclastic textures, similar to those identified in CP94-050-167 (Tomeoka et al., 1999).

Fig.6.7. Brittle deformation in a fine-grained micrometeorite. A cataclasis fabric and shear band deformation zones are identified within CP94-050-167. A) SEM-BSE image of CP94-050-167, with magnified areas C and D shown. A pervasive (E-W trending) fabric can be discerned, highlighted by the alignment of olivine crystals and fractures. B) A schematic sketch of CP94-050-167 illustrates the inferred stress regime and highlights several prominent fractures and position of the cataclastic shear band. C) A zone of local shear, cutting through both matrix phyllosilicates and olivine grains has caused clockwise rotation of material towards the shear zone. D) Grain size decreases towards the fracture plane.

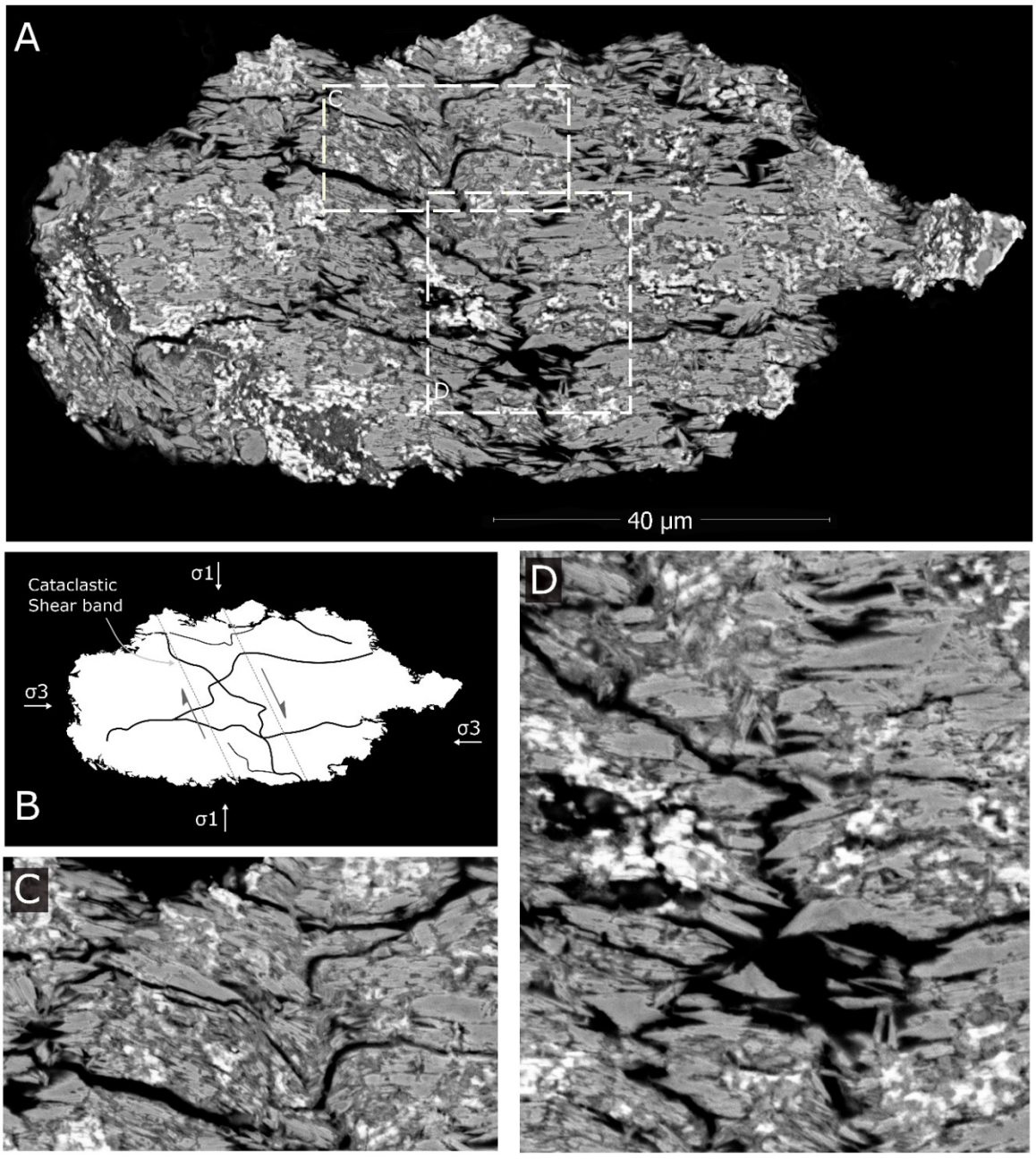

6.7. Discussion: Limitations of 2D petrofabric analysis

Several limitations and assumptions are inherent in the 2D image analysis technique, outlined in this chapter. This section addresses the main problems with data extraction and interpretation. Given these limitations, this analysis should be considered a preliminary study, which points towards the existence of petrofabrics in (most) fine-grained micrometeorites.

6.7.1. Proxies vs. direct measurement of petrofabrics

Previously, petrofabrics in carbonaceous chondrites were identified using electron backscatter diffraction (EBSD, Watt et al., 2006), µCT (Friedrich et al., 2008; Hanna et al., 2015; Lindgren et al., 2015) and X-ray goniometry (Fujimura et al., 1982; 1983). However, these techniques are not viable for use on thermally altered, amorphous materials, nor recrystallized micrometeorites that no longer contain phyllosilicate crystals for measurement. Additionally, the small size of most dehydration cracks lies at the imaging resolution of current µCT techniques. Therefore, void orientations in micrometeorites, measured from high-resolution SEM-BSE imaging was the only suitable proxy for this investigation. Additionally, the ease of data extraction and analysis of this approach allows micrometeorites with notably strong fabrics to be identified and directed towards more rigourous analysis techniques (e.g. serial sectioning).

6.7.2. CM chondrites as reference standards

The two CM chondrites chosen as reference standards provides this study with examples of petrographically similar materials that contain known shock fabric textures. However, since the chondrite chips are approximately 10-50 times bigger than the micrometeorites they are compared against, it could be argued that the nature of the voids within the two populations are different. Voids in the CM2 chondrites are primarily fractures arising, either from shock deformation or residence, collection and dehydration during storage on Earth. By contrast, the voids within the micrometeorites are primarily products of atmospheric entry heating (dehydration cracks). Despite, this difference in origin, both void types are brittle deformation features within a fine-grained (or amorphous) matrix and exploit pre-existing anisotropies. Therefore, both void types are governed by the orientation of the host rock's phyllosilicates. Consequently, comparison of the CM2 chondrite voids to the fine-grained micrometeorite voids remains justified.

6.7.3. Extraction of void orientations by image processing

The greatest source of error in this petrofabric analysis lies in the image analysis procedure. The reduction of a 255-channel greyscale BSE image to a bimodal matrix-void dataset requires a subjective assessment of where to place the threshold. The researcher must define a single point in the image's look up table as the threshold above which all values are white (matrix) and all below which, all values are black (voids). The placement of this threshold position is arbitrary since voids have different greyscale values, dependent on the environmental conditions and software settings during imaging. However, several tests were performed in which the threshold was placed at different values. This produced similar rose diagrams and similar entropy values. Repeat

experiments, therefore, demonstrated that the presence of petrofabrics in the majority of particles is not a statistical artefact.

6.8. Discussion: shock fabrics during entry heating

Six micrometeorites were identified with uniaxial petrofabrics aligned parallel to the elongation axis of the particle. Among these micrometeorites, the pre-existing petrofabric was likely important in defining fragmentation dynamics. However, since several micrometeorites (between 30-40%) did not contain discernible petrofabrics, asteroids are also capable of disrupting without imparting a petrofabric onto the liberated dust. Furthermore, the majority of micrometeorites analysed in this chapter have also been analysed by EMPA (Chapt.3), mid-IR spectroscopy (Chapt.4) and Raman spectroscopy (Chapt.5) and no correlation were identified between these datasets and a particle's petrofabric entropy statistics. This suggests that micrometeorite liberation does not alter the micrometeorite's mineralogy, organic matter or geochemistry significantly and instead, atmospheric entry heating remains the most important overprint process affecting a micrometoerite's petrography. In addition, the presence of micrometeorites with well-defined elongation directions may result in atmospheric entry heating profiles that differ significantly from the predictions of heating models, thereby producing anomalously low or high peak temperature samples.

6.9. Implications: asteroid parent bodies of fine-grained micrometeorites

The conclusions in this chapter support findings from previous studies on CM2 chondrites, which demonstrate a close relationship between intense aqueous alteration and pervasive shock fabrics (Barber, 1981; Fujimura et al., 1983; Lee, 1993; Hanna et al., 2015 and others). However, these combined observations are inconsistent; small, unshocked asteroids cannot develop petrofabrics by simple static compaction (Chapt.6.5 and 6.11). Instead, impact events are required to impart detectable petrofabrics (Lindgren et al., 2015). To reconcile these apparently conflicting observations Lindgren et al., (2015) suggested that the CM parent body (or bodies) most likely avoided hypervelocity impacts during accretion and instead, developed shock fabrics through successive low-intensity impact events (<5GPa). However, simulations of the early solar system argue that hypervelocity impacts were common and the survival of large (>100km) asteroids which evaded all hypervelocity collisions is extremely unlikely (Davison et al., 2013).

Alternatively, Tomeoka et al. (2003) and Rubin (2012) suggested that the high porosity of CM2 chondrites provides a suitable mechanism for the efficient dissipation of impact energy, thereby allowing CM2 chondrites to withstand hypervelocity impacts without inheriting high-grade shock deformation features. This is because the closure of pore space preferentially absorbs shock energy, shielding the anhydrous index minerals from high shock pressures and effectively making most index minerals unreliable indicators of a meteorite's true shock history. This compaction and attenuation mechanism most likely plays an important role in explaining the shock features among hydrated chondrites. However, empirical observations from impact experiments also show that hydrated, chondritic lithologies favour fragmentation over compaction (Durda and Flynn, 1999; Flynn et al., 2009). Under impact (>5kms^{-1}) Murchison produces abundant 100µm-scale dust grains, similar in both

size and mineralogy to fine-grained micrometeorites. The friable nature of these samples, the low compressive strength and the dissipation of energy by pore space collapse, therefore, appears an efficient set of mechanisms that is capable of explaining the absence of shock deformation features recorded in their host olivine grains. The dehydration of phyllosilicates can also be ruled out because the majority of fine-grained microemteorites (and CM chondrites) enter the Earth's atmosphere as hydrated objects (Chapt.4 and Genge, 2006; Nakato et al., 2008; Genge et al., 2017b).

As a result, it seems probable that instead of avoiding hypervelocity impacts, CM parent bodies have, experienced large-scale impact events throughout the solar system's history. For small bodies – whose disruption threshold is strength-dominated rather than gravitionally-dominated – they are likely to respond to high-energy impact events by catastrophic disruption and subsequent re-accretion, forming small, loosely aggregated rubble-pile asteroids (Benz and Asphaug, 1999; Britt and Consolmagno, 2000). Thus, the ability of the CM2 lithology to dissipate impact energy by break-up would then explain the lack of high-grade shock features (preserved in olivine crystals), whilst explaining the presence of subtle shock fabrics, which developed during high-intensity events.

It should also be noted that the inferred and measured densities for prominent C-type asteroids range from 1300-3000kgm^{-3}. These values are much lower than expected for an asteroid composed of CM2 material (Britt and Consolmagno, 2000). As a result, C-type asteroids must contain abundant macroporosity in the form of metre-scale voids (Britt and Consolmagno, 2000; Carry, 2012) to account for this density deficit. In addition, CM2 and CM-like materials are the most common micrometeorite type (Brownlee et al., 1997; Taylor et al., 2012), as well as the principal contaminant among Lunar regolith (Wasson et al., 1975) and are even identified as fossil micrometeorites embedded in ordinary chondrites (Gounelle et al., 2003) and howardites (Wilkening, 1978). This implies that the CM parent body (or bodies) may have experienced significant disruption events both, in the early solar system and in the recent geological past, shedding abundant material into interplanetary space. Therefore, a low compaction strength, a tendency to disrupt, as well as the observation of anomalously low-density C-type asteroids and the ubiquity of CM2 chondrite materials as contaminants on other rocky solar system objects (Wilkening, 1978) all imply that the CM parent body is no longer intact and instead remains as a series of rubble-pile relict asteroids, micrometeorites and interplanetary dust particles.

6.10. Conclusions from quantitative void analysis

Dehydration cracks in thermally altered, unmelted fine-grained micrometeorites form during atmospheric entry and act as proxies for the pre-atmospheric orientation of phyllosilicate crystals. By quantitatively analysing crack orientations this study demonstrated the first evidence of pervasive, grain-scale fabrics within micrometeorites. The occurrence of biaxial fabrics and brittle deformation features suggest that petrofabrics are impact-generated at shock pressures between 78.5MPa-15GPa. Although micrometeorites contain aligned phyllosilicates, other high-grade shock features, such as planar fractures in olivine grains, are absent.

Because CM2 chondrites and fine-grained micrometeorites have not been recognised with shock stages >S3, this may suggest that small-sized parent bodies of hydrated, primitive chondritic materials, which lack sufficient gravitational energy to prevent disruption, cannot survive hypervelocity impacts without mechanical failure, disruption and later re-accretion. This suggestion is supported by laboratory impact experiments on CM2 chondrites, anomalously low-density C-type asteroids and the abundance of CM-like dust throughout the solar system.

6.11. Supplemental: Can phyllosilicate alignment on asteroids be generated by static compaction?

A) Overburden pressure required in terrestrial shales for phyllosilicate alignment: Phyllosilicate alignment occurs as a result of compaction pressure during burial. Empirical observations suggest a minimum of 2400m of marine shales (and overlying seawater) are required before sufficient pressure is achieved. Near the Earth's surface pressure may be calculated as:

$P = \rho * g * h$ – Eq.6.2

Where: ρ is the density of the material, g is the gravitational acceleration [$9.81 ms^{-2}$] and h is the depth of the buried material. For the buried shales the pressure would be:

Water column (P_1) = $1000 kgm^{-3} * 9.81 ms^{-2} * 2000 m = 1.96 * 10^7 Pa$
(*Assuming an average depth of overlying seawater [2000m])*.

Sediments (P_2) = $2500 kgm^{-3} * 9.81 ms^{-2} * 2400 m = 5.89 * 10^7 Pa$
(*Assuming an average value for terrestrial sediments [$2500 kgm^{-3}$])*.

Total Pressure (P_T) = $7.85 * 10^7 Pa$ = **78.5MPa**

B) Overburden pressure estimates for large (C-complex) asteroids: The pressure at the centre of a small asteroid is simply a product of the weight of overburden. In this instance Eq.2 cannot be used as this linear relationship does not account for variations in g and ρ with depth, and would therefore result in a significant overestimate of core pressure. A more accurate equation is shown below, which provides an approximation of core pressure that accounts for variations in g with depth. This equation employs a static, average density value that is calculated as a product of the asteroid's mass and volume.

$P = (^3/_8 \pi) * (GM^2/R^4)$ – Eq6.3

Where: G is the universal gravitational constant [$6.67E^{-11}$], M is the total mass of the asteroid and R is the radius of the asteroid. Empirical mass and radius values, taken as averages of the data listed in Baer et al., (2012), were used to calculate the approximate core pressure on the four largest C-complex asteroids. Results are shown in table below:

Asteroid	**Diameter** (km)	**Volume** (m^3)	**Mass** (kg)	**Inferred average density** (kgm^{-3})	**Gravitational acceleration** (g) at surface (ms^{-2})	**Core pressure** (MPa)
(1) Ceres	975	4.85E+17	9.36E+20	1930	0.26	1220
(10) Hygiea	407	3.53E+16	8.79E+19	2490	0.14	354
(52) Europa	302	1.44E+16	4.00E+19	2775	0.12	242
(65) Cybele	290	1.28E+16	1.33E+19	1039	0.04	31

These results suggest that aligned phyllosilicates, produced as a result of static compaction, may only be possible on the largest C-type parent bodies; those with diameters >300km. But also that core pressure is heavily dependent on material density.

Chapter 7: The role of volatile gases during atmospheric entry

7.0 Overview This chapter explores the petrography of four giant (>250µm) micrometeorites, which were found to contain abundant, interconnected, secondary pore space. Evidence of enhanced heating adjacent to pore walls and observations of a single particle containing a double-walled igneous and magnetite rim, suggest that fragmentation of micrometeorites during atmospheric entry may be common. As incoming extraterrestrial dust is flash heated a layer of melt develops on the micrometeorite exterior, forming an igneous rim that slowly migrates inwards. However, inside the micrometeorite, dehydration cracks develop as phyllosilicates contract and interlayer water is lost. This leads to additional internal heating, driven by the decomposition of low-temperature phases and the release of volatile gases, which then flow through the particle heating the matrix. Furthermore, as these gases become trapped by the igneous rim, internal pressure rises, driving crack growth and leading to the establishment of interconnected void networks. If heating continues the igneous rim is eventually breached and gas exchange with the atmosphere can occur. The importance of volatile gas-driven heating lies in the breakdown of conductive rim-to-core thermal gradients and instead allows particle-wide heating via the convective flow of gases. Interconnected void networks also lower the mechanical strength of particles and increase the likelihood of particle fragmentation during entry. This may, therefore, provide a causal explanation for the rarity of large fine-grained CM-like micrometeorites among collections.

7.1. Micrometeoroid evolution during atmospheric entry

Prior to partial melting and the formation of scoriaceous micrometeorites, the early stages of micrometeorite entry are characterised by the decomposition of low-temperature phases (<1000°C) held within the micrometeorite core (Toppani et al., 2001; Taylor et al., 2011) and their subsequent recrystallization as an anhydrous (metamorphic) groundmass (Chapt.4). On the particle exterior a thin melt layer develops (Toppani and Libourel, 2003; Genge, 2006). Genge et al., (2017b) demonstrated how hydrated fine-grained micrometeorites can support extremely high thermal gradients during entry, through the progressive thermal decomposition and melting of water-bearing phyllosilicates at the particle margin. Likewise, high thermal gradients were also inferred from several micrometeorites in this thesis, which were analysed by Raman spectroscopy. In these particles, the micrometeorite core retained highly disordered carbonaceous phases, suggesting peak temperatures did not exceed 700°C (Chapt.5). Thus, it would appear that most small fine-grained micrometeorites maintain core-to-rim thermal gradients by conductive heating during atmospheric deceleration.

However, as peak temperatures rise, simple conductive core-to-rim thermal gradients appear to break down. In Chapter 5, Raman line transects through some micrometeorites (as in CP94-050-109) produced erratic profiles, instead of the more common zoned profiles (Fig5.8H.). In these micrometeorites disordered carbonaceous phases were absent and, instead, nanocrystalline graphitic carbon was present. This suggests that as temperatures rise, or the duration heating increases, new mechanisms of thermal reprocessing develop that more efficiently heat the particle interior. It was also noted in Chapter 5 that the development of a vesicular matrix appeared to be correlated with the loss of zoned Raman profiles (sect.5.2).

Recent experimental studies conducting flash heating experiments on micrometeorite analogues have suggested that volatile gases may play a significant role in the heating of micrometeorites (Court and Tan, 2016). In particular, decomposing sulfides release SO_2 and SO_3 that interact with organic carbonaceous matter in secondary carbothermic reactions. This has the effect of increasing the volume of gases produced and lowering the peak temperatures at which gas production occurs.

In this chapter, four giant micrometeorites are investigated whose atmospheric entry history appears to have been defined by the generation of volatile gases. These micrometeorites contain abundant interconnected secondary pore space, formed by linked dehydration cracks and vesicles. The walls of these voids are also lined with Fe-rich rims, representing the melting and preferential evaporation of volatile elements. These features imply the thermal decomposition of low-temperature phases and the subsequent release and flow of volatile gases is a critical process in the petrologic evolution of micrometeoroids during atmospheric entry heating. The development of these internal voids also increases the probability of atmospheric disruption events by weakening the mechanical strength of the micrometeorite (Genge, 2008b) and, therefore, could explain the paucity of giant fine-grained micrometeorites among micrometeorite collections.

7.2. Results: Giant micrometeorites and their atmospheric entry characteristics

Four of the giant TAM micrometeorites (TAM19B-7, TAM19-7, TAM2.1Q and TAM37P-03, Figs.7.1-7.4) are investigated in this chapter. These particles contain significant atmospheric entry overprints. Textures relating to the generation of volatile gases and partial melting are the main focus of this chapter.

All four micrometeorites contain well-developed but incomplete magnetite rims that encircle the particle exterior and vary in thicknesses between 1µm and 15µm. Igneous rims are found in close association with magnetite rims and vary in thickness between 5µm and 50µm. For all micrometeorites, the particle matrix is homogeneous on >10µm length scales and contains significant pore space, either in the form of small (<20µm) isolated, circular or elongated voids or as long channels (typically >100µm, Figs.7.1-7.3). These channels are composed of interconnected networks of thin dehydration cracks and rounded, broadly circular vesicles. Channels reach up to 300µm in length and typically have winding and branching (dendritic) profiles. Several channels terminate at the particle's perimeter (Fig.3C), and although widths are variable (typically <5-30µm), in general, channels narrow towards the particle core. Several large voids and most channels contain Fe-rich linings (<5µm thick), which in TAM19B-7 are composed of magnetite, while in TAM19-7 are composed of non-stoichiometric Fe-oxide phases, with atomic O/Fe ratios between 3-5, implying a mixed assemblage of Fe-hydroxides and oxyhydroxides and assumed to be limonite - a secondary weathering product after Fe-Ni metal or Fe-oxides (Table. 7.1). Disseminated Fe-Ni sulfides (troilite and pyrrhotite) and reduced Fe-Ni metal are also present in all particles, though these phases tend to be concentrated near the particle centre or found in association with vesicles, as is reported in Taylor et al., (2011).

7.2.1 TAM19B-7

The micrometeorite's exposed cross-section (Fig.7.1) is broadly rectangular with dimensions of approximately 830x950µm and, therefore, represents the largest fine-grained micrometeorite in this thesis. This particle was previously analysed in detail in Chapter 3, where its pre-atmospheric petrography was investigated. The particle is highly unusual, being classified as an intensely aqueously altered micrometeorite, containing a single pseudomorphic chondrule and, therefore, classified as equivalent to a CM2.0 petrologic subtype (Sect.3.5). However, this micrometeorite is also heavily affected by entry heating overprints. One side of the micrometeorite cross-section completely lacks a magnetite rim, and instead, contains an angular and re-entrant morphology. Two external surfaces of the particle (left and bottom edges in Fig.7.1) are lobate and rounded on scales of 100µm and support a 10-35µm thick igneous rim. The third external surface (the right edge of the micrometeorite in Fig.7.1) has a straight segment that runs approximately ⅔ of the particle's length and terminates at a surface whose orientation is controlled by an internal cavity. The straight surface has a partial magnetite rim but no igneous rim. Finally, the upper surface (as seen in Fig.7.1) has an irregular shape and completely lacks an igneous or magnetite rim.

The internal porosity of this micrometeorite is high; a rough estimate, achieved by analysing the percentage of voids in the exposed 2D cross section, suggests a porosity of ~18%. This is composed primarily of large interconnected channels and rounded vesicles, two of which are highlighted in Fig.2B and 2C. Most of these voids contain internal magnetite rims and show a pronounced Fe-enrichment in the matrix adjacent to voids (Fig.7.2D and 7.2E). Channels vary in morphology from straight to curved cavities with re-entrant margins at smaller scales (Fig.7.2C). Channels vary in width from <1 to ~40µm and reach up to 300µm in length. Two of the larger channels bifurcate, creating Y-shaped voids.

7.2.2. TAM19-7

This large micrometeorite (Fig.7.2A, 410x530µm) is classified as transitional between fine-grained and scoriaceous. The particle contains a geochemically homogenous matrix, showing moderate variation in major-element Fe and Mg concentrations across the particle (Fig.7.2E). Small (<10µm) disseminated Fe-sulfides, in the form of troilite and, less commonly pyrrhotite are present, as well as anhedral, framboidal and platelet magnetite clusters. Both magnetite and sulfides are commonly adjacent to or surrounded by vesicles, implying a genetic association. This co-occurrence was previously described in Genge et al., (1997), Genge and Grady (1999) and Taylor et al., (2011), and suggested to form by the degassing of low-temperature phases during atmospheric entry heating, primarily recording the oxidation of sulfides. The mid-IR spectra of TAM19-7 (G2, Sect.4.2) is characterised by an amorphous dehydroxylated phyllosilicate signature, indicating the former presence of hydrated sheet silicates. However, because the µXRD data cannot identify contributions from amorphous phases, only anhydrous forsterite and enstatite were detected (Fig.3.2). Since large individual anhydrous grains are not seen under BEI, these minerals must be present as a micro-crystalline groundmass, intermixed with the amorphous material. Jarosite is also detected by µXRD (Fig.3.2).

An igneous rim on TAM19-7 is well-developed and reaches a thickness of ~30µm. This consists of micron-scale equant olivine crystals embedded in glass and with vesicular in texture, thus the igneous rim on TAM19-7 is consistent with those described by Genge (2006) from smaller fine-grained micrometeorites. In addition, the igneous rim penetrates inwards, following the margin of the two largest cavities (Fig.7.2B and 7.2C). Here these large cavities vary from 1-15µm in width, approach 300µm in length and include both curved and straight segments with re-entrant margins and Fe oxides linings.

7.2.3. TAM2.1Q

This micrometeorite is relatively small for a TAM particle at 200x280µm (Fig.7.3A). TAM2.1Q is encrusted by terrestrial alteration products and contains an incomplete magnetite rim that is present on three sides of the particle. The geochemistry and mineralogy of this micrometeorite is dominated by secondary alteration products, primarily jarosite, as demonstrated by the combined K-S element map (Fig.7.3C). However, matrix-hosted forsteritc olivines are also present, and reach up to 25µmx50µm in size, several grains also contain Fe-Ni metal droplets. TAM2.1Q contains large voids in the form of channels, notably a single channel runs almost the entire particle length (156µm) and reaches up to 10µm in width. As with TAM19-7 these channels often bifurcate.

7.2.4. TAM37P-03

This micrometeorite has a total volume of ~0.1mm^3 and dimensions of ~450x460x520µm. TAM37P-03 was included in this chapter owing to its large size and because its outer crust is unusual - unlike any other fine-grained micrometeorites previously studied. A well-developed, igneous and magnetite rim surrounds the entire particle (Fig.7.4A-D). However, this rim is unusually thick, reaching up to 100µm in places. This contrasts with the typical igneous rim found on small Antarctic micrometeorites, which are commonly <20µm thick (Fig.7.5 and Genge, 2006). Most of the particle's outer surface is broken into a series of raised, polygonal-shaped plateaus that are separated by deep and steep sided incisions (between 20-100µm deep). As a result, the crust is described as *fissure textured* and closely resembles both the texture of desiccation cracks, found in semi-arid environments (El Maarry et al., 2012) and the fusion crusts of some CM, CV and CO carbonaceous chondrites (Genge and Grady, 1998). In several places, the fissure texture is interrupted by smooth, bulbous areas of igneous rims (Fig.7.4B and 7.4C).

The micrometeorite interior (Fig.7.4E-G) is unmelted, fine-grained, homogenous and appears dark in the CT tomographic slices. Because darker shades represent lower average atomic weights, this implies that the core of TAM37P-03 is Mg-rich. Pre-atmospheric phyllosilicates were, therefore, most likely saponite (Noguchi et al., 2002; Nozaki et al., 2006). Conversely, the small bright rounded inclusions (Fig.7.4F) represent either Fe-Ni sulfides (troilite and pyrrhotite) or Fe-oxides (magnetite an ferrihydrite). Otherwise, dense inclusions such as anhydrous silicates, CAIs and carbonates are absent. Geochemical data from EDS or EMPA are not available for this sample.

TAM37P-03 also supports high porosity. Using data obtained from the pore segmentation routine, extracted from the CT scan (Fig.7.4H), TAM37P-03 has an apparent porosity of 12.85%. Sixty-four

percent (or 8.23% of the micrometeorite's total volume) of pore space volume is interconnected and links to the particle exterior.

Table 7.1 SEM-EDS analyses of micron-scale Fe-rich vesicle rim linings in TAM19-7. The suspected dominant phase is limonite [Atomic ratio: O/Fe=4], which is composed of several related Fe-oxide, hydroxide and oxyhydroxide phases.

Analysis	Na	Mg	Al	Si	S	Cl	K	Cr	Fe	O	Total	Atomic O/Fe
1	0.7	0.7	2.2	4.5	5.5	1.1	0.4	0.2	38.5	48.3	102.0	4.4
2	0.7	3.4	2.0	11.7	3.8	0.8	0.3	0.3	29.9	48.2	101.2	5.6
3	0.5	1.2	1.9	6.6	4.0	0.9	0.0	0.4	42.6	41.1	99.1	3.4
4	0.0	0.2	1.5	2.8	4.3	0.9	0.2	0.3	40.1	39.3	89.6	3.4
5	0.4	2.1	2.0	6.6	4.9	0.8	1.1	0.2	35.3	42.4	95.7	4.2
Average	**0.4**	**1.5**	**1.9**	**6.4**	**4.5**	**0.9**	**0.4**	**0.3**	**37.3**	**43.8**	**97.5**	**4.2**

Fig.7.1. (A) Back scatter electron image of TAM-19B-7. This micrometeorite consists of fine-grained matrix mantled by a paired igneous and magnetite rim. Abundant void space is present in the form of dehydration cracks and vesicles. Magnified images highlight (B) a large vesicle, surrounded by an internal magnetite rim, one of many found within this micrometeorite and (C) a large channel, composed of interconnected secondary pore space that developed during atmospheric entry heating, as a result of volatile gas production. (D) The major element map (Mg, Si, Fe) demonstrates that this micrometeorite is separated into two geochemically distinct domains, the upper right being composed of Fe-rich (Mg-poor) matrix, while the lower left portion contains higher Mg concentrations. Fe enrichment is observed adjacent to channels and forms magnetite rims along channel walls. (E) An Fe-element distribution map also reveals Fe-enrichment in matrix sections in close proximity to secondary pore space, this is taken as evidence of enhanced gas-driven heating.

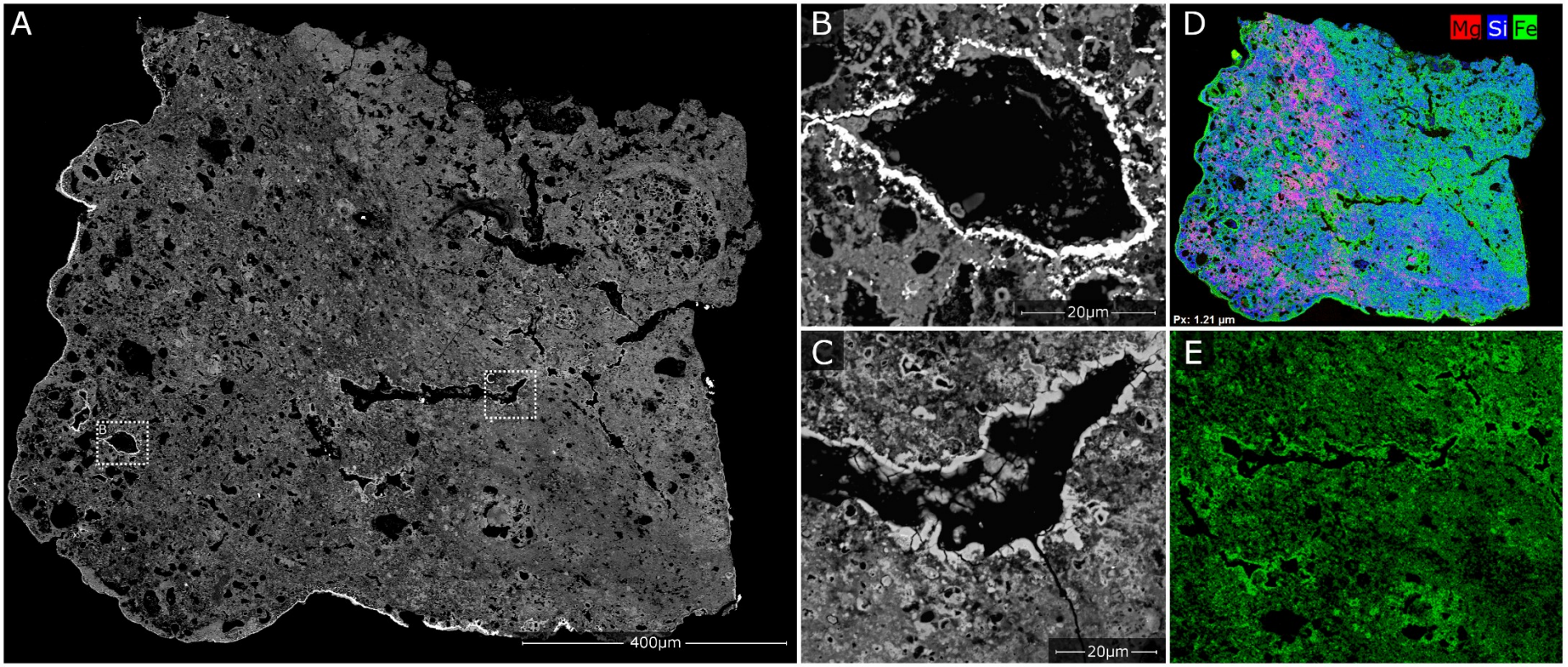

Fig.7.2. (A) Back scatter electron image of TAM19-7. This micrometeorite contains a complete and well-developed, igneous and magnetite rim. The interior mineralogy is composed of mixed dehydroxylated phyllosilicates and micron-scale, recrystalized olivine and pyroxene. Accessory platelet and framboidal magnetite are also present. The internal texture is dominated by a matrix rich in vesicles and contains 4 prominent channels that connect the particle perimeter to the core. Two channels are shown in magnified view (B [and E] and C). (D) The major element map illustrates how secondary pore space channels, notably the channel displayed in C, can result in enhanced thermal processing of adjacent matrix, leading to Fe enrichment, this is also shown in (E) the single element Fe-map. These observations support the suggestion of gas-driven heating during atmospheric entry.

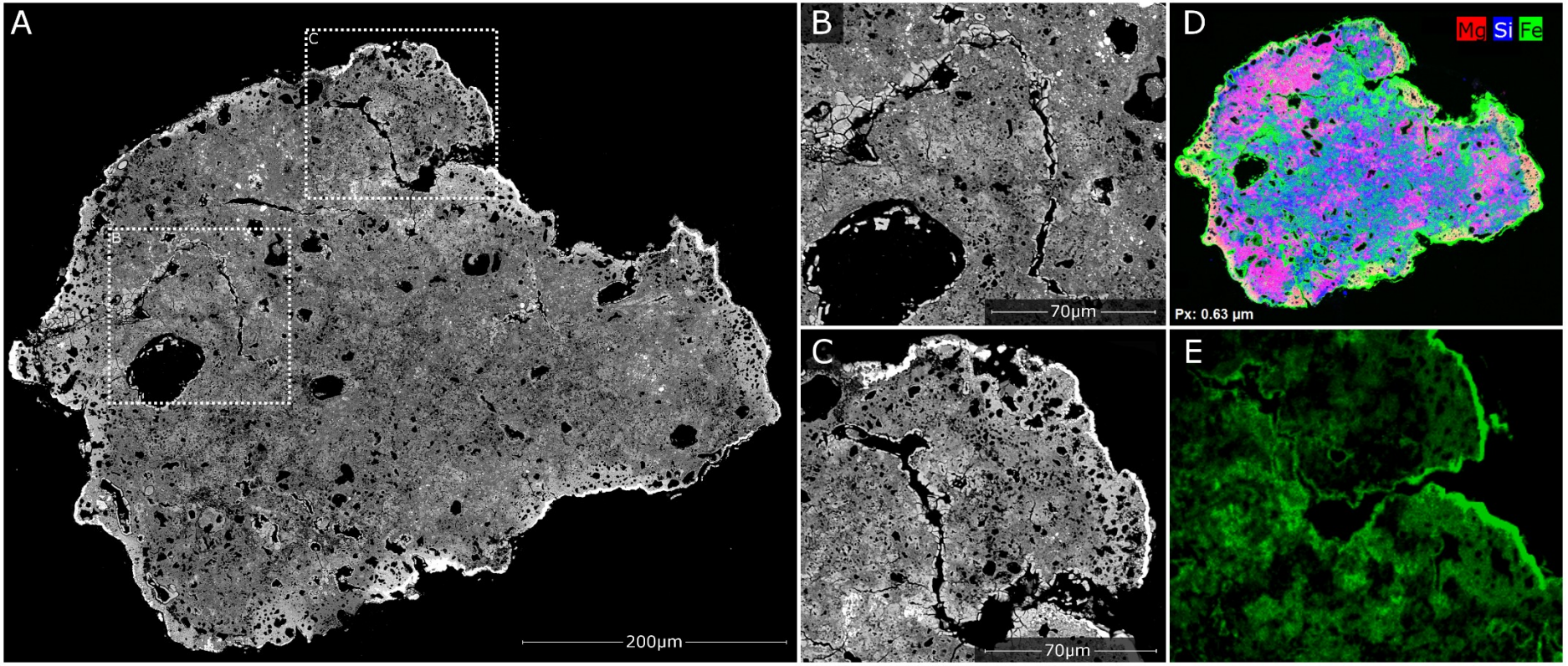

Fig.7.3. (A) Back scatter electron image of TAM2.1Q. This micrometeorite has an incomplete magnetite rim that encloses three sides of the approximately rectangular cross section. The single side missing a magnetite rim is also angular, suggesting minimal entry heating and no melting. This grain edge most likely represents where the particle fragmented during terrestrial residence or collection. (B) The particle interior is dominated by angular forsterite grains (shown in purple), containing poikilitic Fe-Ni droplets and Fe-sulfides (shown in green) sitting within a fine-grained matrix. Several large channels cut this micrometeorite almost completely along the particle's width. (C) Long residence times, held in Antarctic rock traps have resulted in replacement by jarosite, which appears to affect the entire particle except for the anhydrous silicates that appear black in the combined S and K element map.

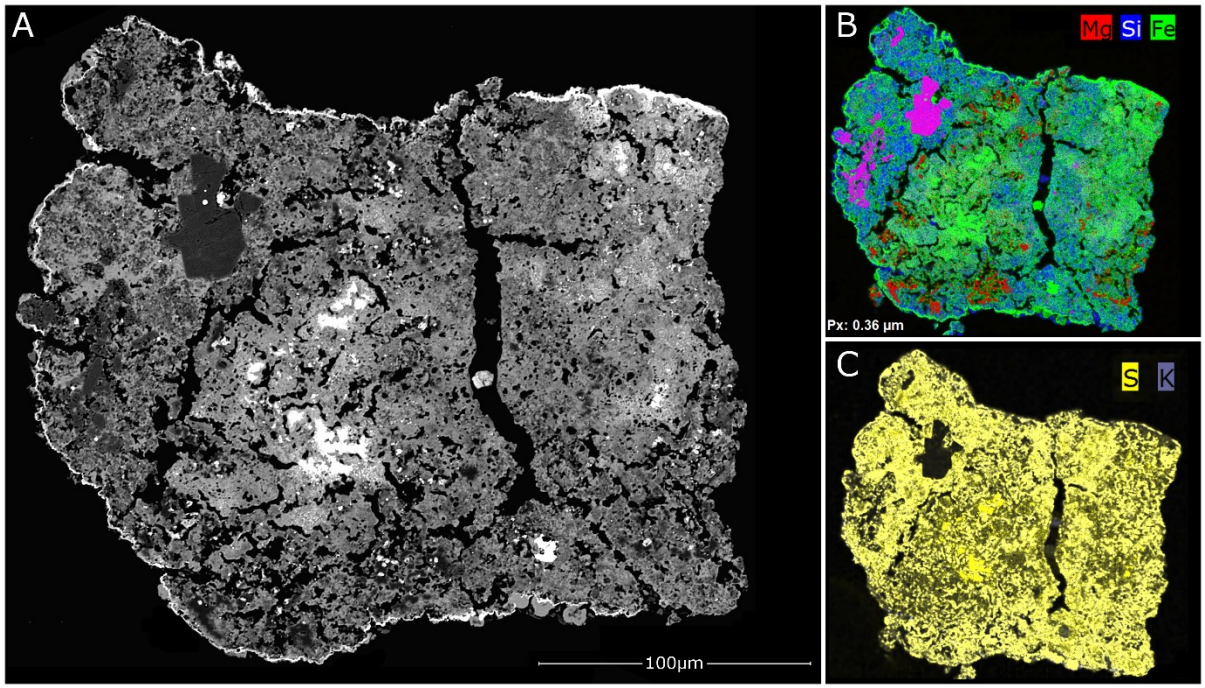

7.3. Discussion: atmospheric entry heating in large fine-grained micrometeorites

Three giant micrometeorites (TAM19-7, TAM19B-7 and TAM2.1Q) were found to contain large, relatively wide (<3-40µm) channels. These channels vary significantly, some taper towards their ends, some have relatively equal widths along most of their length, while others - particularly the largest channels - are widest at the particle perimeter. Several larger channels also bifurcate producing a branching network of passages. Furthermore, some channels are visibly connected to the particle exterior and exceed 300µm in length (Fig.7.2). The origin of these channels is likely to be principally due to contraction of the matrix during dehydration reactions (Noguchi et al., 2002; Nozaki et al., 2006; Che and Glotch, 2012) this is because similar dehydration cracks are present in the thermally altered substrate beneath the fusion crust of meteorites (Genge and Grady, 1999) and clearly form during entry heating. However, crack growth and subsequent widening, developing interconnected channels is likely driven by the expansion of volatile gases. This is supported by the presence of rounded and isolated cavities that are also found within the TAM micrometeorites and form sections of the channels. Genge et al. (1997) described similar cavities and suggested that they are vesicles formed by the expansion of gases within the matrix. Thus, the large, branching channels described

here appear to be composed of both linear dehydration cracks and rounded vesicles and formed during atmospheric entry heating.

During atmospheric entry, several chondritic phases are responsible for volatile release, including: phyllosilicates, sulfides, carbonates and organic matter. The temperature range over which volatile production occurs is also significant, spanning at least 1000°C (Genge et al. 1997; Greshake et al. 1998; Taylor et al., 2011; Court and Tan, 2016). At the low temperatures (<550°C) carbonaceous and organic phases decompose, releasing CH_4, CO_2 and H_2O (Glavin and Bada, 2001). Later, phyllosilicates decompose between 300-800°C, releasing significant H_2O in the form of vapour (Greshake et al., 1998; Genge, 2006; Che and Glotch, 2012). At progressively higher temperatures (~800-1100°C) sulfides thermally decompose, producing SO_2 and SO_3 (Taylor et al., 2011). Above 900°C carbonates break down, also releasing CO_2 (Greshake et al., 1998). Furthermore, recent experimental heating of micrometeorite simulants also demonstrated the importance of secondary gas interactions. Most significantly, the carbothermic decomposition of organic matter, which results in the enhanced production of volatile gases by lowering the thermal decomposition threshold at which sulfides break down (Court and Tan, 2016). Given this complex array of reactions over a sustained temperature range, volatile-driven gas production and subsequent heating of the particle's matrix by these gases is most likely an important process operating in micrometeoroids.

Within the core of a micrometeorite, during entry heating, absorbed water is lost from phyllosilicate interlayers in dehydration reactions. This causes contraction of the sheet silicates and the development of cracks (Shen et al., 1990; Nozaki et al., 2006). Experimental dehydration of phyllosilicates has previously demonstrated that volume losses between 20-30% are common (Esser, 1990). With continued heating, structural water is also lost from OH-bearing octahedral sheets through dehydroxylation reactions (Bray and Redfern, 1999; Che and Glotch, 2012). Dehydration cracks form parallel to the [001] axis of their phyllosilicate hosts (Nozaki et al., 2006) and progressively grow in length whilst also expanding in width (Shen et al., 1990) leading to the development of interconnections. Likewise, vesicles form by the release of volatile gases in heated micrometeorites (Taylor et al., 2011). It therefore, seems probable that small dehydration cracks are the precursors to most vesicles.

In addition, most fine-grained unmelted micrometeorites contain zoned profiles (Fig.1.4A, 1.4B, Chapt.5), defined by an igneous rim surrounding a less heated core. This reflects the migration of a thermal front moving inwards (Fig.1.4C), progressively melting phyllosilicates (Genge, 2006). Due to the high enthalpy of dehydroxylation reactions (>521kJkg^{-1}, Llana-Funez et al., 2007), hydrated micrometeorites can support high thermal gradients (>200Kμm^{-1}, Genge et al., 2017b). The four TAM micrometeorites in this study have well-developed igneous rims. During the early stages of atmospheric entry heating a layer of melt would, therefore, have coated their exteriors and acted as a seal, preventing volatile gases liberated by decomposing phases, from escaping and forcing internal gas pressures to rise (Genge, 2017a).

In TAM37P-03 interconnected channels are absent and instead, a thick igneous rim covers the particle. This rim has, however, split into isolated sections, causing the unmelted particle interior to be exposed. The newly exposed dark matrix also shows minor evidence of melting, resulting in the development of a thin, secondary igneous rim (Fig.7.4E-G). Furthermore, in section 7.2.4 several rounded, droplets on the particle exterior were identified. Collectively, these observations require that the primary igneous rim broke apart, during atmospheric entry heating, whilst the rim was still partially molten. These conditions are necessary otherwise the secondary igneous rim could not have formed.

Fig.7.4. TAM37P-03 analysed under SEM-BEI and µCT. (A-C) External (uncoated) back scatter electron images in 3 different orientations are compared against (D) the computer-generated 3D model of this micrometeorite built from 871 µCT scans. This micrometeorite contains a well-developed, paired magnetite and igneous rim that form an unusual outer crust, composed of polygonal raised plateaus, isolated from each other by deep incisions. The particle's crust is, therefore, superficially similar to (E) desiccation cracks formed on Earth as fine-grained muds dry in semi-arid environments. (F-H) Internal cross-section images (tomographic slices) taken at 3 different depths within the micrometeorite, revealing that the particle core is unmelted, fine-grained homogenous and appears Mg-rich (dark Z values). Dark inclusions representing anhydrous silicates, sulfides or oxides are absent. (I) The 3D micrometeorite model, generated using the µCT data, was evaluated to analyse pore space and permeability. (J-O) This particle was then crushed and some fragments (including pieces of the igneous rim) were embedded in resin and are shown here and found to contain Mg-rich olivine relict grains.

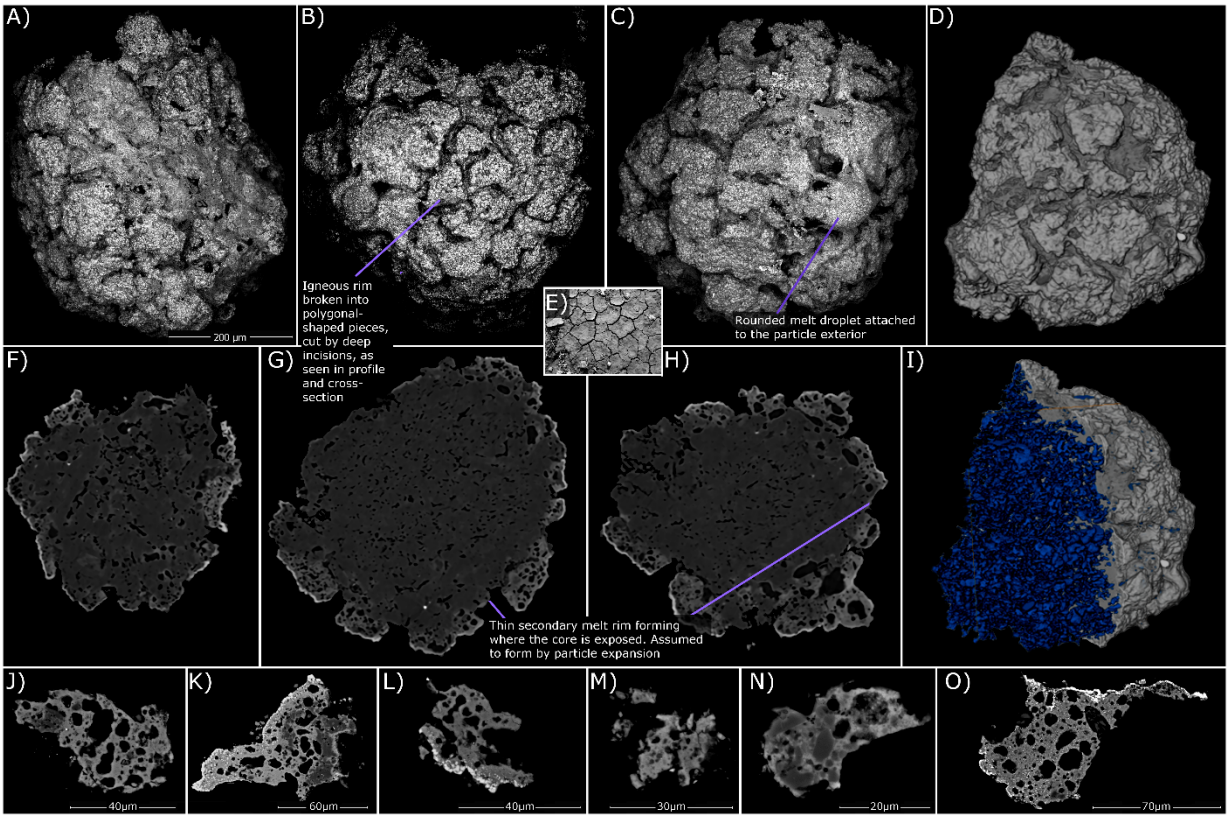

The splitting of the primary igneous rim was most likely driven by volume expansion of the micrometeorite. The polygonal arrangement of fissures on the surface of the particle is clear evidence for the role of expansion in their formation. Genge (2017a) recently demonstrated that scoriaceous

micrometeorites rapidly expand in volume during partial melting, resulting in a *vesicular parachute* that significantly decelerates the falling micrometeoroid. Here, it is argued that although initially dehydration cracks form by phyllosilicate contraction, later growth, expansion and their evolution into vesicles, appears to be primarily driven by the release of volatile gases and rising internal pressures within the micrometeoroid, which forces cavities open and causes expansion of the particle.

The formation of fissures within a melt layer, owing to extension, might seem less likely than thinning of the melt layer, however, vesicular foams are Bingham fluids that can be broken under low shear stresses and high strain rates (Wright and Weinberg, 2009). Therefore, rapid expansion of the particle interior could produce the observed polygonal-shaped fissure network on the micrometeorite exterior. Once fissures are formed, the melt's surface tension may have also played a role in the withdrawal of melt away from the fissured areas. Gas release from the micrometeorite core is also likely to have prevented melt from flowing back.

Consequently, TAM37P-03 records the petrography of a micrometeorite shortly after the escape of volatile gases, generated within the particle interior. Once the igneous rim was breached, gas exchange with the Earth's atmosphere occurred. The µCT data demonstrated that TAM37P-03 has both a high porosity (~13%), and that 64% of pores connect the particle exterior. The total porosity in TAM37P-03 is, therefore, two-to-three times higher than the porosity measured for CI1, CR2, CM2 and the intensely aqueously altered CM2.0 chondrites, as measured by Corrigan et al., (1997). This porosity value is also consistent with previous measurements from unmelted micrometeorites (0-12%), also measured using uCT and performed by Kohout et al., (2014), who demonstrated that micrometeorites in the later stages of atmospheric entry develop significantly higher porosities, up to 27%. These lines of evidence demonstrate that the development of secondary porosity in micrometeorites is a major process during atmospheric entry. With continued heating and the onset of partial melting within the micrometeorite core, TAM37P-03 is likely to have developed the same interconnected channels that are observed in the remaining three giant TAM micrometeorites.

The establishment of interconnected pore space will necessarily allow the movement of expanding hot gases, which will modify the thermal gradients (Chapt.5, sect.5.2) and result in a more rapid, convective heating regime. Gas migration is likely to initially occur inwards due to high ram pressures, whilst gas escape is prevented by the igneous rim. However, once the internal gas pressure is sufficient to breach the igneous rim, gas will then escape outwards.

In two of the giant micrometeorites (TAM19B-7 and TAM19-7), evidence of enhanced thermal processing along channel walls and in the matrix surrounding channels is observed and is consistent with the inward migration of heat by gases. Iron-rich deposits lining channel walls were described in section 7.2.2, these inner-rims are most likely formed by the same mechanism that generates magnetite rims on unmelted micrometeorite exteriors; through melting, evaporative depletion of volatiles, oxidation, cooling and crystallization (Toppani and Libourel, 2003). The magnetite rims lining internal voids in TAM19B-7 (Fig.7.1B and 7.1C) support this suggestion. However, the non-stochiometric Fe-rich rims, most likely composed of limonite, in TAM19-7 (Fig.7.2B and 7.2C) could,

instead, represent later terrestrial weathering (van Ginneken et al., 2016), though most of the Fe, would still be derived from the micrometeorite, rather than the environment. Because the fine-grained matrix in close proximity to the channels also shows increased Fe content (Fig.7.1D, 7.1E, 7.2D, 7.2E) this further suggests enhanced thermal processing. In 2006, Genge suggested that increased Fe/Si ratios within the igneous rims of small Antarctic micrometeorites, as compared to their unmelted cores; resulted from the migration of Fe-S eutectic liquids under reducing conditions and, therefore, regions of Fe enrichment highlight zones which have experienced a greater degree of thermal processing (Genge and Grady, 1998; Genge, 2006). Therefore, the Fe enrichment adjacent to channels observed in these giant micrometeorites implies enhanced thermal processing resulting from gas-driven heating.

7.4. Implications: the fragmentation of micrometeoroids

Particles TAM-19B-7 and TAM2.1Q both have one surface without a magnetite rim suggesting these have been fractured. Fragmentation of these particles could have occurred during transport on the Earth's surface or during collection, instead of during atmospheric entry. Particle TAM-19B-7 has a planar segment on its external surface that is distinct from the lobate outline of the non-fractured surface. The planar segment also has a less well-developed magnetite rim than the lobate surfaces and lacks an igneous rim, testifying to a period of reduced heating. This straight boundary is interpreted as a dehydration crack that is terminated at one end by a second dehydration crack, orientated perpendicular to the first and, which itself penetrates the micrometeorite. These features are consistent with the observation that some dehydration cracks bifurcate and implies that fragmentation of this micrometeorite occurred during atmospheric entry.

Variations in the development of magnetite and igneous rims in micrometeorite may arise owing to fragmentation and the exposure of new surfaces to heating. Parts of micrometeorites with less developed rims may, therefore, be similar to secondary fusion crusts observed on meteorites and formed by delamination and removal of areas of pre-existing crust (Genge and Grady, 1999). In hydrated meteorites this process may also be facilitated by dehydration cracks. Consequently, the thin regions of igneous and/or magnetite rims on TAM37P-03 should be considered secondary rims because they appear to have formed by exposure of the core to heating after fissures formed.

Although secondary melt rims and surfaces without signs of heating may form by fragmentation, preferred orientation during flight might also be expected to cause asymmetric heating effects. For example, exposure of a single micrometeorite face in the flight direction might be caused by stabilisation of a spin axis, owing to the windmill effect (Genge, 2017b). However, flight orientation might be expected to result in a systematic variation in rim development and this is not observed in TAM37P-03. A fragmentation event is likely to result in sudden changes in the velocity of particles and, therefore, has potential to create complex thermal histories such as those observed in this study.

Finally, the fragmentation of micrometeorites during flight is also supported from radar observations of incoming micrometeoroids (Kero et al., 2008; Briczinski et al., 2009). Current estimates suggest that fragmentation is an overlooked process with as many as 80% of the larger infalling meteors (>1cm)

experiencing disruption (Gao & Mathews, 2015). Thus, the paucity of large CM-like fine-grained micrometeorites (van Ginneken et al., 2012) is likely a product of both fragmentation, as argued here, and the over production of smaller dust grains (typically <100µm in diameter, Flynn et al., 2009).

7.5. Conclusions

This chapter investigated four giant fine-grained CM-like micrometeorites. Their petrography, geochemistry and textures provide new insights into the processes of atmospheric entry heating affecting micrometeorite interiors:

(1) Textural analysis, 3D imaging and geochemical data revealed the presence of abundant interconnected secondary pore space, composed of linked dehydration cracks and vesicles in three of the four micrometeorites. In several instances, wide, sinuous and branching channels, containing evidence of increased thermal reprocessing adjacent to their channel walls were observed. These channels form as dehydration cracks and vesicles link up. Although dehydration cracks are initially formed by contraction of phyllosilicates, their later growth appears to be driven by volatile gas release, exerting pressure on pore walls and potentially leading to explosive effects. Collectively, these features imply that the thermal decomposition of low-temperature phases, during atmospheric entry, plays a critical role in the heating micrometeorite cores. The loss of conductive core-to-rim thermal gradients in some micrometeorites may occur as convective gas flow regimes are established (as suggested in Chapt.5).

(2) Furthermore, the development of interconnected pore space promotes the fragmentation of larger micrometeoroids and could potentially explain the paucity of large, hydrated micrometeorites among collections.

Chapter 8: Testing the Veritas Hypothesis: Near-IR spectroscopy of Antarctic micrometeorites

8.0 Overview – In this chapter, the *Veritas hypothesis* is tested through comparison of fine-grained micrometeorites NIR spectra (collected in the CRA-W lab) against Veritas (and Themis) family member asteroid spectra, previously collected via ground-based telescope (Chapman et al., 2011). Attention is directed towards absorption features, potentially relating to surface mineralogy. Strong similarities are observed between the Themis and Veritas asteroid families with possible shared absorption bands located at approximately 0.9µm, 1.1µm, 1.4µm, 1.8-2.0µm and 2.2µm. These spectral features correspond to the positions of hydroxyl group bending and stretching mode overtones and, consequently, imply intact hydrated phyllosilicates on the surfaces of some C-type asteroids. Furthermore, the red-sloped Themis family members, when compared against the flat or blue-sloped Veritas members, which also contain deeper absorption features supports previous modelling and spectral observations, arguing that the Themis family is significantly older and more space weathered than the Veritas family. Comparisons against NIR micrometeorite spectra were unsuccessful, as these spectra do not contain unambiguous absorption features. This is most likely explained by the effects of atmospheric entry heating, which result in the amorphisation and subsequent recrystallization of phyllosilicates, altering their mineralogy. The NIR data is consistent with previous µXRD, mid-IR and EMPA data that reveal the majority of unmelted micrometeorites have low degrees of crystallinity. Unmelted Antarctic micrometeorites are, therefore, not close spectral matches to C-type asteroids. Additionally, both the micrometeorite and asteroid spectra are low quality, noisy spectra which suffer from analytical and environmental artefacts, making analysis of their spectra difficult and identification of absorption bands ambiguous.

8.1. The Veritas asteroid family

The Veritas asteroid family is a young (<8.5Ma, Nesvorný et al., 2003) relatively tight cluster, containing 1394 members. This family is located between 3.157AU and 3.185AU (Fig.8.1., Nesvorný et al., 2015) and is, therefore, within a dynamically active region of the outer asteroid belt. Several family members, including (490) Veritas, evolve on chaotic orbits as a result of ([5, -2, -2] or [7, -5, -2]) three body mean motion orbital resonances between Jupiter, Saturn and Veritasian asteroids (Milani and Farinella, 1994; Michell et al., 2011). This has caused the Veritas family to segregate, as three distinct groups are excited, causing their eccentricity and inclination to increase. Meanwhile the remaining Veritasian asteroids remain as a tight cluster (Fig.8.1B and Michell et al., 2011). Those asteroids in unstable orbits also have the potential to source meteorites to Earth.

Recently, Meier et al., (2016b) argued that CM chondrites with CRE ages around 8Ma most likely represent *Veritas meteorites* liberated in the initial catastrophic break-up event. This includes the thermally altered and dehydrated chondrite Jbilet Winselwan as well as 17% of CM chondrites with measured CRE ages. Thus, it is possible that a significant fraction of both the CM chondrite collection and the micrometeorite flux are sourced from this asteroid family.

Numerical simulations of the break-up event combined with empirical data on the size distribution of Veritas members, strongly suggests that the namesake asteroid - (490) Veritas – is most probably an interloper in the family named after it, and not a genetic member. If (490) Veritas was not part of the original planetesimal, the revised parent body diameter is closer to 112km than previous estimates of 140km (Michell et al., 2011). Furthermore, a secondary sub-cluster is also recognised within the Veritas family, whose largest member, (1086) Nata reaches 68km diameter (Nesvorný et al., 2003). Because the hierarchical clustering algorithm requires the use of an arbitrarily defined cut-off parameter, the distinction between the Nata sub-cluster and the wider Veritas family is poorly defined. However, if a cut-off of $8ms^{-1}$ is applied (similar to that used to define the Karin sub-cluster within the Koronis family [Nesvorný et al., 2003]), the Nata sub-cluster is found to contain just 17 members (Michell et al., 2011). This group of asteroids most likely represent a more recent secondary collision and probably contains the least space weathered surfaces, with the highest chances of preserving mineral absorption bands in their NIR spectra (Clark et al., 2002; Jedicke et al 2004).

Fig.8.1. The Veritas asteroid family, showing all known family members and their proper orbital elements. A) Semi-major axis vs. inclination space, displaying the associated IRAS gamma dust band (9.35°), marked with a dotted blue line. This dust band is expected to supply a significant proportion of infalling micrometeorites to Earth. B) Semi-major axis vs. eccentricity space. Blue ovals mark the positions of Kirkwood gaps. The two largest family members, 490 Veritas and 1086 Nata are marked by black and red crosses respectively. Dark blue dots indicate family members for which NIR spectra are available.

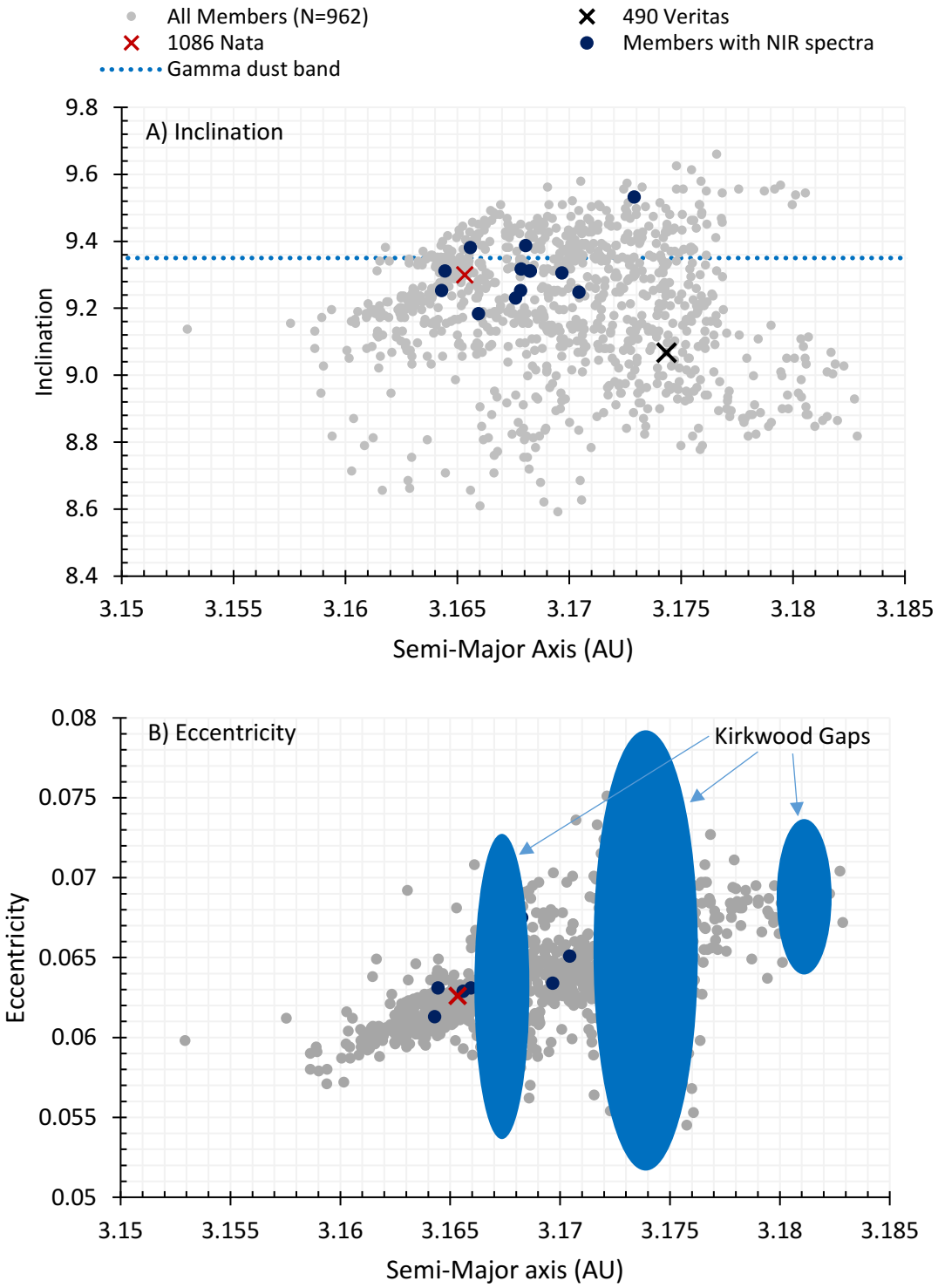

Table.8.1. Veritas family members with recorded NIR spectra. Rows highlighted in blue represent members of the Nata sub-cluster. This table displays proper orbital elements and absolute magnitude data.

Ast. No.	Name / provisional designation	Semi Major axis	Eccentricity	Sin(I)	Inclination	ABS Magnitude
490	Veritas	3.1743	0.0655	0.1576	9.0676	8.44
1086	Nata	3.1653	0.0626	0.1616	9.2998	9.49
2147	Kharadze	3.1704	0.0651	0.1607	9.2475	11.88
2428	Kamenyar	3.1697	0.0634	0.1617	9.3056	11.36
5592	Oshima	3.1680	0.0599	0.1631	9.3869	11.75
5594	Jimmiller	3.1682	0.0604	0.1618	9.3114	11.65
6343	1993 VK	3.1683	0.0675	0.1618	9.3114	12.11
7612	1996 CN_2	3.1676	0.0628	0.1604	9.2301	11.94
10793	Quito	3.1679	0.064	0.1619	9.3172	12.47
15732	Vitusbering	3.1645	0.0631	0.1618	9.3114	12.37
19845	2000 SY_{319}	3.1729	0.068	0.1656	9.5321	12.8
28022	1998 BA_9	3.1678	0.0655	0.1608	9.2533	12.71
28546	2000 EE_{20}	3.1656	0.0629	0.163	9.3811	12.37
31743	1999 JK_{79}	3.1643	0.0613	0.1608	9.2533	12.58
49622	1999 GO_3	3.1660	0.0631	0.1596	9.1837	13.13

8.2. The Veritas and Themis family spectra

8.2.1 Previous spectral studies

Di Martino et al., (1997) collected the first reflectance spectra of Veritas asteroids over the visible wavelength range (0.38-0.9µm), classifying this family as either C or D-type asteroids. Meanwhile, the Themis family had previously been observed as part of Tholen's (1984) photometry survey and later by the small main belt asteroid survey (SMASS, Bus and Binzel, 2002) and, likewise, classified as C-type asteroids. More recently, several of the larger members of both families have been observed over NIR wavelengths (0.8-2.5µm) using the SpeX ground-based telescope in Hawaii (Chapman et al., 2011; Ziffer et al., 2011) and over mid-IR wavelengths (5-14µm) by the Spitzer space telescope (Licandro et al., 2012; Landsman et al., 2016).

In DeMeo et al., (2009)'s extended asteroid taxonomy, the Veritas asteroids are classified as part of the *Ch* spectral class, within the C-complex (Ziffer et al., 2011). This sub-class was formerly part of the G-type asteroids under Tholen's 1984 classification and are characterised by a weak drop-off in reflectance over UV wavelengths, increasing reflectance over visible wavelengths, giving a flat profile with a broad shallow absorption band around 0.7µm and a small positive slope in the NIR, beginning at 1.1µm (DeMeo et al., 2009). Other large asteroids of the *Ch* spectral class include (19) Fortuna, (48) Doris and (49) Pales, the latter two form a binary asteroid system and share low densities, fast rotational periods and low albedos (JPL Small-Body Database, 2017). The presence of a 0.7µm band suggests hydrated phyllosilicates on the asteroid's surface formed by aqueous alteration (Fornasier et al., 2014). Furthermore, the spectral profiles of *Ch* and *Cgh* asteroid classes most closely match the spectra of heated CM chondrites, as recorded in the RELAB database, and demonstrated by Lantz et al., (2013). This further strengthens the link between (dehydrated) CM

chondrites and the Veritas family asteroids. By contrast, the Themis asteroids represent a more diverse set of bodies, with members in the *C*, *Ch*, *Cgh*, *B* and *Bu* spectral classes (DeMeo et al., 2009; Ziffer et al., 2011). Both B and C type asteroids share a weak absorption feature at 0.6µm and blue-sloped or flat profiles in the visible range, while their NIR range is characterised by a concave upwards or *smile-shaped* spectral profile (DeMeo et al., 2009).

The NIR spectra of the Themis and Veritas families were compared by Ziffer et al., (2011) who identified distinct spectral differences between the two groups. This study focused on asteroid continuum slopes - that is the colour of the asteroid over a given wavelength range; being either blue-sloped, flat or red-sloped (Sect1.8). In general, over the NIR1 range (1.00-1.75µm), Themis asteroids have *smile-shaped* profiles (concave-up), while Veritas asteroids have a *frown-shaped* profiles (concave-downwards) (Figs.8.2 and 8.3). While at higher wavelengths, over the NIR2 range (1.8-2.5µm) Themis asteroids are mildly red-sloped and Veritas members are generally flat (Ziffer et al., 2011).

Mid-IR spectral data for both families are also available, having been recently collected by space telescope as hemispherical emissivity spectra and recorded in units of flux density (Jy). This is the ratio of thermal energy radiated at each wavelength with respect to that radiated by perfect black body and, therefore, contains information on both the asteroid's surface temperature and composition. Consequently, the raw spectral data must be fitted against a thermal continuum model; typically, the near-Earth asteroid thermal model is used (NEATM, Harris, 1998) which removes the temperature component. The resulting emissivity spectrum may contain a pronounced silicate emission band over the wavelength range 8.0-12.5µm, which corresponds to mineralogy and particle grain size of the asteroid's regollith (Landsman et al., 2016).

Landsman et al., (2016) collected mid-IR data from both Themis and Veritas asteroids and compared their spectral profiles. Broad, smooth and weak silicate emission features (referred to as 10µm bands), are interpreted as a porous fine-grained regolith, and identified in 11 Themis and 6 Veritas asteroids. These spectra are, thus, similar to heated CM chondrite powders in the mid-IR, which contain low abundances of phyllosilicates and may represent close analogues of ancient asteroid surfaces, exposed to space weathering for several million years (Landsman et al., 2016). In contrast, the remaining Veritas asteroids lacked a discernible silicate emission features, potentially indicating an amorphous regolith coating their surface.

8.2.2 Chapman et al., (2011) NIR Spectra: Quality and processing

High resolution NIR spectra of Veritas and Themis family members were collected by Chapman et al., (2011) as part of a NASA short-term research project (grant #NNX07AK75G). These data currently represent the highest quality spectra available and are of particular interest to this study, because, unlike previous IR data collected from Vertias asteroids, some spectra contain relatively narrow absorption bands, potentially relating to asteroid surface mineralogy. However, Chapman et al., (2011) also note that the Veritas and Themis spectra are of variable quality due to differences in brightness, differences in observation time, atmospheric artefacts and low signal-to-noise ratios.

In particular, asteroid continuum slopes are considered unreliable owing to a lack of available standard stars for calibration. Additionally, despite atmospheric correction, the Veritas and Themis spectra contain residual water vapour features, around 1.4-1.5µm and 1.8-2.1µm (Fig.8.3), that typically present as weak, irregular undulations arising from O-H bending and stretching overtones (Birlan et al., 2004). These features remain due to variations in the thickness, density and humidity of the airmass through which ground-based astronomical observations were collected (Chapman et al., 2011).

All NIR asteroid spectra collected by the SpeX telescope, are published as normalized reflectance. The raw spectral output must, therefore, be corrected for interstellar reddening by calibration against standard stars, for removal of terrestrial atmospheric effects and smoothed using a 21-point boxcar method. This standard spectral processing is outlined in Birlan et al., (2004) and was performed by Chapman et al., (2011) using the SpeXtool.

Fig.8.2. Veritas asteroids with NIR spectra collected and processed by Chapman et al., (2011).

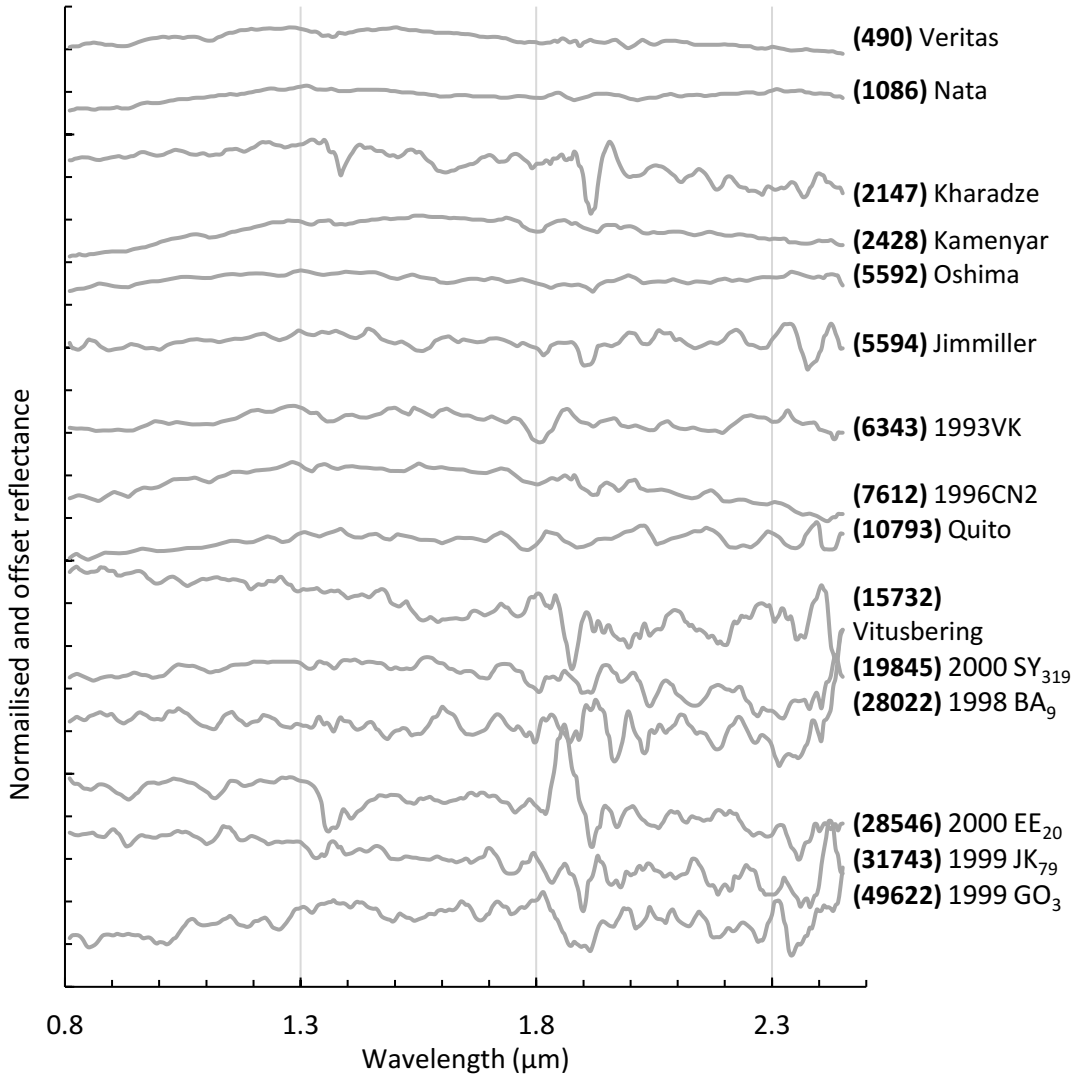

In this study, the published asteroid spectra of Chapman et al., (2011) were further processed. Initially, their baselines were calculated and removed. Both a 4th order polynomial and a cubic spline were used for baseline modelling (Fig.8.5). The 4th order polynomial accurately traces the overall shape of the spectra and these were used to calculate the continuum slope NIR1 and NIR2 values (Fig.8.6). However, this model also cuts through absorption bands, preventing their detection (Fig.8.5) and, therefore, a second model was required. Smoothed cubic splines were matched to prominent reflectance maxima in each spectrum, ensuring that any absorption bands were preserved. The splines were then subtracted from the original spectra of Chapman et al., (2011) to generate *slope-removed* spectra (as seen in Fig.8.8 and 8.9). Reflectance minima that dropped by >3% below the spline baseline were considered significant absorption bands.

Fig.8.3. Themis asteroids with NIR spectra collected and processed by Chapman et al., (2011).

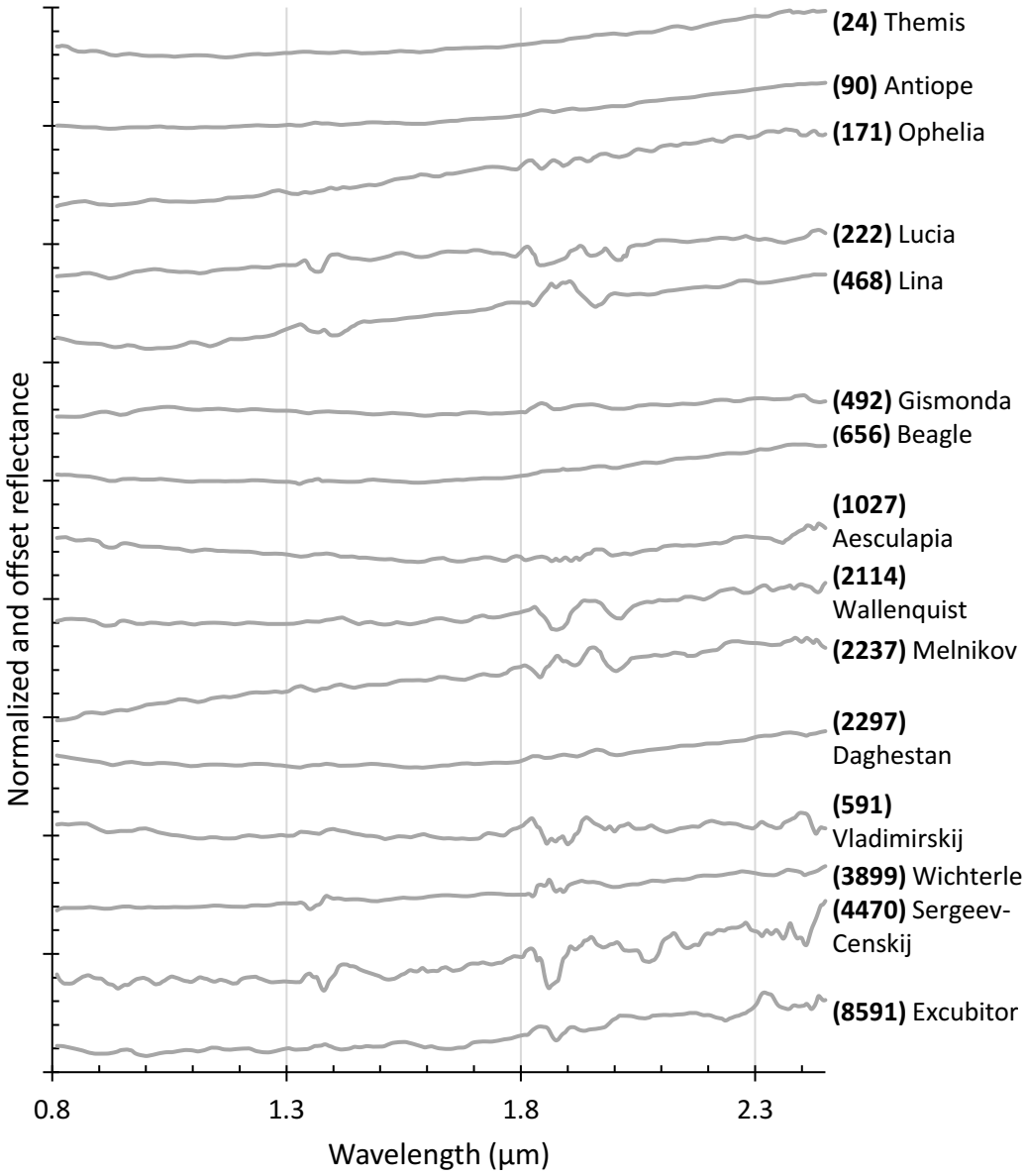

Fig.8.4. An atmospheric transmission spectrum, taken over the wavelength range 0.9-2.5μm and collected at Mauna Kea, Hawaii by the Gemini Observatory (Gemini Observatory, 2017). This spectrum demonstrates the wavelengths at which atmospheric interference, arising principally from water vapour absorption bands (both stretching and bending mode overtones) occur. Atmospheric conditions for this spectrum are a 1.6mm vapour column and an air mass density of 1.0. The spectral ranges 1.35-1.45μm and 1.8-2.0μm are most heavily affected by atmospheric absorption and, thus, partially obscure absorption features in any spectra collected by ground-based telescope.

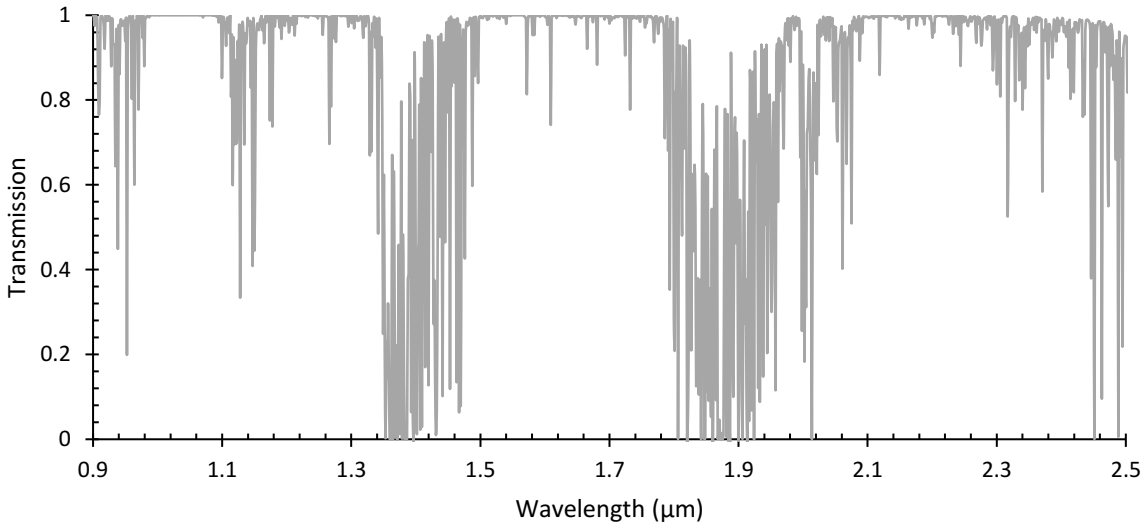

Fig.8.5. The processing of NIR asteroid spectra demonstrated on Veritas member (2147) Kharadze (blue line). Two baseline models were fitted to each spectrum. The 4th order polynomial (dashed grey line) accurately models the continuum slope and was used to determine NIR1 and NIR2 values, while the cubic spline (dashed black line) preserves absorption bands (reflectance minima) and was, therefore, used in the identification and calculation of spectral features (marked by black dots).

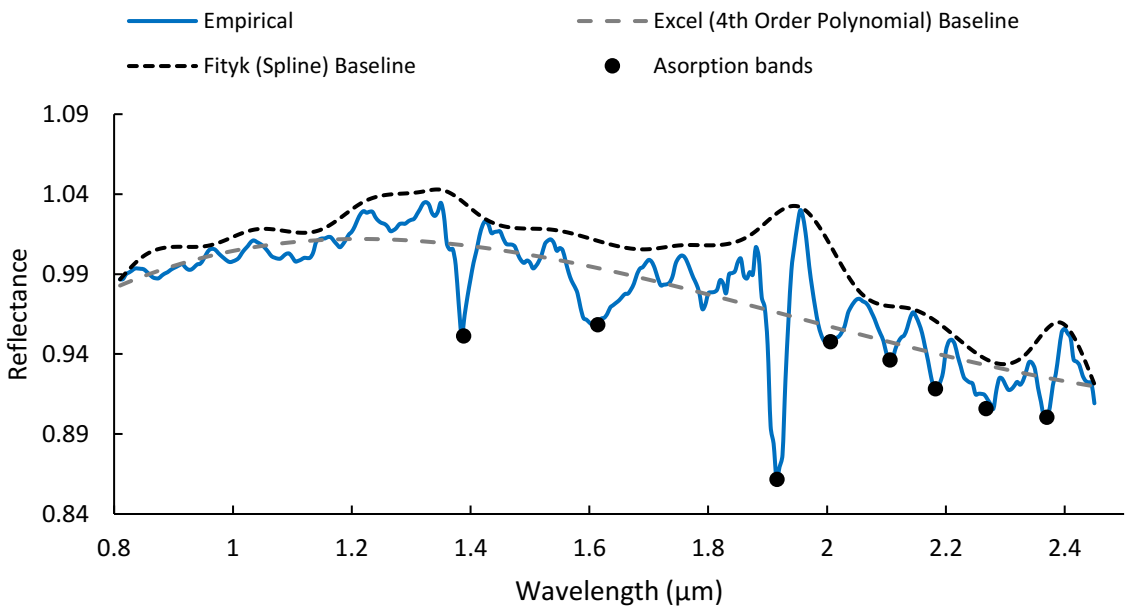

Fig.8.6. Continuum slopes for the Veritas and Themis family asteroids. Baselines were determined using a 4th order polynomial (Sect.8.2.2). The dashed grey lines, located at 0.0,0.0 represent a flat spectrum. Veritas asteroids are plotted in light blue while Themis asteroids are plotted in dark blue. The two crosses represent the average baseline for each family: flat and moderately red-sloped respectively.

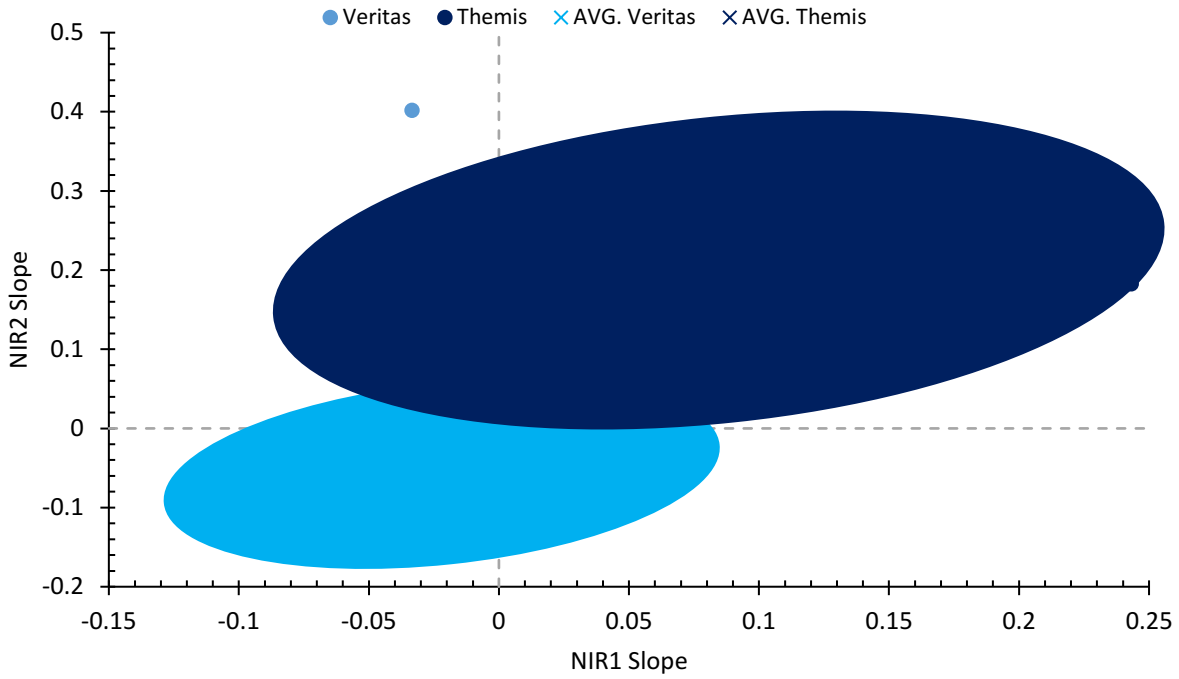

8.2.3. Chapman et al., (2011) NIR Spectra: continuum slope

The average Veritas spectra has a flat baseline over both the NIR1 and NIR2 ranges. Their overall NIR1 range varies between -0.12 and 0.09 and their overall NIR2 range varies between -0.07 and 0.40. In contrast, the Themis family have moderately red-sloped spectra over both ranges, varying between -0.07 to 0.24 and -0.01 to 0.36 respectively (averaging 0.06 and 0.18). The two families, therefore, have distinctly different spectral slopes (Fig.8.6).

8.2.4. Chapman et al., (2011) NIR Spectra: absorption bands

Each asteroid spectrum contains at least 1 potential absorption feature. Within the Veritas family, reflectance minima cluster at several locations. The most frequent and often most pronounced reflectance minima are located between 1.8-2.0µm, commonly centred around 1.9µm, exhibit reflectance decreases between 2-16% below the continuum and have narrow, occasionally asymmetrical shapes - with a shallower profile on the low wavelength side. Minima are also common at 2.2µm, 2.4µm, and 1.4µm. Six asteroids also have weak, relatively narrow minima, dropping by approximately 2% below the continuum located between 0.83-0.93µm. Asteroid (2147) Kharadze, shown in Fig.8.5, demonstrates the clearest absorption bands, with 3 narrow and deep reflectance minima (located at ~1.4µm, 1.6µm and 1.9µm), which are easily identified from its spectrum.

The Themis family are similar to the Veritas asteroids, with reflectance minima common at 0.9µm, 1.4µm, 1.8-2.0µm and at 2.2µm. However, some Themis asteroids also have small reflectance minima around 1.7µm, which were not seen in the Veritas asteroids.

Fig.8.7. Synthetic asteroid spectra for the Veritas (light blue, bottom) and Themis (dark blue, top) families. Each spectrum is generated by averaging the baseline-removed, rescaled spectra from the 15 asteroid family members. These spectra were taken by the SpeX telescope in Hawaii and originally processed by Chapman et al., (2011). Common absorption bands are located around 0.9μm, 1.1μm, 1.4μm, 1.8-1.9μm, 2.2μm and 2.3μm.

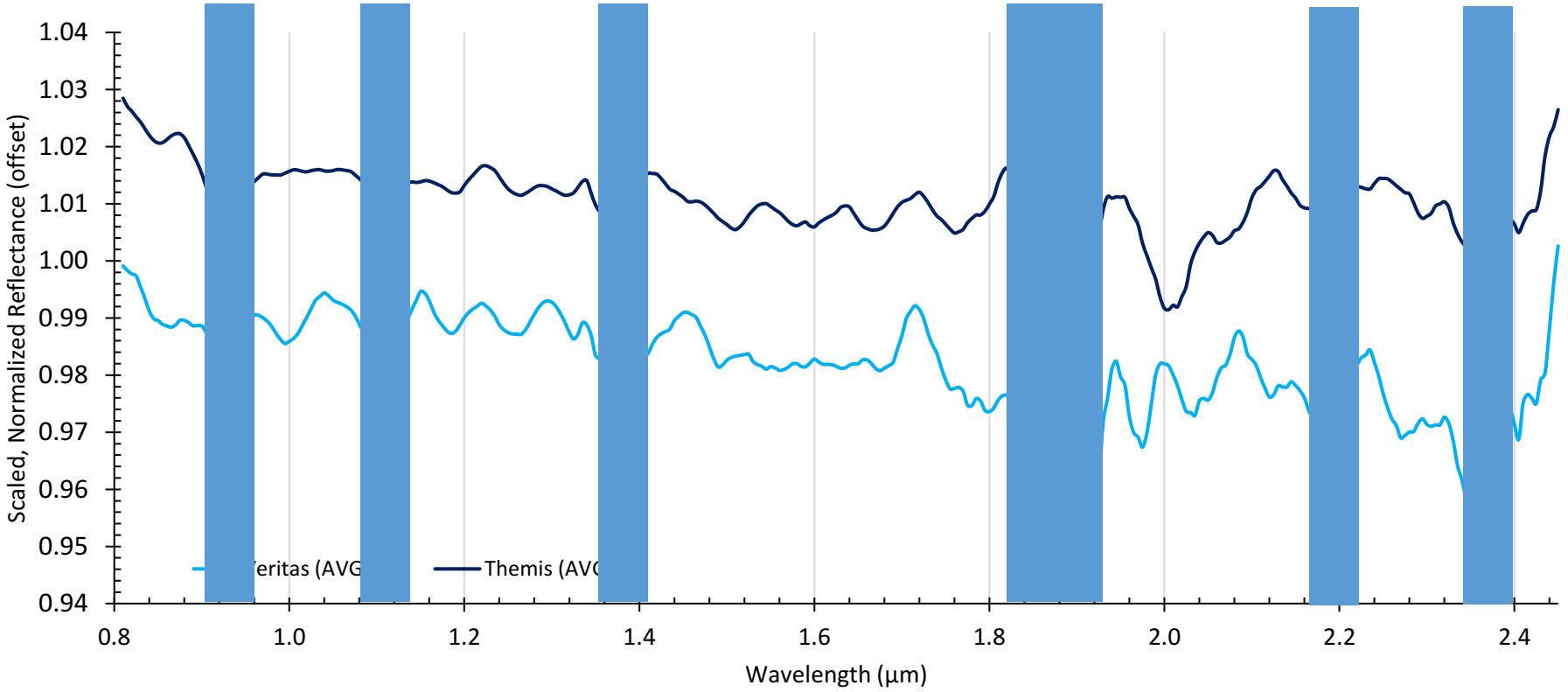

The synthetic averaged family spectra (Fig.8.7.) reveal strong similarities between the two groups. Typically, reflectance minima are narrower, less pronounced and less abundant over the NIR1 range, while at higher wavelengths, spectra are more erratic, contain deeper and sharper minima and show less agreement between families.

Fig.8.8. Veritas family spectra *slope-removed* and re-scaled after Chapman et al., (2011).

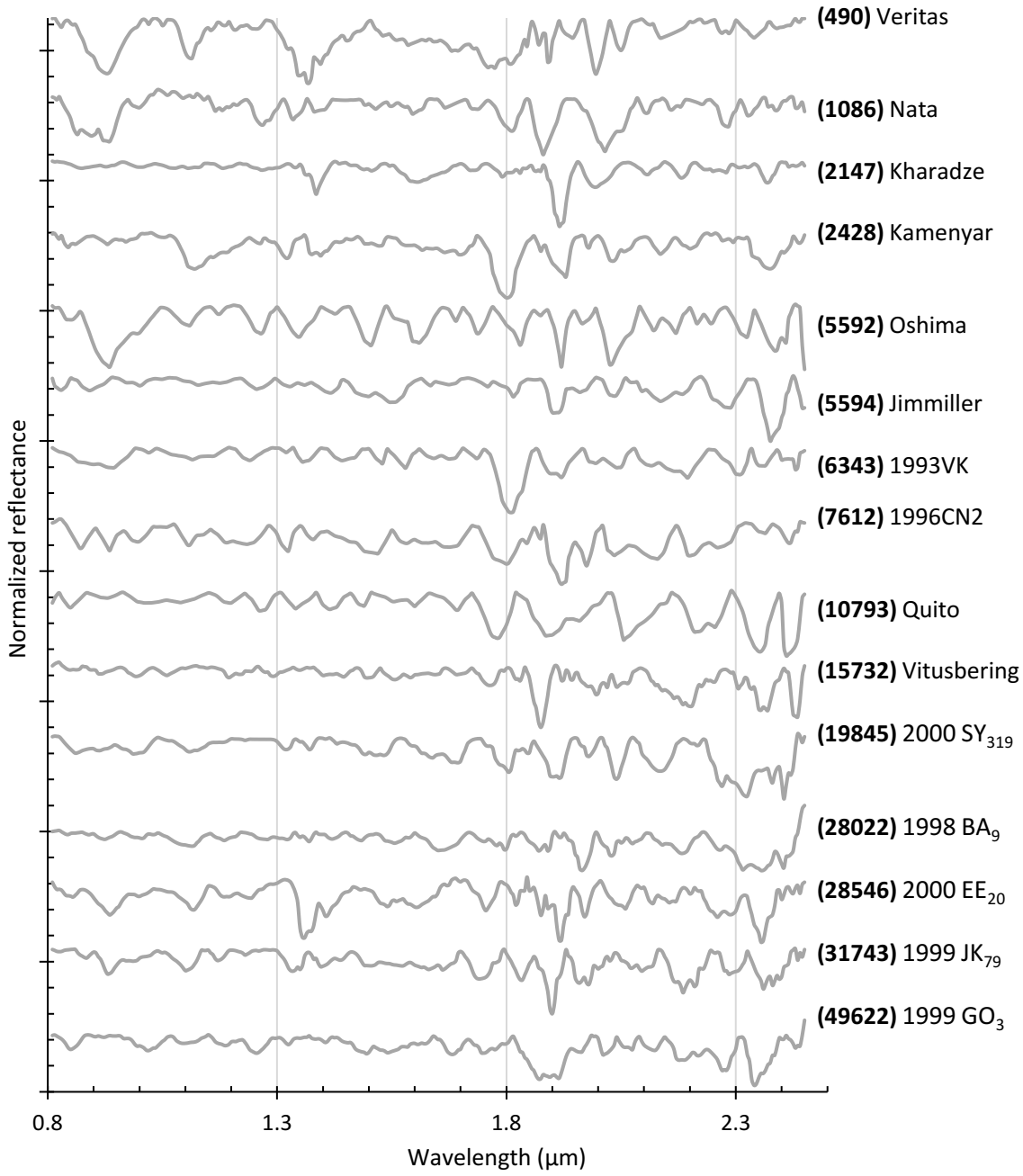

Fig.8.9. Themis family spectra *slope-removed* and re-scaled after Chapman et al., (2011).

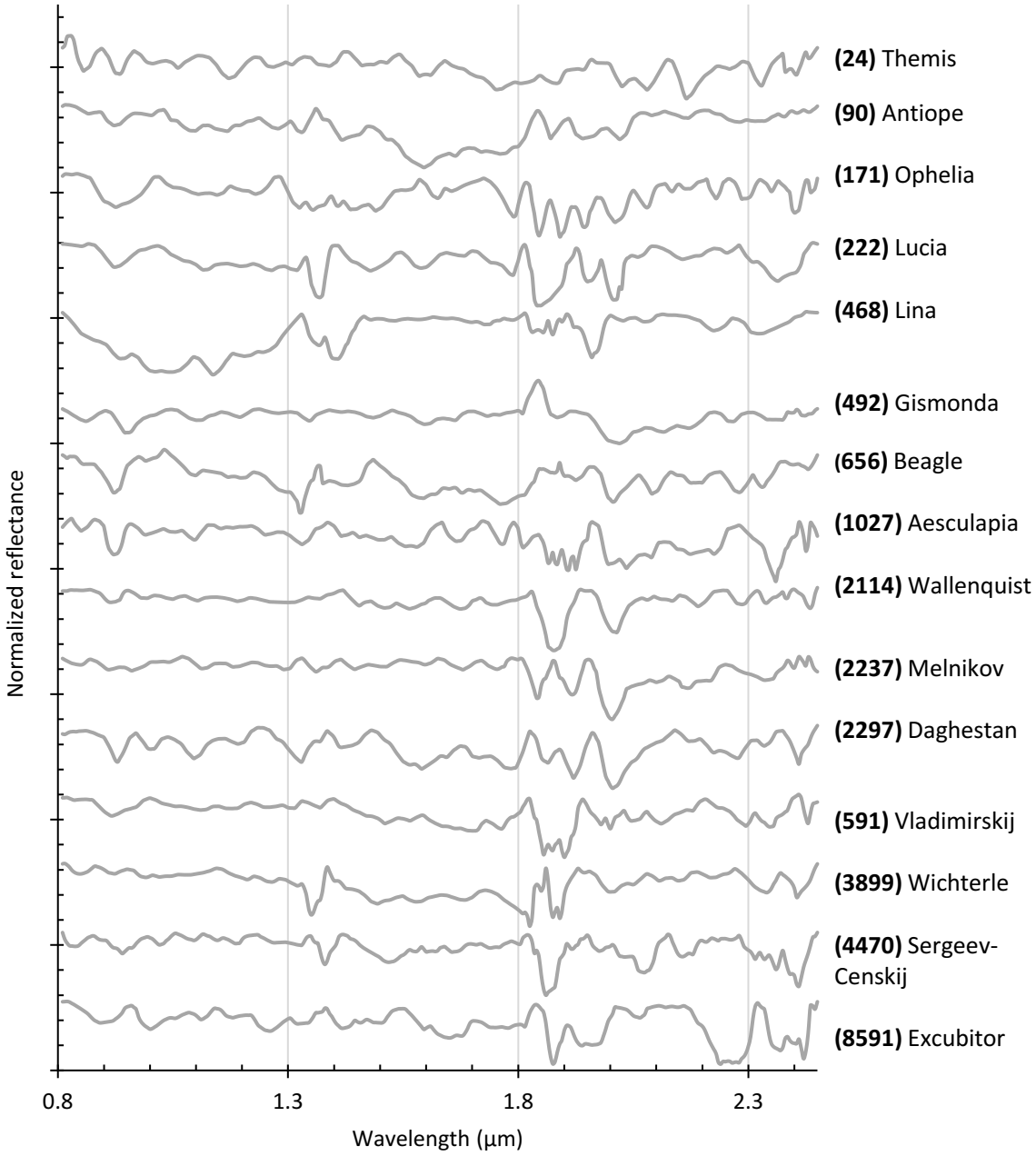

8.3. Results: Micrometeorite NIR spectra

Near-IR spectra were collected from nine micrometeorites (Fig.8.10) and processed using the same method as the asteroids (Sect.8.2.2). These micrometeorite spectra have strongly red-sloped baselines over the NIR1 range (NIR1: 0.52 to 0.93) and highly variable slopes over the NIR2 range (NIR2: -0.27 to 0.66). This is approximately 2-4 times greater than the slopes recorded from the NIR asteroid spectra (Fig.8.6). Such highly variable and strong continuum slopes may be a product of the experimental setup. This is because background correction, against a gold standard was not possible. Instead, a white Teflon block was used as a baseline standard. Thus, micrometeorite continuum slopes are not considered reliable or diagnostic of sample composition and are not analysed further in this study.

Fig.8.10. Micrometeorite NIR spectra, slope-removed and rescaled for comparison against the Veritas (Fig.8.8) and Themis (Fig.8.9) family spectra, processed in the same way.

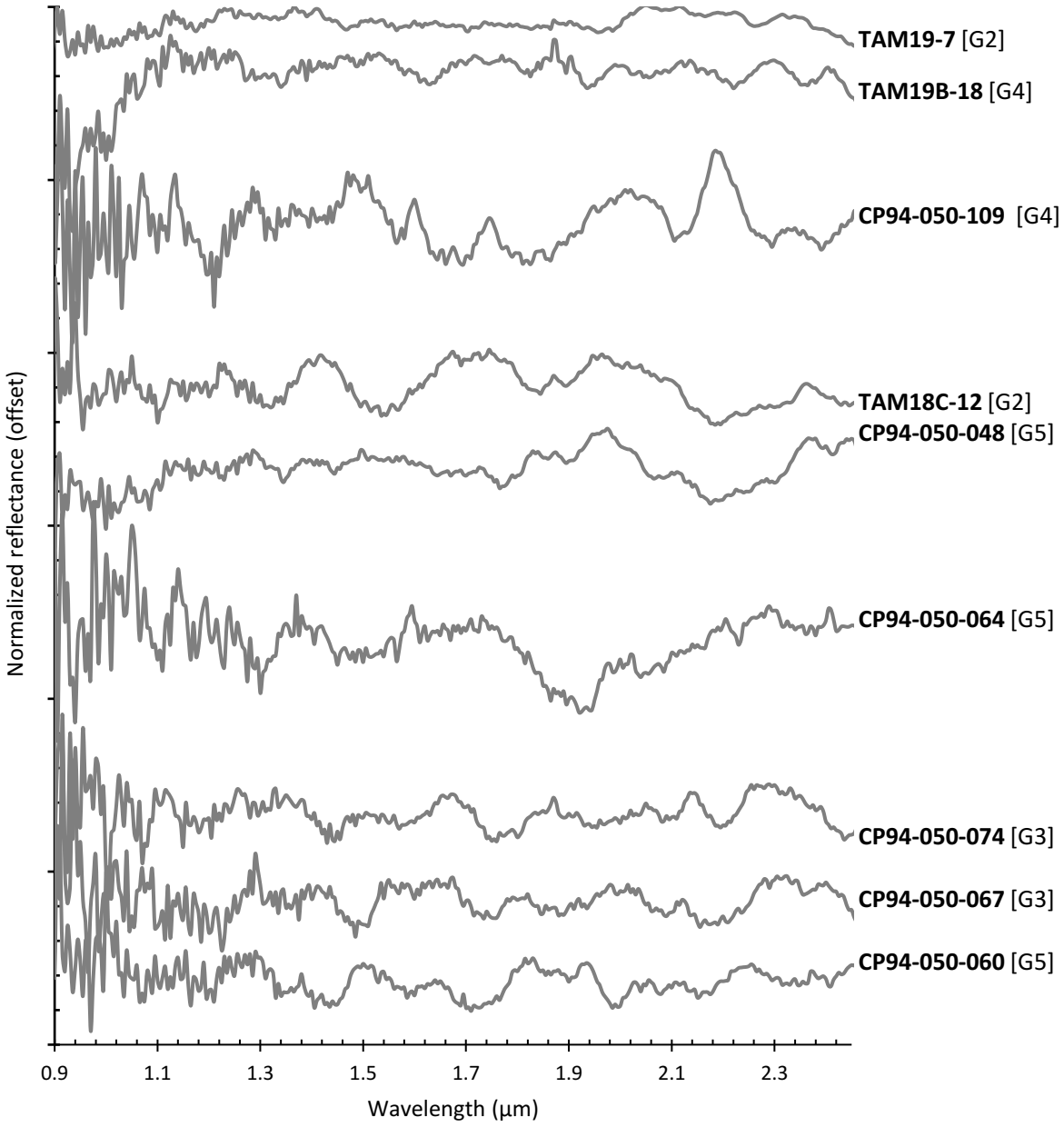

Micrometeorite spectra are also noisy, particularly over the 0.8-1.3µm region, resulting in saw-tooth spectral profiles. This is due to the use of a TE-InGaAs detector for data collection, which is optimised over the reduced wavelength range between 1.3-2.5µm. Noise is so significant over the 0.8-0.9µm region that this range was omitted in the spectra from Fig.8.10.

Each of the micrometeorite spectra contains several shallow reflectance minima, which drop <3% below the baseline. The positions of these reflectance minima are, however, highly variable and appear to be randomly centred. Their shapes are also variable and maybe symmetrical, sharp sudden drops, as in CP94-050-0109 (1.1-1.3µm) or asymmetrical wide bands as in CP94-050-064 (1.7-2.2µm). No shared absorption features are found in more than two micrometeorite spectra.

8.4. Discussion: Interpreting NIR asteroid spectra

The NIR spectral region contains active molecular vibrations formed by overtones and combinations of fundamental IR stretching and bending modes. Interpretation of NIR reflectance spectra is complicated by weaker signals – typically 10 times less than their fundamental vibrations – which result in significantly higher signal-to-noise ratios, as well as interference generated where overlapping vibrational modes co-occur (Stuart, 2000). Additionally, the observation of asteroids using ground-based telescopes is further complicated by atmospheric absorption effects, oblique viewing angles and difficulties associated with the measurement of small, low albedo, cold and distant targets (Birlan et al., 2004; Chapman et al., 2011).

Despite these difficulties, compositional information can be derived from NIR asteroid spectra. Analysis of the two major absorption bands found in S-type asteroids - band I (0.7-1.4µm) and band II (1.4-2.4µm) – can be used to identify and distinguish between achondrites and ordinary chondrites (Sunshine et al., 2004). Band area ratios are also able to subclassify asteroids of the ordinary chondrite type into their respective subgroups (LL, L and H, Gaffey et al., 2002; Dunn et al., 2010; Nakamura et al., 2011). Alternatively, these bands have been used to infer the relative proportions of olivine and pyroxene on an asteroid's surface (Gaffey et al., 2002; Storm et al., 2007; Vernazza et al., 2008).

Similar results for the dark, C-type asteroids have so far not been possible. This is because the absorption bands in C-complex asteroid spectra are either extremely weak (Ziffer et al., 2011; Fornaiser et al., 2014) or entirely absent (Fornaiser et al., 2016). Researchers, therefore, analyse the continuum slope of asteroids (their *colour*) and compare these against mineral standards (Yang and Jewitt, 2008; Ostrowski et al., 2010), meteorites (Birlan et al., 2004; Ostrowski et al., 2010; Lantz et al., 2013; McAdam et al., 2015) and linear mixing models (Rivikin et al., 2011). Where close spectral matches are identified, this may indicate similar compositions. Frequently, hydrated and dehydrated CM, CI and CR chondrites are found to produce close spectral matches to C-type asteroids (Burbine, 1998; Ostrowski et al., 2010; Lantz et al., 2013; Fornaiser et al., 2016). Conversely, several studies have inferred the presence of absorption bands, based on the spectral slope of regions surrounding an obscured spectral feature. For example, Campins et al., (2010) argued for the existence of water-ice on the surface of (24) Themis, as suggested by an asymmetric down sloping profile between 2.2-2.5µm

and a rising profile between 2.9-3.6µm - potentially indicating the presence of an (obscured) 3µm OH absorption band, characteristic of water.

By contrast, the NIR spectra of Chapman et al., (2011), which were found to contain several resolvable reflectance minima (Figs.8.2, 8.3, 8.5, 8.7). This offers a unique opportunity to explore the composition of Veritas and Themis asteroids, through the identification of spectral features linked to specific minerals.

8.5. Discussion: composition and mineralogy of the Veritas and Themis family asteroids

In this study, the Themis asteroids were found to have red-sloped and *smile-shaped* profiles over both the NIR1 and NIR2 continuum slopes, while the Veritas asteroids are either flat or blue-sloped. In addition, the unprocessed Veritas asteroids (Fig.8.2) have more pronounced (deeper) reflectance minima than the Themis asteroids (Fig.8.3). Both these findings are consistent with previous spectral analyses by Ziffer et al., (2011) and the numerical modelling of Nesvorný et al., (2003) who argue that the Themis family is significantly older than the Veritas family and is, thus, more heavily affected by space weathering, resulting in spectral reddening and loss of compositional information as absorption band depth decreases (Chapman, 1996; Sasaki et al., 2001; Clark et al., 2002; Matsuoka et al., 2015; Kaluna et al., 2016). This agreement with previous spectral studies adds confidence to the reliability of these asteroid spectra.

Both asteroid families were found to share common reflectance minima positions, the most prominent features are centred at approximately 0.9µm, 1.1µm 1.4µm, 1.8-2.0µm, 2.2-2.4µm. In addition, some Themis members contain a weak absorption feature at 1.7µm, as demonstrated in the synthetic averaged spectra (Fig.8.6).

The 0.9µm spectral feature, seen in some Veritas and Themis members, is a shallow relatively narrow trough (Figs. 8.7, 8.8 and 8.9), which occupies the same position as the band I centre found in S-type asteroids. In silicate-bearing asteroids, the band I feature corresponds to electronic transitions from vibrating Fe^{2+} ions, located in the M1 and M2 crystal lattice sites of pyroxene and, to a lesser extent, olivine (Burns, 1970; Klima et al., 2007; Lindsay et al., 2015). Consequently, the 0.9µm feature found in these C-type asteroids could also represent the excitation of Fe^{2+} ions within mafic silicates. Because CM chondrites contain a significant fraction of olivine (~26 vol% forsterite, Howard et al., 2009; 2011) weak vibrational signals may be expected. Previous spectral studies identify shallow and wide absorption bands centred at 0.9-1.0µm in most CM chondrites and interpret these as contributions from forsterite (McAdam et al., 2015). However, the 0.9µm features in CM chondrites and S-type asteroids are wide reflectance minima, while the 0.9µm features found in the Veritas and Themis asteroid spectra are, instead, narrow features with a width of <2.0µm. This disparity in spectral shape suggests that olivine and pyroxene are not responsible and, instead, may contribute more to the continuum slope of an asteroid's spectra rather than producing a well-defined absorption band.

Alternatively, hydroxyl-bearing sheet minerals, which are the most abundant component of hydrated carbonaceous chondrites, may explain several of the absorption features identified in Sect.8.2.4 from

the Veritas and Themis asteroids. Phyllosilicates, both 1:1 and 2:1 structures, as well as brucite ($Mg[OH]_2$) – a thermal decomposition product of phyllosilicates (Zhang et al., 2010; Che and Glotch, 2012), which has a stacked sheet structure composed of octahedral Mg hydroxide complexes – produce absorption features across the NIR range arising from hydroxyl group vibrational modes.

The fundamental IR active absorption bands of liquid water occur at mid-IR wavelengths: v_1=3.106µm [symmetric stretch], v_2=6.08µm [asymmetric stretch] and v_3=2.903µm [bending mode]. Combinations and overtones of these modes appear in the NIR at: 0.94µm [$2v_1+v_3$], 1.14µm [$v_1+v_2+v_3$], 1.45µm [v_1+v_3] and 1.88µm [v_2+v_3]. Where water is held within minerals, either in a hydrated form as in $CaSO_4 \bullet H_2O$ or as structural water in hydroxyl groups [M-OH], the main vibrational bands, occurring at approximately 1.4µm and 1.9µm are always observed and, therefore, considered diagnostic (Anderson and Wickersheim, 1964; Hunt, 1977; Schroeder, 2002). However, structural water also produces additional subtle spectral signatures, as a result of the metal-hydroxyl [M-OH] bond. A vibrational pair, located between 2.2-2.4µm, is formed by the bending overtone of this bond (Hunt, 1977). Although, the exact location of this vibrational pair is dependent on the species of metal cation bonded to the hydroxyl group. For example, bonding with an Al^{3+} ion gives a main peak at 2.2µm and the secondary peak at 2.3µm, while bonding to a Mg^{2+} ion, shifts this peak pair to 2.3µm and 2.4µm respectively (Hunt, 1977). Finally, the 1.9µm stretching overtone feature is enhanced in phyllosilicate minerals by overlap and interference with Si-O stretching overtones produced by the silicate crystal lattice (Anderson and Wickersheim, 1964), resulting in a more pronounced, deeper reflectance minimum.

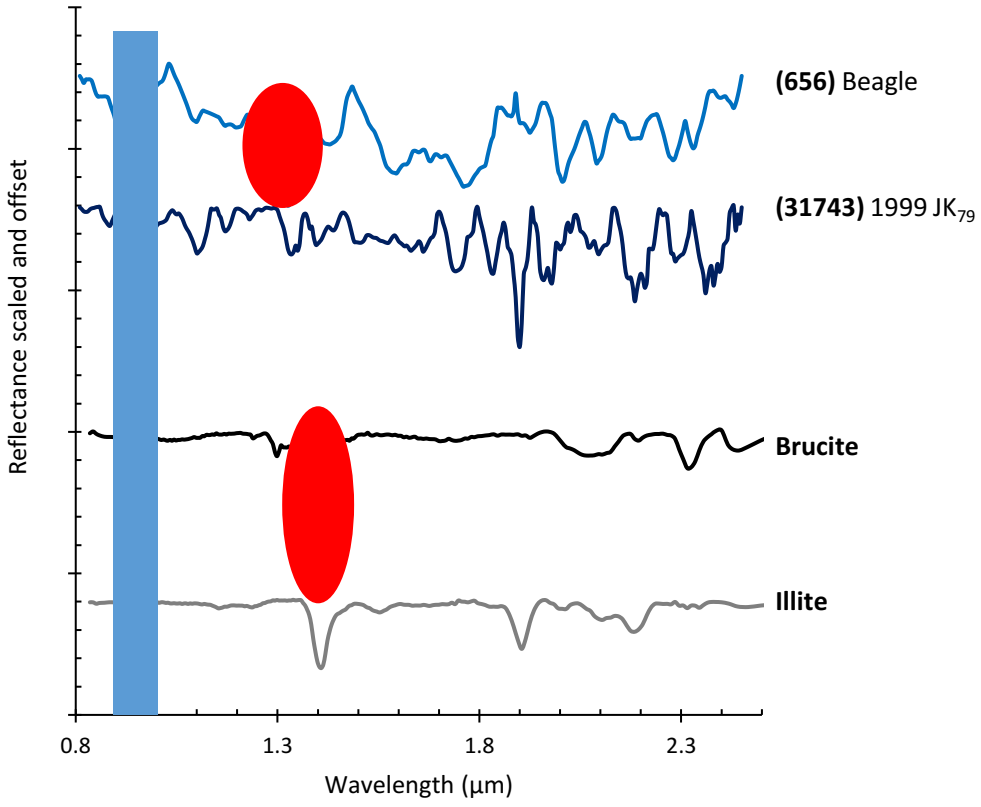

Fig.8.11. (overleaf) Comparison between the narrow 0.9µm absorption feature found in some Veritas and Themis asteroids and the mineral standards brucite (black) and illite (grey). Both mineral standards have had their baseline removed to ensure a fair comparison against the baseline-removed asteroid spectra. Also note the presence of a prominent 1.4µm and less pronounced 1.9µm feature in both the mineral and asteroid spectra, these absorption bands correspond to vibrational combination and overtones from hydroxyl functional groups. The similarity between the 1.4µm band in brucite and asteroid (656) Beagle (a Themis member) [both highlighted by red circles] is particularly striking

Fig.8.12. (Below) Comparison between the NIR spectra of phyllosilicate mineral standards, micrometeorites, Veritas and Themis family asteroids. Diagnostic vibration bands, corresponding to the excitation of hydroxyl functional groups, located at 1.4µm, 1.9µm and 2.2-2.4µm are highlighted by blue bands. Micrometeorite spectra are dominated by noise and reveal no unambiguous absorption bands, conversely, the C-type asteroids contain possible shared spectral features with phyllosilicate minerals.

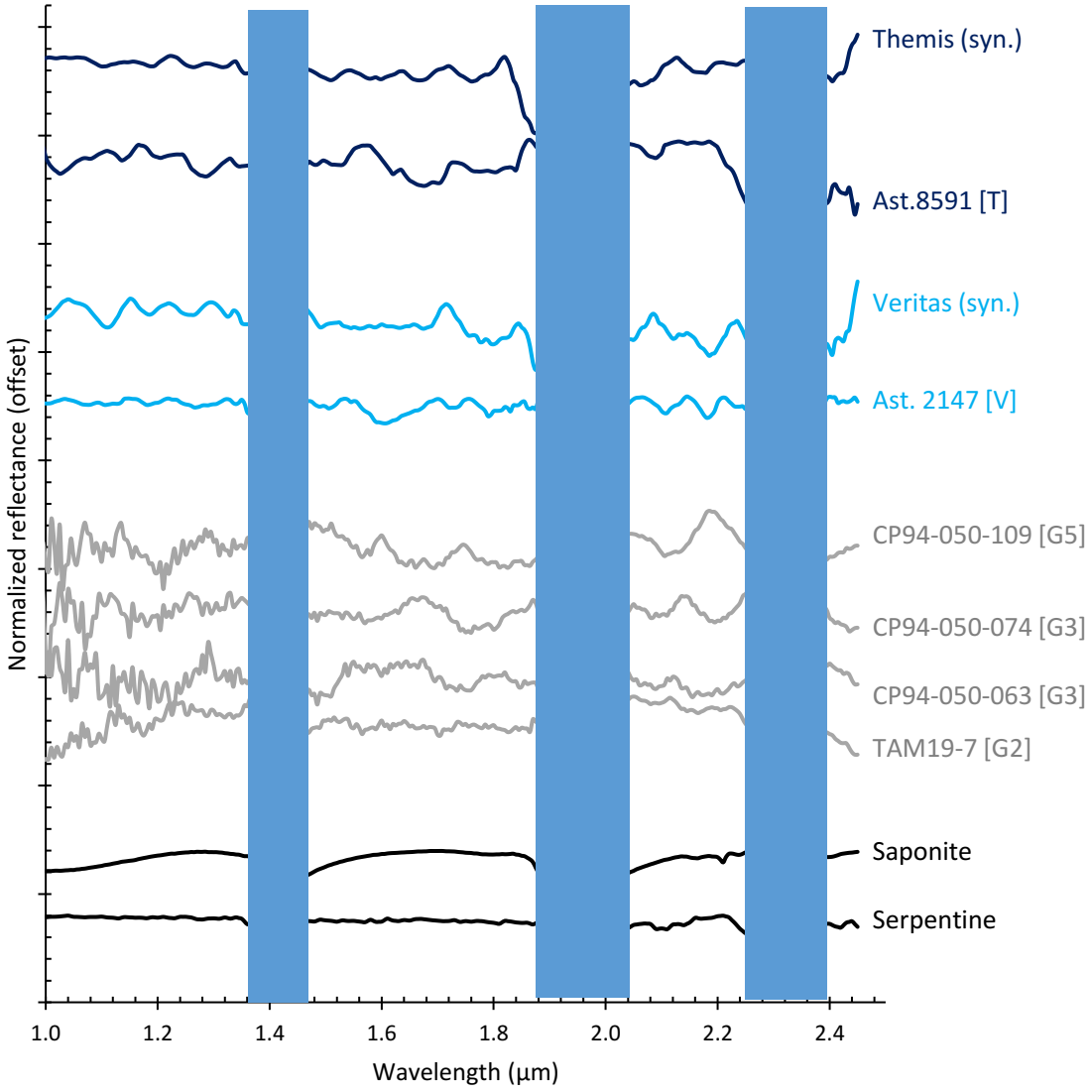

Thus, the co-occurrence of absorption features at key wavelengths in the spectra of phyllosilicate mineral standards and these asteroid spectra strongly suggests a compositional similarity. The NIR spectra of phyllosilicates (as in Fig.8.11 and 8.12) are characterised by primary absorption band at 1.4µm, which appears as a sharp asymmetric reflectance minimum, and occasionally contains either a double peak or a shoulder (Che and Glotch, 2012). A spectral feature at 1.9µm is also common with a similar profile to the 1.4µm feature, while features at 0.9µm and 1.1µm are less pronounced or absent. The functional group attachment bond [M-OH] is always present, located between 2.2-2.4µm and of variable intensity. This feature helps to distinguish structural water, found in phyllosilicates, from liquid water, atmospheric water vapour and water molecules adsorbed onto a mineral's surface (Hunt, 1977).

Simple hydroxyl bearing brucite layers are present on the surfaces of at least some Veritas and Themis members. Furthermore, their origin as atmospheric water vapour features can also be ruled out. This is because all the spectra were previously corrected for atmospheric effects, theoretically eliminating any atmospheric contribution. Additionally, almost all of the asteroids studied also contain the vibrational pair located in the 2.2-2.4µm, which originates only from M-OH bonds and is therefore diagnostic of hydrated minerals, rather than water molecules (Hunt, 1977). These hydrated spectral signatures are, therefore, tentatively interpreted as phyllosilicate minerals, which imply formation by aqueous alteration (Fornaiser et al., 2014; McAdam et al., 2015) and is consistent with previous spectral studies of C-type asteroids (Feierberg et al., 1985; DeMeo et al., 2009; Landsman et al., 2016 and others).

Although, hydration features are present, they are not found in every asteroid analysed. For example, (24) Themis, (28022) 1998BA_9, (19845) 2000SY_{319} and several other members entirely lack resolvable absorption bands, or as in (6343) 1993VK, which contains some of the characteristic hydroxyl-group features (e.g. the 1.9µm) but lacks the diagnostic 1.4µm band. This can be explained by considering how phyllosilicate minerals respond to increasing temperatures.

Experimental heating of phyllosilicate mineral standards reveals that thermal decomposition results in the progressive loss of spectral features, as well as continuum slope reddening (Madejová, 2003; Ostrowski et al., 2010; Che and Glotch, 2012). As temperatures rise absorption band depth decreases. This is most significant between 0-300°C, where band depth decreases by approximately 50% (Che and Glotch, 2012). Furthermore, the shape of absorption bands also evolves; at low temperatures, the 1.4µm band in phyllosilicates has a shoulder at the higher wavelength side of the reflectance minimum, however, this switches to the lower wavelength side at 400°C, and increases slightly in depth as temperatures rise, between 400-600°C (Che and Glotch, 2012). At 800°C, the 1.4µm feature is effectively lost and a featureless, flat spectra remains. This progressive reduction in absorption band intensity occurs as structural water is lost in dehydroxylation reactions (Chapt.4, Wang et al., 2002; Zhang et al., 2010; Che and Glotch, 2011; 2012).

In the simplest case, the detection of phyllosilicate on the surface of some Veritas and Themis members implies that all asteroids, of both families, contain phyllosilicates. The lack of diagnostic absorption features in some asteroid spectra can, therefore, be explained by heating, at least at their surface, resulting in the partial (as in [6343] 1993V) or complete (as in [24] Themis) dehydroxylation of their regolith phyllosilicate. This suggestion is also supported by the observation that most of the asteroid spectra studied here have an asymmetric 1.4μm feature with a shallow low wavelength side, sometimes with multiple troughs or a shoulder feature, and a steep higher wavelength side (see Fig.8.11). These observations are consistent with the NIR spectral profiles of saponite (and other 2:1 phyllosilicates) heated to above 400°C and below 900°C (Che and Glotch, 2012) and, therefore, potentially indicate the presence of partially dehydrated phyllosilicate material.

Finally, it should be noted that much of the spectral variability, including smaller reflectance minima/maxima are a product of either the baseline processing method, grain size effects on the host asteroid, atmospheric interference (e.g. scattering, absorption or reemission) or analytical errors arising from a sensitive detector. Given the challenging conditions, analysing spectra as noisy as these, most of the minor reflectance minima must be ignored and only the significant troughs considered. This underpins the difficulties associated with the interpretation of NIR asteroid spectral data.

8.6. Discussion: interpreting micrometeorite NIR spectra

Micrometeorites were selected from each of the mid-IR spectral groups (Sect.4.2), and, therefore, represent the complete range of bulk mineralogies commonly found in unmelted micrometeorites affected by entry heating (Chapt.4). This includes amorphous dehydroxylates (G2 and G3), mixed dehydroxylate and recrystalized olivine (G4) as well as particles composed entirely of metamorphic nanocrystalline olivine (G5). Despite a range of mineralogies and degrees of crystallinity, no correlation is observed between mid-IR spectral signatures and the position or occurrence of absorption bands in their NIR spectra. For example, the spectra of CP94-050-060, CP94-050-067 and CP94-050-074 are very similar (Fig.8.10) - characterised by a series of regular undulations, with an approximate wavelength of two microns and an amplitude of approximately 0.1 (arbitrary reflectance units) – however, their mineralogies are distinct, being either amorphous (dehydroxylates only) or composed of crystalline olivine (only). Furthermore, repeating undulations like those seen in the micrometeorite spectra are characteristic of noise-dominated spectra, produced by random interference at the detector. Likewise, the remaining six micrometeorite spectra have similar features, containing erratic saw-tooth profiles with shallow and randomly located reflectance minima. Thus, unambiguous absorption features produced by covalent bonds in silicate minerals are not present in these spectra and no compositional information can be derived. This is not surprising since the NIR spectral region contains absorption bands at least an order of magnitude lower in intensity than the fundamental vibrations in the mid-IR region (Stuart, 2000). Given that the spectral features described in Chapt.4 have absolute reflectance values between 1-20% the expected signals over the NIR range are approximately 0.1-2% depth below the continuum; with such low signal strengths statistical and analytical noise overwhelm any mineralogical information.

8.7. Conclusions from NIR spectroscopy

This chapter investigated the NIR spectra of two young C-type asteroid families. Thirty spectra, previously collected by ground-based telescope from Veritas and Themis members, were analysed by baseline removal and reflectance minima detection. Common absorption bands, located at 0.9µm, 1.1µm, 1.4µm, 1.9µm and 2.2-2.4µm were identified in most asteroid spectra. Both the wavelength ranges and shape of these absorption bands correspond to the vibrational overtone or combination modes of metal-hydroxyl group (M-OH) covalent bonds and, therefore, imply the existence of hydrated minerals on the surface of several Veritas and Themis members. This study is, therefore, consistent with previous spectral analyses of C-type asteroids which have observed either a close spectral match to CM/CI or CR chondrites (Vernazza et al., 2008; Ostrowski et al., 2010; Lantz et al., 2013 and others) or identified water absorption features in their mid-IR or visible spectra (Campins et al., 2010; Fornaiser et al., 2014; 2016). However, this study remains novel because it represents the first identification of hydrated phyllosilicate minerals on Veritas family asteroids.

Those asteroids with strong evidence of hydration were: (490) Veritas, (1086) Nata, (2147) Kharadze, (222) Lucia, (656) Beagle and (3899) Wichterle. This finding is consistent with previous spectral studies of C-type asteroids,

This study also collected the first NIR spectra of micrometeorites. However, no absorption bands relating to compositional information were identified because these spectra are, instead, dominated by random noise, arising from a poor quality analytical setup, small sample size and low degrees of crystallinity. A direct comparison of Veritas asteroids to unmelted micrometeorites was, therefore, not possible.

Chapter 9: Fossil micrometeorites from Cretaceous chalk

9.0 Overview – This chapter reports the results of a small-scale investigation into the recovery of fossil micrometeorites from Cretaceous chalk. The aim of this project was to obtain fine-grained micrometeorites that fell to Earth in the geological past and are, therefore, potentially sourced from different asteroid families than the current dust flux. Although unmelted micrometeorites were not recovered, an abundance of diagenetically altered cosmic spherules were identified. Thus, this study provides an insight into the fossilization and preservation mechanisms affecting extraterrestrial dust in the geological record.

Four stratigraphic horizons, within the Late Cretaceous, were searched (Fig.9.5; ND1 & LC1-3) representing Cenomanian-Coniacian age deposits. In total, 112 microspherules were recovered. Particles vary from pristine, ancient and unaltered S-type and I-type cosmic spherules to pseudomorphic recrystalized fossil micrometeorites, consisting of either Mn-bearing magnetite or Fe-silicide. The pristine spherules are readily identified as micrometeorites by their characteristic mineralogies, textures and compositions. Conversely, the pseudomorphic spherules are identifiable only on the basis of size, morphology and textures, as their composition and mineralogy are inherited from the host sediments. Both altered spherule types (magnetite and silicide) contain dendritic crystals and spherical morphologies, testifying to rapid crystallisation of high temperature iron-rich metallic and oxide liquids. These particles also contain spherical cavities, representing the weathering and removal of Fe-Ni metal beads and irregular cavities, where vesicles were formed by trapped gas during inward crystallization. Therefore, the textures of the altered spherules are directly comparable to textures observed in modern Antarctic I-type cosmic spherules. These results demonstrate that cosmic spherules, preserved in sedimentary rocks, are affected by a suite of complex diagenetic processes, which can result in disparate replacement minerals, even within the same host rock. As a result, the identification of fossil micrometeorites requires careful observation of particle textures and comparisons with modern micrometeorite collections.

9.1. Fossil micrometeorites from previous studies

Fossil micrometeorites have been recovered from a variety rock types and several different geological periods, spanning Archean (Tomkins et al., 2016) to Miocene (Meier et al., 2016). Most fossil micrometeorite studies search rocks formed in deep marine environments. This is because the low sedimentation rates, ease of extraction, ease of identification and abundance of material promote the recovery of extraterrestrial dust (Taylor and Brownlee, 1991; Onoue et al., 2011). Commonly limestones are investigated, as these host rocks represent marine environments up to the carbonate compensation depth (today approximately 3000m, Pälike et al., 2012) and are susceptible to weak acid digestion. Similarly, evaporite salt deposits are also soluble in warm water and have yielded high concentrations of micrometeorites in the past (Mutch, 1964; Davidson et al., 2007). By dissolving the host rock, only a detrital residue remains (Voldman et al., 2013;). Typically, this will be between 1-5% of the original rock by mass for pure marine limestones such as Cretaceous Chalk (Hancock, 1975;

Hopson, 2005). These residues can be searched rapidly for cosmic dust. Alternatively, several fossil micrometeorites have been successfully extracted from non-carbonate rocks, such as cherts and shales (Onoue et al., 2011). This is achieved by mechanical disaggregation, using a rock crusher. However, such studies may require an additional separation technique to concentrate micrometeorites further above the background sediment, where the quantity of insoluble fines is significant. Typically, either density or magnetic separation techniques are used (Onoue et al., 2011; Voldman et al., 2013).

Previously, micrometeorites found in ancient sediments have been identified by their distinctive mineralogies, compositions and textures. However, the occurrence of pristine ancient micrometeorites is rare (Dredge et al., 2010; Voldman et al., 2013; Tomkins et al., 2016), even modern Antarctic collections contain abundant, weathered micrometeorites (van Ginneken et al., 2016). Instead, during terrestrial residence, alteration of glass to palagonite, hydration of Fe-Ni metal, dissolution of anhydrous phases and secondary replacement, as well as surface encrustation by halite, calcite and jarosite are all common artefacts arising from preservation in the Antarctic environment (van Ginneken et al., 2016). Likewise, modern micrometeorite collections recovered from deep-sea sediments are subject to dissolution of S-type spherules, resulting in collections with an overabundance of I-types (Taylor and Brownlee, 1991). Those silicate spherules which do survive residence on the sea-floor show etching of glass and anhydrous phases and the removal of Fe-Ni metal (Taylor and Brownlee, 1991; van Ginneken et al., 2016). Consequently, long terrestrial residence prior to diagenesis and subsequent storage over geological time are highly likely to result in alteration, corrosion and replacement among fossil micrometeorite collections (Taylor and Brownlee, 1991). These processes will prevent the unambiguous identification of cosmic dust retrieved from ancient sediments. Therefore, new criteria to identify fossil cosmic spherules are essential before a more complete geological history of local solar system events can be reconstructed.

This chapter reports the discovery of ancient S-type and replaced fossil I-type cosmic spherules. The recovered micrometeorites exhibit a wide range of diagenetic effects, allowing, for the first time, the fossilization of cosmic dust to be characterised.

9.2. Recovery and analysis of fossil micrometeorites from Cretaceous chalk

Since the total number of fossil micrometeorite collections is low, any new collection which recovers cosmic dust from an unexplored period of the geological column will provide a significant contribution to the science of micrometeoritics. This study conducted a small-scale investigation into the extraction and characterisation of cosmic dust from Cretaceous chalk.

Cretaceous chalk was chosen as a suitable rock type to search for fossil micrometeorites. Chalk sediments are restricted to the Late Cretaceous (and Early Tertiary) (Hancock, 1975; Zijlstra, 1994), spanning a geological significantly period of time, approximately Cenomanian-Maastrichtian, between 100.5-66Ma (ICS, 2016). Chalk sediments are abundant and locally available, along the Surrey Hills in the North Downs and along the South-East coast of the UK. Furthermore, chalk sediments represent pelagic seas, with water depths between 200m and 700m (Hancock, 1975). At these depths, the

nanometre-scale coccolithophore elements can settle out of suspension and therefore, even the smallest micrometeorites will be deposited. Since chalk is a limestone, acid digestion, as well as mechanical disaggregation are viable extraction methods, allowing this study to compare techniques and to evaluate collection biases. In addition, the majority of extraterrestrial studies, which have investigated the Cretaceous focus on the K-Pg mass extinction event, as a result, relatively little is known about the background cosmic flux during the Early Cretaceous.

The first chalk samples were collected from an outcropping 7m tall exposed escarpment at Ranmore Common, close to Hogden lane [51°15'18.4"N, 0°23'32.0"W], in Surrey, UK. British Geological Survey (BGS) maps constrain the entire bedrock across this region, between Dorking and Guildford, as Aptian-Santonian in age, representing between 125-83Ma (Fig.9.1., BGS, 2017; ICS, 2017). The North Downs is composed primarily of Late Cretaceous chalk deposits, which form the Northern limb of the eroded Wealden anticline. In Surrey the chalk is cut unconformably at ~83Ma, overlain by the Lambeth group clay silt and gravels of Eocene age.

The Hogden Lane locality (Fig.9.2) is located at the site of a road cutting, which provides a large clean exposure of chalk cliff with resolvable bedding. However, this site is within a section of undifferentiated bedrock on BGS maps (Fig.9.1) and is therefore a member of either the Lewes Nodular Chalk Formation, the Seaford Chalk Formation or the Newhaven Chalk Formation. The chalk lithology at the Hogden Lane locality, best fits the description of the Seaford formation - a firm white chalk with regular semi-nodular and tabular flint beds and occasional paired marls (Aldiss et al., 2004; Hopson, 2005). This restricts the chalk deposits from mid-Coniacian to mid-Santonian in age, between ~89.8-83.6Ma (ICS, 2017). To further constrain the deposit's age, a sample of powdered chalk (from which spherules had been picked) was sent to Dr. Cristina Manning, at Royal Holloway University, London for Sr isotope characterisation. The resulting isotope ratio ($^{87/86}$Sr=0.707395 ± 0.000008) was compared against the Sr stratigraphy curve for English chalk developed by McArthur et al., (1993) (Fig.9.3) and produced an age of 87Ma ± ~0.5M, restricting the chalk sediments to the mid-Conacian (Fig.9.5).

Micrometeorites were searched for by acid digestion and mechanical separation; two 9kg chalk blocks of similar dimensions were used. Previously, a range of acid species and concentrations have been used in the recovery of fossil micrometeorites, for example: 10% acetic (Voldman & Genge, 2013), glacial (>99%) acetic (Taylor & Brownlee, 1991) to 20% HCl (Dredge et al., 2010) have all been used. However, since silicate minerals, magnetite and wüstite (all common minerals present in cosmic spherules) are sparingly soluble in concentrated acids, the choice of acid, concentration and dissolution time is critical (Lenher & Merrill, 1917; Belikov et al., 2002). This study used 10% HCl acid with reaction times terminated after 6 hours. This was sufficient to dissolve the chalk in the minimum amount of time. Prior to dissolution, the chalk block was washed and broken into pebble sized clasts. Insoluble fines were extracted using rock sieves, air dried and searched by magnetic separation and optical picking. In addition, another chalk block, extracted from the same outcrop and sedimentary horizon, was investigated via mechanical separation. A benchtop rock crusher pulverised the chalk

Figure 9.1. Geological map of North Downs displaying the bedrock between Dorking and Guildford. This chart highlights the Hogden Lane locality from which the first chalk blocks were extracted, during the search for fossil micrometeorites from Cretaceous sediments. Data adapted from the BGS (2016).

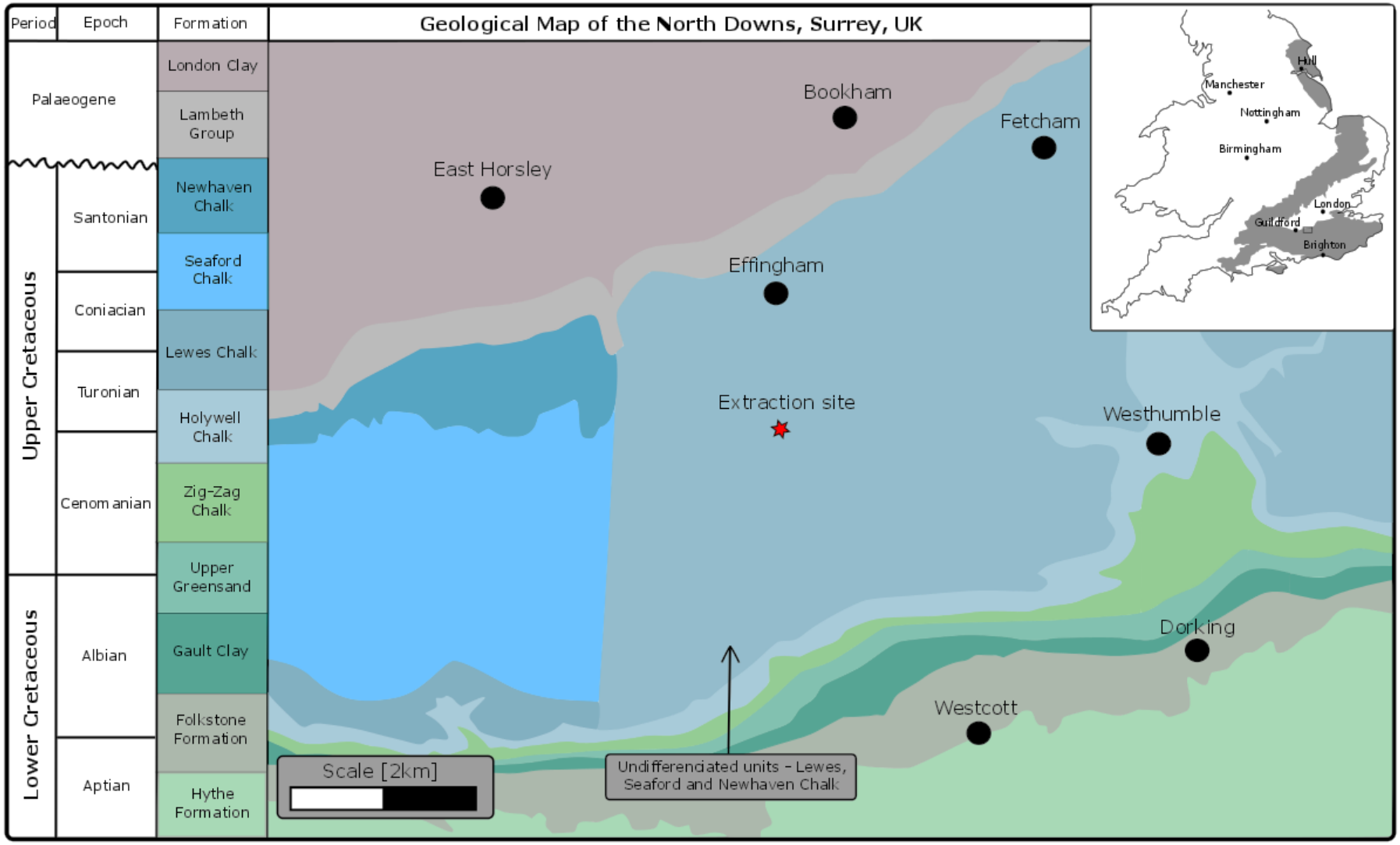

Figure 9.2. (A) The chalk cliff face from which (B) 2x9kg chalk blocks were extracted. Black arrows are used to indicate scale, while dashed yellow lines indicate bedding, resolvable from the presence of tabular flint bands. Photographs taken on 15/04/15.

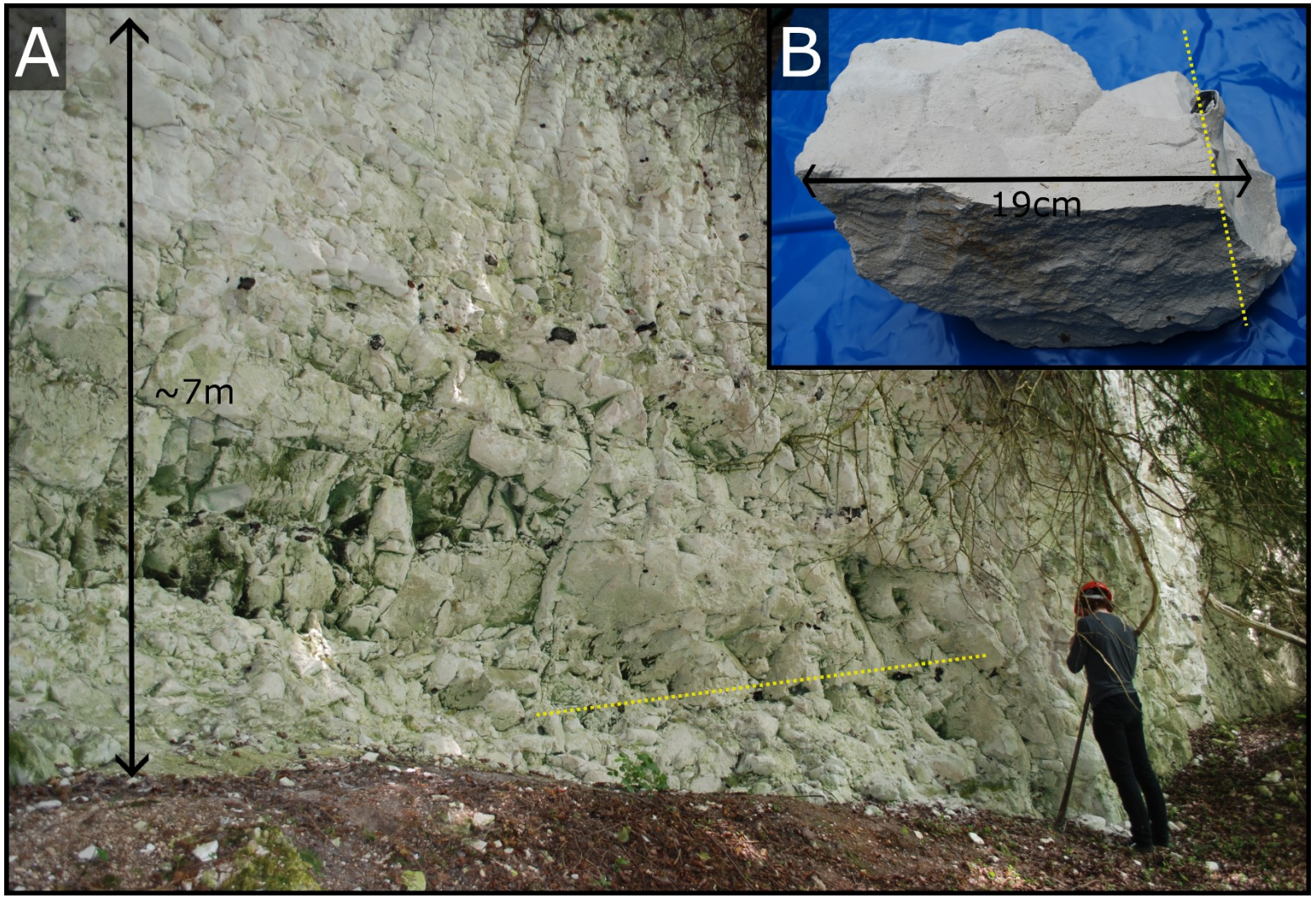

block. Following each pass through the crusher any <500µm powder was removed, 2kg of fine powder were then searched for micrometeorites, again by magnetic separation and optical picking. Potential extraterrestrial particles were placed on adhesive tape, set in resin, sectioned, polished and carbon-coated. These were then investigated using SEM-BSE and EMPA techniques using the same instruments and under the same operating conditions as the Antarctic micrometeorites.

In addition to investigating chalk blocks extracted from Hogden Lane, a second project searched for fossil micrometeorites in chalk sediments at Lulworth Cove [50°37'9.1"N, 2°14'42.0"W], along the Dorset coast, UK. This project was conducted by Jack Dunning, an undergraduate MSci student at Imperial College London and under the supervision and guidance of M. Suttle. This project was conducted between Sep-Jan, 2016-17. Three separate sedimentary horizons, exposed on the Northern cliff face at Lulworth Cove were investigated (Fig.9.4). These horizons sample the Lower chalk, the Plenus Marl and the Middle chalk respectively. Figure 9.5 illustrates how the Lulworth Cove and Hogden Lane chalk samples are related in terms of age and regional stratigraphy. All 3 Lulworth Cove blocks, each weighing approximately 10kg in mass, were processed by mechanical disaggregation, only. Following the separation and recovery procedures outlined above. Spherules were then set in resin, sectioned, polished, carbon-coated and analysed under SEM.

Figure 9.3. $^{87/86}$Sr Stratigraphy curve for English Chalk, taken from McArthur et al., (1993) [Fig.3], with the Hogden Lane chalk sample plotted. The age of chalk extracted from this site is, therefore, either mid-Conacian or mid-Turonian. Since Turonian age sedimentary do not outcrop between Dorking and Guildford the chalk at Hogden lane is Con acian in age, at approximately 87Ma.

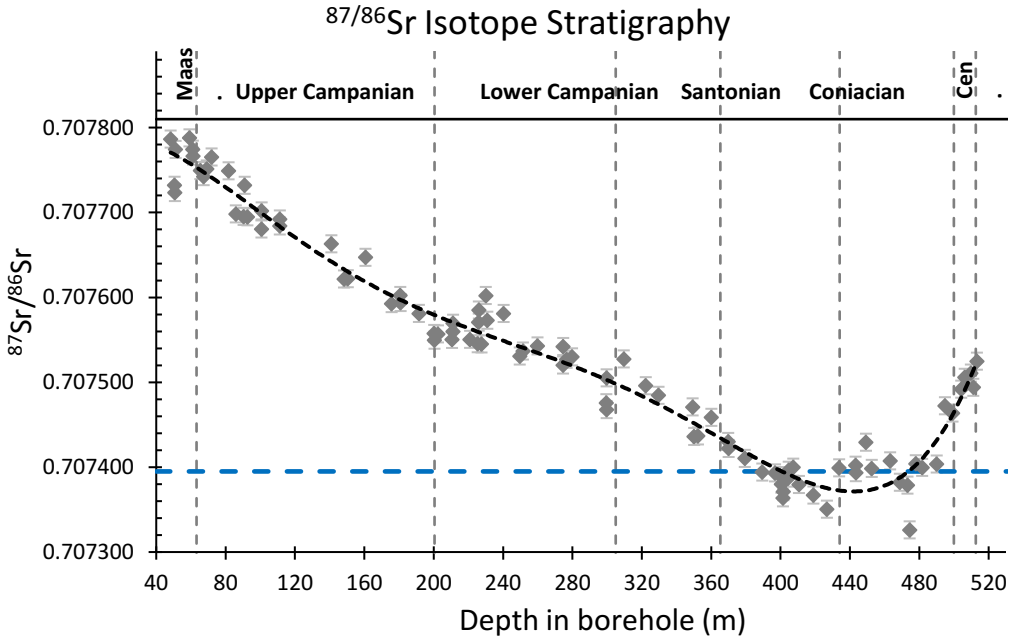

Figure 9.4. (Below) The exposed chalk cliff face at Lulworth Cove, from which 3x10kg chalk blocks were extracted. Black dashed lines indicate the attitude of bedding and the separation of the exposure into distinct sedimentary horizons. At the base of the outcrop (A) The Zig-Zag Chalk formation is exposed, this is a member of the Lower Chalk (previously known as the Grey-Chalk) Supergroup, which is characterised by soft-medium hardness pale grey chalk that lacks flints. The Zig-Zag chalk is overlain by a the Plenus Marl (B) a thin band of green-grey soft and brittle laminated limestones. This member forms the base of the Middle Chalk in the older stratigraphic framework and the base of the White Chalk Supergroup in the current stratigraphic nomenclature. At Lulworth Cove the Plenus Marl is overlain by the Holywell Nodular Chalk formation. This is a highly variable lithology, characterised by hard, creamy white chalk, containing sparse paired marl bands, an abundance of phosphatic nodules, flints and occasional fossils. The Holywell Chalk is a transitional deposit which spans the Cenomanian/Turonian boundary. Black squares are used to indicate the exact location from which chalk blocks were extracted. (Note: this figure is reproduced with permission from J. Dunning's MSci thesis).

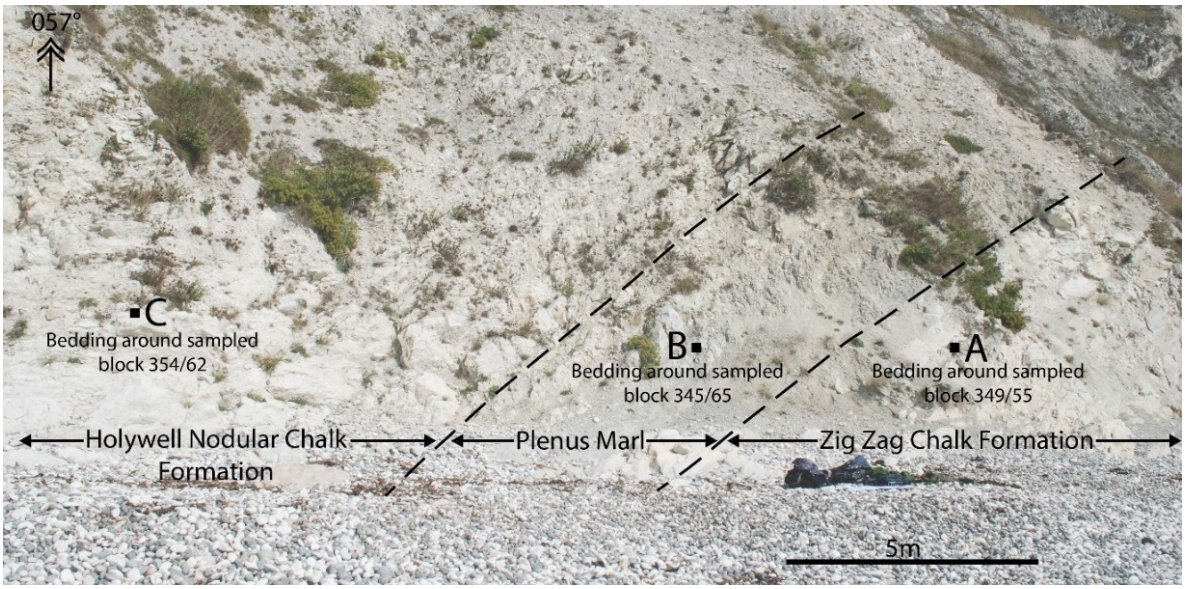

Figure 9.5. Stratigraphic chart for chalk of South East England, showing the approximate age of chalk blocks investigated in this thesis. Initially a single chalk block was extracted from Hogden Lane in the North Downs, this block was mid-Conacian age and derived from the Seaford Chalk Formation (ND1). A further three blocks were extracted from sedimentary horizons at Lulworth Cove (LC1-3). These deposits extracted from the Lower Chalk Supergroup (Zig-Zag Formation), the transitional Plenus Marls and the base of the White Chalk Supergroup (Holywell Nodular Chalk Formation).

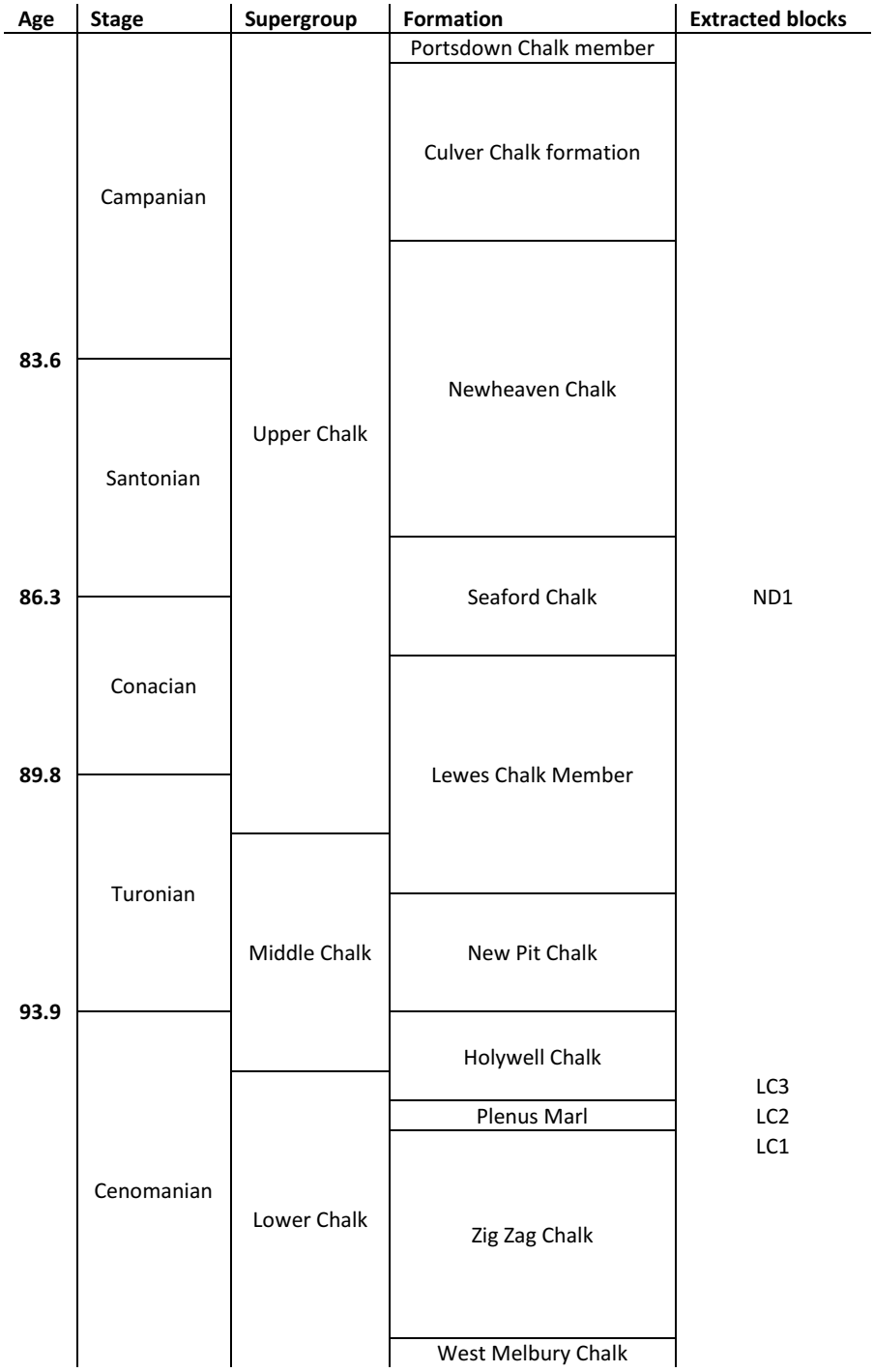

9.3. Results

According to Hancock (1975) and Hopson (2005), the upper Cretaceous chalk contains >95% $CaCO_3$. The residual non-carbonate fraction is mainly clay minerals (smectite, montmorillonite, illite and kaolinite), mica, quartz and ilmenite. Among the acid digested residues clay minerals were dominant, these collected together in the dissolution container and formed an ooze that effectively clogged the cascade sieves. However, among the mechanically disaggregated chalk, detrital material could be recovered and examined. Small (<300µm) quartz grains were common, while the magnetic separates contained rhombohedral ilmenite, anhedral pyrite and irregular goethite grains. Among the detrital material >100 small (<170µm) spherules were recovered. The textures and geochemistry of these spherules are shown in Figures 9.6, 9.8 and 9.9 and Tables 9.1. and 9.2. Particles range in diameter from ~10-165µm and, except for the 3 silicate spherules, are dominated by Fe-rich mineralogies.

9.3.1 Extraction of Spherules [ND1]

Both recovery methods yielded spherules; acid dissolution techniques produced ten relatively large spherules (>60µm), while sixty-six smaller spherules were retrieved from approximately 2kg of crushed chalk powder (<500µm), prepared by mechanical separation. During dissolution, the liberated clay fines formed a colloidal suspension before flocculating, which efficiently trapped any small (<60µm) spherules, preventing collection. Among the mechanically extracted spherules, two particles contained sheared edges, most likely damaged during the crushing process. It is, therefore, probable that several other spherules were destroyed during mechanical disaggregation. Despite this loss, the relative ease of extraction and significantly higher yields obtained by crushing make this extraction method a more attractive option for future recovery efforts.

9.3.2 Spherule geochemistry and mineralogy [ND1]

Three compositional types were recovered; Fe-oxides (60), Fe-silicides (13) and silicate spherules (3). Ninety-eight percent of the Fe-oxide spherules are composed of magnetite, with minor Al (~0.05-2.0wt%), Si (0.06-4.0wt%) and Mn (0.4-0.6wt%) and trace (<0.05wt%) Na, Mg, K, Ca, P, Ti and Cr. Nickel was not detected in any magnetite spherule. Additionally, a single Fe-oxide spherule (C16-0003, Fig.9.6D) was found, which contained Ni-bearing (Ni = 0.53wt%) wüstite and magnetite. Raman spectroscopy (Fig.9.7) on the Fe-oxide spherules confirmed that all particles (except C16-0003) were composed of magnetite. The broad absorption peaks and relatively low intensity, as compared to magnetite mineral standards and magnetite in modern Antarctic I-types, suggest that either the crystal grain size or degree of crystallinity in the Cretaceous spherules is lower than their modern counterparts (Jubb and Allen, 2010).

Iron silicide particles have stoichiometries of approximately $Fe_{2.89}Si_{1.11}$ and, therefore, approach the ideal formula for suessite (Fe_3Si). Nickel was not detected, and Cr occurs at <1wt%. Analytical totals suggest minor oxygen content (<1.21wt%). Manganese is present at between 0.3-0.7wt%.

The 3 silicate spherules (Fig.9.9) have chondritic bulk compositions. Major element abundances vary, relative to CI, by Mg (1.1-1.6), Al (1.6-2.0), Si (1.4-1.9) and Fe (1.4-1.8). Trace Mn, at

concentrations <0.12wt%, was also detected, at concentrations lower than the Mn identified in the Fe-oxide and Fe-silicide grains. The average chemical compositions of each spherule type are shown in Table 9.1.

9.3.3 Spherule Textures [ND1]

Both the Fe-oxide and Fe-silicide spherules have similar external and internal textures (Table.9.2.), either: (1) homogeneous, lacking visible crystal boundaries or (2) dendritic, consisting of interlocking crystals. Homogeneous spherules include particle C16-0003, the Ni-bearing wüstite spherule (Fig.9.6D), which contains small equant magnetite grains within a wüstite groundmass and an incomplete magnetite rim. Several of the homogeneous magnetite and silicide spherules lack detailed external or internal textures and contain few cavities.

Dendrites are apparent on the external surface of particles (Fig.9.6A-C). Dendritic spherules contain crystals with cruciform, lattice-like morphologies (Fig.9.6A) or re-entrant fine-dendrites that often occur in several domains (Fig.9.6B and C). Crystals with grain-sizes >5% of particle radii often form an internal texture with a cellular appearance owing to the intersection of dendrites with the cut surface (Fig.9.6E). Among the Fe-silicide spherules, dendrites have poorly defined grain boundaries (Fig.9.8B).

However, clearly resolvable crystals can be seen on the external surfaces of most spherules (Fig.9.6A, C and D) and are present internally in C16-0010 (Fig.9.8E and F). In this particle, the dendrites consist of two different silicide phases, although the stoichiometry of these minerals could not be determined by EDS owing to their small size.

Cavities are most common within the dendritic spherules (Table 9.2) and include: (1) large (>10µm in diameter) sub-spherical cavities (Fig.9.6D and F), (2) rounded to irregular cavities (Fig.9.6H and Fig.9.8B), and (3) cavity networks between dendrites (Fig.9.6G and I and Fig.9.8B, 9.8E and 9.8F).

Although most particles have a high degree of sphericity, some Fe-silicide particles exhibit surface protrusions (Fig.9.8D). Spherical and irregular rounded protrusions exist and consist of fine-grained masses of Fe-silicide, which are distinct from accompanying dendrites. Similar fine-grained masses of silicide partially fill interior cavities in some particles.

The internal textures of the silicate spherules exhibit: (1) barred olivine laths (of widths 1.2-2.5µm) with interstitial magnetite crystallites suspended in glass (Fig.9.9B), or (2) micro-porphyritic iron-rich olivine grains (<2µm in length) within a glassy matrix, containing equant magnetite. The micro-porphyritic spherule (Fig.9.9A) also contains anhedral, 25µm long, Mg-silicate grains and ~10% (of the exposed surface area) vesicles.

Fig.9.6. (Below) External and internal textures of Fe-oxide spherules, interpreted as fossilized cosmic spherules. Particle D (C16-0003) is the single unaltered Ni-bearing I-type, composed of wüstite (FeO), while the remaining spherules are composed of Mn-bearing magnetite (Fe_3O_4). Surface dendrites and residual chalk sediment, including fragmented coccolithophore tests can be seen coating external surfaces of spherules (A-C). In spherule D and F sub-circular cavities are present, representing the loss of an Fe-Ni metal bead by corrosion during residence on the Cretaceous seafloor, these spherules are therefore, identified as metal-bearing (MET) I-types. In contrast, spherule G contains isolated irregular small cavities, representing vesicles formed by residual gas trapped during inward crystallisation and is therefore an oxidised (OX) I-type.

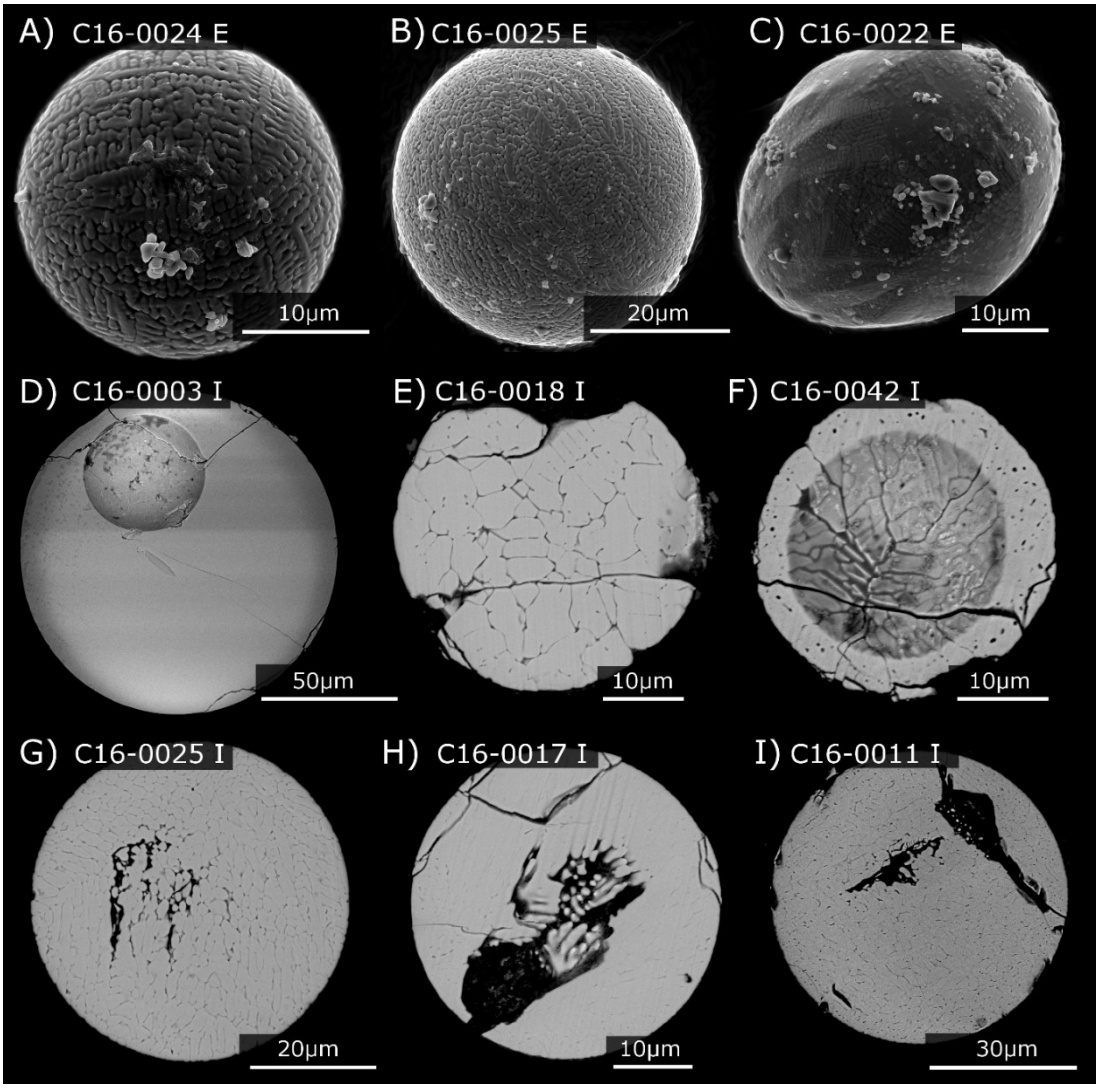

Fig.9.7. (Overleaf) Raman spectra collected from the cross-sectioned surfaces of the Cretaceous spherules (light grey) and those from modern I-type micrometeorites, recovered from Larkman Nunatak (Suttle et al., 2015) (black and dark grey). Spectra from three Cretaceous spherules are displayed, although all of the Fe-oxide spherules produced similar spectra, containing the characteristic absorption peaks of magnetite (A_{1G}~670cm^{-1}, T_{1G}~550cm^{-1} and T_{1G}~310cm^{-1}, as in Jubb and Allen 2010). By contrast, all modern I-type micrometeorites are two-phase composed of either Fe-Ni metal (which contains no active phonon vibrations) and Ni-bearing wüstite or Ni-bearing wüstite and magnetite. The Raman spectra of wüstite and magnetite are shown in dark grey and black respectively. Note that the Cretaceous spherules also tend to produce spectra with broader and lower intensity peaks, suggesting a lower degree of crystallinity than the modern Antarctic spherules. This could reflect the recrystallization of magnetite or the incorporation of Mn into the crystal structure.

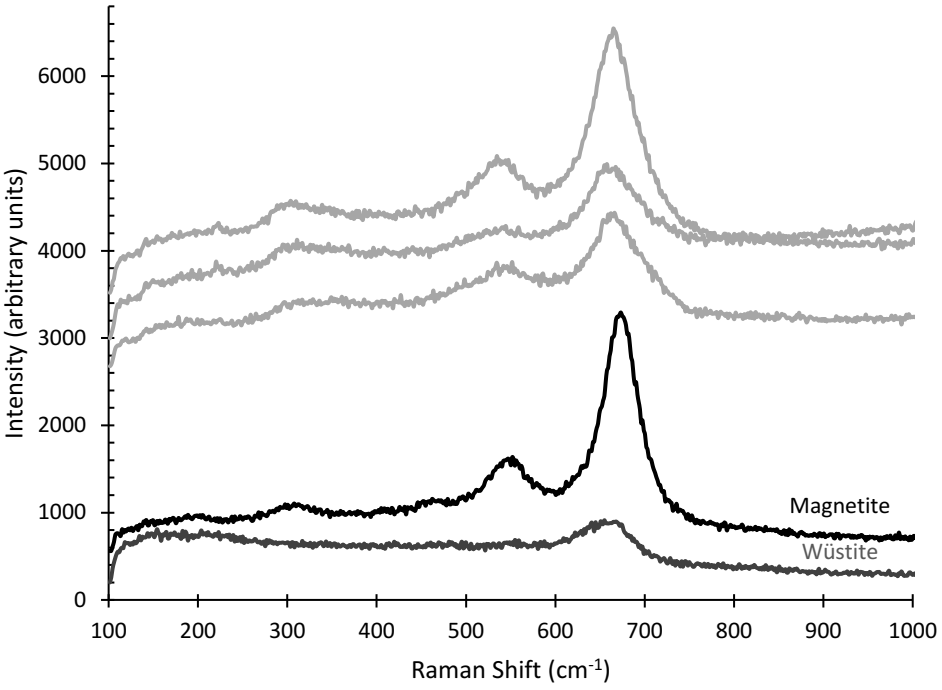

Fig.9.8. (Below) External and internal textures of Fe-silicide spherules, most probably composed of suessite (Fe_3Si). These spherules are interpreted as fossilized cosmic spherules. Replacement by silicides imperfectly pseudomorphs the original texture, leading to changes in volume (accounting for the presence of micron sized voids seen in 3F) and protrusions (3D), protecting from the particle's surface. Despite preservation artefacts, original textures can be discerned, allowing their identification as cosmic spherules. Dendritic crystals are observable in all particles and attest to a rapid cooling history as molten droplets. Particle C16-0009 (3A and B) preserves only a single phase (most likely wüstite) while particle C16-0010 (3D-F) preserves both the original magnetite and wüstite as different silicide minerals. Cavities in 3B are a result of volatile gases released during atmospheric entry.

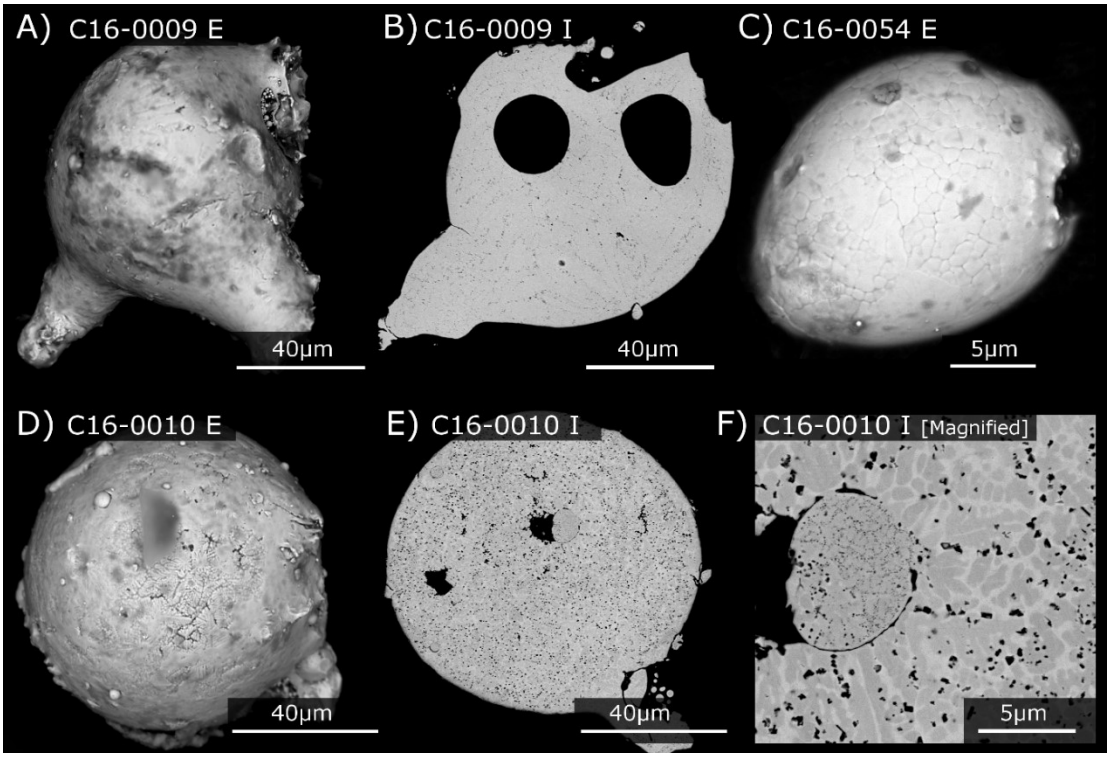

Table 9.1. (Below) Geochemical data (shown in wt%) for different compositional types of fossil cosmic spherule. The detection limit and analytical uncertainties of EDS analyses are on the order of 0.01wt%, "-" indicates values below the detection limit while "*" indicates matrix correction "*by oxygen stoichiometry*" and "†" indicates matrix correction by "*All elements*".

Spherule Type	Sample	*N*	Na	Mg	Al	Si	Ca	P	Ti	Cr	Mn	Fe	Ni	O	Total
Wüstite spherule*	C16-0003	-	-	-	-	-	-	-	-	-	-	77.0	0.5	24.9	102.4
Magnetite spherules*	C16-0047	-	-	-	0.1	0.1	-	-	-	-	0.4	70.0	-	20.4	91.0
	C16-0028	-	0.3	-	-	0.9	-	-	-	-	0.5	69.3	-	21.1	92.1
	Average	**35**	**0.2**	**-**	**0.3**	**0.6**	**0.2**	**-**	**0.1**	**-**	**0.6**	**68.9**	**-**	**21.1**	**92.0**
	Min	35	-	-	-	-	-	-	-	-	-	58.9	-	20.1	89.6
	Max	35	4.5	0.6	3.2	4.9	2.6	0.1	4.5	0.2	9.9	71.9	-	26.4	100.9
Iron silicide spherules†	C16-0009	-	-	-	-	13.0	-	-	-	0.8	0.7	83.7	-	-	98.1
	C16-0056	-	-	-	-	15.3	-	-	-	-	-	85.0	-	-	100.4
	Average	**6**	**-**	**-**	**-**	**14.7**	**-**	**-**	**-**	**0.3**	**0.5**	**84.0**	**-**	**0.2**	**99.7**
	Min	6	-	-	-	13.0	-	-	-	-	-	81.7	-	-	94.7
	Max	6	-	-	0.1	15.7	-	-	-	1.2	0.7	85.0	-	1.2	103.9
Chondritic silicate spherules*	C16-0001	-	-	10.9	1.7	15.3	3.4	-	-	-	-	33.2	0.6	37.1	102.0
	C16-0002	-	-	15.3	1.6	18.8	0.6	-	-	-	0.1	28.2	0.6	41.6	107.2
	C16-0045	-	-	15.2	1.4	19.8	1.7	-	-	-	0.1	26.9	-	42.4	107.9
	Average	**3**	**-**	**13.8**	**1.6**	**17.9**	**1.9**	**-**	**-**	**-**	**0.1**	**29.4**	**0.4**	**40.4**	**105.7**
	Min	3	-	10.9	1.4	15.3	0.6	-	-	-	-	26.9	-	37.1	102.0
	Max	3	-	15.3	1.7	19.8	3.4	-	-	-	0.1	33.2	0.6	42.4	107.9

Table 9.2. (Below) Particle textures observed among the Cretaceous spherule population. Textures listed in this table include characteristic features of quench-cooled I-type cosmic spherules, artefacts of terrestrial residence and artefacts arising from diagenetic alteration.

	Texture	Variations	Prevalence	Example	Interpretation	Reference
1	External dendrites	Cruciform, re-entrant or cellular	>80% of spherules	Fig.9.1(A-C) & Fig.9.3(C-D)	Evidence of rapid quench cooling.	Genge et al., 2016
2	Internal dendrites		>50% of spherules	Fig.9.1(E-I), Fig.9.3(B, E, F) & Fig.9.4(A-E)		
3	Off-centre, rounded, sub-spherical cavities	Occupying between 10-40% volume	~10% spherules	Fig.9.1(D, F) & Fig.9.6(A-B)	Indicates the former presence of an unoxidised Fe-Ni bead. Cavities are a result of weathering and removal of metal during residence on the sea-floor.	van Ginneken et al., 2016
4	Rounded, irregular cavities	Circular, ecliptic or irregular & >5µm in size. Several may be present.	~30% of spherules	Fig.9.3(B) & Fig.9.4(C)	Indicates the presence of vesicles formed by exsolution of volatile gases	Genge et al., 2017
5	Interconnected cavity networks between dendrites	Complex shapes, occupying <10% of the exposed surface area.	~50% of spherules	Fig.9.1(G-I), Fig.9.3(E, F) & Fig.9.6(C, E)	Residual voids resulting from inward crystallization of a molten spherule, produced during quench cooling.	Feng et al., 2005
6	Abundant small voids and protrusions	Voids <3µm, circular, oval or elongate. Protrusions may be spherical & bud from the main body.	~40% of spherules	Fig.9.1(E, F) & Fig.9.3(E, F)	Artefacts of pseudomorphic replacement fossilization, produced by volume changes during recrystallization.	*This study*

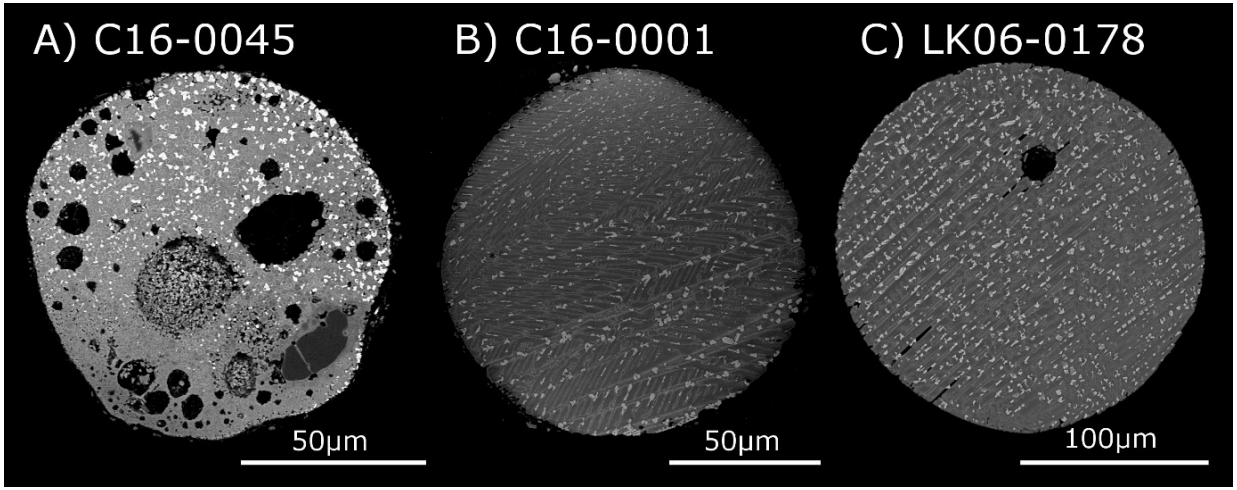

Fig.9.9. Sectioned BEI images of silicate cosmic spherules. Spherules A and B are ancient, unaltered chondritic ancient S-type spherules, classified as micro-porphyritic (A) and barred olivine (B) subtypes. For comparison particle C is a modern, barred olivine spherule recovered from Larkman Nunatak, Antarctica (Suttle et al., 2015; Genge et al., 2017c).

9.3.4. Spherules from Lulworth Cove [LC1-3]

Thirty-six spherules, ranging in size from 20-113µm, were picked from the Lulworth Cove residues. Particle mineralogies and petrologies were identical to those found in the North Downs residues, being composed of either Mn-bearing magnetite or Fe-silicide. However, silicate spherules were not recovered. Likewise, minor (<3.0wt%) Al, Si and Mn and trace (<0.1wt%), Na, Mg, K, Ca, P, Ti and Cr were detected in most particles. Similarly, spherule textures can be classified into homogenous or dendritic and were found to contain the same cavity types; sub-spherical, irregular rounded or networked. Furthermore, a single Fe-oxide spherule (Fig.9.10A) was identified which contained an Fe metal bead surrounded by Mn-bearing magnetite. This particle is, therefore, similar to the many Fe-oxide spherules from the North Downs collection that contain a single large sub-spherical cavity as in figure 9.6D and 9.6F.

These findings demonstrate that the Fe-oxide and Fe-silicide spherules, recovered from Cretaceous chalk, are ubiquitous components of this sediment, found a wide geographic and temporal range. Interestingly, however, the Lulworth Cover spherules were found to contain significantly more fractures than their North Downs counterparts, most likely inherited from the sediment following tectonic upheavals.

Fig.9.10. Examples of spherules collected from the Lulworth Cove residues. Note: this figure is reproduced, with permission, from J. Dunning's MSci dissertation.

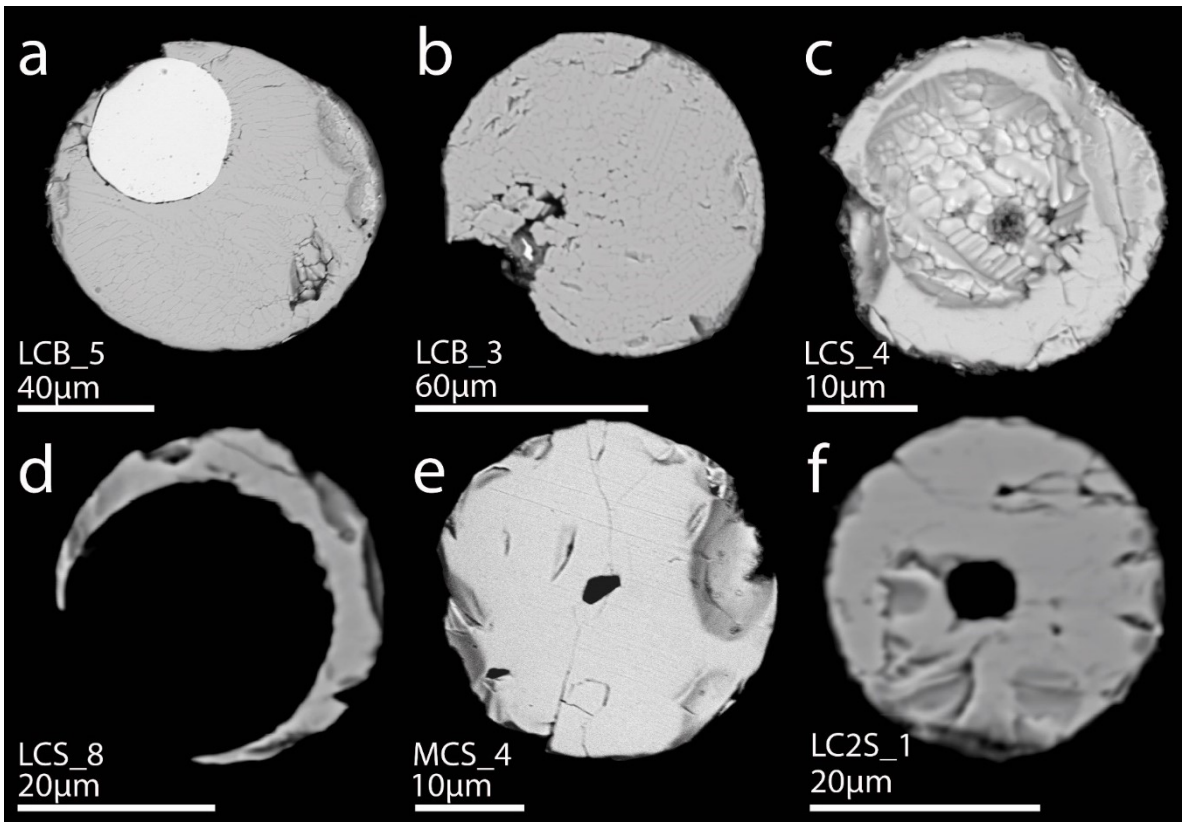

9.4. Discussion: Identification of unaltered, ancient micrometeorites

Four spherules have petrologic features that allow them to be unambiguously identified as pristine, unaltered, ancient micrometeorites. All 3 silicate spherules are indistinguishable from modern Antarctic barred olivine (C16-0001, Fig.9.9B and C16-0002, not shown) and micro-porphyritic (C16-0045, Fig.9.9A) cosmic spherules. Their chondritic compositions, quench textures and droplet morphologies, are conclusive evidence of extraterrestrial origin (Taylor and Brownlee, 1991; Genge et al., 2008; Genge et al., 2016b).

Recent oxygen isotope data from modern S-type cosmic spherules suggests that the majority (>90%) of barred olivine and micro-porphyritic cosmic spherules are derived from carbonaceous chondrite parent bodies, most probably hydrated CM or CR-like asteroids (van Ginneken et al., 2017). Consequently, these 3 Cretaceous S-type spherules also most probably originate from a carbonaceous chondrite parent body. Additionally, particle C16-0001 (Fig.9.6D), the wüstite-dominated Fe-oxide spherule, can be identified as extraterrestrial on the basis of the Ni-bearing wüstite and a magnetite rim. This particle is classified as an I-type cosmic spherule (Genge et al., 2017a). The sub-spherical cavity in this particle is consistent with the weathering and removal of an Fe-Ni metal bead (van Ginneken et al., 2016) and is identical to those observed in modern, weathered Antarctic I-types. Examples of Antarctic I-types are displayed in Figure 9.11 for comparison. These voids originate through the corrosion and removal of metal (van Ginneken et al., 2016; Genge et al., 2017a).

9.5. Discussion: Origin of single-phase Mn-bearing magnetite spherules as altered, fossil I-types

The spherical shape and presence of dendritic crystals observed in all the magnetite spherules strongly imply formation as rapidly-cooled molten droplets and thus require a high-temperature origin (>1350°C, Toppani et al., 2001). Dendrites in the magnetite spherules have similar cruciform and cellular morphologies and similar dimensions to those observed in modern I-type cosmic spherules (Fig.9.11) (Genge et al., 2017a). This implies crystallisation at similar peak temperatures and cooling rates.

Large, smooth and off-centre, sub-spherical cavities are also observed (C16-0042, Fig.9.6F and in the wüstite [spherule C16-0003, Fig.9.6D]). Modern micrometeorite collections, derived from Antarctic surface sediments, contain cosmic spherules with corroded, hydrated or partially replaced metal (van Ginneken et al., 2016). The large sub-spherical cavities reported from the Fe-oxide spherules found in this study are, therefore, interpreted as cavities, formed after the complete dissolution of an Fe-Ni metal bead. This could occur during long residence times on the Cretaceous sea-floor. Therefore, the former presence of Fe-Ni metal, surrounded by Fe-oxide shell, implies these spherules formed by progressive oxidation. Similarly, the irregular rounded cavity networks between dendrites seen in some magnetite spherules (e.g. C16-0025, Fig.9.6G) are also observed in oxidised (OX) I-type cosmic spherules (Fig.9.8D and E) and are suggested to form by trapped residual gas during crystallisation (Feng et al., 2005; Genge et al., 2017a). Because the magnetite spherules are texturally identical to Antarctic I-type cosmic spherules, their formation history is most likely the same: as iron-dominated liquid droplets, which cooled rapidly in the atmosphere.

The magnetite spherules, therefore, have textural properties that suggest they are cosmic spherules. However, their mineralogy and compositions are distinct from modern I-type micrometeorites, which contain a two-phase mineralogy composed of either Fe-Ni metal and Ni-bearing wüstite (MET-type) or Ni-bearing wüstite and magnetite (OX-type) (Genge et al., 2017a). Furthermore, Mn is never detected by EDS analysis in modern Antarctic I-type spherules. By contrast, all but one of the Cretaceous Fe-oxide spherules are composed of Mn-bearing magnetite, only. The lack of both Ni and wüstite and the presence of additional cation trace element contamination, therefore, suggest the Cretaceous Fe-oxide spherules to have experienced alteration.

A diagenetic origin for the Mn-bearing magnetite is consistent with both the observed mineralogy and trace element geochemistry of the Fe-oxide particles. Authigenic magnetite (and hematite) are reported from pelagic limestones, including the White Chalk Supergroup (Montgomery et al., 1998; Hopson, 2005), and form along with phyllosilicates, glauconite, microsparite cement, nodular flint and phosphates as part of a complex diagenetic mineral assemblage (Hancock, 1975). Authigenic magnetite requires the presence of oxidising pore fluids (Weibel, 1998). Under these conditions wüstite, which is metastable below 570°C, will most likely recrystallize as magnetite and Fe-metal (Darken and Gurry, 1946; Genge et al., 2017a). The exposed Fe-metal will then be susceptible to corrosion and dissolution by sea water, leaving behind the small-scale voids. This scenario can, therefore, explain the presence of micro-scale irregular voids, which were observed in some Fe-oxide spherules (Fig.9.6F).

The altered and replacement micrometeorites are also likely to incorporate trace element contamination from circulating seawater during crystallization. Notably Mn, which is common at low concentrations in marine sediments and, when combined with Fe can form oxidized nodules on the sea-floor (Hesse and Schacht, 2011). The incorporation of low concentrations of Mn into the altered magnetite micrometeorites may be an expected signature of marine diagenetic alteration.

Studies of pseudomorphic replacement reactions suggest that coupled dissolution-precipitation rates can result in preservation of microscopic features and the dynamics of replacement are highly dependent on the pH and fO_2 of the fluid (Xia et al., 2009). Here, the preservation of dendritic textures in the magnetite spherules indicates that pseudomorphic replacement can occur on the nano-scale and lead to exceptional quality fossilized micrometeorites.

Figure 9.11. Unaltered I-type cosmic spherules recovered from Larkman Nunatak, Antarctica (Suttle et al., 2015). A progressive oxidation sequence (from A-E) is shown. Spherules A and B are MET I-types composed of a Ni-bearing wüstite shell surrounding an Fe-Ni bead. During atmospheric entry, the metal bead is consumed, forming the liquid oxide coating. This results in an increasingly Ni-rich reservoir. Spherule C is transitional between and MET and an OX spherule, containing a residual bead, whose Ni concentration is approximately 95wt%. This bead is surrounded by a mantle of Ni-bearing wüstite and the outer margin of the spherule contains magnetite dendrites and irregular, rounded void space (vesicles). Spherules D and E are fully oxidised, OX spherules, composed of Ni-bearing wüstite and magnetite. Magnetite forms either cruciform or re-entrant dendrites within the wüstite groundmass (Genge et al., 2017a). The void space is formed by trapped residual gas during inward crystallization (Feng et al., 2005). All particles are between 50-100µm in diameter.

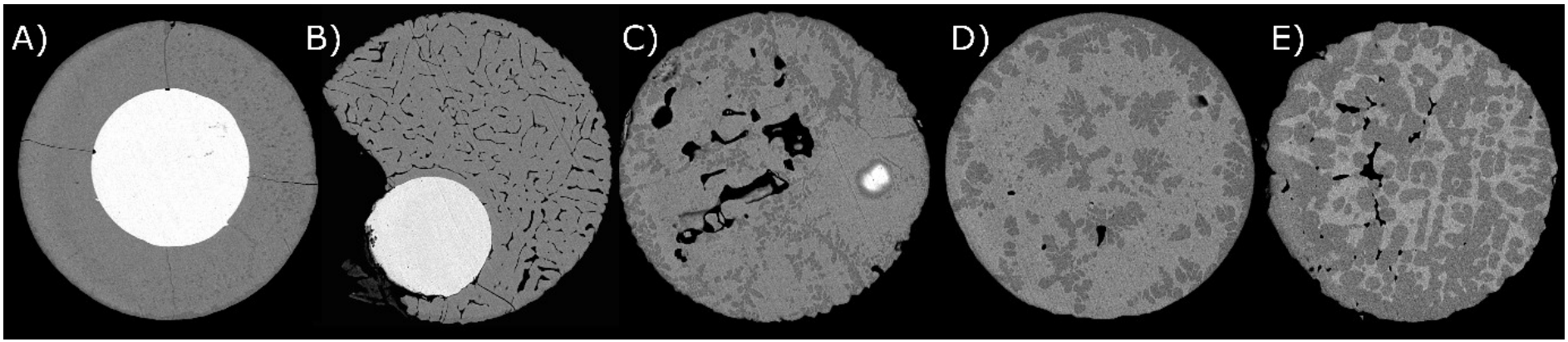

9.6. Discussion: Origin of Fe-Silicide spherules as altered I-types

Naturally occurring metal silicides are extremely rare and require highly reducing conditions to form. Currently, Fe-silicides have been found in deep-sea hydrothermal vents, formed by precipitation reactions (Astakhova and Kolesnik, 2014), in fulgurites, formed by lighting-induced fusion (Pasek et al., 2012) and in ultramafic rocks, as amygdales, formed by post-magmatic concretion growth (Novgorodova et al., 1984). Fe-silicides are also associated with extraterrestrial materials and found in ureilite meteorites (Keil et al., 1982) and enstatite chondrites (MacPherson et al., 2009). These silicide phases commonly contain meteoritic Co and Ni and most likely form by the reaction of silica with carbonaceous matrix during impact heating, thereby resulting in reducing conditions and the liberation of Fe and Si that subsequently react to form silicides (Keil et al., 1982). Silicide formation, therefore, occurs on Earth and in space and at both high and low temperatures.

Terrestrial Fe-silicide minerals, formed in hydrothermal precipitation reactions are found together with other transition metal silicide, sulphide, carbide and phosphide minerals as part of a wider reduced mineral assemblage (Astakhova and Kolesnik, 2014). The silicides within ultramafic rock cavities are much larger (250-4000µm) than the Cretaceous silicide spherules, they show concentric growth patterns, are coated by thin rims of graphite or calcite and contain trace Ti, Cr and V (Novgorodova et al., 1984). Furthermore, Fe-silicides found within fulgurites appear as rounded, irregular droplets between 500-1500µm in size, embedded in silicate glass and containing trace P and Ti (Pasek et al., 2012). By contrast, extraterrestrial Fe-silicides in the Haig meteorite (a ureilite) are present as melt veins (up to 150µm thickness) or as interstitial melt, coating silicate grains (<1µm in thickness) and contain trace Ni and Co (Keil et al., 1982).

By contrast, the Cretaceous Fe-silicide spherules found in this study have homogeneous internal textures, typically showing external dendrites only. However, two spherules (C16-009 and C16-0010) were recovered that exhibit internal dendrites and cavities closely resembling the textures found in I-type cosmic spherules. Particle C16-0009 (Fig.9.8A and 9.8B) contains a network of rounded cavities between dendrites while particle C16-0010 (Fig.9.8D-F) contains two distinct silicide minerals and as well as internal, irregular, rounded cavities. These textures are similar to the OX I-types (Genge et al., 2017b). However, their geochemistry and mineralogy is distinct.

The geochemical and textural characteristics of the Cretaceous Fe-silicide spherules do not match the properties of documented terrestrial silicides derived from lightning, post-magmatic or hydrothermal sources. In addition, an origin as unaltered extraterrestrial Fe-silicides can also be ruled out. As argued for the Fe-oxide spherules, the Fe-silicide spherules contain textural evidence of complete melting (spherical shape) and quench cooling (dendritic crystals). However, if these particles entered the atmosphere as Fe-silicide, whilst in a molten state, and without abundant C to act as a reducing agent, an FeSi melt would readily oxidise, forming an FeSi bead surrounded by an oxide shell. Two spherules matching this description were reported by Yu (1984) and appear as small (100-500µm diameter) spherules containing an Fe-Silicide core, mantled by a concentric layer of Fe-Ni metal and coated by Fe-oxides (wüstite, maghemite and magnetite) (Yu, 1984). These rare particles most likely represent

ablation spherules, rather than cosmic spherules, derived by melt extraction from the fusion crust of an infalling ureilite (Rietmeijer et al., 2008). Instead, the Cretaceous Fe-silicide spherules, identified in this study, most likely formed by a similar process as the Fe-oxide spherules, owing to their similar textural and trace element properties. Consequently, the Fe-silicide spherules are interpreted as diagenetically altered I-type cosmic spherules, that were altered under highly reducing, rather than oxidizing conditions.

Locally reducing conditions were present within the chalk during diagenesis, leading to the formation of pyrite (FeS_2, Hancock, 1975; Zijlstra, 1994). Likewise, within this study several submillimeter (~50-150µm) pyrite grains were found within the chalk residues (Fig.9.12). Reduction was most likely mediated by bacterial decay, through H_2S production, or may be associated with anoxia, occurring locally in worm burrows (Zijlstra, 1994). The replacement of Fe-oxides by silicide would, therefore, be consistent with the mobility of both Fe and Si and the reducing environmental conditions found in some pore spaces. The poor preservation of particle textures implies that Fe-silicides imperfectly pseudomorph the original mineral assemblages, with some precipitation producing protrusions on particle surfaces (Fig.9.8D). Most of the detrital pyrite grains identified in this study have surface coatings of limonite (~FeO[OH]), suggesting later interaction with oxidising fluids. This oxidation appears to have also affected the Fe-silicide spherules by introducing trace oxygen into the mineral structure.

Figure 9.12. Detrital pyrite (FeS_2) grains recovered from chalk fines. All grains show an oxidised limonite (FeO[OH]) coating consuming pyrite core. These anhedral sectioned faces occasionally expose pentagonal morphologies (B), consistent with the pyritohedral symmetry known to occur in cubic crystal systems such as pyrite.

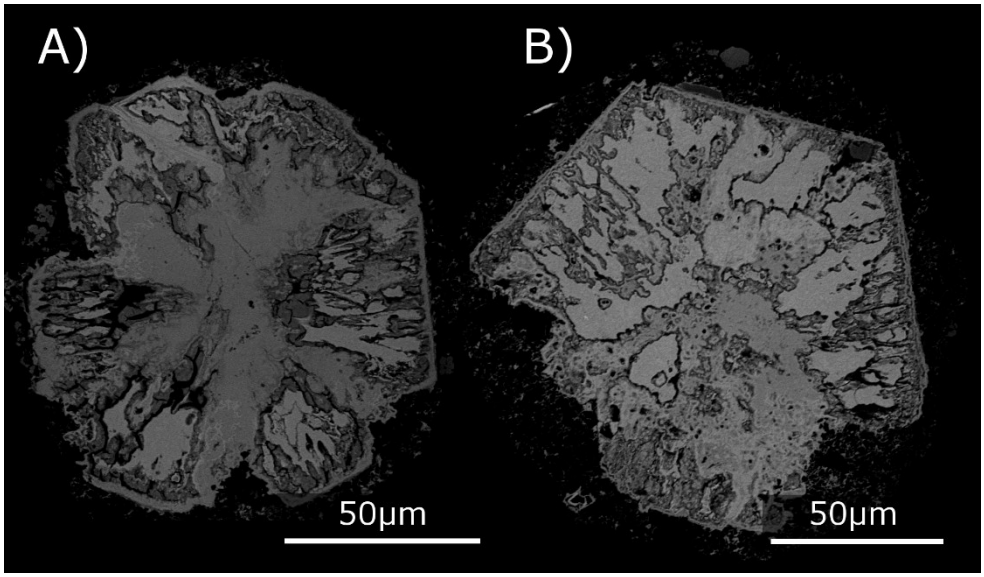

Previously Muszer (2014) reported the discovery of both Fe-oxide and Fe-silicide spherules containing sub-spherical cavities, dendrites and trace element Mn concentrations 1.65wt%. These spherules were recovered from Permian age deep marine sedimentary rocks and appear petrographically

identical to the Cretaceous spherules discovered in this study (see Fig.5 in Muszer, 2014). The host rocks containing the Permian spherules were dolomitized red shales and carbonates, which also contained a diverse mineral assemblage of Fe-sulphides, Fe-oxides and Cu-bearing ore minerals, that were formed either by hydrothermal or diagenetic processes, most likely during dolomitization. Notably, Musezer (2014) describes the occurrence of irregular and oval-shaped Fe-silicide grains forming clusters and co-occurring with pyrite. These detrital grains do not fit the textural or morphological properties of cosmic spherules. Therefore, the Permian sediments appear to contain both altered cosmic spherules, (reduced Fe-silicide and oxidized magnetite-hematite spherules) and authigenic minerals; Fe-silicides, oxides, sulphides and hydroxides. Muszer (2014) had suggested that the magnetic spherules among this assemblage could represent either cosmic dust or terrestrial magmatic material. However, without knowledge of the textural characteristics of I-types, a definitive identification could not be made. It now seems probable that Muszer (2014) had found diagenetically altered cosmic spherules captured within a deep-sea sediment that later experienced extensive diagenetic alteration.

9.7. Implications: Diagenetic alteration affecting cosmic dust

Lithified deep-sea rocks, such as limestones, shales and cherts, represent geological repositories for the collection and storage of fossil micrometeorites. In such environments, low sedimentation rates promote the accumulation and recovery of extraterrestrial dust (Jéhanno et al., 1988; Love and Brownlee, 1991). Consequently, all fossil micrometeorite collections have been recovered from materials that were deposited as marine sediments. However, long residence times on the sea-floor reduce the preservation potential of silicate-rich, S-type micrometeorites, through corrosion (Taylor and Brownlee, 1991). As a result, the majority of fossil micrometeorites are I-type cosmic spherules (Taylor and Brownlee, 1991; Onoue et al., 2011; Tomkins et al., 2016).

In the case of the Cretaceous chalk collection reported here, 96% of spherules are I-types. The majority of these particles have experienced diagenetic replacement mineralization, resulting in either the loss of unstable wüstite and replacement by magnetite under oxidizing conditions or, recrystallization as Fe-silicides under reducing conditions. In addition, minor diagenetic trace element contamination also affects the entire population: with Mn (typically between 0.3-0.8wt%) detected in all three spherule types (including the otherwise unaltered silicate spherules). Trace Mn is most likely sourced from the seawater, with Mn deposits commonly found in modern deep-sea sediments (Hesse and Schacht, 2011). Similar contamination may be expected in other fossil micrometeorite collections (for example, Muszer, 2014) and provide an easily identifiable signature by which to determine their ancient, fossilised provenance. The absence of Ni and the presence of Mn, therefore, does not preclude an extraterrestrial origin for sediment-hosted cosmic spherules but instead, may be an expected consequence of marine diagenesis.

Often mineralogy, texture and bulk composition together are taken as essential criteria for the identification of these particles. However, the diagenesis of I-type cosmic spherules is shown, herein, to have altered their original mineralogy, resulting in replacement by oxidising (magnetite) or reducing

(Fe-silicide) mineral assemblages. Despite replacement, altered spherules can be recognised as I-type micrometeorites on the basis of characteristic textures, even where replacement imperfectly pseudomorphs the pre-existing textures (Fig.9.8D).

Previous studies have noted alteration in fossil micrometeorites from Triassic halite (Davidson et al., 2007) and Triassic cherts (Onoue et al., 2011), but provide little detailed textural information by which identification was made. Our study shows that recognising altered micrometeorites is crucial to the successful reconstruction of the extraterrestrial dust flux over geological time, because here, only a single unaltered I-type was discovered amongst 73 I-type cosmic spherules. Without textural comparisons, the number of micrometeorites identified would have been a significant under-estimate of the true population. As a result, the following characteristics, present within a collection of spherules, are proposed as important criteria for the identification of fossilized micrometeorites: (1) spherical morphologies and diameters between 10μm and 500μm, (2) dendritic textures exhibiting cruciform or cellular arrangements (reflecting a quench-cooled formation during atmospheric entry), (3) large sub-circular cavities (representing the former position of Fe-Ni metal beads), (4) irregular cavity networks (representing vesicles and vesicle networks of residual trapped volatile gases), and (5) an Fe-rich mineralogy consistent with local diagenetic processes. Owing to the difficulty associated with positively identifying pseudomorphic I-type micrometeorites, all five criteria, found among a relatively small number of spherules, are necessary before a high confidence of extraterrestrial origin can be concluded.

Although diagenesis of micrometeorites causes significant changes in mineralogy and composition, that complicates their identification, it also transforms particles into more stable mineral assemblages, which can be preserved over geological timescales. Therefore, altered micrometeorites may be the most common form of extraterrestrial dust present in the geological column.

9.8. Conclusions from the Cretaceous chalk spherules

The discovery of pseudomorphic micrometeorites recovered from Coniacian Cretaceous chalk demonstrates that extraterrestrial dust, preserved in marine sediments, can be successfully extracted and identified even where complete secondary replacement (fossilization) has occurred. Until now geochemical criteria have been required for the positive identification of cosmic dust; however, because complete secondary replacement can occur, fossil micrometeorites imply new identification criteria, independent of geochemical metrics. The abundance of spherules found among the North Downs and Lulworth Cove Chalk and their high-quality preservation, combined with the diversity of stable replacement minerals, suggest that fossil micrometeorites are common, recognisable and scientifically valuable components of pelagic sediments.

Chapter 10: Conclusions

This thesis investigated eighty-one fine-grained and scoriaceous Antarctic micrometeorites. By combining a range of analytical techniques, using both large-scale spectroscopic studies and in-depth petrographic studies on specific micrometeorites, this study revealed new information on the parent body history and atmospheric entry of micrometeorites.

10.1 Thesis aims in review

The stated aims, listed in Sect.1.11 were: (1) to better constrain the geology of micrometeorite parent asteroids, (2) to test the Veritas hypothesis, (3) to analyse the early stages of atmospheric entry heating and (4) to recover fossil micrometeorites from an unstudied time period.

(1) ***The parent bodies of micrometeorites***: The primary aim, to discover new data on the properties of micrometeorite parent asteroids was addressed in chapters 3 and 6. In Chapter 3 the extent of aqueous alteration in fine-grained micrometeorites was investigated. Their mineralogies are dominated by hydrated mineral assemblages, primarily composed of phyllosilicates. They, therefore, have strong geochemical, mineralogical and textural similarities to CM2, CI and CR2 chondrites. Additional hydrated and altered structural components were identified within the micrometeorite matrix including partially replaced CAIs, a pseudomorphic chondrule and residual anhydrous silicate crystal clusters, mantled by thick phyllosilicate overgrowth rims. Using a reduced set of criteria, adapted from Rubin et al., (2007), the extent of aqueous alteration in thirty-seven C2 (CM-like) particles were evaluated and assigned a petrologic subtype. The degree of replacement affecting anhydrous silicates, as well as the FeO/SiO_2 ratio of coarse-grained phyllosilicate clumps and the abundance of FeNi metal were employed as semi-quantitative metrics tracing the degree of alteration. The majority of C2 micrometeorites were shown to be intensely altered, with an average grade of CM2.2. This conclusion supports previous studies which suggest that the fine-grained micrometeorite flux is sampling a "*chondrite-without-chondrules*" parent body (Engrand and Maurette, 1998). This study, therefore, argues that the genetic link to CM chondrites and the apparent lack of chondrules can only be reconciled if the parent asteroids of micrometeorites have lost most of their chondrules by intense aqueous alteration. Thus, this study predicts that the source asteroids are <CM2.2 grade bodies.

Chapter 6 asked if fine-grained micrometeorites contain evidence of impact events and shock deformation. A novel method was developed to answer this question. The 2D analysis of dehydration crack orientations was used to identify subtle petrofabrics. Circular statistics and entropy calculations were combined to quantitatively evaluate the degree of preferred alignment. In most micrometeorites, voids are orientated around a resultant (average) vector, giving a uniaxial distribution. However, biaxial and triaxial distributions and random void orientations were also reported.

Although dehydration cracks are formed during atmospheric entry, they always grow along the 001 axis of phyllosilicate crystals and, therefore, reveal the pre-atmospheric, parent body orientation of

micron-scale crystals within the particle's matrix. Calculations showed that pressures in excess of 78.5MPa are required to align phyllosilicates and, thus, static compaction on an accreting planetesimal is an unlikely scenario. Instead, micrometeorite petrofabrics are most likely the result of successive impact events. These findings are consistent with previous studies on CM chondrites that found low-grade shock textures, including pervasive petrofabrics are common and are particularly abundant in intensely aqueously altered, low petrologic subtype chondrites.

(2) ***NIR spectroscopy***: The secondary aim of this thesis was addressed in Chapt.8. The near-IR spectra of thirty young C-type asteroids from two major families (Veritas and Themis) were analysed for absorption band features, relating to their surface mineralogy. After removal of the baselines, several reflectance minima, located at key wavelength positions, and with similar depth and shape profiles were identified. These features correspond to the vibrational frequencies of metal-hydroxyl group (M-OH) bonds - similar to those found in hydrated sheet silicates and, therefore, imply that intact phyllosilicates are present on the surfaces of some Veritas and Themis family asteroids. The strongest evidence for hydration is observed on: (490) Veritas, (1086) Nata, (2147) Kharadze and (656) Beagle. The majority of these asteroids are Veritas family members, although, (656) Beagle is the namesake asteroid of a young subcluster, within the Themis family. This study is the first to analyse, identify and assign absorption bands in C-type asteroids over NIR wavelengths. Furthermore, this study adds support to the proposal that the young Veritas family is a significant contributor to the current flux of fine-grained micrometeorites, since both the asteroid and dust grains are composed of phyllosilicates.

Unfortunately, a direct comparison between the NIR spectra of Veritas asteroids and unmelted micrometeorites was not possible. This is because the quality of the micrometeorite spectra was poor. It is unlikely that future NIR spectra from micrometeorites could be much improved. This is because most particles experience major alteration of their mineralogy during atmospheric entry (Chapt.4) making comparisons redundant. Furthermore, the small sample size, low intensity of the expected signals and paucity of suitable experimental setups also impact data quality and prevent a meaningful NIR analysis.

(3) ***Atmospheric entry***: Chapters 4, 5 and 7 investigated various processes operating inside micrometeoroids during entry.

In Chapt.4 the solid-state evolution of matrix mineralogy prior to melting was investigated. During entry heating micrometeorites reach peak temperatures between 600-1700°C. Significant changes in mineralogy occur as phyllosilicates decompose. Initially, interlayer water is lost in dehydration reactions. Later, phyllosilicate crystal structure breaks down as structural water is lost in condensation reactions. This results in the formation of amorphous dehydroxylates. With further heating, the amorphous matrix recrystalizes, annealing to generate a fine-grained metamorphic olivine groundmass. At higher peak temperatures, above 1350°C, the matrix melts and complete melting is achieved around 1500°C. Despite significant changes in mineralogy, pre-atmospheric parent-body textures are preserved in all unmelted micrometeorites. Using mid-IR spectroscopy, it was possible to

define the above thermal processing pathway, to demonstrate that all fine-grained micrometeorites follow this evolution and to assign each individual particle with an approximate peak temperature.

Furthermore, previous experimental data on phyllosilicate pyrolysis demonstrated that both phyllosilicate species and cation composition strongly affect the peak temperature at which these decomposition reactions occur. Thus, serpentine-bearing micrometeorites, containing an Fe-rich matrix are significantly more susceptible to melting than saponite-bearing, Mg-rich micrometeorites. Consequently, the degree of aqueous alteration also affects the preservation potential of incoming cosmic dust. This implies that CI-like micrometeorites should preferentially survive whilst CM-like micrometeorites melt. However, the micrometeorite flux is, instead, predominantly composed of CM-like particles, suggesting that the flux of cosmic dust to Earth contains relatively little CI-like material.

Additionally, a small population of anomalous micrometeorites were identified that contain an Fe-rich metamorphic olivine groundmass, but also retain disordered carbonaceous matter and lack igneous rims. The absence of an igneous rim suggests that melting of phyllosilicates did not occur during entry and, thus, the pre-atmospheric mineralogy was anhydrous. This is because, without hydrated minerals, small dust grains cannot support thermal gradients. Similarly, the retention of carbonaceous matter suggests peak entry temperatures did not exceed 900°C. Consequently, these micrometeorites are interpreted as regolith dust grains, derived from asteroid surfaces that dehydrated in space, whilst on the parent asteroid.

In chapter 5, the residual volatile carbonaceous matter preserved inside micrometeorites was investigated. A subset of the micrometeorite population were analysed by Raman spectroscopy using both randomly located point spectra and line transects. Most micrometeorites produced characteristic G and D bands, reflecting the presence of carbonaceous phases preserved within the micrometeorite matrix. Spectra were processed to extract band parameters, including peak height and width ratios (R_1 and R_2) as well as the D band width (FWHM-D). These parameters were evaluated as metrics of disorder. The R_1 ratio, which is dependent on the length of aromatic ring clusters, reflects the degree of graphitisation in the carbon backbone and, therefore, corresponds to the peak temperature experienced by a sample. Line transects through several micrometeorites revealed U-shaped profiles, with higher R_1 ratios, reflecting more graphitized carbonaceous matter at micrometeorite margins, and more disordered carbonaceous matter preserved in the particle cores. These observations support previous suggestions by Genge (2006) and Genge et al., (2017b) who argued that conductive core-to-rim thermal gradients exist in hydrated, phyllosilicate-bearing micrometeorites during atmospheric entry. The disordered carbonaceous matter preserved in several fine-grained micrometeorite cores, appears to be entirely unaffected by atmospheric entry, because their peak parameters are similar to those measured from unheated C2 carbonaceous chondrites such as Cold Bokkeveld, Mighei and Tagish Lake. By contrast, some unmelted and scoriaceous micrometeorites (and a chip of Murchison fusion crust) did not show bimodal thermal gradients and, instead, contained erratic R_1 transect profiles, indicating high and variable temperatures throughout the sample's matrix. These particles also had a vesicular matrix, containing abundant secondary pore

space. These combined observations suggest that conductive thermal gradients inside micrometeorites break down in the later stages of entry heating and that this may be due to gas flow. This hypothesis was further explored in Chapter 7.

In chapter 7, the role of volatile gases in the heating, expansion and subsequent fragmentation of micrometeorites was explored. Textural evidence showed that interconnected secondary pore space in fine-grained micrometeorites develops as linear dehydration cracks and rounded vesicles connect, creating large channels with branching dendritic profiles. Some of these channels connect to the particle exterior and exceed 300µm in length. A model for their formation was proposed: Initially, small dehydration cracks form by the contraction of sheet silicates as interlayer water is lost. However, the later growth and expansion of cavities within micrometeorites is driven by the increasing internal gas pressure as abundant volatiles are formed from the decomposition of low-temperature phases. Volatile gases are prevented from escaping by the micrometeorite's igneous rim. However, eventually this seal is breached and gas exchange with the atmosphere occurs. Breaching of the igneous rim is preserved in the unique, double-walled micrometeorite TAM37P-03, that requires this micrometeorite to have rapidly expanded from the core outwards, forcing the igneous rim to crack and leading to the development of small channels on the particle surface. The later stages of gas-driven heating are also preserved in TAM19-7 and TAM19B-7 where the larger interconnected channels have formed, and the melting of matrix lining cavity walls produced magnetite rims.

Furthermore, increases in micrometeorite porosity, lower the mechanical strength of the particle and promote fragmentation during flight. Two of the giant TAM micrometeorites are in advanced states of fragmentation, as evidenced by their truncated irregular particle edges, exposed dehydration cracks and poorly developed magnetite rims - representing where fresh matrix was suddenly exposed to heating, late in the particles flight. It is, therefore, argued that the fragmentation of fine-grained micrometeorites may explain the paucity of large particles among collections.

(4) ***Fossil micrometeorites***: in Chapter 9 an abundance of fossilized cosmic dust was recovered from Cretaceous chalk (~83Ma) at two separate localities. Although unmelted fine-grained micrometeorites were not found, this study did identify diagenetically altered cosmic spherules, containing replaced terrestrial mineralogies which preserve diagnostic textural features, indicating their origin.

Chalk blocks were processed by crushing and acid digestion, and the resulting finds analysed by electron microscopy. Particles were identified as fossil micrometeorites whose extraterrestrial mineralogy has been entirely replaced by terrestrial magnetite or Fe-silicides. All spherules contain a distinct geochemical diagenetic overprint in the form of trace cation contamination, notably including a <2wt% Mn. These fossilized micrometeorites were, therefore, identifiable only by their characteristic internal and external textures, formed by flash melting and quench cooling of molten Fe-oxide liquids. Similar spherules were previously described in other studies from deep-sea sediments but not recognised as cosmic dust. These findings suggest that fossilized pseudomorphic micrometeorites may

be the most common type of cosmic dust present on Earth. A set of identification criteria were developed to aid future studies searching for fossil cosmic spherules.

10.2. Journal articles arising from this thesis

Several components of this thesis have been re-worked into journal articles or conference presentations and are either published, or under review.

Journal articles:

1. **Suttle**, M.D., Genge, M.J., Folco, L. and Russell, S.S., 2017. The thermal decomposition of micrometeorites, observations from mid-IR spectroscopy. *Geochimica et Cosmochimica Acta*, 206:112-136, doi: 10.1016/j.gca.2017.03.002. [**Adapted from Chapt.4**]

2. **Suttle**, M.D., Genge, M.J. and Russell, S.S., 2017. Shock fabrics in fine-grained micrometeorites. *Meteoritics & Planetary Science*, 52:2258-2274, doi:10.1111/maps.12927. [**Adapted from Chapt.6**]

3. **Suttle**, M.D. and Genge, M.J., 2017. Diagenetically altered fossil micrometeorites suggest cosmic dust is common in the geological record. *Earth and Planetary Science Letters*, 476:132-142, doi:10.1016/j.epsl.2017.07.052. [**Adapted from Chapt.9**]

4. **Suttle**, M.D., Genge, M.J., Folco, L., Lin, Q., Russell, S.S. and Najorka, J., 2018. The fragmentation of giant micrometeoroids during atmospheric entry. *Meteoritics and Planetary Science*, *accepted*. [**Adapted from Chapt.7**]

5. **Suttle**, M.D., Genge, M.J., Folco, L., Lin, Q., Russell, S.S. and Najorka, J., 2018. The degree of aqueous alteration affecting fine-grained micrometeorites. *Geochimica et Cosmochimica Acta*, *submitted*. [**Adapted from Chapt.3**]

6. **Suttle**, M.D., Genge, M.J., and Russell, S.S. 2018. A microchondrule-bearing micrometeorite. *Meteoritics and Planetary Science*, *submitted*. [**Adapted from Chapt.3**]

Conference presentations:

1. **Suttle**, M.D., Giles Miller, C. and Genge, M.J., 2017. Fossil micrometeorites hidden within acid-digestion residues. 61st Annual Meeting of the Palaeontological Association, held on December 17-19, 2017 at Imperial College London, UK.

2. **Suttle**, M.D., Genge, M.J. and Russell, S.S., 2017. A microchondrule-bearing micrometeorite. 80th Annual Meeting of the Meteoritical Society, held July 23-28th, 2017 in Santa Fe, New Mexico, USA. (abstract #6107).

3. **Suttle**, M.D. and Genge, M.J. 2017. The Diagenesis and Replacement of Cosmic Dust in the Geological Record. 80th Annual Meeting of the Meteoritical Society, held July 23-28, 2017 in Santa Fe, New Mexico, USA. (abstract #6010).

4. **Suttle**, M.D., Genge, M.J. and Russell, S.S., 2016. The Thermal Decomposition of Micrometeorites from Mid-Infrared Spectroscopy and Comparison with T-Tauri Star Systems. 79th Annual Meeting of the Meteoritical Society, held August 7-12th, 2016 in Berlin, Germany. (abstract #6030).

5. **Suttle**, M.D., Genge, M.J. and Russell, S.S., 2016. Shock Fabrics in Fine-grained Micrometeorites. 79th Annual Meeting of the Meteoritical Society, held August 7-12, 2016 in Berlin, Germany. (abstract #6031).

6. **Suttle**, M.D. and Genge, M.J., 2015. Characterisation of Carbonaceous Phases within FgMMs, fingerprinting the hydrated dust signature. Cosmic dust in space and on Earth: interplanetary, interstellar and anthropogenic. Held December 11th, 2015 at The Royal Astronomical Society, Burlington House, London.

7. **Suttle**, M.D., van Ginneken, M. and Genge, M.J., 2015. Larkman Nunatak Micrometeorites, a Statistical Study. 78th Annual Meeting of the Meteoritical Society, held July 27-31, 2015 in Berkeley, California. (abstract #5063).

10.3. Future research on the Veritas hypothesis

This study showed that a direct spectral match between Veritas asteroids and unmelted, unheated micrometeorites is impractical, owing to the rarity of entirely unaltered micrometeorites (Chapt.4), as well as the low quality of NIR spectra, collected from ground-based telescope and lab-based NIR microscope (Chapt.8).

Alternative ways of testing the Veritas hypothesis must, therefore, be found. One such method would be to search marine sediments for fossil micrometeorites, at time intervals before and after the estimated age of the Veritas break-up event (8.3Ma, Nesvorný et al., 2003; 2006). By calculating accretion rates at 7Ma and 9Ma, an enhanced cosmic dust flux, typically associated with asteroid family formation events (Schmitz et al., 1997; 2001; Heck et al., 2008) may be identified. The research of Meier et al., (2016a) currently focuses on this question, by searching Miocene sediments in Italy, dated at ~7Ma and has already identified a moderately elevated dust flux. Although micrometeorites have not been recovered, instead, abnormally high abundances of cosmogenic ^{3}He have been used to infer an enhanced cosmic dust flux. These findings imply that the recent cosmic dust flux contains appreciable Veritas material.

Another method of testing the Veritas hypothesis could be through a small-scale space mission. In 2017, the CASTAway mission was proposed to the European Space Agency's (ESA) medium-class (M5) mission call (Bowles et al., 2017). This inner solar system mission planned to send a small probe into the asteroid belt on a 7-year mission, capable of close-approach fly-bys on 10-20 asteroids as well as the collection of high-quality NIR spectra (0.6-5µm) from several hundred small bodies. This would necessarily include many C-type asteroids and most likely several Veritas and Themis members. Although this proposal was not selected, similar missions, such as the MarcoPolo-R (Barucci et al., 2012) and NEOcam (Mainzer, 2016) have previously been proposed for ESA and NASA mission calls and plans currently exist for CASTAway mission to be remodelled and proposed for the next ESA M-class mission call (No.6). Such a mission would significantly improve the field of asteroid spectroscopy by generating many high-quality, reliable spectra for study, without the problems associated with ground-based observations and atmospheric absorption. A more effective analysis of C-type asteroid composition could then be performed, allowing us to test research questions relating to the

compositional diversity of asteroid families (Michel et al., 2011; Fornaiser et al., 2016) and whether carbonaceous chondrite parent bodies are partially differentiated? (Carporzen et al., 2011; Elkins-Tanton et al., 2011; Sahijpal and Gupta, 2011).

10.4. Future research in the field of micrometeorites

I started this PhD in September 2014, since this time the field of micrometeoritics has changed rapidly. There are at least forty newly released publications dedicated to micrometeorite research in the last 3.8 years (2014-2018). These include new methods and locations for the extraction of micrometeorites, such as by direct air filtration in Antarctica (Wozniakiewicz et al., 2015), from Antarctic supraglacial moraines (Soens et al., 2016; Genge et al., 2018) or by collection from roof tops in urban areas (Genge et al., 2016b). Meanwhile, the collection of highly friable cometary micrometeorites from Antarctic snow continues to reveal new information from small bodies in the cold outer solar system – beyond the snow line (Noguchi et al., 2015; 2017; Dartois et al., 2018).

Recently, several new discoveries have also opened new avenues of research. A major discovery in our field has been the realisation that fossil cosmic spherules provide a novel, yet highly valuable mechanism for investigating the evolution of atmospheric oxygen on Earth over geological time (Tomkins et al., 2016) and are also suitable as modern atmospheric proxies for upper atmosphere oxygen concentration (Pack et al., 2017). Thus, the investigation of oxygen isotopes in cosmic spherules has revealed an unknown parent body source, characterised by an ^{16}O-poor reservoir, which is most likely related to the ordinary chondrite class, and may be responsible for up to 10% of the micrometeorite flux (Suavet et al., 2010; van Ginneken et al., 2017). Other interesting discoveries include: (1) a population of unmelted cosmic metal particles on the sea-floor, which may represent cosmic dust (Prasad et al., 2017) or meteoritic ablation debris (Genge and van Ginneken, 2017) and (2) the use of noble gases measured from unmelted ordinary chondrite-like micrometeorites, which show significantly higher than expected abundances of cosmogenic nuclides, implying irradiation by galactic cosmic rays in the outer solar system (>4au, Ott et al., 2016).

I predict that future research in micrometeoritics will progressively focus on cometary particles and fossil collections. This is because both topics have huge potential, providing a wealth of material for study and revealing insights into the outer solar system from volatile-rich bodies or the evolution of the asteroid belt over geological time. However, the study of fine-grained micrometeorites will also remain relevant. As demonstrated in this thesis, new discoveries from CM-like micrometeorites will continue to inform the wider meteorite community and especially those studying CM and CI chondrites. Furthermore, the ability of micrometeorites to sample many more parent bodies than the larger meteorite flux, ensures that micrometeorite diversity exceeds meteorite diversity, presenting opportunities to describe new and exotic extraterrestrial material.

Chapter 11: References

1. Abe, M., Takagi, Y., Abe, S., and Kitazato, K., 2011. Hayabusa NIRS Calibrated Spectra V1.0. HAY-A-NIRS-3-NIRSCAL-V1.0. NASA Planetary Data System. available at: https://pds.nasa.gov/ds-view/pds/viewDataset.jsp?dsid=HAY-A-NIRS-3-NIRSCAL-V1.0
2. Aldiss, D.T., Bloomfield, J.R., Buckley, D.K., Doran, S.K., Evans, D.J., Hopson, P.M., Royse, K.R. and Woods, M.A., 2004. A geological model of the Chalk of East Kent. A NERC funded British Geological Survey, commissioned report: CR/04/092N.
3. Alexander, C.O.D., Barber, D.J. and Hutchison, R., 1989. The microstructure of Semarkona and Bishunpur. Geochimica et Cosmochimica Acta, 53:3045-3057, doi:10.1016/0016-7037(89)90180-4.
4. Alexander, C.O.D., 2005. From supernovae to planets: the view from meteorites and interplanetary dust particles. In: Chondrites and the Protoplanetary Disk, ASP Conference Series 341:972-1002.
5. Alexander, C.O.D., Grossman, J.N., Ebel, D.S. and Ciesla, F.J., 2008. The formation conditions of chondrules and chondrites. Science, 320:1617-1619, doi:10.1126/science.1156561.
6. Altheide, T. S., Chevrier, V. F., & Dobrea, E. N. 2010. Mineralogical characterization of acid weathered phyllosilicates with implications for secondary Martian deposits. Geochimica et Cosmochimica Acta, 74:6232-6248, doi:10.1016/j.gca.2010.08.005.
7. Amri, C., Maurel, M.C., Sagon, G. and Baron, M.H., 2005. The micro-distribution of carbonaceous matter in the Murchison meteorite as investigated by Raman imaging. Spectrochimica Acta Part A: Molecular and Biomolecular Spectroscopy, 61:2049-2056, doi:10.1016/j.saa.2004.08.005.
8. Anderson, J.H. and Wickersheim, K.A., 1964. Near infrared characterization of water and hydroxyl groups on silica surfaces. Surface Science, 2:252-260, doi:10.1016/0039-6028(64)90064-0.
9. Astakhova, N.V. and Kolesnik, O.N., 2014. Ore mineralization in volcanic rocks from the submarine rises of the Sea of Japan. Geochemistry International, 52:144-161, doi:10.1134/S0016702914020037.
10. AstDyS-2 2016. Asteroid Dynamics Site (2) Available at: http://hamilton.dm.unipi.it/astdys/index.php?pc=0.
11. Asphaug, E., Agnor, C.B. and Williams, Q., 2006. Hit-and-run planetary collisions. Nature, 439:155-160, doi:10.1038/nature04311.
12. Altobelli, N., Postberg, F., Fiege, K., Trieloff, M., Kimura, H., Sterken, V.J., Hsu, H.W., Hillier, J., Khawaja, N., Moragas-Klostermeyer, G. and Blum, J., 2016. Flux and composition of interstellar dust at Saturn from Cassini's Cosmic Dust Analyzer. Science, 352:312-318, doi:10.1126/science.aac6397.
13. Baer, J., Chesley, S. and Britt, D., 2012. Asteroid Masses V3.0. EAR-A-COMPIL-5-ASTMASS-V3.0. NASA Planetary Data System, 191. Available at: https://pdsquery.jpl.nasa.gov/query?Identifier=EAR-A-COMPIL-5-ASTMASS-V3.0&resclass=data.dataset
14. Bailey, S.W., 1966. The status of clay mineral structures. Clays and Clay Minerals, 14:1-23, doi:10.1346/CCMN.1966.0140101.
15. Bailey, S.W., 1980. Structures of layer silicates. In: Brindley, G.W., Brown, G. (Eds.), Crystal Structures of Clay Minerals and their X-ray Identification. Mineralogical Society, London, 1–124, doi:10.1180/mono-5.1.
16. Barber, D.J., 1981. Matrix phyllosilicates and associated minerals in C2M carbonaceous chondrites. Geochimica et Cosmochimica Acta, 45:945–970, doi:10.1016/0016-7037(81)90120-4.
17. Barrat, J.A., Greenwood, R.C., Keil, K., Rouget, M.L., Boesenberg, J.S., Zanda, B. and Franchi, I.A., 2016. The origin of aubrites: Evidence from lithophile trace element abundances and oxygen isotope compositions. Geochimica et Cosmochimica Acta, 192:29-48, doi:10.1016/j.gca.2016.07.025.
18. Barucci, M.A., Cheng, A.F., Michel, P., Benner, L.A.M., Binzel, R.P., Bland, P.A., Böhnhardt, H., Brucato, J.R., Bagatin, A.C., Cerroni, P. and Dotto, E., 2012. MarcoPolo-R near earth asteroid sample return mission. Experimental Astronomy, 33:645-684, doi:10.1007/s10686-011-9231-8.
19. Battandier, M., Bonal, L., Quirico, E., Beck, P., Engrand, C., Duprat, J. and Dartois, E., 2018. Characterization of the organic matter and hydration state of antarctic micrometeorites: a reservoir distinct from carbonaceous chondrites. Icarus.doi:10.1016/j.icarus.2018.02.002.
20. Beattie, P., 1994. Systematics and energetics of trace-element partitioning between olivine and silicate melts: implications for the nature of mineral/melt partitioning. Chemical Geology, 117:57-71, doi:10.1016/0009-2541(94)90121-X.
21. Beck, P., Quirico, E., Montes-Hernandez, G., Bonal, L., Bollard, J., Orthous-Daunay, F.R., Howard, K.T., Schmitt, B., Brissaud, O., Deschamps, F. and Wunder, B., 2010. Hydrous mineralogy of CM and CI chondrites from infrared

spectroscopy and their relationship with low albedo asteroids. Geochimica et Cosmochimica Acta, 74:4881-4892, doi:10.1016/j.gca.2010.05.020.

22. Beck, P., Garenne, A., Quirico, E., Bonal, L., Montes-Hernandez, G., Moynier, F. and Schmitt, B., 2014. Transmission infrared spectra (2–25μm) of carbonaceous chondrites (CI, CM, CV–CK, CR, C2 ungrouped): Mineralogy, water, and asteroidal processes. Icarus, 229:263-277, doi:10.1016/j.icarus.2013.10.019.
23. Belikov, V.G., Kuregyan, A.G. and Ismailova, G.K., 2002. Standardization of magnetite. Pharmaceutical Chemistry Journal, 36:333-336, doi:10.1023/A:1020845110683.
24. Berens, P., 2009. CircStat: a MATLAB toolbox for circular statistics. J Stat Software, 31:1-21, doi:10.18637/jss.v031.i10.
25. Benz, W. and Asphaug, E., 1999. Catastrophic disruptions revisited. Icarus, 142:5-20, doi:10.1006/icar.1999.6204.
26. Beyssac, O., Goffé, B., Petitet, J. P., Froigneux, E., Moreau, M., & Rouzaud, J. N. 2003. On the characterization of disordered and heterogeneous carbonaceous materials by Raman spectroscopy. Spectrochimica Acta Part A: Molecular and Biomolecular Spectroscopy, 59:2267-2276, doi:10.1016/S1386-1425(03)00070-2.
27. Bi, D., Morton, R.D. and Wang, K., 1993. Cosmic nickel-iron alloy spherules from Pleistocene sediments, Alberta, Canada. Geochimica et cosmochimica acta, 57:4129-4136, doi:10.1016/0016-7037(93)90359-5.
28. Birlan, M., Barucci, M.A., Vernazza, P., Fulchignoni, M., Binzel, R.P., Bus, S.J., Belskaya, I. and Fornasier, S., 2004. Near-IR spectroscopy of asteroids 21 Lutetia, 89 Julia, 140 Siwa, 2181 Fogelin and 5480 (1989YK8), potential targets for the Rosetta mission; remote observations campaign on IRTF. New Astronomy, 9:343-351, doi:10.1016/j.newast.2003.12.005.
29. Bizzarro, M., Baker, J.A., Haack, H. and Lundgaard, K.L., 2005. Rapid timescales for accretion and melting of differentiated planetesimals inferred from 26Al-26Mg chronometry. The Astrophysical Journal Letters, 632:L41.
30. BGS – British Geological Survey. 2017. Geological Map of Britain, interactive viewer. Available online at: https://www.bgs.ac.uk/
31. Bland, P.A., Alard, O., Benedix, G.K., Kearsley, A.T., Menzies, O.N., Watt, L.E. and Rogers, N.W., 2005. Volatile fractionation in the early solar system and chondrule/matrix complementarity. Proceedings of the National Academy of Sciences of the United States of America, 102:13755-13760, doi:10.1073/pnas.0501885102.
32. Blum, J., 2010. Dust growth in protoplanetary disks—a comprehensive experimental/theoretical approach. Research in Astronomy and Astrophysics, 10:1199, doi:10.1088/1674-4527/10/12/002.
33. Brearley, A.J., 1995. Aqueous alteration and brecciation in Bells, an unusual, saponite-bearing, CM chondrite. Geochimica et Cosmochimica Acta, 59:2291-2317, doi:10.1016/0016-7037(95)00107-B.
34. Briani, G., Gounelle, M., Bourot-Denise, M. and Zolensky, M.E., 2012. Xenoliths and microxenoliths in H chondrites: Sampling the zodiacal cloud in the asteroid Main Belt. Meteoritics & Planetary Science, 47:880-902, doi10.1111/j.1945-5100.2012.01367.x.
35. Britt, D.T. and Consolmagno S.J., 2000. The porosity of dark meteorites and the structure of low-albedo asteroids. Icarus, 146:213-219, doi:10.1006/icar.2000.6374.
36. Briczinski, S.J., Mathews, J.D. and Meisel, D.D., 2009. Statistical and fragmentation properties of the micrometeoroid flux observed at Arecibo. Journal of Geophysical Research: Space Physics, 114, doi:10.1029/2009JA014054.
37. Brogan, C.L., Pérez, L.M., Hunter, T.R., Dent, W.R.F., Hales, A.S., Hills, R.E., Corder, S., Fomalont, E.B., Vlahakis, C., Asaki, Y. and Barkats, D., 2015. The 2014 ALMA Long Baseline Campaign: First Results from High Angular Resolution Observations toward the HL Tau Region. The Astrophysical Journal Letters, 808:L3, doi:10.1088/2041-8205/808/1/L3/meta.
38. Browning, L.B., McSween, H.Y. and Zolensky, M.E., 1996. Correlated alteration effects in CM carbonaceous chondrites. Geochimica et Cosmochimica Acta, 60:2621-2633, doi:10.1016/0016-7037(96)00121-4.
39. Brownlee, D.E., Bates, B. and Schramm, L., 1997. The Leonard Award Address Presented 1996 July 25, Berlin, Germany: the elemental composition of stony cosmic spherules. Meteoritics & Planetary Science, 32:157-175, doi:10.1111/j.1945-5100.1997.tb01257.x.
40. Brož, M., Morbidelli, A., Bottke, W.F., Rozehnal, J., Vokrouhlický, D. and Nesvorný, D., 2013. Constraining the cometary flux through the asteroid belt during the late heavy bombardment. Astronomy & Astrophysics, 551:A117, doi:10.1051/0004-6361/201219296.
41. Boley, A.C., Durisen, R.H. and Pickett, M.K., 2005. The Three-Dimensionality of Spiral Shocks: Did Chondrules Catch a Breaking Wave? In: Chondrites and the protoplanetary disk, 341:839-848.
42. Bonal, L., Quirico, E., Bourot-Denise, M. and Montagnac, G., 2006. Determination of the petrologic type of CV3 chondrites by Raman spectroscopy of included organic matter. Geochimica et Cosmochimica Acta, 70:1849-1863, doi:10.1016/j.gca.2005.12.004.
43. Bottke, W.F., Vokrouhlický, D., Brož, M., Nesvorný, D. and Morbidelli, A., 2001. Dynamical spreading of asteroid families by the Yarkovsky effect. Science, 294:1693-1696, doi:10.1126/science.1066760.

44. Bottke Jr, W.F., Vokrouhlický, D., Rubincam, D.P. and Nesvorný, D., 2006. The Yarkovsky and YORP effects: Implications for asteroid dynamics. The Annual Review of Earth and Planetary Science, 34:157-191, doi:10.1146/annurev.earth.34.031405.125154.
45. Bowles, N.E., Snodgrass, C., Gibbings, A., Sanchez, J.P., Arnold, J.A., Eccleston, P., Andert, T., Probst, A., Naletto, G., Vandaele, A.C. and de Leon, J., 2017. CASTAway: an asteroid main belt tour and survey. Advances in Space Research, doi:10.1016/j.asr.2017.10.021
46. Bray, H.J. and Redfern, S.A.T., 1999. Kinetics of dehydration of Ca-montmorillonite. Physics and Chemistry of Minerals, 26:591-600, doi:10.1007/s002690050223.
47. Brearley A. J. and Jones R. H. 1998. Chondritic meteorites. In Reviews in Mineralogy, Planetary Materials (J. J. Papike, ed.), 36:3,1-3,398. Mineralogical Society of America, Washington.
48. Brunetto, R., Pino, T., Dartois, E., Cao, A. T., d'Hendecourt, L., Strazzulla, G., & Bréchignac, P. 2009. Comparison of the Raman spectra of ion irradiated soot and collected extraterrestrial carbon. Icarus, 200:323-337, doi:10.1016/j.icarus.2008.11.004.
49. Brunetto, R., Borg, J., Dartois, E., Rietmeijer, F.J.M., Grossemy, F., Sandt, C., d'Hendecourt, L.L.S., Rotundi, A., Dumas, P., Djouadi, Z. and Jamme, F. 2011. Mid-IR, Far-IR, Raman micro-spectroscopy, and FESEM–EDX study of IDP L2021C5: Clues to its origin. Icarus, 212:896-910, doi:10.1016/j.icarus.2011.01.038.
50. Buades, A., Coll, B. and Morel, J.M., 2008. Nonlocal image and movie denoising. International journal of computer vision 76:123-139, doi:10.1007/s11263-007-0052-1.
51. Bunch, T.E. and Chang, S., 1980. Carbonaceous chondrites—II. Carbonaceous chondrite phyllosilicates and light element geochemistry as indicators of parent body processes and surface conditions. Geochimica et Cosmochimica Acta, 44:1543-1577, doi:10.1016/0016-7037(80)90118-0.
52. Burbine, T.H., 1998. Could G-class asteroids be the parent bodies of the CM chondrites? Meteoritics & Planetary Science, 33:253-258, doi:10.1111/j.1945-5100.1998.tb01630.x.
53. Burbine, T.H., McCoy, T.J., Meibom, A., Gladman, B. and Keil, K., 2002. Meteoritic parent bodies: Their number and identification. In: Asteroids III, W. F. Bottke Jr., A. Cellino, P. Paolicchi, and R. P. Binzel (eds), University of Arizona Press, Tucson, chapter 5.2.1:653-667.
54. Burns, R.G., 1970. Crystal field spectra and evidence of cation ordering in olivine minerals. American Mineralogist, 55:1608-1632.
55. Bus, S.J. and Binzel, R.P., 2002. Phase II of the small main-belt asteroid spectroscopic survey: A feature-based taxonomy. Icarus, 158:146-177, doi:10.1006/icar.2002.6856.
56. Bus, S. J., 2011. Ed., IRTF Near-IR Spectroscopy of Asteroids V2.0. EAR-A-I0046-4-IRTFSPEC-V2.0. NASA Planetary Data System. Available at: https://pdsquery.jpl.nasa.gov/query?Identifier=EAR-A-I0046-4-IRTFSPEC-V2.0&resclass=data.dataset
57. Busemann, H., Alexander, M.D. and Nittler, L.R., 2007. Characterization of insoluble organic matter in primitive meteorites by microRaman spectroscopy. Meteoritics & Planetary Science, 42:1387-1416, doi:10.1111/j.1945-5100.2007.tb00581.
58. Campins, H., Hargrove, K., Pinilla-Alonso, N., Howell, E.S., Kelley, M.S., Licandro, J., Mothé-Diniz, T., Fernández, Y. and Ziffer, J., 2010. Water ice and organics on the surface of the asteroid 24 Themis. Nature, 464:1320-1321, doi:10.1038/nature09029.
59. Caro, G.M., Dartois, E. and Nakamura-Messenger, K., 2008. Characterization of the carbon component in cometary Stardust samples by means of infrared and Raman spectroscopy. Astronomy & Astrophysics, 485:743-751, doi:10.1051/0004-6361:20078879.
60. Carporzen, L., Weiss, B.P., Elkins-Tanton, L.T., Shuster, D.L., Ebel, D. and Gattacceca, J., 2011. Magnetic evidence for a partially differentiated carbonaceous chondrite parent body. Proceedings of the National Academy of Sciences, 108:6386-6389, doi:10.1073/pnas.1017165108.
61. Carrasco-González, C., Henning, T., Chandler, C.J., Linz, H., Pérez, L., Rodríguez, L.F., Galván-Madrid, R., Anglada, G., Birnstiel, T., van Boekel, R. and Flock, M., 2016. The VLA View of the HL Tau Disk: Disk Mass, Grain Evolution, and Early Planet Formation. The Astrophysical Journal Letters, 821:L16, doi:10.3847/2041-8205/821/1/L16.
62. Carrillo-Sánchez, J.D., Plane, J.M.C., Feng, W., Nesvorný, D. and Janches, D., 2015. On the size and velocity distribution of cosmic dust particles entering the atmosphere. Geophysical Research Letters, 42:6518-6525, doi:10.1002/2015GL065149.
63. Carry, B., 2012. Density of asteroids. Planetary and Space Science, 73:98-118, doi:10.1016/j.pss.2012.03.009.
64. Chambers, J.E., 2004. Planetary accretion in the inner Solar System. Earth and Planetary Science Letters, 223:241-252, doi:10.1016/j.epsl.2004.04.031.

65. Charnoz, S. and Morbidelli, A., 2003. Coupling dynamical and collisional evolution of small bodies: an application to the early ejection of planetesimals from the Jupiter–Saturn region. Icarus, 166:141-156, doi:10.1016/S0019-1035(03)00213-6.
66. Chapman, C.R., Johnson, T.V. and McCord, T.B., 1971. A review of spectrophotometric studies of asteroids. NASA Special Publication, 267:51-64.
67. Chapman, C.R., Morrison, D. and Zellner, B., 1975. Surface properties of asteroids: A synthesis of polarimetry, radiometry, and spectrophotometry. Icarus, 25:104-130, doi: 10.1016/0019-1035(75)90191-8.
68. Chapman, C.R., 1996. S-type asteroids, ordinary chondrites, and space weathering: The evidence from Galileo's fly-bys of Gaspra and Ida. Meteoritics & Planetary Science, 31:699-725, doi:10.1111/j.1945-5100.1996.tb02107.
69. Chapman, C.R., Merline, W.J., Tamblyn, P., Enke, B., Nesvorný, D. and Young, El., 2011. Reflectance spectra of very young asteroid families. Final Report for NASA PAST grant #NNX07AK75G.
70. Che, C., Glotch, T.D., Bish, D.L., Michalski, J.R. and Xu, W., 2011. Spectroscopic study of the dehydration and/or dehydroxylation of phyllosilicate and zeolite minerals. Journal of Geophysical Research: Planets, 116:1-23 doi: 10.1029/2010JE003740.
71. Che, C. and Glotch, T.D., 2012. The effect of high temperatures on the mid-to-far-infrared emission and near-infrared reflectance spectra of phyllosilicates and natural zeolites: Implications for Martian exploration. Icarus, 218:585-601, doi:10.1016/j.icarus.2012.01.005.
72. Clark, B.E., Hapke, B., Pieters, C. and Britt, D., 2002. Asteroid space weathering and regolith evolution. In Asteroids III, W. F. Bottke Jr., A. Cellino, P. Paolicchi, and R. P. Binzel (eds), University of Arizona Press, Tucson, chapter 4.4.1:585-599.
73. Clark, R.N., Swayze, G.A., Wise, R., Livo, E., Hoefen, T., Kokaly, R., Sutley, S.J., 2007, USGS digital spectral library splib06a: U.S. Geological Survey, Digital Data Series 231, http://speclab.cr.usgs.gov/spectral.lib06. [NIR spectra of brucite and illite]
74. Clayton, R.N. and Mayeda, T.K., 1999. Oxygen isotope studies of carbonaceous chondrites. Geochimica et Cosmochimica Acta, 63:2089-2104, doi:10.1016/S0016-7037(99)00090-3.
75. Cloutis, E.A., Hiroi, T., Gaffey, M.J., Alexander, C.O.D. and Mann, P., 2011. Spectral reflectance properties of carbonaceous chondrites: 1. CI chondrites. Icarus, 212:180-209, doi:10.1016/j.icarus.2010.12.009.
76. Cordier, C., Folco, L., Suavet, C., Sonzogni, C. and Rochette, P., 2011. Major, trace element and oxygen isotope study of glass cosmic spherules of chondritic composition: The record of their source material and atmospheric entry heating. Geochimica et Cosmochimica Acta, 75:5203-5218, doi:10.1016/j.gca.2011.06.014.
77. Corrigan, C.M., Zolensky, M.E., Dahl, J., Long, M., Weir, J., Sapp, C. and Burkett, P.J., 1997. The porosity and permeability of chondritic meteorites and interplanetary dust particles. Meteoritics & Planetary Science, 32:509-515, doi:10.1111/j.1945-5100.1997.tb01296.x.
78. Court, R.W. and Tan, J., 2016. Insights into secondary reactions occurring during atmospheric ablation of micrometeoroids. Meteoritics & Planetary Science, 51:1163-1183, doi:10.1111/maps.12652.
79. Czajkowski, J., 1987. Cosmo and geochemistry of the Jurassic hardgrounds. Ph.D. Thesis, California Univ., San Diego (USA).
80. Darken, L. and Gurry, R.W., 1946. The system iron—oxygen. II. Equilibrium and thermodynamics of liquid oxide and other phases. Journal of the American Chemical society, 68:798-816, doi:10.1021/ja01209a030.
81. Dartois, E., Engrand, C., Duprat, J., Godard, M., Charon, E., Delauche, L., Sandt, C. and Borondics, F., 2018. Dome C ultracarbonaceous Antarctic micrometeorites-Infrared and Raman fingerprints. Astronomy & Astrophysics, 609:A65, doi:10.1051/0004-6361/201731322. [***reviewed by M.Suttle***]
82. Dawson, R.I., Lee, E.J. and Chiang, E., 2016. Correlations between compositions and orbits established by the giant impact era of planet formation. The Astrophysical Journal, 822:54-78, doi:10.3847/0004-637X/822/1/54.
83. Davidson, J., Genge, M.J., Mills, A.A., Johnson, D. and Grady, M., 2007. Ancient cosmic dust from Triassic halite: 38th Lunar and Planetary Science Conference. (abstract #1545) CD-ROM.
84. Davidson, J., Busemann, H., Nittler, L.R., Alexander, C.M.D., Orthous-Daunay, F.R., Franchi, I.A. and Hoppe, P., 2014. Abundances of presolar silicon carbide grains in primitive meteorites determined by NanoSIMS. Geochimica et Cosmochimica Acta, 139:248-266, doi:10.1016/j.gca.2014.04.026.
85. Davison, T. M., Ciesla, F. J., and Collins, G. S. 2012. Post-impact thermal evolution of porous planetesimals. Geochimica et Cosmochimica Acta 95:252-269, doi:10.1016/j.gca.2012.08.001.
86. Day-Stirrat, R. J., Aplin, A. C., Środoń, J., and Van der Pluijm, B. A. 2008. Diagenetic reorientation of phyllosilicate minerals in Paleogene mudstones of the Podhale Basin, southern Poland. Clays and Clay Minerals, 56:100-111, doi:10.1346/CCMN.2008.0560109.

87. DeMeo, F.E., Binzel, R.P., Slivan, S.M. and Bus, S.J., 2009. An extension of the Bus asteroid taxonomy into the near-infrared. Icarus, 202:160-180, doi:10.1016/j.icarus.2009.02.005.
88. DeMeo, F.E. and Carry, B., 2014. Solar System evolution from compositional mapping of the asteroid belt. Nature, 505:629-634, doi:10.1038/nature12908.
89. Desch, S.J. and Connolly, H.C., 2002. A model of the thermal processing of particles in solar nebula shocks: Application to the cooling rates of chondrules. Meteoritics & Planetary Science, 37:183-207, doi:10.1111/j.1945-5100.2002.tb01104.x.
90. Di Martino, M., Migliorini, F., Zappalà, V., Manara, A. and Barbieri, C., 1997. Veritas asteroid family: Remarkable spectral differences inside a primitive parent body. Icarus, 127:112-120, doi:10.1006/icar.1996.5674.
91. Dobrică, E., Engrand, C., Duprat, J., Gounelle, M., Leroux, H., Quirico, E. and Rouzaud, J.N., 2009. Connection between micrometeorites and Wild 2 particles: From Antarctic snow to cometary ices. Meteoritics and Planetary Science, 44:1643-1661, doi:10.1111/j.1945-5100.2009.tb01196.
92. Dobrică, E., Engrand, C., Quirico, E., Montagnac, G. and Duprat, J., 2011. Raman characterization of carbonaceous matter in CONCORDIA Antarctic micrometeorites. Meteoritics & Planetary Science, 46:1363-1375, doi:10.1111/j.1945-5100.2011.01235.
93. Dobrică, E., Engrand, C., Leroux, H., Rouzaud, J.N. and Duprat, J., 2012. Transmission electron microscopy of CONCORDIA ultracarbonaceous Antarctic micrometeorites (UCAMMs): mineralogical properties. Geochimica et Cosmochimica Acta, 76:68-82, doi:10.1016/j.gca.2011.10.025
94. Dohnanyi, J.S., 1972. Interplanetary objects in review: Statistics of their masses and dynamics. Icarus, 17:1-48, doi:10.1016/0019-1035(72)90044-9.
95. Dohnanyi J. S. 1976. Sources of interplanetary dust: Asteroids. In Interplanetary dust and zodiacal light, edited by Elsasser H. Berlin: Springer-Verlag. 569–639.
96. Dredge, I., Parnell, J., Lindgren, P. and Bowden, S., 2010. Elevated flux of cosmic spherules (micrometeorites) in Ordovician rocks of the Durness Group, NW Scotland. Scottish Journal of Geology, 46:7-16, doi: 10.1144/0036-9276/01-394.
97. Drits, V.A. and McCarty, D.K., 2007. The nature of structure-bonded H_2O in illite and leucophyllite from dehydration and dehydroxylation experiments. Clays and Clay Minerals, 55:45-58, doi:10.1346/CCMN.2007.0550104.
98. Dullemond, C.P. and Dominik, C., 2005. Dust coagulation in protoplanetary disks: A rapid depletion of small grains. Astronomy & Astrophysics, 434:971-986, doi:10.1051/0004-6361:20042080.
99. Dunn, T.L., McCoy, T.J., Sunshine, J.M. and McSween, H.Y., 2010, March. A coordinated mineralogical, spectral, and compositional study of ordinary chondrites: Implications for asteroid spectroscopic classification. 41st Lunar and Planetary Science Conference, held March 1-5th, 2010 in Houston, Texas. (abstract #1750).
100. Duprat, J., Engrand, C., Maurette, M., Kurat, G., Gounelle, M. and Hammer, C., 2007. Micrometeorites from central Antarctic snow: The CONCORDIA collection. Advances in Space Research, 39:605-611, doi: 10.1016/j.asr.2006.05.029.
101. Durda, D.D., Greenberg, R. and Jedicke, R., 1998. Collisional models and scaling laws: A new interpretation of the shape of the main-belt asteroid size distribution. Icarus, 135:431-440, doi:10.1006/icar.1998.5960.
102. Durda, D.D. and Flynn, G.J., 1999. Experimental study of the impact disruption of a porous, inhomogeneous target. Icarus, 142:46-55, doi:10.1006/icar.1999.6203.
103. Durda, D.D., Bottke, W.F., Nesvorný, D., Enke, B.L., Merline, W.J., Asphaug, E. and Richardson, D.C., 2007. Size–frequency distributions of fragments from SPH/N-body simulations of asteroid impacts: Comparison with observed asteroid families. Icarus, 186:498-516, doi:10.1016/j.icarus.2006.09.013.7.
104. Ebel, D.S., Weisberg, M.K. and Beckett, J.R., 2012. Thermochemical stability of low-iron, manganese-enriched olivine in astrophysical environments. Meteoritics & Planetary Science, 47:585-593, doi:10.1111/j.1945-5100.2012.01347.x.
105. Elkins-Tanton, L.T., Weiss, B.P. and Zuber, M.T., 2011. Chondrites as samples of differentiated planetesimals. Earth and Planetary Science Letters, 305:1-10, doi:10.1016/j.epsl.2011.03.010.
106. El Maarry, M.R., Kodikara, J., Wijessoriya, S., Markiewicz, W.J. and Thomas, N., 2012. Desiccation mechanism for formation of giant polygons on Earth and intermediate-sized polygons on Mars: Results from a pre-fracture model. Earth and planetary science letters, 323:19-26, doi:10.1016/j.epsl.2012.01.016.
107. Engrand, C. and Maurette, M., 1998. Carbonaceous micrometeorites from Antarctica. Meteoritics & Planetary Science, 33:565-580, doi: 10.1111/j.1945-5100.1998.tb01665.
108. Esser, K.B., 1990. X-ray diffraction indices for relative quantification of interlayering in phyllosilicates. Soil Science Society of America Journal, 54:923-926, doi:10.2136/sssaj1990.03615995005400030052x
109. Fabian, D., Jäger, C., Henning, T., Dorschner, J. and Mutschke, H., 2000. Steps toward interstellar silicate mineralogy. V. Thermal evolution of amorphous magnesium silicates and silica. Astronomy and Astrophysics, 364:282-292.

110. Feierberg, M.A., Lebofsky, L.A. and Tholen, D.J., 1985. The nature of C-class asteroids from 3-µm spectrophotometry. Icarus, 63:183-191, doi:10.1016/0019-1035(85)90002-8.
111. Feng, H., Jones, K.W., Tomov, S., Stewart, B., Herzog, G.F., Schnabel, C. and Brownlee, D.E., 2005. Internal structure of type I deep-sea spherules by X-ray computed microtomography. Meteoritics and Planetary Science, 40:195-206, doi:10.1111/j.1945-5100.2005.tb00375.
112. Ferrari, A.C. and Robertson, J., 2000. Interpretation of Raman spectra of disordered and amorphous carbon. Physical review B, 61:14095, doi:10.1103/PhysRevB.61.14095.
113. Fitzgerald, J.J., Hamza, A.I., Dec, S.F. and Bronnimann, C.E., 1996. Solid-state 27 Al and 29 Si NMR and 1 H CRAMPS studies of the thermal transformations of the 2:1 phyllosilicate pyrophyllite. The Journal of Physical Chemistry, 100:17351-17360, doi:10.1021/jp961499f.
114. Flynn, G.J., Durda, D.D., Sandel, L.E., Kreft, J.W. and Strait, M.M., 2009. Dust production from the hypervelocity impact disruption of the Murchison hydrous CM2 meteorite: Implications for the disruption of hydrous asteroids and the production of interplanetary dust. Planetary and Space Science, 57:.119-126, doi:10.1016/j.pss.2008.09.005.
115. Fogg, M.J. and Nelson, R.P., 2007. On the formation of terrestrial planets in hot-Jupiter systems. Astronomy & Astrophysics, 461:1195-1208, doi:10.1051/0004-6361:20066171.
116. Folco, L., Rochette, P., Perchiazzi, N., d'Orazio, M., Laurenzi, M.A. and Tiepolo, M., 2008. Microtektites from Victoria Land Transantarctic Mountains. Geology, 36:291-294, doi:10.1130/G24528A.
117. Folco, L., 2015. Personal Communications during trip to the University of Pisa for collection of loaned TAM micrometeorites.
118. Fornasier, S., Lantz, C., Barucci, M.A. and Lazzarin, M., 2014. Aqueous alteration on main belt primitive asteroids: Results from visible spectroscopy. Icarus, 233:163-178, doi:10.1016/j.icarus.2014.01.040.
119. Fornasier, S., Lantz, C., Perna, D., Campins, H., Barucci, M.A. and Nesvorny, D., 2016. Spectral variability on primitive asteroids of the Themis and Beagle families: Space weathering effects or parent body heterogeneity? Icarus, 269:1-14, doi:10.1016/j.icarus.2016.01.002.
120. Fossen, H. 2010. Structural geology, 3rd ed. New York. Cambridge University Press.
121. Frank, D.R., Zolensky, M.E. and Le, L., 2014. Olivine in terminal particles of Stardust aerogel tracks and analogous grains in chondrite matrix. Geochimica et Cosmochimica Acta, 142:240-259, doi:10.1016/j.gca.2014.05.037.
122. Friedrich, J.M., Weisberg, M.K., Ebel, D.S., Biltz, A.E., Corbett, B.M., Iotzov, I.V., Khan, W.S. and Wolman, M.D., 2015. Chondrule size and related physical properties: A compilation and evaluation of current data across all meteorite groups. Chemie der Erde-Geochemistry, 75:419-443, doi:10.1016/j.chemer.2014.08.003.
123. Fujimura, A., Kato, M. and Kumazawa, M., 1982. Preferred orientation of phyllosilicates in Yamato-74642 and-74662, in relation to deformation of C2 chondrites. Memoirs of National Institute of Polar Research. 25:207-215.
124. Fujimura, A., Kato, M., and Kumazawa, M. 1983. Preferred orientation of phyllosilicate [001] in matrix of Murchison meteorite and possible mechanisms of generating the oriented texture in chondrites. Earth and Planetary Science Letters. 66:25-32, doi:10.1016/0012-821X(83)90123-1.
125. Furukawa, Y., Sekine, T., Kakegawa, T. and Nakazawa, H., 2011. Impact-induced phyllosilicate formation from olivine and water. Geochimica et Cosmochimica Acta, 75:6461-6472, doi:10.1016/j.gca.2011.08.029.
126. Gaffey, M.J., Cloutis, E.A., Kelley, M.S. and Reed, K.L., 2002. Mineralogy of asteroids. In Asteroids III, W. F. Bottke Jr., A. Cellino, P. Paolicchi, and R. P. Binzel (eds), University of Arizona Press, Tucson, Chapter 2.2.7:183-204.
127. Gao, B. and Mathews, J.D., 2015. High-altitude meteors and meteoroid fragmentation observed at the Jicamarca Radio Observatory: Monthly Notices of the Royal Astronomical Society, 446:3404-3415, doi:10.1093/mnras/stu2176.
128. Gardner, J.P., Mather, J.C., Clampin, M., Doyon, R., Greenhouse, M.A., Hammel, H.B., Hutchings, J.B., Jakobsen, P., Lilly, S.J., Long, K.S. and Lunine, J.I., 2006. The James Webb space telescope. Space Science Reviews, 123:485-606, doi:10.1007/s11214-006-8315-7.
129. Gattacceca, J., Rochette, P., Denise, M., Consolmagno, G., and Folco, L. 2005. An impact origin for the foliation of chondrites. Earth and Planetary Science Letters 234:351-368, doi:10.1016/j.epsl.2005.03.002.
130. Gemini Observatory, 2017. Available at:http://www.gemini.edu/about
131. Genge, M.J., 2002. Hydrated Chondrule Fragments Amongst Micrometeorites. 65th Annual Meeting of the Meteoritical Society, held July 21-26, 2002 in Los Angeles, California. (abstract #5102).
132. Genge, M.J., 2006. Igneous rims on micrometeorites. Geochimica et Cosmochimica Acta, 70:2603-2621, doi:10.1016/j.gca.2006.02.005.
133. Genge, M.J., 2007. Evidence for Shock in Micrometeorites. 70th Annual Meeting of the Meteoritical Society, held August 13-17, 2007 in Tucson, Arizona. (abstract #5007).
134. Genge, M.J., 2008a. Koronis asteroid dust within Antarctic ice. Geology, 36:687-690, doi:10.1130/G24493A.1.

135. Genge, M.J., 2008b. Micrometeorites and their implications for meteors. Earth, Moon, and Planets, 102:525-535, doi:10.1007/s11038-007-9185-z.
136. Genge, M.J., 2016a. The origins of I-type spherules and the atmospheric entry of iron micrometeoroids. Meteoritics & Planetary Science, 51:1063–1081, doi: 10.1111/maps.12645.
137. Genge, M.J., 2016b. Vesicle dynamics during the atmospheric entry heating of cosmic spherules: Meteoritics & Planetary Science, doi:10.1111/maps.12805.
138. Genge, M.J., 2017. Vesicular parachutes increase the abundance of micrometeorites from water-rich asteroids on Earth. Geophysical Research Letters, doi:10.1002/2016GL072490.
139. Genge, M.J., Grady, M.M. and Hutchison, R., 1997. The textures and compositions of fine-grained Antarctic micrometeorites: Implications for comparisons with meteorites. Geochimica et Cosmochimica Acta, 61:5149-5162, doi:10.1016/S0016-7037(97)00308-6.
140. Genge, M.J. and Grady, M.M., 1998. Melted micrometeorites from Antarctic ice with evidence for the separation of immiscible Fe-Ni-S liquids during entry heating. Meteoritics and Planetary Science, 33:425-434, doi:10.1111/j.1945-5100.1998.tb01647.x
141. Genge, M.J. and Van Ginneken, M., 2018. Comment on “Unmelted cosmic metal particles in the Indian Ocean” by Prasad et al. Meteoritics & Planetary Science, doi:10.1111/maps.13013
142. Genge, M.J., Bradley, J.P., Engrand, C., Gounelle, M., Harvey, R.P. and Grady, M.M., 2001. The petrology of fine-grained micrometeorites: evidence for the diversity of primitive asteroids: The 32nd Lunar and Planetary Science Conference, held March 12-16, 2001, Houston, Texas. (abstract #1546).
143. Genge, M.J., Gileski, A. and Grady, M.M., 2005. Chondrules in Antarctic micrometeorites. Meteoritics and Planetary Science, 40:225-238, doi:10.1111/j.1945-5100.2005.tb00377.x.
144. Genge, M.J., Engrand, C., Gounelle, M. and Taylor, S., 2008. The classification of micrometeorites. Meteoritics and Planetary Science, 43:497-515, doi:10.1111/j.1945-5100.2008.tb00668.
145. Genge, M.J., Suttle, M. and van Ginneken, M., 2016a. Olivine settling in cosmic spherules during atmospheric deceleration: An indicator of the orbital eccentricity of interplanetary dust. Geophysical Research Letters, 43: 10,646–10,653, doi:10.1002/2016GL070874.
146. Genge, M.J., Larsen, J., van Ginneken, M. and Suttle, M.D., 2016b. An urban collection of modern-day large micrometeorites: Evidence for variations in the extraterrestrial dust flux through the Quaternary. Geology, 44:G38352-1, doi:10.1130/G38352.1.
147. Genge, M.J., Davies, B., Suttle, M.D., van Ginneken, M. and Tomkins, A.G., 2017a. The mineralogy and petrology of I-type cosmic spherules: Implications for their sources, origins and identification in sedimentary rocks. Geochimica et Cosmochimica Acta, 218:167-200, doi:10.1016/j.gca.2017.09.004.
148. Genge, M.J., Suttle, M. and van Ginneken, M., 2017b. Thermal shock fragmentation of Mg silicates within scoriaceous micrometeorites reveal hydrated asteroidal sources. Geology, 45:891-894, doi:10.1130/G39426.1.
149. Genge, M.J., van Ginneken, M., Suttle, M.D. and Harvey, R.P., 2018. Accumulation mechanisms of micrometeorites in an ancient supra-glacial moraine at Larkman Nunatak, Antarctica, Meteoritics and Planetary Science, doi: 0.1111/maps.13107.
150. Ginter, M., Hairapetian, V. and Grigoryan, A., 2011. Chondrichthyan microfossils from the Famennian and Tournaisian of Armenia. Acta Geologica Polonica, 61:153-173.
151. Glavin, D.P. and Bada, J.L., 2001. Survival of amino acids in micrometeorites during atmospheric entry. Astrobiology, 1:259-269, doi:10.1089/15311070152757456.
152. Green, O.R., 2001. Extraction Techniques for Phosphatic Fossils: In A Manual of Practical Laboratory and Field Techniques in Palaeobiology. 318-330, doi: 10.1007/978-94-017-0581-3_27. ISBN -978-94-017-0581-3, Springer Netherlands.
153. Greenwood, R. C., Hutchison, R., and Jones, C. G. 1993. The structure and evolution of a CM2 regolith: A three-dimensional study of Cold Bokkeveld. Meteoritics 28:357-358.
154. Greenwood, R.C., Lee, M.R., Hutchison, R. and Barber, D.J., 1994. Formation and alteration of CAIs in Cold Bokkeveld (CM2). Geochimica et Cosmochimica Acta, 58:1913-1935, doi:10.1016/0016-7037(94)90424-3.
155. Greenwood, R.C., Burbine, T.H., Miller, M.F. and Franchi, I.A., 2016. Melting and differentiation of early-formed asteroids: The perspective from high precision oxygen isotope studies. Chemie der Erde-Geochemistry, doi:10.1016/j.chemer.2016.09.005.
156. Greshake, A., Kloeck, W., Arndt, P., Maetz, M., Flynn, G.J., Bajt, S. and Bischoff, A., 1998. Heating experiments simulating atmospheric entry heating of micrometeorites: Clues to their parent body sources. Meteoritics & Planetary Science, 33:267-290, doi:10.1111/j.1945-5100.1998.tb01632.

157. Grossman, L., 1972. Condensation in the primitive solar nebula. Geochimica et Cosmochimica Acta, 36:597-619, doi:10.1016/0016-7037(72)90078-6.
158. Grossman, J.N. and Brearley, A.J., 2005. The onset of metamorphism in ordinary and carbonaceous chondrites. Meteoritics & Planetary Science, 40:87-122, doi: 10.1111/j.1945-5100.2005.tb00366.
159. Goldstein, J., Newbury, D.E., Echlin, P., Joy, D.C., Romig Jr, A.D., Lyman, C.E., Fiori, C. and Lifshin, E., 2012. Scanning electron microscopy and X-ray microanalysis: a text for biologists, materials scientists, and geologists. Springer Science & Business Media, 61, doi:10.107/978-1-4613-0491-3
160. Gomes, R., Levison, H.F., Tsiganis, K. and Morbidelli, A., 2005. Origin of the cataclysmic Late Heavy Bombardment period of the terrestrial planets. Nature, 435:466-469, doi:10.1038/nature03676.
161. Gounelle, M., 2011. The asteroid–comet continuum: In search of lost primitivity. Elements, 7:29-34, doi:10.2113/gselements.7.1.29 R.
162. Gounelle, M., Zolensky, M.E., Liou, J.C., Bland, P.A. and Alard, O., 2003. Mineralogy of carbonaceous chondritic microclasts in howardites: Identification of C2 fossil micrometeorites. Geochimica et Cosmochimica Acta, 67:507-527, doi:10.1016/S0016-7037(02)00985-7.
163. Gounelle, M., Chaussidon, M., Morbidelli, A., Barrat, J.A., Engrand, C., Zolensky, M.E. and McKeegan, K.D., 2009. A unique basaltic micrometeorite expands the inventory of solar system planetary crusts. Proceedings of the National Academy of Sciences, 106:6904-6909, doi:10.1073/pnas.0900328106.
164. Guo, W. and Eiler, J.M., 2007. Temperatures of aqueous alteration and evidence for methane generation on the parent bodies of the CM chondrites. Geochimica et Cosmochimica Acta, 71:5565-5575, doi:10.1016/j.gca.2007.07.029.
165. Hallenbeck, S.L., Nuth, J.A. and Daukantas, P.L., 1998. Mid-infrared spectral evolution of amorphous magnesium silicate smokes annealed in vacuum: Comparison to cometary spectra. Icarus, 131:1198-209, doi:10.1006/icar.1997.5854.
166. Hancock, J.M., 1975. The petrology of the Chalk. Proceedings of the Geologists' Association, 86:499-535, doi:10.1016/S0016-7878(75)80061-7.
167. Hanna, R.D., Ketcham, R.A., Zolensky, M. and Behr, W.M., 2015. Impact-induced brittle deformation, porosity loss, and aqueous alteration in the Murchison CM chondrite. Geochimica et Cosmochimica Acta, 171:256-282, doi:10.1016/j.gca.2015.09.005.
168. Hanowski, N.P. and Brearley, A.J., 2001. Aqueous alteration of chondrules in the CM carbonaceous chondrite, Allan Hills 81002: Implications for parent body alteration. Geochimica et Cosmochimica Acta, 65:495-518, doi:10.1016/S0016-7037(00)00552-4.
169. Hargrove, K.D., Emery, J.P., Campins, H. and Kelley, M.S., 2015. Asteroid (90) Antiope: Another icy member of the Themis family?. Icarus, 254:150-156, doi:10.1016/j.icarus.2015.03.008.
170. Harker, D.E., Woodward, C.E., Kelley, M.S., Sitko, M.L., Wooden, D.H., Lynch, D.K. and Russell, R.W., 2010. Mid-infrared Spectrophotometric Observations of Fragments B and C of Comet 73P/Schwassmann-Wachmann 3. The Astronomical Journal, 141:26, doi:10.1088/0004-6256.
171. Harris, A.W., 1998. A thermal model for near-Earth asteroids. Icarus, 131:291-30, doi:10.1006/icar.1997.5865
172. Harvey, R.P. and Maurette, M., 1991. The origin and significance of cosmic dust from the Walcott Névé, Antarctica: Proceedings of the Lunar and Planetary Science Conference, 21:569-578.
173. Heck, P.R., Schmitz, B., Baur, H. and Wieler, R., 2008. Noble gases in fossil micrometeorites and meteorites from 470 Myr old sediments from southern Sweden, and new evidence for the L-chondrite parent body breakup event: Meteoritics and Planetary Science, 43:517-528, doi:10.1111/j.1945-5100.2008.tb00669.
174. Herter, T.L., Adams, J.D., De Buizer, J.M., Gull, G.E., Schoenwald, J., Henderson, C.P., Keller, L.D., Nikola, T., Stacey, G. and Vacca, W.D., 2012. First science observations with SOFIA/FORCAST: the FORCAST mid-infrared camera. The Astrophysical Journal Letters, 749:L18, doi:10.1088/2041-8205/749/2/L18.
175. Hesse, R. and Schacht, U., 2011. Early diagenesis of deep-sea sediments. Deep-Sea Sediments. Developments in Sedimentology. Elsevier, Amsterdam, 63:557-714, doi:10.1016/B978-0-444-53000-4.00009-3. ISBN: 978-0-444-53000-4.
176. Hevey, P. J., & Sanders, I. S. 2006. A model for planetesimal meltdown by 26Al and its implications for meteorite parent bodies. Meteoritics & Planetary Science, 41:95-106, doi:10.1111/j.1945-5100.2006.tb00195.x.
177. Hewins, R.H., 1997. Chondrules. Annual Review of Earth and Planetary Sciences, 25:61-83, doi:10.1146/annurev.earth.25.1.61.
178. Hewins, R.H., Bourot-Denise, M., Zanda, B., Leroux, H., Barrat, J.A., Humayun, M., Göpel, C., Greenwood, R.C., Franchi, I.A., Pont, S. and Lorand, J.P., 2014. The Paris meteorite, the least altered CM chondrite so far. Geochimica et Cosmochimica Acta, 124:190-222, doi:10.1016/j.gca.2013.09.014
179. Hirayama, K., 1918. Groups of asteroids probably of common origin: Proceedings of the Tokyo Mathematico-Physical Society. 2nd Series, Tokyo Sugaku-Buturigakkwai Kizi Dai, 9:354-361, doi:10.11429/ptmps1907.9.17_354.

180. Ho, N. C., Peacor, D. R., and Van der Pluijm, B. A. 1999. Preferred orientation of phyllosilicates in Gulf Coast mudstones and relation to the smectite-illite transition. Clays and Clay Minerals, 47:495-504, doi:10.1346/CCMN.1999.0470412.
181. Hodgkinson, R.L., 1991. Microfossil processing: a damage report. Micropaleontology, 37:320-326, doi: 10.2307/1485894.
182. Holcombe, R., 2017. GEOrient. Available at: https://www.holcombe.net.au/software/
183. Hopson, P., 2005. A stratigraphical framework for the Upper Cretaceous Chalk of England and Scotland with statements on the Chalk of Northern Ireland and the UK Offshore Sector. A NERC funded British Geological Survey research report: RR/05/01. ISBN 0 85272 517 5. Available at: http://nora.nerc.ac.uk/3230/1/RR05001.pdf
184. Houck, J.R., Roellig, T.L., Van Cleve, J., Forrest, W.J., Herter, T., Lawrence, C.R., Matthews, K., Reitsema, H.J., Soifer, B.T., Watson, D.M. and Weedman, D., 2004. The Infrared Spectrograph*(IRS) on the Spitzer Space Telescope. The Astrophysical Journal Supplement Series, 154:18, doi:10.1086/423134.
185. Housen, K.R., Wilkening, L.L., Chapman, C.R. and Greenberg, R., 1979. Asteroidal regoliths. Icarus, 39:317-351, doi:10.1016/0019-1035(79)90145-3.
186. Howard, K.T., Benedix, G.K., Bland, P.A. and Cressey, G., 2009. Modal mineralogy of CM2 chondrites by X-ray diffraction (PSD-XRD). Part 1: Total phyllosilicate abundance and the degree of aqueous alteration. Geochimica et Cosmochimica Acta, 73:4576-4589, doi:10.1016/j.gca.2009.04.038.
187. Howard, K.T., Benedix, G.K., Bland, P.A. and Cressey, G., 2010. Aqueous Alteration, 'Serpentinization' and the CM-C2ung-CI Connection by PSD-XRD. 73rd Annual Meeting of the Meteoritical Society, held July 26-30, 2010 in New York, New York. (abstract #5186). Published in the Meteoritics and Planetary Science Supplement, 73.
188. Howard, K.T., Benedix, G.K., Bland, P.A. and Cressey, G., 2011. Modal mineralogy of CM chondrites by X-ray diffraction (PSD-XRD): Part 2. Degree, nature and settings of aqueous alteration. Geochimica et Cosmochimica Acta, 75:2735-2751, doi:10.1016/j.gca.2011.02.021.
189. Hunt, G.R., 1977. Spectral signatures of particulate minerals in the visible and near infrared. Geophysics, 42:501-513, doi:10.1190/1.1440721
190. ICS – International Commission on Stratigraphy. 2017. Available online at: http://www.stratigraphy.org/
191. Imae, N., Taylor, S. and Iwata, N., 2013. Micrometeorite precursors: Clues from the mineralogy and petrology of their relict minerals. Geochimica et Cosmochimica Acta, 100:116-157, doi:10.1016/j.gca.2012.09.052.
192. Ivleva, N. P., Messerer, A., Yang, X., Niessner, R., & Pöschl, U. (2007). Raman microspectroscopic analysis of changes in the chemical structure and reactivity of soot in a diesel exhaust aftertreatment model system.Environmental science & technology, 41:3702-3707, doi:10.1021/es0612448
193. Izidoro, A., Raymond, S.N., Morbidelli, A. and Winter, O.C., 2015. Terrestrial planet formation constrained by Mars and the structure of the asteroid belt. Monthly Notices of the Royal Astronomical Society, 453:3619-3634, doi:10.1093/mnras/stv1835.
194. Jacquet, E., Alard, O. and Gounelle, M., 2015. Trace element geochemistry of ordinary chondrite chondrules: The type I/type II chondrule dichotomy. Geochimica et Cosmochimica Acta, 155:47-67, doi:10.1016/j.gca.2015.02.005.
195. Jedicke, R., Nesvorný, D., Whiteley, R., Ivezić, Ž. and Jurić, M., 2004. An age–colour relationship for main-belt S-complex asteroids. Nature, 429:275-277, doi:10.1038/nature02578.
196. Jéhanno, C., Boclet, D., Bonté, P., Castellarin, A. and Rocchia, R., 1988. Identification of two populations of extraterrestrial particles in a Jurassic hardground of the Southern Alps: Lunar and Planetary Science Conference Proceedings, 18:623-630.
197. Jenniskens, P., Shaddad, M.H., Numan, D., Elsir, S., Kudoda, A.M., Zolensky, M.E., Le, L., Robinson, G.A., Friedrich, J.M., Rumble, D. and Steele, A., 2009. The impact and recovery of asteroid 2008 TC3. Nature, 458:485-488, doi:10.1038/nature07920.
198. Johnson, C.A. and Prinz, M., 1993. Carbonate compositions in CM and CI chondrites and implications for aqueous alteration. Geochimica et Cosmochimica Acta, 57:2843-2852, doi:10.1016/0016-7037(93)90393-B.
199. Johnson, B.C., Minton, D.A., Melosh, H.J. and Zuber, M.T., 2015. Impact jetting as the origin of chondrules. Nature, 517:339-341, doi:10.1038/nature14105.
200. Jones, R.H., 2012. Petrographic constraints on the diversity of chondrule reservoirs in the protoplanetary disk. Meteoritics & Planetary Science, 47:1176-1190, doi:10.1111/j.1945-5100.2011.01327.x.
201. JPL Small-Body Database 2017. Available at: https://ssd.jpl.nasa.gov/sbdb.cgi
202. Jubb, A.M. and Allen, H.C., 2010. Vibrational spectroscopic characterization of hematite, maghemite, and magnetite thin films produced by vapor deposition. ACS Applied Materials & Interfaces, 2:2804-2812, doi:10.1021/am1004943.
203. Kagi, H., Tsuchida, I., Wakatsuki, M., Takahashi, K., Kamimura, N., Iuchi, K. and Wada, H., 1994. Proper understanding of down-shifted Raman spectra of natural graphite: Direct estimation of laser-induced rise in sample temperature. Geochimica et Cosmochimica Acta, 58:3527-3530, doi:10.1016/0016-7037(94)90104.

204. Kaluna, H.M., Masiero, J.R. and Meech, K.J., 2016. Space weathering trends among carbonaceous asteroids. Icarus, 264:62-71, doi:10.1016/j.icarus.2015.09.007.
205. Keil, K., Berkley, J.L. and Fuchs, L.H., 1980. Suessite, Fe_3Si, a new mineral in the North Haig ureilite. 13th Lunar and Planetary Science Conference, held March 15-19, 1982 in Houston, Texas (abstract #154).
206. Keil, K., 2000. Thermal alteration of asteroids: evidence from meteorites. Planetary and Space Science, 48:887-903, doi:10.1016/S0032-0633(00)00054-4.
207. Keller, L.P., Thomas, K.L., Clayton, R.N., Mayeda, T.K., DeHart, J.M. and McKay, D.S., 1994. Aqueous alteration of the Bali CV3 chondrite: Evidence from mineralogy, mineral chemistry, and oxygen isotopic compositions. Geochimica et Cosmochimica Acta, 58:5589-5598, doi:10.1016/0016-7037(94)90252-6.
208. Ketcham, R.A. and Carlson, W.D., 2001. Acquisition, optimization and interpretation of X-ray computed tomographic imagery: applications to the geosciences. Computers & Geosciences 27:381-400, doi:10.1016/S0098-3004(00)00116-3.
209. Kero, J., Szasz, C., Pellinen-Wannberg, A., Wannberg, G., Westman, A. and Meisel, D.D., 2008. Three-dimensional radar observation of a submillimeter meteoroid fragmentation. Geophysical Research Letters, 35:L04101, doi:10.1029/2007GL032733.
210. Kerridge, J.F., Mackay, A.L. and Boynton, W.V., 1979. Magnetite in CI carbonaceous meteorites: Origin by aqueous activity on a planetesimal surface. Science, 205:395-397, doi:10.1126/science.205.4404.395.
211. Khisina, N.R., Badyukov, D.D. and Wirth, R., 2016. Microtexture, nanomineralogy, and local chemistry of cryptocrystalline cosmic spherules. Geochemistry International, 54:68-77, doi:10.1134/S0016702916010067.
212. Kieffer, S.W., 1979. Thermodynamics and lattice vibrations of minerals: 2. Vibrational characteristics of silicates. Reviews of Geophysics, 17:20-34, doi:10.1029/RG017i001p00020.
213. Kimberley, J. and Ramesh, K.T., 2011. The dynamic strength of an ordinary chondrite. *Meteoritics & Planetary Science*, *46*:1653-1669, doi: 10.1111/j.1945-5100.2011.01254.x.
214. King, A.J., Schofield, P.F. and Russell, S.S., 2016. Characterizing Type 1 Aqueous Alteration in CM Carbonaceous Chondrites with Modal Mineral Abundances: 47th Lunar and Planetary Science Conference, held March 21-25 2016 in The Woodlands, Texas. (abstract# 1130).
215. Kita, N.T., Huss, G.R., Tachibana, S., Amelin, Y., Nyquist, L.E. and Hutcheon, I.D., 2005. Constraints on the origin of chondrules and CAIs from short-lived and long-lived radionuclides. In: Chondrites and the protoplanetary disk ASP Conference Series 341:558-584.
216. Kleine, T., Münker, C., Mezger, K. and Palme, H., 2002. Rapid accretion and early core formation on asteroids and the terrestrial planets from Hf–W chronometry. Nature, 418:952-955, doi:10.1038/nature00982.
217. Kleine, T., Mezger, K., Palme, H., Scherer, E. and Münker, C., 2005. Early core formation in asteroids and late accretion of chondrite parent bodies: Evidence from 182 Hf-182 W in CAIs, metal-rich chondrites, and iron meteorites. Geochimica et Cosmochimica Acta, 69:5805-5818, doi:10.1016/j.gca.2005.07.012.
218. Klima, R.L., Pieters, C.M. and Dyar, M.D., 2007. Spectroscopy of synthetic Mg-Fe pyroxenes I: Spin-allowed and spin-forbidden crystal field bands in the visible and near-infrared. Meteoritics & Planetary Science, 42:235-253, doi:10.1111/j.1945-5100.2007.tb00230.x.
219. Klöck, W., Thomas, K.L., McKay, D.S. and Palme, H., 1989. Unusual olivine and pyroxene composition in interplanetary dust and unequilibrated ordinary chondrites. Nature, 339:126-128, doi:10.1038/339126a0.
220. Kohout, T., Kallonen, A., Suuronen, J.P., Rochette, P., Hutzler, A., Gattacceca, J., Badjukov, D.D., Skala, R., Böhmová, V. and Čuda, J., 2014. Density, porosity, mineralogy, and internal structure of cosmic dust and alteration of its properties during high-velocity atmospheric entry. Meteoritics & Planetary Science, 49:1157-1170, doi:10.1111/maps.12325.
221. Koike, C., Mutschke, H., Suto, H., Naoi, T., Chihara, H., Henning, T., Jäger, C., Tsuchiyama, A., Dorschner, J. and Okuda, H., 2006. Temperature effects on the mid-and far-infrared spectra of olivine particles. Astronomy & Astrophysics, 449:583-596, doi:10.1051/0004-6361:20053256.
222. Korochantseva, E.V., Trieloff, M., Lorenz, C.A., Buykin, A.I., Ivanova, M.A., Schwarz, W.H., Hopp, J. and Jessberger, E.K., 2007. L-chondrite asteroid breakup tied to Ordovician meteorite shower by multiple isochron 40Ar-39 Ar dating. Meteoritics & Planetary Science, 42:113-130, doi:10.1111/j.1945-5100.2007.tb00221.
223. Kostecki, R., Tran, T., Song, X., Kinoshita, K., & McLarnon, F. 1997. Raman Spectroscopy and Electron Microscopy of Heat-Treated Petroleum Cokes for Lithium-Intercalation Electrodes. Journal of The Electrochemical Society, 144:3111-3117, doi:10.1149/1.1837967.
224. Kunihiro, T., Rubin, A.E., McKeegan, K.D. and Wasson, J.T., 2004. Initial 26 Al/27 Al in carbonaceous-chondrite chondrules: too little 26 Al to melt asteroids. Geochimica et Cosmochimica Acta, 68:2947-2957, doi:10.1016/j.gca.2004.02.006.

225. Kurat, G., Brandstaetter, F., Maurette, M. and Coeberl, C., 1992. CI-like micrometeorites from Cap Prud'homme, Antarctica. 23rd Lunar and Planetary Science Conference, held March 16-20, 1992 in Houston, Texas. (abstract #747).
226. Kurat, G., Koeberl, C., Presper, T., Brandstätter, F. and Maurette, M., 1994. Petrology and geochemistry of Antarctic micrometeorites. Geochimica et Cosmochimica Acta, 58:3879-3904, doi:10.1016/0016-7037(94)90369-7.
227. Krot, A.N. and Rubin, A.E., 1996. 1996Microchondrule-bearing chondrule rims: constraints on chondrule formation. In Chondrules, the Protoplanetary Disk (eds. R. H. Hewins, R. H. Jones and E. R. D. Scott). Cambridge University Press, Chapter 19:181–184.
228. Krot, A.N., Rubin, A.E., Keil, K. and Wasso, J.T., 1997. Microchondrules in ordinary chondrites: Implications for chondrule formation. Geochimica et Cosmochimica Acta, 61:463-473, doi:10.1016/S0016-7037(96)00342-0.
229. Krot, A.N., Amelin, Y., Cassen, P. and Meibom, A., 2005. Young chondrules in CB chondrites from a giant impact in the early Solar System. Nature, 436:989-992, doi:10.1038/nature03830.
230. Krot, A.N., Amelin, Y., Bland, P., Ciesla, F.J., Connelly, J., Davis, A.M., Huss, G.R., Hutcheon, I.D., Makide, K., Nagashima, K. and Nyquist, L.E., 2009. Origin and chronology of chondritic components: A review. Geochimica et Cosmochimica Acta, 73:4963-4997, doi:10.1016/j.gca.2008.09.039.
231. Landis, E.N. and Keane, D.T., 2010. X-ray microtomography. Materials characterization 61:1305-1316, doi:doi.org/10.1016/j.matchar.2010.09.012.
232. Landsman, Z.A., Licandro, J., Campins, H., Ziffer, J., de Prá, M. and Cruikshank, D.P., 2016. The Veritas and Themis asteroid families: 5–14 μm spectra with the Spitzer Space Telescope. Icarus, 269:62-74, doi:10.1016/j.icarus.2016.01.008.
233. Lecar, M., Podolak, M., Sasselov, D. and Chiang, E., 2006. On the location of the snow line in a protoplanetary disk. The Astrophysical Journal, 640:1115, doi:10.1086/500287.
234. Lee, M. R. 1993. The petrography, mineralogy and origins of calcium sulphate within the Cold Bokkeveld CM carbonaceous chondrite. Meteoritics, 28:53-62, doi:10.1111/j.1945-5100.1993.tb00248.x.
235. Lee, M.R. and Ellen, R., 2008. Aragonite in the Murray (CM2) carbonaceous chondrite: implications for parent body compaction and aqueous alteration. Meteoritics & Planetary Science, 43:11219-1231, doi:10.1111/j.1945-5100.2008.tb01124.x.
236. Lee, M. R., and Nicholson, K. 2009. Ca-carbonate in the Orgueil (CI) carbonaceous chondrite: Mineralogy, microstructure and implications for parent body history. Earth and Planetary Science Letters 280:268-275, doi:10.1016/j.epsl.2009.01.038.
237. Lee, M.R., Lindgren, P., Sofe, M.R., Alexander, C.O.D. and Wang, J., 2012. Extended chronologies of aqueous alteration in the CM2 carbonaceous chondrites: Evidence from carbonates in Queen Alexandra Range 93005. Geochimica et Cosmochimica Acta, 92:148-169, doi:10.1016/j.gca.2012.06.005.
238. Lee, M. R., Lindgren, P., King, A. J., Greenwood, R. C., Franchi, I. A., & Sparkes, R. 2016. Elephant Moraine 96029, a very mildly aqueously altered and heated CM carbonaceous chondrite: implications for the drivers of parent body processing. Geochimica et Cosmochimica Acta, 187:237-259, doi:10.1016/j.gca.2016.05.008.
239. Llana-Fúnez, S., Brodie, K.H., Rutter, E.H. and Arkwright, J.C., 2007. Experimental dehydration kinetics of serpentinite using pore volumometry. Journal of Metamorphic Geology, 25:423-438, doi:10.1111/j.1525-1314.2007.00703.x.
240. Lenher, V. and Merrill, H.B., 1917. The solubility of silica: Journal of the American Chemical Society, 39:2630-2638, doi:10.1021/ja02257a013.
241. Lewis, J.S., 1974. The temperature gradient in the solar nebula. Science, 186:440-443, doi:10.1126/science.186.4162.440.
242. Levi-Donati, G.R., 1970. Microchondrules. Meteoritics & Planetary Science, 5:33-42, doi:10.1111/j.1945-5100.1970.tb00387.x.
243. Levison, H.F., Bottke, W.F., Gounelle, M., Morbidelli, A., Nesvorný, D. and Tsiganis, K., 2009. Contamination of the asteroid belt by primordial trans-Neptunian objects. Nature, 460:364-366, doi:10.1038/nature08094.
244. Licandro, J., Hargrove, K., Kelley, M., Campins, H., Ziffer, J., Alí-Lagoa, V., Fernández, Y. and Rivkin, A., 2012. 5–14μm Spitzer spectra of Themis family asteroids. Astronomy & Astrophysics, 537, doi:10.1051/0004-6361/201118142
245. Lin, Q., Al-Khulaifi, Y., Blunt, M.J. and Bijeljic, B., 2016. Quantification of sub-resolution porosity in carbonate rocks by applying high-salinity contrast brine using X-ray microtomography differential imaging. Advances in Water Resources 96:306-322, doi:10.1016/j.advwatres.2016.08.002.
246. Lindgren, P., Hanna, R.D., Dobson, K.J., Tomkinson, T. and Lee, M.R., 2015. The paradox between low shock-stage and evidence for compaction in CM carbonaceous chondrites explained by multiple low-intensity impacts. Geochimica et Cosmochimica Acta, 148:159-178, doi:10.1016/j.gca.2014.09.014.

247. Lindsay, S.S., Marchis, F., Emery, J.P., Enriquez, J.E. and Assafin, M., 2015. Composition, mineralogy, and porosity of multiple asteroid systems from visible and near-infrared spectral data. Icarus, 247:53-70, doi:10.1016/j.icarus.2014.08.040.
248. Love, S.G. and Brownlee, D.E., 1991. Heating and thermal transformation of micrometeoroids entering the Earth's atmosphere. Icarus, 89:26-43, doi:10.1016/0019-1035(91)90085-8.
249. Love, S.G. and Brownlee, D.E., 1993. A direct measurement of the terrestrial mass accretion rate of cosmic dust. Science, 262:550-550, doi:10.1126/science.262.5133.550.
250. MacPherson, G.J., Mittlefehldt, D.W., Lipschutz, M.E., Clayton, R.N., Bullock, E.S., Ivanov, A.V., Mayeda, T.K. and Wang, M.S., 2009. The Kaidun chondrite breccia: Petrology, oxygen isotopes, and trace element abundances. Geochimica et Cosmochimica Acta, 73:5493-5511, doi:10.1016/j.gca.2009.06.012.
251. Madejová, J., 2003. FTIR techniques in clay mineral studies. Vibrational spectroscopy, 31:1-10, doi:10.1016/S0924-2031(02)00065-6.
252. Mainzer, A.K., 2016, October. NEOCam: The near-earth object camera. In AAS/Division for Planetary Sciences Meeting Abstracts (Vol. 48).
253. Mardia, K.V. and Jupp, P.E., 2000. Directional Statistics, doi:10.1002/9780470316979.
254. Mathews, J.D., Janches, D., Meisel, D.D. and Zhou, Q.H., 2001. The micrometeoroid mass flux into the upper atmosphere: Arecibo results and a comparison with prior estimates. Geophysical Research Letters, 28:1929-1932, doi:10.1029/2000GL012621.
255. Matsuoka, M., Nakamura, T., Kimura, Y., Hiroi, T., Nakamura, R., Okumura, S. and Sasaki, S., 2015. Pulse-laser irradiation experiments of Murchison CM2 chondrite for reproducing space weathering on C-type asteroids. Icarus, 254:135-143, doi:10.1016/j.icarus.2015.02.029.
256. Maurette, M., Hammer, C., Brownlee, D.E., Reeh, N. and Thomsen, H.H., 1986. Placers of cosmic dust in the blue ice lakes of Greenland. Science, 233:869-872, doi:10.1126/science.233.4766.869.
257. Maurette, M., Olinger, C., Michel-Levy, M.C., Kurat, G., Pourchet, M., Brandstätter, F. and Bourot-Denise, M., 1991. A collection of diverse micrometeorites recovered from 100 tonnes of Antarctic blue ice. Letters to Nature, 351:44-47, doi:10.1038/351044a0.
258. Maurette, M., Immel, G., Hammer, C., Harvey, R., Kurat, G. and Taylor, S., 1994. Collection and curation of IDPs from the Greenland and Antarctic ice sheets. In Analysis of interplanetary dust: NASA/LPI workshop, 310:277-290. AIP Publishing.
259. McAdam, M.M., Sunshine, J.M., Howard, K.T. and McCoy, T.M., 2015. Aqueous alteration on asteroids: Linking the mineralogy and spectroscopy of CM and CI chondrites. Icarus, 245:320-332, doi:10.1016/j.icarus.2014.09.041.
260. McKeegan, K.D. and Davis, A.M., 2003. Early solar system chronology. In: Davis, A.M., Holland, H.D., and Turekian, K.K., Treatise on Geochemistry. ISBN 0-08-043751-6. Elsevier, 431-460, doi:10.1016/B0-08-043751-6/01147-6
261. McSween, H.Y., 1977. On the nature and origin of isolated olivine grains in carbonaceous chondrites. Geochimica et Cosmochimica Acta, 41:411IN1413-412IN2418, doi:10.1016/0016-7037(77)90269-1.
262. McSween, H.Y., 1979. Alteration in CM carbonaceous chondrites inferred from modal and chemical variations in matrix. Geochimica et Cosmochimica Acta, 43:1761-1770, doi:10.1016/0016-7037(79)90024-3.
263. McSween, H.Y., 1987. Aqueous alteration in carbonaceous chondrites: Mass balance constraints on matrix mineralogy. Geochimica et Cosmochimica Acta, 51:2469-2477, doi: 10.1029/RG017i005p01059.#.
264. Meier, M.M.M., Maden, C. and Busemann, H., 2016a. Constraining the Age of the Veritas Asteroid Break-Up Event with Helium-3 from the Tortonian Monte Dei Corvi Section in Italy. 79th Annual Meeting of the Meteoritical Society, held August 7-12, 2015 in Berlin, Germany. (abstract #1921).
265. Meier, M.M.M., Grimm, S., Maden, C. and Busemann, H., 2016b. Do we have meteorites from the Veritas asteroid break-up event 8 Ma ago? 79th Annual Meeting of the Meteoritical Society, held August 7-12th, 2015 in Berlin, Germany. (abstract #6291).
266. Melosh, H.J., 2011. Planetary surface processes. Cambridge University Press. ISBN-13:978-0521861526, doi:10.1017/CBO9780511977848
267. Meteoritical Bulletin, 2017. Available at: https://www.lpi.usra.edu/meteor/about.php
268. Metzler, K., Bischoff, A., and Stöffler, D. 1992. Accretionary dust mantles in CM chondrites: Evidence for solar nebula processes. Geochimica et Cosmochimica Acta 56:2873-2897, doi:10.1016/0016-7037(92)90365-P.
269. Michel, P., Benz, W. and Richardson, D.C., 2004. Catastrophic disruption of asteroids and family formation: a review of numerical simulations including both fragmentation and gravitational reaccumulations. Planetary and Space Science, 52:1109-1117, doi:10.1016/j.pss.2004.07.008.
270. Michel, P., Jutzi, M., Richardson, D.C. and Benz, W., 2011. The Asteroid Veritas: An intruder in a family named after it? Icarus 211:535-545, doi:10.1016/j.icarus.2010.10.012.

271. Milani, A. and Farinella, P., 1994. The age of the Veritas asteroid family deduced by chaotic chronology. Nature 370:40-42, doi:10.1038/370040a0.
272. Mizuno, H. and Boss, A.P., 1985. Tidal disruption of dissipative planetesimals. Icarus, 63:109-133, doi:10.1016/j.icarus.2007.11.010.
273. Mohajeri, N., and Gudmundsson, A. 2012. Entropies and scaling exponents of street and fracture networks. Entropy 14:800-833, doi:10.3390/e14040800.
274. Mohajeri, N., Gudmundsson, A., Kämpf, J., and Scartezzini, J. L. 2014. Visualizing street orientation and solar radiation in relation to complex topography. In Proceedings of the EuroGraphics 2014 on Urban Data Modelling and Visualisation (No. EPFL-CONF-198289, pp. 1-6). EuroGraphics Digital Library, doi:10.2312/udmv.20141070.
275. Montgomery, P., Hailwood, E.A., Gale, A.S. and Burnett, J.A., 1998. The magnetostratigraphy of Coniacian-late Campanian chalk sequences in southern England. Earth and Planetary Science Letters 156:209-224, doi:10.1016/S0012-821X(98)00008-9.
276. Montmerle, T., Augereau, J.C., Chaussidon, M., Gounelle, M., Marty, B. and Morbidelli, A., 2006. Solar system formation and early evolution: the first 100 million years. In From Suns to Life: A Chronological Approach to the History of Life on Earth. Springer New York, 3:39-95, doi:10.1007/s11038-006-9087-5.
277. Morbidelli, A., Levison, H.F., Tsiganis, K. and Gomes, R., 2005. Chaotic capture of Jupiter's Trojan asteroids in the early Solar System. Nature, 435:462-465, doi:10.1038/nature03540.
278. Morbidelli, A., Bitsch, B., Crida, A., Gounelle, M., Guillot, T., Jacobson, S., Johansen, A., Lambrechts, M. and Lega, E., 2016. Fossilized condensation lines in the Solar System protoplanetary disk. Icarus, 267:368-376, doi:10.1016/j.icarus.2015.11.027 0019-1035.
279. Morris, M.A., Boley, A.C., Desch, S.J. and Athanassiadou, T., 2012. Chondrule formation in bow shocks around eccentric planetary embryos. The Astrophysical Journal, 752:27, doi:10.1088/0004-637X/752/1/27.
280. Muirhead, D.K., Parnell, J., Taylor, C. and Bowden, S.A., 2012. A kinetic model for the thermal evolution of sedimentary and meteoritic organic carbon using Raman spectroscopy. Journal of Analytical and Applied Pyrolysis, 96:153-161, doi:10.1016/j.jaap.2012.03.017.
281. Mutch, T.A., 1964. Extraterrestrial particles in Paleozoic salts. Annals of the New York Academy of Sciences, 119:166-185, doi:10.1111/j.1749-6632.1965.tb47432.x.
282. Muszer, A., 2014. Silicide spherules from Permian sediments of the Fore-Sudetic Monocline (SW Poland). Physicochemical Problems of Mineral Processing, 50:107-118, doi:10.5277/ppmp140110.
283. Muñoz Caro, G. M., Dartois, E., & Nakamura-Messenger, K. 2008. Characterization of the carbon component in cometary Stardust samples by means of infrared and Raman spectroscopy. Astronomy & Astrophysics, 485:743-751.
284. Nahmias, S., & Olsen, T. L. 2015. Production and operations analysis. Waveland Press.
285. Nakamura, T., 2005. Post-hydration thermal metamorphism of carbonaceous chondrites. Journal of Mineralogical and Petrological Sciences, 100:260-272, doi:10.2465/jmps.100.260.
286. Nakamura, T., 2006. Yamato 793321 CM chondrite: Dehydrated regolith material of a hydrous asteroid. Earth and Planetary Science Letters, 242:26-38, doi:10.1016/j.epsl.2005.11.040.
287. Nakamura, T., Noguchi, T., Yada, T., Nakamuta, Y., and Takaoka, N. 2001. Bulk mineralogy of individual micrometeorites determined by X-ray diffraction analysis and transmission electron microscopy. Geochimica et Cosmochimica Acta 65:4385-4397, doi:10.1016/S0016-7037(01)00722-0.
288. Nakamura, T., Noguchi, T., Tanaka, M., Zolensky, M.E., Kimura, M., Tsuchiyama, A., Nakato, A., Ogami, T., Ishida, H., Uesugi, M. and Yada, T., 2011. Itokawa dust particles: a direct link between S-type asteroids and ordinary chondrites. Science, 333:1113-1116, doi:10.1126/science.1207758.
289. Nakashima, D., Nakamura, T. and Noguchi, T., 2003. Formation history of CI-like phyllosilicate-rich clasts in the Tsukuba meteorite inferred from mineralogy and noble gas signatures. Earth and Planetary Science Letters, 212:321-336, doi:10.1016/S0012-821X(03)00282-6.
290. Nakato, A., Nakamura, T., Kitajima, F. and Noguchi, T., 2008. Evaluation of dehydration mechanism during heating of hydrous asteroids based on mineralogical and chemical analysis of naturally and experimentally heated CM chondrites. Earth, planets and space, 60:855-864, doi:10.1186/BF03352837.
291. Nakato, A., Brearley, A.J., Nakamura, T., Noguchi, T., Ahn, I., Lee, J.I., Matsuoka, M. and Sasaki, S., 2013. PCA 02012: A unique thermally metamorphosed carbonaceous chondrite. (abstract #2708) 44th Lunar and Planetary Science Conference. CD-ROM.
292. Nazarov, M. A., Kurat, G., Brandstaetter, F., Ntaflos, T., Chaussidon, M., & Hoppe, P. 2009. Phosphorus-bearing sulfides and their associations in CM chondrites. Petrology, 17:101-123, doi:10.1134/S0869591109020015.

293. Nelson, V.E. and Rubin, A.E., 2002. Size-frequency distributions of chondrules and chondrule fragments in LL3 chondrites: Implications for parent-body fragmentation of chondrules. Meteoritics & Planetary Science, 37:1361-1376, doi:10.1111/j.1945-5100.2002.tb01034.x.
294. Nesvorný, D., Bottke Jr, W.F., Dones, L. and Levison, H.F., 2002. The recent breakup of an asteroid in the main-belt region. Nature, 417:720-771, doi:10.1038/nature00789.
295. Nesvorný, D., Bottke, W. F., Levison, H. F., and Dones, L., 2003. Recent Origin of the Solar System Dust Bands. The Astrophysical Journal, 591:486–497, doi:10.1086/374807.
296. Nesvorný, D., Vokrouhlický, D., Bottke, W.F. and Sykes, M., 2006. Physical properties of asteroid dust bands and their sources. Icarus, 181:107-144, doi:10.1016/j.icarus.2005.10.02.
297. Nesvorný, D., Vokrouhlický, D., Bottke, W.F., Gladman, B. and Häggström, T., 2007. Express delivery of fossil meteorites from the inner asteroid belt to Sweden. Icarus, 188:400-413, doi:10.1016/j.icarus.2006.11.021.
298. Nesvorný, D., Bottke, W. F., Vokrouhlický, D., Sykes, M., Lien, D.J. and Stansberry, J., 2008. Origin of the near-ecliptic circumsolar dust band. The Astrophysical Journal Letters, 679:L143–L146.
299. Nesvorný, D., Jenniskens, P., Levison, H. F., Bottke, W. F., Vokrouhlický, D., and Gounelle, M., 2010. Cometary Origin of the Zodiacal Cloud and Carbonaceous Micrometeorites. Implications for Hot Debris Disks. The Astrophysical Journal, 713:816–836, doi:10.1088/0004-637X/713/2/816.
300. Nesvorný, D., Nesvorný HCM Asteroid Families V3.0. EAR-A-VARGBDET-5-NESVORNYFAM-V3.0. NASA Planetary Data System, 2015. Available at: https://sbn.psi.edu/pds/resource/nesvornyfam.html
301. Niemeijer, A. R., and Spiers, C. J. 2005. Influence of phyllosilicates on fault strength in the brittle-ductile transition: Insights from rock analogue experiments. Geological Society, London, Special Publications, 245:303-327, doi:10.1144/GSL.SP.2005.245.01.15.
302. Nishiizumi, K., Arnold, J.R., Brownlee, D.E., Caffee, M.W., Finkel, R.C. and Harvey, R.P., 1995. Beryllium-10 and aluminum-26 in individual cosmic spherules from Antarctica: Meteoritics, 30:728-732, doi: 10.1111/j.1945-5100.1995.tb01170.
303. Noguchi, T., Nakamura, T. and Nozaki, W., 2002. Mineralogy of phyllosilicate-rich micrometeorites and comparison with Tagish Lake and Sayama meteorites. Earth and Planetary Science Letters, 202:229-246, doi:10.1016/S0012-821X(02)00777-X.
304. Noguchi, T., Tsujimoto, S., Okazaki, R., Nakamura, T., Ebihara, M., Ito, S., Nagahara, H., Tachibana, S., Terada, K. and Yabuta, H., 2013. A Fine-Grained Polycrystalline Micrometeorite: An Asteroidal Dust Particle with a Unique Mineralogy. 76th Annual Meeting of the Meteoritical Society, held 29-02 July-August, 2013 in Edmonton, Alberta, Canada. (abstract #5081).
305. Noguchi, T., Ohashi, N., Tsujimoto, S., Mitsunari, T., Bradley, J.P., Nakamura, T., Toh, S., Stephan, T., Iwata, N. and Imae, N., 2015. Cometary dust in Antarctic ice and snow: Past and present chondritic porous micrometeorites preserved on the Earth's surface. Earth and Planetary Science Letters, 410:1-11, doi:10.1016/j.epsl.2014.11.012.
306. Noguchi, T., Yabuta, H., Itoh, S., Sakamoto, N., Mitsunari, T., Okubo, A., Okazaki, R., Nakamura, T., Tachibana, S., Terada, K. and Ebihara, M., 2017. Variation of mineralogy and organic material during the early stages of aqueous activity recorded in Antarctic micrometeorites. Geochimica et Cosmochimica Acta, 208:119-144, doi: 10.1016/j.gca.2017.03.034
307. Novgorodova, M.I., Yusupov, R.G., Dmitrieva, M.T., Tsepin, A.I., Sivtsov, A.V., Gorshkov, A.I., Korovushkin, V.V. and Yakubovskaya, N.Y., 1984. First Occurrence of Suessite on the Earth. International Geology Review, 26:98-101, doi:10.1080/00206818409452999.
308. Novakovic, B., 2012. Veritas Asteroid Family Still Holds Secrets?: Publications de l'Observatoire Astronomique de Beograd, 91:177-184.
309. Nozaki, W., Nakamura, T. and Noguchi, T., 2006. Bulk mineralogical changes of hydrous micrometeorites during heating in the upper atmosphere at temperatures below 1000C. Meteoritics & Planetary Science, 41:1095-1114, doi: 10.1111/j.1945-5100.2006.tb00507.
310. Onoue, T., Nakamura, T., Haranosono, T. and Yasuda, C., 2011. Composition and accretion rate of fossil micrometeorites recovered in Middle Triassic deep-sea deposits. Geology, 39:567-570, doi:10.1130/G31866.1.
311. Ostrowski, D.R., Gietzen, K., Lacy, C. and Sears, D.W., 2010. An investigation of the presence and nature of phyllosilicates on the surfaces of C asteroids by an analysis of the continuum slopes in their near-infrared spectra. Meteoritics & Planetary Science, 45:615-637, doi:10.1111/j.1945-5100.2010.01047.x.
312. Ott, U., Baecker, B., Folco, L. and Cordier, C., 2016. Noble Gas Inventory of Micrometeorites Collected at the Transantarctic Mountains (TAM) and Indications for Their Provenance. 79th Annual Meeting of the Meteoritical Society, held August 7-12th, 2016 in Berlin, Germany. (abstract #6210)

313. Pack, A., Höweling, A., Hezel, D.C., Stefanak, M.T., Beck, A.K., Peters, S.T., Sengupta, S., Herwartz, D. and Folco, L., 2017. Tracing the oxygen isotope composition of the upper Earth's atmosphere using cosmic spherules. Nature Communications, doi:10.1038/ncomms15702.
314. Pälike, H., Lyle, M.W., Nishi, H., Raffi, I., Ridgwell, A., Gamage, K., Klaus, A., Acton, G., Anderson, L., Backman, J. and Baldauf, J., 2012. A Cenozoic record of the equatorial Pacific carbonate compensation depth. Nature, 488:609-614, doi:10.1038/nature11360.
315. Palme, H., Hezel, D.C. and Ebel, D.S., 2015. The origin of chondrules: Constraints from matrix composition and matrix-chondrule complementarity. Earth and Planetary Science Letters, 411:11-19, doi:10.1016/j.epsl.2014.11.033.
316. Pasek, M.A., Block, K. and Pasek, V., 2012. Fulgurite morphology: a classification scheme and clues to formation. Contributions to Mineralogy and Petrology, 164:477-492, doi:10.1007/s00410-012-0753-5.
317. Peucker-Ehrenbrink, B., 1996. Accretion of extraterrestrial matter during the last 80 million years and its effect on the marine osmium isotope record. Geochimica et Cosmochimica Acta, 60:3187-3196, doi:10.1016/0016-7037(96)00161-5.
318. Prasad, M.S., Rudraswami, N.G. and Panda, D.K., 2013. Micrometeorite flux on Earth during the last ~50,000 years. Journal of Geophysical Research: Planets, 118:2381-2399, doi:10.1002/2013JE004460.
319. Prasad, M.S., Rudraswami, N.G., De Araujo, A., Babu, E.V.S.S.K. and Vijaya Kumar, T., 2015. Ordinary chondritic micrometeorites from the Indian Ocean. Meteoritics & Planetary Science, 50:1013-1031, doi: 10.1111/maps.12451.
320. Prasad, M., Rudraswami, N.G., De Araujo, A.A. and Khedekar, V.D., 2017. Unmelted cosmic metal particles in the Indian Ocean. Meteoritics & Planetary Science, 52:1060-1081, doi:10.1111/maps.12858.
321. Prost, R., 1973. The influence of the Christiansen effect on IR spectra of powders. Clays and Clay Minerals, 21:363-368, doi:10.1346/CCMN.1973.0210512.
322. Poynting, J.H., 1904. Radiation in the solar system: its effect on temperature and its pressure on small bodies. Philosophical Transactions of the Royal Society of London. Series A, Containing Papers of a Mathematical or Physical Character, 202:525-552, doi:10.1098/rsta.1904.0012.
323. Pujol, J. 2007. The solution of nonlinear inverse problems and the Levenberg-Marquardt method. Geophysics, 72:W1-W16, doi:10.1190/1.2732552.
324. Quirico, E., Raynal, P.I. and Bourot-Denise, M., 2003. Metamorphic grade of organic matter in six unequilibrated ordinary chondrites. Meteoritics & Planetary Science, 38:795-811, doi:10.1111/j.1945-5100.2003.tb00043.x.
325. Quirico, E., Borg, J., Raynal, P.I., Montagnac, G. and d'Hendecourt, L., 2005. A micro-Raman survey of 10 IDPs and 6 carbonaceous chondrites. Planetary and Space Science, 53:1443-1448, doi:10.1016/j.pss.2005.07.009.
326. Quirico, E., Orthous-Daunay, F.R., Beck, P., Bonal, L., Brunetto, R., Dartois, E., Pino, T., Montagnac, G., Rouzaud, J.N., Engrand, C. and Duprat, J., 2014. Origin of insoluble organic matter in type 1 and 2 chondrites: New clues, new questions. Geochimica et Cosmochimica Acta, 136:80-99, doi:10.1016/j.gca.2014.03.025.
327. Rahl, J.M., Anderson, K.M., Brandon, M.T. and Fassoulas, C., 2005. Raman spectroscopic carbonaceous material thermometry of low-grade metamorphic rocks: calibration and application to tectonic exhumation in Crete, Greece. Earth and Planetary Science Letters, 240:339-354, doi:10.1016/j.epsl.2005.09.055.
328. Reshma, K., Rudraswami, N.G. and Prasad, M.S., 2013. Chondrule-like object from the Indian Ocean cosmic spherules. Journal of earth system science, 122:1161-1171, doi:10.1007/s12040-013-0333-8.
329. Rietmeijer, F.J., Nakamura, T., Tsuchiyama, A., Uesugi, K., Nakano, T. and Leroux, H., 2008. Origin and formation of iron silicide phases in the aerogel of the Stardust mission. Meteoritics & Planetary Science, 43:121-134, doi:10.1111/j.1945-5100.2008.tb00613.x.
330. Rinaldi, R. and Llovet, X., 2015. Electron Probe Microanalysis: A Review of the Past, Present, and Future. Microscopy and Microanalysis, 21:1053-1069, doi:10.1017/S1431927615000409.
331. Rivkin, A.S., Howell, E.S., Vilas, F. and Lebofsky, L.A., 2002. Hydrated minerals on asteroids: The astronomical record. In: Asteroids III, W. F. Bottke Jr., A. Cellino, P. Paolicchi, and R. P. Binzel (eds), University of Arizona Press, Tucson, Chapter 2.2.10, pp.235-253.
332. Rivkin, A.S., Li, J.Y., Milliken, R.E., Lim, L.F., Lovell, A.J., Schmidt, B.E., McFadden, L.A. and Cohen, B.A., 2011. The surface composition of Ceres. In The Dawn Mission to Minor Planets 4 Vesta and 1 Ceres (pp. 95-116). Springer New York.
333. Rochette, P., Folco, L., Suavet, C., Van Ginneken, M., Gattacceca, J., Perchiazzi, N., Braucher, R. and Harvey, R.P., 2008. Micrometeorites from the transantarctic mountains. Proceedings of the National Academy of Sciences, 105:18206-18211, doi:10.1073/pnas.0806049105.
334. Rubin, A.E., 1984. Coarse-grained chondrule rims in type 3 chondrites. Geochimica et Cosmochimica Acta, 48:1779-1789, doi:10.1016/0016-7037(84)90032-2.
335. Rubin, A.E., 1995. Petrologic evidence for collisional heating of chondritic asteroids. Icarus, 113:156-167, doi:10.1006/icar.1995.1013.

336. Rubin, A.E., 2012. Collisional facilitation of aqueous alteration of CM and CV carbonaceous chondrites. Geochimica et Cosmochimica Acta, v.90, p.181-194, doi:10.1016/j.gca.2012.05.016.
337. Rubin, A.E., Scott, E.R. and Keil, K., 1982. Microchondrule-bearing clast in the Piancaldoli LL3 meteorite: a new kind of type 3 chondrite and its relevance to the history of chondrules. Geochimica et Cosmochimica Acta, 46:1763-1776, doi:10.1016/0016-7037(82)90116-8.
338. Rubin, A.E. and Wasson, J.T., 1987. Chondrules, matrix and coarse-grained chondrule rims in the Allende meteorite: Origin, interrelationships and possible precursor components. Geochimica et Cosmochimica Acta, 51:1923-1937, doi:10.1016/0016-7037(87)90182-7.
339. Rubin, A.E. and Grossman, J.N., 2010. Meteorite and meteoroid: New comprehensive definitions. Meteoritics & Planetary Science, 45:114-122, doi:10.1111/j.1945-5100.2009.01009.x.
340. Rubin, A.E., Scott, E.R. and Keil, K., 1982. Microchondrule-bearing clast in the Piancaldoli LL3 meteorite: a new kind of type 3 chondrite and its relevance to the history of chondrules. Geochimica et Cosmochimica Acta, 46:1763-1776, doi:10.1016/0016-7037(82)90116-8.
341. Rubin, A.E., Trigo-Rodríguez, J.M., Huber, H. and Wasson, J.T., 2007. Progressive aqueous alteration of CM carbonaceous chondrites: Geochimica et Cosmochimica Acta, 71:2361-2382, doi:10.1016/j.gca.2007.02.008.
342. Russell, C.T., Raymond, C.A., Coradini, A., McSween, H.Y., Zuber, M.T., Nathues, A., De Sanctis, M.C., Jaumann, R., Konopliv, A.S., Preusker, F. and Asmar, S.W., 2012. Dawn at Vesta: Testing the protoplanetary paradigm. Science, 336:684-686, doi:10.1126/science.1219381.
343. Sahijpal, S. and Gupta, G., 2011. Did the carbonaceous chondrites evolve in the crustal regions of partially differentiated asteroids?. Journal of Geophysical Research: Planets, 116(E6), doi:10.1029/2010JE003757.
344. Salisbury, J. W. 1993. Mid-infrared spectroscopy: Laboratory data. In Pieters, C. M., and Englert, P. A. J. (eds), Remote geochemical analysis: Elemental and mineralogical composition. 68-79. Cambridge Univ. Press.
345. Salisbury, J.W. and Wald, A., 1992. The role of volume scattering in reducing spectral contrast of reststrahlen bands in spectra of powdered minerals. Icarus, 96:121-128, doi:10.1016/0019-1035(92)90009-V.
346. Salisbury, J.W., D'Aria, D.M. and Jarosewich, E., 1991. Midinfrared (2.5–13.5 μm) reflectance spectra of powdered stony meteorites. Icarus, 92:280-297, doi:10.1016/0019-1035(91)90052-U.
347. Salisbury, J.W., Wald, A. and D'Aria, D.M., 1994. Thermal-infrared remote sensing and Kirchhoff's law: 1. Laboratory measurements. Journal of Geophysical Research: Solid Earth, 99:11897-11911, doi:10.1029/93JB03600.
348. Salmeron, R. and Ireland, T.R., 2012. Formation of chondrules in magnetic winds blowing through the proto-asteroid belt. Earth and Planetary Science Letters, 327:61-67, doi:10.1016/j.epsl.2012.01.033.
349. Sanders, I.S. and Scott, E.R., 2012. The origin of chondrules and chondrites: Debris from low-velocity impacts between molten planetesimals? Meteoritics & Planetary Science, 47:2170-2192, doi:10.1111/maps.12002.
350. Sandford, S. A., 1984. Infrared transmission spectra from 2.5 to 25μm of various meteorite classes. Icarus, 60:115-126, doi:10.1016/0019-1035(84)90141-6.
351. Sasaki, S., Nakamura, K., Hamabe, Y., Kurahashi, E. and Hiroi, T., 2001. Production of iron nanoparticles by laser irradiation in a simulation of lunar-like space weathering. Nature, 410:555-557, doi:10.1038/35069013.
352. Schindelin, J., Rueden, C. T., Hiner, M. C., and Eliceiri, K. W. 2015. The ImageJ ecosystem: An open platform for biomedical image analysis. Molecular reproduction and development 82:518-529, doi:10.1002/mrd.22489.
353. Schulz, R., Stüwe, J.A. and Boehnhardt, H., 2004. Rosetta target comet 67P/Churyumov-Gerasimenko-Postperihelion gas and dust production rates: Astronomy & Astrophysics, 422:L19-L21, doi: 10.1051/0004-6361:20040190.
354. Schulz, R., Hilchenbach, M., Langevin, Y., Kissel, J., Silen, J., Briois, C., Engrand, C., Hornung, K., Baklouti, D., Bardyn, A. and Cottin, H., 2015. Comet 67P/Churyumov-Gerasimenko sheds dust coat accumulated over the past four years. Nature, 518:216-218, doi:10.1038/nature14159.
355. Schmitz, B., Peucker-Ehrenbrink, B., Lindström, M. and Tassinari, M., 1997. Accretion rates of meteorites and cosmic dust in the Early Ordovician. Science, 278:88-90, doi:10.1126/science.278.5335.88.
356. Schmitz, B., Tassinari, M. and Peucker-Ehrenbrink, B., 2001. A rain of ordinary chondritic meteorites in the early Ordovician. Earth and Planetary Science Letters, 194:1-15, doi:10.1016/S0012-821X(01)00559-3.
357. Schroeder, P.A., 2002. Infrared spectroscopy in clay science. In CMS Workshop Lectures, 11:181-206, Teaching Clay Science, A. Rule and S. Guggenheim, eds., The Clay Mineral Society, Aurora, CO.
358. Scott, E. R., Keil, K., and Stöffler, D. 1992. Shock metamorphism of carbonaceous chondrites. Geochimica et Cosmochimica Acta 56:4281-4293.
359. Shen, P., Hwang, S. L., and Chu, H. T. 1990. Defect microstructure and dehydroxylation mechanism of interstratified phyllosilicates. a TEM study. Journal of materials science 25:3072-3078, doi:10.1007/BF00587652.
360. Sheng, C., 2007. Char structure characterised by Raman spectroscopy and its correlations with combustion reactivity. Fuel, 86:2316-2324, doi:10.1016/j.fuel.2007.01.029.

361. Smith, D.L., Ernst, R.E., Samson, C. and Herd, R., 2006. Stony meteorite characterization by non-destructive measurement of magnetic properties. Meteoritics and Planetary Science, 41:355-373, doi:10.1111/j.1945-5100.2006.tb00468.x.
362. Speck, A.K., Whittington, A.G. and Hofmeister, A.M., 2011. Disordered silicates in space: a study of laboratory spectra of "amorphous" silicates. The Astrophysical Journal, 740:93, doi:10.1088/0004-637.
363. Soens, B., Goderis, S., McKibbin, S., Pittarello, L., Van Ginneken, M., Debaille, V. and Claeys, P., 2016. Environmental Control on Antarctic Micrometeorite Preservation State: The Widerøfjellet Mountain Case Study. 79th Annual Meeting of the Meteoritical Society, held August 7-12th, 2016 in Berlin, Germany. (abstract #6274).
364. Šrámek, O., Milelli, L., Ricard, Y. and Labrosse, S., 2012. Thermal evolution and differentiation of planetesimals and planetary embryos. Icarus, 217:339-354, doi: 10.1016/j.icarus.2011.11.021.
365. Stuart, B., 2000. Infrared Spectroscopy. Kirk-Othmer Encyclopedia of Chemical Technology doi:10.1002/0471238961.0914061810151405.a01.pub2. Available at: http://onlinelibrary.wiley.com/doi/10.1002/0471238961.0914061810151405.a01.pub2/otherversions
366. Steele, I.M., 1986. Compositions and textures of relic forsterite in carbonaceous and unequilibrated ordinary chondrites. Geochimica et Cosmochimica Acta, 50:1379-1395, doi:10.1016/0016-7037(86)90312-1
367. Steele, I.M., 1992. Olivine in Antarctic micrometeorites: Comparison with other extraterrestrial olivine. Geochimica et Cosmochimica Acta, 56:2923-2929, doi:10.1016/0016-7037(92)90368-S.
368. Stöffler, D., and Keil, K. 1991. Shock metamorphism of ordinary chondrites. Geochimica et Cosmochimica Acta 55:3845-3867, doi:10.1016/0016-7037(91)90078-J.
369. Storm, S., 2007. Olivine-Pyroxene Distribution of S-type Asteroids Throughout the Main Belt. American Astronomical Society, DPS meeting #39, id.20.03; Bulletin of the American Astronomical Society, 39:448
370. Strub, P., Krüger, H. and Sterken, V.J., 2015. Sixteen Years of Ulysses Interstellar Dust Measurements in the Solar System. II. Fluctuations in the Dust Flow from the Data. The Astrophysical Journal, 812:140-155, doi:10.1088/0004-637X/812/2/140.
371. Suavet, C., Rochette, P., Kars, M., Gattacceca, J., Folco, L. and Harvey, R.P., 2009. Statistical properties of the Transantarctic Mountains (TAM) micrometeorite collection. Polar Science, 3:100-109, doi:10.1016/j.polar.2009.06.003.
372. Suavet, C., Alexandre, A., Franchi, I.A., Gattacceca, J., Sonzogni, C., Greenwood, R.C., Folco, L. and Rochette, P., 2010. Identification of the parent bodies of micrometeorites with high-precision oxygen isotope ratios. Earth and Planetary Science Letters, 293:313-320, doi:10.1016/j.epsl.2010.02.046.
373. Suavet, C., Cordier, C., Rochette, P., Folco, L., Gattacceca, J., Sonzogni, C. and Damphoffer, D., 2011a. Ordinary chondrite-related giant (>800μm) cosmic spherules from the Transantarctic Mountains, Antarctica. Geochimica et Cosmochimica Acta, 75:6200-6210, doi:10.1016/j.gca.2011.07.034.
374. Suavet, C., Gattacceca, J., Rochette, P. and Folco, L., 2011b. Constraining the terrestrial age of micrometeorites using their record of the Earth's magnetic field polarity. Geology, 39:123-126, doi:10.1130/G31655.1.
375. Sunshine, J.M., Bus, S.J., McCoy, T.J., Burbine, T.H., Corrigan, C.M. and Binzel, R.P., 2004. High-calcium pyroxene as an indicator of igneous differentiation in asteroids and meteorites. Meteoritics & Planetary Science, 39:1343-1357, doi:10.1111/j.1945-5100.2004.tb00950.x.
376. Suttle, M.D., Van Ginneken, M. and Genge, M.J., 2015. Larkman Nunatak Micrometeorites, a Statistical Study: 78th Annual Meeting of the Meteoritical Society, held July 27-31, 2015 in Berkeley, California. (abstract #5063).
377. Suzuki, A., Yamanoi, Y., Nakamura, T. and Nakashima, S., 2010. Micro-spectroscopic characterization of organic and hydrous components in weathered Antarctic micrometeorites. Earth, planets and space, 62:33-46, doi:10.5047/eps.2008.11.001.
378. Takayama, A. and Tomeoka, K., 2012. Fine-grained rims surrounding chondrules in the Tagish Lake carbonaceous chondrite: Verification of their formation through parent-body processes. Geochimica et Cosmochimica Acta, 98:1-18, doi:10.1016/j.gca.2012.08.015.
379. Taylor, S. and Brownlee, D.E., 1991. Cosmic spherules in the geologic record. Meteoritics, 26:203-211, doi:10.1111/j.1945-5100.1991.tb01040.
380. Taylor, S., Lever, J.H. and Harvey, R.P., 1998. Accretion rate of cosmic spherules measured at the South Pole. Nature, 392:899-903, doi:10.1038/31894.
381. Taylor, S., Lever, J.H. and Harvey, R.P., 2000. Numbers, types, and compositions of an unbiased collection of cosmic spherules. Meteoritics & Planetary Science, 35:651-666, doi:10.1111/j.1945-5100.2000.tb01450.
382. Taylor, S., Herzog, G. F., & Delaney, J. S. 2007. Crumbs from the crust of Vesta: Achondritic cosmic spherules from the South Pole water well. Meteoritics & Planetary Science, 42:223-233, doi:10.1111/j.1945-5100.2006.tb00195.x.

383. Taylor, S., Jones, K.W., Herzog, G.F. and Hornig, C.E., 2011. Tomography: A window on the role of sulfur in the structure of micrometeorites. Meteoritics & Planetary Science, 46:1498-1509, doi:10.1111/j.1945-5100.2011.01245.
384. Taylor, S., Matrajt, G. and Guan, Y., 2012. Fine-grained precursors dominate the micrometeorite flux. Meteoritics & Planetary Science, 47:550-564, doi:10.1111/j.1945-5100.2011.01292.
385. Tholen, D.J., 1984. Asteroid taxonomy from cluster analysis of photometry. PhD thesis. The University of Arizona.
386. Thomson, J.L. and Salisbury, J.W., 1993. The mid-infrared reflectance of mineral mixtures (7–14μm). Remote Sensing of Environment, 45:1-13, doi:10.1016/0034-4257(93)90077-B.
387. Tomeoka, K. and Buseck, P.R., 1988. Matrix mineralogy of the Orgueil CI carbonaceous chondrite. Geochimica et Cosmochimica Acta, 52:1627-1640, doi:10.1016/0016-7037(88)90231-1.
388. Tomeoka, K., McSween Jr, H.Y. and Buseck, P.R., 1989. Mineralogical alteration of CM carbonaceous chondrites: A review. In Proceedings of the NIPR Symposium on Antarctic Meteorites 2:221-234.
389. Tomeoka, K., Yamahana, Y., and Sekine, T. 1999. Experimental shock metamorphism of the Murchison CM carbonaceous chondrite. Geochimica et Cosmochimica Acta, 63:3683-3703, doi:10.1016/S0016-7037(99)00149-0.
390. Tomioka, N., Tomeoka, K., Nakamura-Messenger, K. and Sekine, T., 2007. Heating effects of the matrix of experimentally shocked Murchison CM chondrite: Comparison with micrometeorites. Meteoritics & Planetary Science, 42:19-30, doi:10.1111/j.1945-5100.2007.tb00214.x.
391. Tomkins, A.G., Bowlt, L., Genge, M., Wilson, S.A., Brand, H.E. and Wykes, J.L., 2016. Ancient micrometeorites suggestive of an oxygen-rich Archaean upper atmosphere. Nature, 533:235-238, doi:10.1038/nature17678.
392. Tonui, E.K., Zolensky, M.E., Lipschutz, M.E., Wang, M.S. and Nakamura, T., 2003. Yamato 86029: Aqueously altered and thermally metamorphosed CI-like chondrite with unusual textures. Meteoritics & Planetary Science, 38:269-292, doi:10.1111/j.1945-5100.2003.tb00264.
393. Tonui, E., Zolensky, M., Hiroi, T., Nakamura, T., Lipschutz, M.E., Wang, M.S. and Okudaira, K., 2014. Petrographic, chemical and spectroscopic evidence for thermal metamorphism in carbonaceous chondrites I: CI and CM chondrites. Geochimica et Cosmochimica Acta, 126:284-306, doi:10.1016/j.gca.2013.10.053.
394. Toppani, A. and Libourel, G., 2003. Factors controlling compositions of cosmic spinels: Application to atmospheric entry conditions of meteoritic materials. Geochimica et Cosmochimica Acta,67:4621-4638, doi: 10.1016/S0016-7037(03)00383-1.
395. Toppani, A., Libourel, G., Engrand, C. and Maurette, M., 2001. Experimental simulation of atmospheric entry of micrometeorites. Meteoritics & Planetary Science, 36:1377-1396, doi:10.1111/j.1945-5100.2001.tb01831.
396. Trigo-Rodriguez, J.M., Rubin, A.E. and Wasson, J.T., 2006. Non-nebular origin of dark mantles around chondrules and inclusions in CM chondrites. Geochimica et Cosmochimica Acta, 70:1271-1290, doi:10.1016/j.gca.2005.11.009.
397. Tsai, W.H., 1985. Moment-preserving thresholding: A new approach. Computer. Vision, Graphics, and Image Processing 29:377-393. doi:10.1016/0734-189X(85)90133-1
398. Tsiganis, K., Gomes, R., Morbidelli, A. and Levison, H.F., 2005. Origin of the orbital architecture of the giant planets of the Solar System. Nature, 435:459-461, doi:10.1038/nature03539.
399. van Boekel, R.J.H.M., Min, M., Leinert, C., Waters, L.B.F.M., Richichi, A., Chesneau, O., Dominik, C., Jaffe, W., Dutrey, A., Graser, U. and Henning, T., 2004. The building blocks of planets within the 'terrestrial' region of protoplanetary disks. Nature, 432:479-482, doi:10.1038/nature03088.
400. van Ginneken, M., Folco, L., Cordier, C. and Rochette, P., 2012. Chondritic micrometeorites from the Transantarctic Mountains. Meteoritics & Planetary Science, 47:228-247, doi:10.1111/j.1945-5100.2011.01322.
401. van Ginneken, M., Genge, M.J., Folco, L. and Harvey, R.P., 2016. The weathering of micrometeorites from the Transantarctic Mountains. Geochimica et Cosmochimica Acta, 179:1-31, doi:10.1016/j.gca.2015.11.045.
402. van Ginneken, M., Gattacceca, J., Rochette, P., Sonzogni, C., Alexandre, A., Vidal, V. and Genge, M.J., 2017. The parent body controls on cosmic spherule texture: Evidence from the oxygen isotopic compositions of large micrometeorites. Geochimica et Cosmochimica Acta, doi:10.1016/j.gca.2017.05.008
403. Velbel, M.A. and Palmer, E.E., 2011. Fine-grained serpentine in CM2 carbonaceous chondrites and its implications for the extent of aqueous alteration on the parent body: A review. Clays and Clay Minerals, 59:416-432, doi:10.1346/CCMN.2011.0590405.
404. Velbel, M.A., Tonui, E.K. and Zolensky, M.E., 2012. Replacement of olivine by serpentine in the carbonaceous chondrite Nogoya (CM2). Geochimica et Cosmochimica Acta, 87:117-135, doi:10.1016/j.gca.2012.03.016.
405. Verdier-Paoletti, M.J., Marrocchi, Y., Avice, G., Roskosz, M., Gurenko, A. and Gounelle, M., 2016. Oxygen isotope constraints on the alteration temperatures of CM chondrites. Earth and Planetary Science Letters, doi:10.1016/j.epsl.2016.10.055.
406. Vernazza, P., Binzel, R.P., Thomas, C.A., DeMeo, F.E., Bus, S.J., Rivkin, A.S. and Tokunaga, A.T., 2008. Compositional differences between meteorites and near-Earth asteroids. Nature, 454:858-860, doi:10.1038/nature07154.

407. Vernazza, P., Carry, B., Emery, J., Hora, J.L., Cruikshank, D., Binzel, R.P., Jackson, J., Helbert, J. and Maturilli, A., 2010. Mid-infrared spectral variability for compositionally similar asteroids: Implications for asteroid particle size distributions. Icarus, 207:800-809, doi:10.1016/j.icarus.2010.01.011.
408. Vernazza, P., Delbo, M., King, P.L., Izawa, M.R.M., Olofsson, J., Lamy, P., Cipriani, F., Binzel, R.P., Marchis, F., Merín, B. and Tamanai, A., 2012. High surface porosity as the origin of emissivity features in asteroid spectra. Icarus, 221:1162-1172, doi:10.1016/j.icarus.2012.04.003.
409. Vokrouhlický, D. and Farinella, P., 2000. Efficient delivery of meteorites to the Earth from a wide range of asteroid parent bodies. Nature, 407:606-608, doi:10.1038/35036528.
410. Voldman, G.G., Genge, M.J., Albanesi, G.L., Barnes, C.R. and Ortega, G., 2013. Cosmic spherules from the Ordovician of Argentina. Geological Journal, 48:222-235, doi:10.1002/gj.2418.
411. Walsh, K.J., Morbidelli, A., Raymond, S.N., O'brien, D.P. and Mandell, A.M., 2011. A low mass for Mars from Jupiter/'s early gas-driven migration. Nature, 475:206-209, doi:10.1038/nature10201.
412. Walsh, K.J., Morbidelli, A., Raymond, S.N., O'brien, D.P. and Mandell, A.M., 2012. Populating the asteroid belt from two parent source regions due to the migration of giant planets— "The Grand Tack". Meteoritics & Planetary Science, 47:1941-1947, doi:10.1111/j.1945-5100.2012.01418.x.
413. Wang, L., Zhang, M., Redfern, S.A. and Zhang, Z., 2002. Dehydroxylation and transformations of the 2:1 phyllosilicate pyrophyllite at elevated temperatures: An infrared spectroscopic study. Clays and Clay Minerals, 50:272-283, doi:10.1346/000986002760832874.
414. Wasson, J.T., Boynton, W.V., Chou, C.L. and Baedecker, P.A., 1975. Compositional evidence regarding the influx of interplanetary materials onto the lunar surface. The Moon, 13:121-141, doi:10.1007/BF00567511.
415. Wasson, J.T. and Rubin, A.E., 2003. Ubiquitous low-FeO relict grains in type II chondrules and limited overgrowths on phenocrysts following the final melting event. Geochimica et Cosmochimica Acta, 67:2239-2250, doi:10.1016/S0016-7037(03)00023-1.
416. Watt, L.E., Bland, P.A., Prior, D.J. and Russell, S.S., 2006. Fabric analysis of Allende matrix using EBSD. Meteoritics & Planetary Science, 41:989-1001, doi:10.1111/j.1945-5100.2006.tb00499.x.
417. Wawersik, W. R., and Fairhurst, C. 1970. A study of brittle rock fracture in laboratory compression experiments. International Journal of Rock Mechanics and Mining Sciences and Geomechanics, 7:561-575, doi:10.1016/0148-9062(70)90007-0.
418. Weibel, R., 1998. Diagenesis in oxidising and locally reducing conditions—an example from the Triassic Skagerrak formation, Denmark. Sedimentary Geology, 121:259-276, doi:10.1016/S0037-0738(98)00085-2.
419. Weisberg, M.K., Prinz, M., Clayton, R.N. and Mayeda, T.K., 1993. The CR (Renazzo-type) carbonaceous chondrite group and its implications. Geochimica et Cosmochimica Acta, 57:1567-1586, doi:10.1016/0016-7037(93)90013-M.
420. Weisberg, M.K., McCoy, T.J. and Krot, A.N., 2006. Systematics and evaluation of meteorite classification. In: Meteorites and the early solar system II, Lauretta, D. S. and McSween Jr. H. Y., (eds.), University of Arizona Press, Tucson, p.19-52.
421. Welten, K.C., Folco, L., Nishiizumi, K., Caffee, M.W., Grimberg, A., Meier, M.M.M. and Kober, F., 2008. Meteoritic and bedrock constraints on the glacial history of Frontier Mountain in northern Victoria Land, Antarctica. Earth and planetary science letters, 270:308-315, doi:10.1016/j.epsl.2008.03.052.
422. Westphal, A.J., Stroud, R.M., Bechtel, H.A., Brenker, F.E., Butterworth, A.L., Flynn, G.J., Frank, D.R., Gainsforth, Z., Hillier, J.K., Postberg, F. and Simionovici, A.S., 2014. Evidence for interstellar origin of seven dust particles collected by the Stardust spacecraft. Science, 345:786-791, doi:10.1126/science.1252496.
423. Wilkening, L.L., 1978. Carbonaceous chondritic material in the solar system. Naturwissenschaften, 65:73-79, doi:10.1007/BF00440544.
424. Wright, H.M. and Weinberg, R.F., 2009. Strain localization in vesicular magma: Implications for rheology and fragmentation. Geology 37:1023-1026, doi:10.1130/G30199A.1.
425. Wozniakiewicz, P.J., Price, M.C., Bradley, J.P., Ishii, H.A., Russell, S.S., Zolensky, M.E. and Brownlee, D.E., 2015. Analysis of cosmic spherule candidates from the Kwajalein micrometeorite collection.
426. Woolfson, M.M., 1993. The Solar System – Its Origin and Evolution. Quarterly Journal of the Royal Astronomical Society, 34:1-20.
427. Wyatt, S.P. and Whipple, F.L., 1950. The Poynting-Robertson effect on meteor orbits. *The Astrophysical Journal*, 111:134-141.
428. Xia F., Brugger J., Chen G., Ngorthai Y., O'Neil B., Putnis A., and Pring A. 2009. Mechanisms and kinetics of pseudomorphic mineral replacement reactions: A case study of the replacement of pentlandite by violarite. Geochimica et Cosmochimica Acta, 73:1945-1969, doi:10.1016/j.gca.2009.01.007.

429. Yang, B. and Jewitt, D., 2010. Identification of magnetite in B-type asteroids. The Astronomical Journal, 140:692-698, doi:10.1088/0004-6256/140/3/692.
430. Yiou, F., Raisbeck, G.M. and Jéhanno, C., 1989. Influx of cosmic spherules to the Earth during the last ~10^5 years as deduced from concentrations in Antarctic ice cores: Meteoritics, 24:344.
431. Yong Technology Inc., 2014. GeoRose. http://www.yongtechnology.com/download/georose.
432. Yu, Z., 1984. Two new minerals, gupeiite and xifengite in cosmic spherules from Yanshan China. Acta Petrologica Mineralogica Analytica 3:231–238.
433. Zappala, V., Bendjoya, P., Cellino, A., Farinella, P. and Froeschlé, C., 1995. Asteroid families: Search of a 12,487-asteroid sample using two different clustering techniques. Icarus, 116:291-314, doi10.1006/icar.1995.1127.
434. Zega, T.J. and Buseck, P.R., 2003. Fine-grained-rim mineralogy of the Cold Bokkeveld CM chondrite. Geochimica et Cosmochimica Acta, 67:1711-1721, doi:10.1016/S0016-7037(02)01172-9.
435. Zhang, M., Redfern, S.A., Salje, E.K., Carpenter, M.A. and Wang, L., 2010. H_2O and the dehydroxylation of phyllosilicates: An infrared spectroscopic study. American Mineralogist, 95:1686-1693, doi:10.2138/am.2010.3561.
436. Ziffer, J., Campins, H., Licandro, J., Walker, M.E., Fernandez, Y., Clark, B.E., Mothe-Diniz, T., Howell, E. and Deshpande, R., 2011. Near-infrared spectroscopy of primitive asteroid families. Icarus, 213:538-546, doi:10.1016/j.icarus.2011.04.008.
437. Zijlstra, J.J.P., 1994. Sedimentology of the Late Cretaceous and Early Tertiary (tuffaceous) chalk of northwest Europe, 119:1-192. Utrecht University, ISBN -90-71577-73-2.
438. Zolensky, M., Barrett, R. and Browning, L., 1993. Mineralogy and composition of matrix and chondrule rims in carbonaceous chondrites. Geochimica et Cosmochimica Acta, 57:3123-3148, doi:10.1016/0016-7037(93)90298-B
439. Zolensky, M.E., Ivanov, A.V., Yang, S.V., Mittlefehldt, D.W. and Ohsumi, K., 1996a. The Kaidun meteorite: Mineralogy of an unusual CM1 lithology. Meteoritics & Planetary Science, 31:484-493, doi:10.1111/j.1945-5100.1996.tb02090.x.
440. Zolensky, M.E., Weisberg, M.K., Buchanan, P.C. and Mittlefehldt, D.W., 1996b. Mineralogy of carbonaceous chondrite clasts in HED achondrites and the Moon. Meteoritics & Planetary Science, 31:518-537, doi:10.1111/j.1945-5100.1996.tb02093.x.
441. Zolensky, M.E., Mittlefehldt, D.W., Lipschutz, M.E., Wang, M.S., Clayton, R.N., Mayeda, T.K., Grady, M.M., Pillinger, C. and David, B., 1997. CM chondrites exhibit the complete petrologic range from type 2 to 1. Geochimica et Cosmochimica Acta, 61:5099-5115, doi:10.1016/S0016-7037(97)00357-8.
442. Zolensky, M.E., Nakamura, K., Gounelle, M., Mikouchi, T., Kasama, T., Tachikawa, O. and Tonui, E., 2002. Mineralogy of Tagish Lake: An ungrouped type 2 carbonaceous chondrite. Meteoritics & Planetary Science, 37:737-761, doi:10.1111/j.1945-5100.2002.tb00852.x.
443. Zolensky, M., Bland, P., Brown, P. and Halliday, I., 2006. Flux of extraterrestrial materials. In: Lauretta, D.S., McSween, H.Y., ed. Meteorites and the early solar system II. University of Arizona Press, p.869-888.
444. Zolensky, M., Mikouchi, T., Hagiya, K., Ohsumi, K., Komatsu, M., and Le, L. 2014a. Evidence for Impact Shock Melting in CM and CI Chondrite Regolith Samples (abstract #2261) 44th Lunar and Planetary Science Conference. CD-ROM.
445. Zolensky, M., Mikouchi, T., Fries, M., Bodnar, R., Jenniskens, P., Yin, Q.Z., Hagiya, K., Ohsumi, K., Komatsu, M., Colbert, M. and Hanna, R., 2014b. Mineralogy and petrography of C asteroid regolith: The Sutter's Mill CM meteorite. Meteoritics and Planetary Science 49:1997-2016, doi:10.1111/maps.12386.
446. Zolensky, M., Mikouchi, T., Hagiya, K., Ohsumi, K., Komatsu, M., Chan, Q.H., Le, L., Kring, D., Cato, M., Fagan, A.L. and Gross, J., 2016. Unique View of C Asteriod Regolith from the Jbilet Winselwan CM Chondrite: 47th Lunar and Planetary Science Conference, held 21-25 Mar. 2016; The Woodlands, TX; United States. (abstract #3154).
447. Zolensky, M. and Le, L., 2017. Asteroid Pond Mineralogy: View from a Cognate Clast in LL3 NWA 8330: 80th Annual Meeting of the Meteoritical Society, held July 23rd-28th, 2017 in Santa Fe, New Mexico, USA. (abstract #6164).
448. Zolotov, M.Y., 2012. Aqueous fluid composition in CI chondritic materials: chemical equilibrium assessments in closed systems. Icarus, 220:713-729, doi:10.1016/j.icarus.2012.05.036.